1

OAK RIDGE NATIONAL LABORATORY
operated by
UNION CARBIDE CORPORATION
NUCLEAR DIVISION
for the
U.S. ATOMIC ENERGY COMMISSION

UNION CARBIDE

ORNL - TM - 2217

FUELS AND MATERIALS DEVELOPMENT PROGRAM QUARTERLY PROGRESS REPORT FOR PERIOD ENDING MARCH 31, 1968

Compiled by
P. Patriarca

LEGAL NOTICE

ORNL-TM-2217

Contract No. W-7405-eng-26

FUELS AND MATERIALS DEVELOPMENT PROGRAM QUARTERLY PROGRESS REPORT FOR PERIOD ENDING MARCH 31, 1968

Compiled by
P. Patriarca

JUNE 1968

OAK RIDGE NATIONAL LABORATORY
Oak Ridge, Tennessee
operated by
UNION CARBIDE CORPORATION
for the
U.S. ATOMIC ENERGY COMMISSION

FOREWORD

This is the sixteenth quarterly progress report describing work performed at the Oak Ridge National Laboratory for the Fuels and Materials Branch, Division of Reactor Development and Technology, U.S. Atomic Energy Commission. The specific programs covered are as follows:

Program Title	Person in Charge	Principal Investigator(s)
Part I. Metals and Ceramics Division		
Fuel Element Fabrication Development	G. M. Adamson, Jr.	W. R. Martin
Joining Research on Nuclear Materials	G. M. Adamson, Jr.	G. M. Slaughter
Mechanical Properties Research and LMFBR Cladding	C. J. McHargue	J. R. Weir, Jr.
Mixed Nitride Fuels Development	W. O. Harms	J. L. Scott
Nondestructive Test Development	W. O. Harms	R. W. McClung
Sintered Aluminum Products Development	G. M. Adamson, Jr.	W. R. Martin D. G. Harman
Sol-Gel Fast Reactor Fuels	P. Patriarca	A. L. Lotts J. L. Scott R. G. Wymer*
Zirconium Metallurgy	C. J. McHargue	P. L. Rittenhouse
Part II. Reactor Chemistry Division		
Fission-Gas Release and Physical Properties of Fuel Materials During Irradiation	O. Sisman	R. M. Carroll J. G. Morgan
Part III. Solid State Division		
Irradiation Effects on Alloys and Structural Materials	D. S. Billington	M. S. Wechsler J. T. Stanley

*Chemical Technology Division.

CONTENTS

Part III. Solid State Division

SUMMARY

PART I. METALS AND CERAMICS DIVISION

1. Fuel Element Fabrication Development

We continue to investigate the fabrication characteristics and in-reactor performance of dead-burned U_3O_8 because of the economical potential offered by this type fuel over the presently used hi-fired type oxide. While such an oxide possesses many characteristics that do not meet those presently required by HFIR specifications, acceptable fuel plates have been fabricated using it; however, its radiation performance has not been demonstrated. Difficulty has been encountered in obtaining adequate size separation of both hi-fired and burned U_3O_8. While reproducible results can be obtained under a given set of conditions, additional screening usually reveals changes. To obtain stable separations, several screening runs with either a Ro-Tap or Cenco vibrating shaker are required. The trouble arises primarily from incomplete separation aggravated by some particle breakup.

The size distribution obtained by grinding UAl_x has been shown to be not greatly dependent upon the grinding technique. Difficulty is encountered in obtaining material which passes a −140 mesh screen without yielding a large proportion of fines. Heat treating the powders before grinding shows some promise of alleviating the problem.

Studies exploring the potential of various growth inhibitors indicate that additions of silicon, germanium, tin, and zirconium reduce the swelling of UAl_3 on heating; the effectiveness of silicon and germanium is increased with additive concentration while tin and zirconium show a maximum effect in the concentration curves. Either silicon or zirconium concentrations of about 3%, however, show the most promise.

An economic evaluation was made for the production of UO_2 powder using the flame reactor. The process is competitive with other techniques. It has shown that it is possible to deposit duplex powders containing UO_2 and tungsten by use of the flame reactor. Powders with varying tungsten contents were produced and pressed into pellets.

Such compacts show a very large reduction in electrical resistance when compared to UO_2. While the as-produced powders were high in fluorine content, it was reduced to acceptable by wet hydrogen treatments.

It was shown that the powder produced in the plutonium chemical vapor deposition rig was plutonium oxide.

2. Joining Research on Nuclear Materials

Weld cracking studies performed under subcontract at Rensselaer Polytechnic Institute indicate that a newly developed test (TIG-A-MA-JIG) may be quite sensitive in its ability to measure the effects of minor deviations in chemical analysis. With stainless steel, it was shown that sulfur definitely increases the hot-cracking sensitivity, while silicon and manganese produce minor, if any, effects. Phosphorus appears to be beneficial in the amounts tested. It has also been shown that small variations in the impurities in the argon shielding gas can produce dramatic weld-penetration differences in commercial Inconel 600.

Work has been initiated at ORNL on the effects of sulfur on the hot ductility of a high-nickel alloy (Inconel 600). Preliminary results show that the presence of 0.01% S decreases the "on heating" ductility at 2400°F to about 4%. Ductilities in excess of 90% were obtained for similar compositions without sulfur.

3. Mechanical Properties Research and LMFBR Cladding and Structural Materials Development

This program involves studies of radiation damage to alloys of interest mainly as fuel cladding. The current results are for types 304 and 316 stainless steel, Incoloy 800, and Hastelloy N, each containing various amounts of titanium.

Results of postirradiation tests of large (1500-lb) heats of titanium-modified types 304 and 304L stainless steel are currently being compared. Insufficient data on the high-carbon version are available to allow conclusions to be drawn concerning the relative behavior of the two compositions.

Successful experimental tubing fabrication of the titanium-modified type 304L stainless steel has been completed. We found that it was necessary to homogenize the ingots prior to extrusion to remove a second phase resulting from segregation during solidification. We observed some minor differences in the tube fabrication behavior of the modified alloy as compared to standard type 304 stainless steel.

Neutron irradiation produces reductions in the creep-rupture strength and ductility of standard type 316 stainless steel, and the magnitude of the effects is dependent on irradiation temperature in the range 550 to 750°C. Tensile data are presented for a few heats of titanium-modified type 316 stainless steel. The few creep-rupture results indicate that the postirradiation strength and ductility of the titanium-modified type 316 stainless steel are improved over that of the standard alloy.

Data for Incoloy 800 containing various titanium levels indicate that an alloy containing 0.1% Ti exhibits improved postirradiation ductility at low strain rates.

Examination in the electron microscope of EBR-II cladding revealed the existence of voids throughout the alloy. The size distribution of the voids depends on both the fluence and the irradiation temperature.

4. Mixed Nitride Fuels Development

We continued the study of the kinetics of the synthesis of uranium carbides, nitrides, and carbonitrides from sol-gel UO_2 as well as the reaction of nitrogen with "UC_2" to produce U(C,N). The equipment was altered to permit removal of samples during a run and also to provide for automatic control of nitrogen pressure. Base-line data were obtained for conversion of aged "UC_2" containing free carbon; the reaction followed the predictions for a diffusion-controlled reaction to 100% conversion. We also extended the investigation of the new compound found when UO_2 is reacted in the presence of carbon and nitrogen.

We synthesized and fabricated UN and U(C,N) powders and pellets to satisfy a continuing need for research materials. Process techniques and glove box procedures were altered to further reduce oxygen contamination in the nitride product. Difficulty in preparing high-density pellets by a sequence that had previously produced a satisfactory product led to the disclosure that the U_2N_3 intermediary is not completely decomposed on heating at 850°C.

British work has shown that grain-boundary segregation of impurities at low concentration can take place in several metal-oxide systems. Since this segregation may influence greatly those properties related to diffusion in and of grain boundaries, we plan to look for segregation of oxygen in UN by autoradiography and microhardness measurements. An apparatus was assembled in which UN powder will be oxidized with ^{18}O; this in turn will be converted by proton bombardment to ^{18}F which decays by positron emission. No dependence on oxygen impurity was found for microhardness measurements.

We are preparing to study the compatibility of UN and U(C,N) with container materials. Capsules were fabricated and a rig for heating the samples was built.

We are also assembling the equipment necessary to obtain hot-hardness measurements up to 1200°C on fuel ranging in composition between UC and UN. These measurements will give an indication of high-temperature strength and will, in turn, provide a guide for selecting the most appropriate compositions for creep measurements under irradiation.

Additional thermodynamic measurements were made on the U-C-N system during this quarter. The analytical portion of the work was completed on equilibration experiments for compositions spanning the single-phase U(C,N) region. The results show that the UC-UN solid solution does not obey Vegard's law in the ranges studied and that the width of the phase is narrow.

We calculated equilibrium interactions of vanadium with uranium, plutonium, and mixed metal oxides, carbides, and nitrides using available thermodynamic data. We began experimental measurements of the equilibrium phase behavior of the uranium-vanadium-nitrogen system.

We intend to determine by calculations and experiments the effect of changing chemical composition due to irradiation of the fuel on mixed nitride fuel and its container. Calculations show that the excess nitrogen released due to fissioning of heavy-metal atoms could lead to formation of several percent of U_2N_3. Available thermodynamic data indicate that U_2N_3 can nitride possible clad elements such as Cr, V, Nb, Ti, and Zr. Methods of prohibiting the formation of U_2N_3 are discussed.

5. Nondestructive Test Development

We are developing new techniques and equipment for the nondestructive evaluation of materials and components. Major emphasis has been on eddy-current, ultrasonic, penetrating-radiation, and holographic methods.

Our analytical work on electromagnetic phenomena is being directed to the derivation of integral equations to allow calculation of defect sensitivity. Computer programs have been derived and used for the numerical evaluation of the effect of lift-off and specimen thickness in techniques using the phase-sensitive eddy-current instruments.

Design changes were made to allow a larger viewing area in the optical system for the visualization of ultrasound. The signal-to-noise ratio has been improved in the ultrasonic frequency analysis system and sufficient modifications have been made so an X-Y recorder can be used for cataloging of spectra.

We are continuing the study of holography for applications to nondestructive testing. A device is being built to measure laser-beam intensity to allow better control on the ratio between reference and object beams.

6. Sintered Aluminum Products Development

We have investigated the processes used to fabricate primary billets of SAP. We have experimentally studied the effects of many processing variables during each of the steps of primary billet fabrication. We have finished all experiments and are now preparing final specification and reports.

Our recent experiments have shown that the concentration of iron and carbon can be controlled easily during processing at levels below that necessary to affect short-time properties. Reproducibility of the billet fabrication process has been established and is presently limited only by product variations during the ball-milling operation. The tensile strength of SAP material produced by the ORNL process is superior to that of commercial SAP that contains an equivalent concentration of oxide.

We have finished a study of the influence of secondary working processes on the properties of SAP and are writing a final report.

Our experimental efforts toward developing a ductile SAP alloy are continuing. We are milling and consolidating dispersion-strengthened aluminum (DSA) atomized alloy powders by the ORNL primary billet fabrication process.

7. Sol-Gel Fast Reactor Fuels

We continued the preparation, development, and testing of sol-gel-derived fuels for fast reactors. We installed additional equipment for the fabrication and out-of-reactor characterization of plutonium-bearing materials. Approximately 1/2 kg of UO_2–20% PuO_2 was prepared for fabrication studies and for irradiation test capsules, and 485 g of PuO_2 sol was prepared for pelletizing studies.

We investigated methods for converting mixed urania-plutonia sols into powders suitable for pressing and sintering into dense pellets. Various pressing and sintering procedures were also investigated. Thus far in the program we have achieved 86% of theoretical density by pressing at 40,000 psi and sintering by a schedule attaining a maximum temperature of 1450°C. The experiments have indicated that the heating rates up to 1000°C must be optimized in order to get increased density above 86% of theoretical. In the Sphere-Pac program, we developed a graphical construction, which can be used to correlate and generalize all of the experiments that have been conducted to relate the variables of particle size and particle size distribution to fuel density.

The examination of the third uninstrumented capsule removed from the ETR has continued with emphasis upon burnup analyses. The primary reason for removing this third capsule after exposure of only one reactor cycle was to obtain experimental confirmation of our fission-rate calculations. The analytical results agree quite well with the predictions of the ANISN code that is used for design calculations. The first ORR capsule, which is an instrumented test of Sphere-Pac fuel, was constructed and is ready for installation in the ORR poolside position during the April 5, 1968, shutdown.

8. Zirconium Metallurgy

Biaxial testing of Zircaloy tubing is continuing at a number of stress ratios. The properties defined by these tests are to be correlated with texture measurements now being made.

The fabrication of experimental lots of Zircaloy-4 tubing is in progress. We have completed the tube shell extrusions and are preparing to cold reduce by tube rocking. Techniques for cold drawing have been developed.

A new x-ray device has been developed to aid in the analysis of circumferential texture variations in tubing. This device is capable of both rotating and translating the tubes so that the x-ray scan covers the entire surface.

In our study of the development of texture in zirconium and zirconium alloys, we are using computer programs to obtain sophisticated Schmid factor analysis techniques. Investigation of elevated temperature deformation mechanisms is beginning.

PART II. REACTOR CHEMISTRY DIVISION

Fission-Gas Release and Physical Properties of Fuel Materials During Irradiation

Fission-gas release from UO_2 is being studied in an effort to determine the mechanism by which the gas migrates and escapes from the fuel. From these studies we hope to develop a model to make engineering calculations of noble-gas escape from operating fuel materials. Our

experimental method is to irradiate carefully selected and characterized specimens in a facility where the neutron flux and temperature are controlled independently. Fission gas released from the specimen is entrained in a moving stream of sweep gas and carried outside the reactor, where it is analyzed by gamma-ray spectrometry.

Spheres of 48%-enriched single-crystal UO_2 are being irradiated to find the effect of fission density and burnup. We find that at fission densities of greater than 9×10^{13} fissions cm^{-3} sec^{-1} an increase of fission density results in an enhanced escape rate of fission gas. Using this and other data, we have determined the relation of fission-gas release as a function of fission density.

The enriched single-crystal UO_2 spheres were irradiated to 4.6% U burnup. The fission-gas release decreased at first because of irradiation smoothing of the specimen surface. An equilibrium release rate was soon achieved which lasted until a burnup of 1.9% U. The gas release then increased rapidly with burnup until about 2.5% U burnup. From 2.5 to 4.6% U burnup, the gas-release rate increased slowly as burnup progressed.

PART III. SOLID STATE DIVISION

Irradiation Effects on Alloys and Structural Materials

Investigations into radiation damage, hardening, and embrittlement in the body-centered cubic metals are continuing. This report covers recent work on pressure vessel steels, niobium, and vanadium.

Tensile and impact samples of a particular heat of ASTM A-212, grade B, steel have been irradiated in the same facility in the Oak Ridge Research Reactor to the same fluence and at the same temperature. The samples were tested over a range of temperatures from about 30 to 473°K and, for the tensile samples, at several strain rates. The yield stress increased strongly with decreasing test temperature, but the increase in yield stress upon irradiation was largely the same for all test temperatures. Strain rate and triaxiality corrections were applied to the tensile data in order to evaluate yield conditions near the root

of the notched-bar impact samples. The ductile-to-brittle transition temperature under notch-impact loading for unirradiated and irradiated steel was found to be consistent with a simple criterion for brittle fracture. However, it was necessary to assume that cleavage crack initiation occurs at a point of lower triaxiality (closer to the root of the notch) in the irradiated steel.

Annealing and strain aging experiments on irradiated steel were also conducted, which indicate the effect of the trapping of interstitial elements at radiation-produced defect clusters.

In order to determine whether thermal neutrons have an effect on the radiation hardening of ASTM A-212 and A-302, grade B, steels tensile samples were irradiated with and without cadmium shielding. No difference in the radiation hardening was detected, in agreement with similar previous experiments on Charpy impact samples.

Mechanical property tests are described on samples taken from a 12-in.-thick plate of ASTM A-533, grade B, steel.

Internal friction and electrical resistivity measurements have revealed the trapping of interstitial elements (chiefly oxygen and nitrogen) in neutron-irradiated niobium and vanadium. For niobium, the temperatures for the dissociation of interstitial elements from the traps have also been determined.

Various aspects of radiation hardening in niobium are described. Transmission electron microscopy was used to detect the density and size distribution of defect clusters observed upon irradiation and upon postirradiation annealing. The extent to which these may be correlated with radiation hardening and radiation-anneal-hardening is discussed. A discussion is also given of experiments on the fluence and temperature dependence of radiation hardening in niobium.

Finally, work is described bearing on the techniques of preparation and evaluation of niobium materials.

[redacted]

PART I.

METALS AND CERAMICS DIVISION

[redacted]

1. FUEL ELEMENT FABRICATION DEVELOPMENT

G. M. Adamson, Jr.

Factors affecting plate fabrication and irradiation performance for research reactor fuel elements are being investigated. These studies should lead to the fabrication of plates with increased fuel loadings, permit the use of cheaper fuels, provide assurance that a given fabrication practice will produce satisfactory plates, permit predictions of the effects on plate quality of changes in production equipment and processes, reduce the development work and lead time necessary for long-range new-generation fuels, generate data that will improve the quality of specifications, and permit rapid solution to the problems that continually arise in the shops of the industrial fabricators. Other efforts are being devoted to improving the reliability and reducing the cost of the nondestructive inspection techniques for the fuel plates.

We have continued at a reduced effort the direct conversion of fissionable halides to refractory fuel compounds by chemical vapor deposition. Emphasis is gradually being shifted from the uranium to the plutonium system.

Characterization of Burned U_3O_8 Powders

J. T. Venard W. R. Martin

In our quest for a more economical fuel for HFIR, we became interested in a material referred to as "burned U_3O_8." This material is obtained very early in the processing scheme used by Y-12 for the production of the dead-burned U_3O_8 now used in HFIR.

The burned U_3O_8 that was characterized came from a single 2-kg lot of −100 mesh depleted material supplied by Y-12. A photomicrograph showing the structure of the material appears in Fig. 1.1. Lines from a Debye-Scherrer powder camera sample were indexed to be the hexagonal form of U_3O_8 and no lines were found for metallic uranium. A sample of the material was submitted for microprobe analysis of metallic chips.

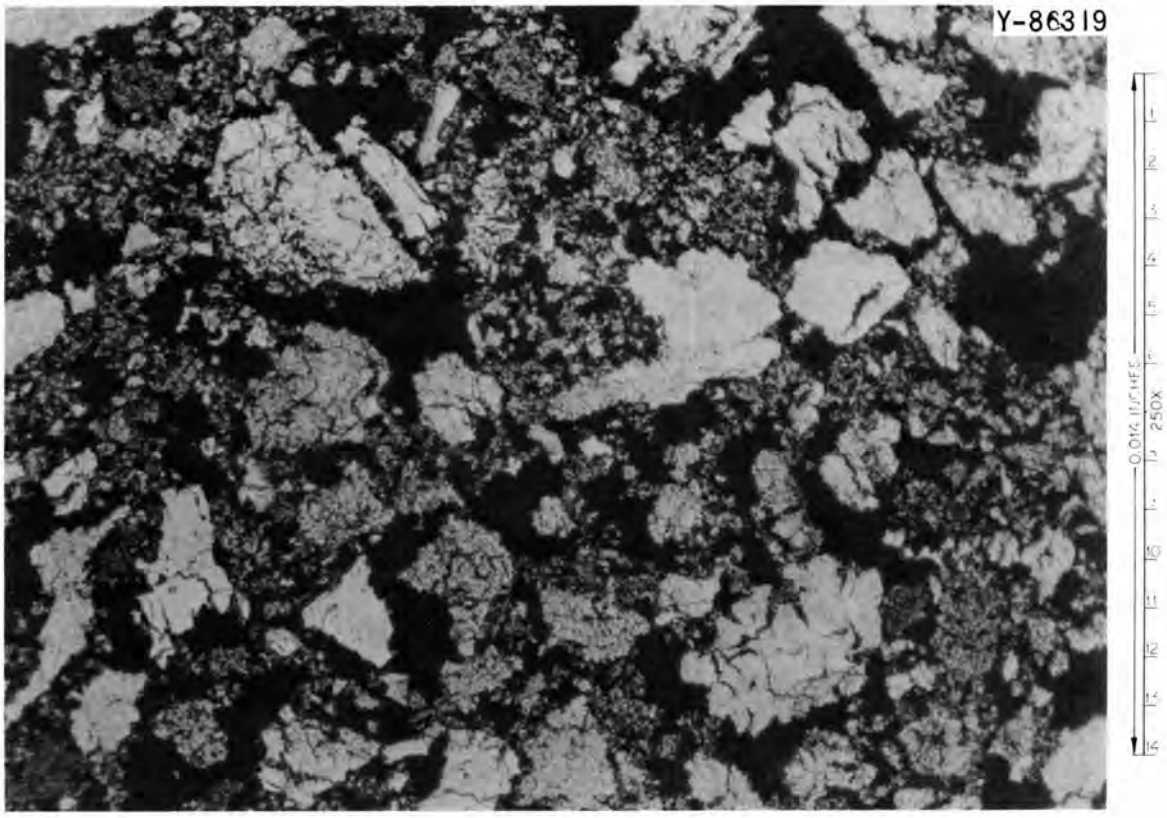

Fig. 1.1. Photomicrograph of Burned U_3O_8 Showing Particle Shape and Internal Cracking of Powders.

Some of these were reported to be primarily iron, others primarily aluminum, and still others a copper-zirconium combination. No free uranium was found with the microprobe. Other analyses and their results are given in Table 1.1, which includes for comparison the current HFIR specification.

Judging from Table 1.1, insofar as the material can be compared with the HFIR specification, surface area, density, and screen analysis do not agree with that specified. The material is also out of specification with respect to fluorine, iron, manganese, and silicon impurity levels. The chemical purity of the material is not, however, felt to be a serious problem since starting material that can be selected will affect these impurity levels. The high surface area and low density of this fuel powder are probably inherent characteristics of the process, and their

Table 1.1. Characterization of Burned U_3O_8, Batch 1-3017

Measurement	Batch 1-3017	HFIR Specification
Uranium content, wt %		≥ 84.5
Enrichment, wt %	Depleted	> 93
Surface area (krypton BET determination), m^2/g	0.46	< 0.07
Density (toluene pycnometer), g/cm^3	7.94	> 8.2
UO_2, wt %		< 1
Oxygen-to-uranium ratio	2.66	None
Impurity analysis (spectrographic unless otherwise noted), ppm		
Al	2	100
B	0.2	0.2
Ba		10
Be	0.02	0.2
Ca	0.5	50
Cd (atomic absorption)	< 0.2	0.5
Co	< 0.1	3
Cr	1	15
Cu	2	220
F	30	< 10
Fe	140	100
K (flame spectroscopy)	1.5	20
Li (flame spectroscopy)	< 0.1	5
Mg	0.1	100
Mn	6	5
Na (flame spectroscopy)	< 1	5
Ni	6	20
P (calorimetric)	15	< 100
Si	70	50
V	0.05	2
Syntron sieve analysis (100-g sample for 1 hr), wt %		
+170	14.7	0
−170 +325	71.1	> 90
−325	14.2	< 10

importance must await fabrication and irradiation performance experience before a judgment is made.

All the above information gives one a reasonably clear picture of the "characteristics" of this fuel material. It has been shown that it is possible to fabricate fuel plates from this oxide with homogeneity and dimensions that meet the HFIR specifications. The decision on whether or not it will perform adequately as HFIR fuel must be based on additional blending, homogeneity, fabrication, and irradiation experiments now in progress.

U_3O_8 Size Separation

J. T. Venard M. M. Martin
W. R. Martin

We have experienced considerable difficulty in being able to characterize the particle-size distribution of either hi-fired or burned U_3O_8 with the accuracy desired for development work. It has been shown to be quite difficult to obtain size separations that do not change with additional screening. As was demonstrated during the original development work and confirmed during this study, the present screening techniques, if properly controlled, will, however, produce reproducible results with an accuracy sufficient for showing whether the material meets specifications.

Table 1.2 shows the results of successive operations to separate −170 +200 mesh fraction from 4 kg of hi-fired U_3O_8 as received from the production plant. As shown in Table 1.2, the third screening with a Cenco shaker yielded a size range that contained 93.7% of the −170 +200 mesh particles. In a subsequent sieve analysis using a Ro-Tap shaker, this separated fraction analyzed only 87.3% within the −170 +200 mesh range. Additional separations with the Ro-Tap shaker further concentrated the −170 +200 mesh fraction to 95.9%. With the exception of the initial Cenco screening of the U_3O_8, negligible generation of −325 mesh fines occurred during either Cenco or Ro-Tap shaking. Similar results were achieved on −200 +230 mesh material.

Table 1.2. Separation of the −170 +200 Mesh Fraction from As-Supplied U_3O_8

	Separation Trial					
	A	B	C	D	E	F
Sieve shaker	Cenco	Cenco	Cenco	Ro-Tap	Ro-Tap	Ro-Tap
Shaking period, min	30	30	30	15	15	15
Maximum sieved per run, g	500–800	200	155	100	163	152
Initial distribution, wt %						
−170 +200	a	100	100	100	100	100
Prior treatment	Cenco-sieved at Y-12 Plant	A	B	C	D	E
Final distribution, wt %						
+170	4.0	0.0	0.0	0.0	0.0	0.0
−170 +200	40.2	77.4	93.7	87.3	93.2	95.9
−200 +230	8.7	17.1	6.0	12.0	6.4	3.9
−230 +270	15.8	5.2	0.2	0.7	0.1	< 0.1
−270 +325	16.2	0.2	< 0.1	< 0.1	< 0.1	0.1
−325	15.1	0.1	< 0.1	< 0.1	0.3	0.1

[a]100% passing through 170 and retained upon 325 screen in the producer's plant.

To prepare a desired fuel compound blend for the fabrication studies discussed in a following section, the U_3O_8 particles were separated into known mesh fractions and then recombined in the desired proportions. The powders were sieved twice using the Ro-Tap shaker to effect the separation. The weighed proportions were then blended obliquely for 2 hr inside a glass bottle that contained approximately 75% mixing void volume. Table 1.3 shows the particle-size distribution achieved by this technique as shown by samples of the final blend.

A set of screening experiments were made to determine the reproducibility of screening techniques when used with the less dense burned U_3O_8. Identical 100-g samples were taken from the −100 mesh as-received batch and five of these samples were run on the Cenco shaker for 1 hr

Table 1.3. Sieve Analysis of Hi-Fired U_3O_8 Prepared for Compression Yield Strength Studies on Fuel Dispersions

Particle Size		Distribution, wt %	
ASTM Mesh Number	Micrometer	Actual	Designed
+200 −170	> 74 < 88	22.9	25.0
+230 −200	> 63 < 74	23.5	25.0
+270 −230	> 53 < 63	26.0	25.0
+325 −270	> 44 < 53	25.2	25.0
−325	< 44	2.4	0
Total		100.0	100.0

while another five samples were screened on a Ro-Tap for 15 min. Table 1.4 indicates that, for a given technique, the results are comparable and reproducible.

To determine whether or not these standard techniques give a true screen analysis, two additional 100-g samples were given five successive screenings. Each sample was shaken on the Cenco or Ro-Tap for a total time of 75 min, respectively. After 15 min, the screen fractions were weighed and then replaced in their respective screens and run in the shaker for an equivalent time until five successive screenings had been made. Figures 1.2 and 1.3 are plots showing these results. In comparing these data, it is clear that the distribution shifts with each screening towards a greater portion of the sample falling in smaller screens. It is also seen that five successive screenings on the Cenco are required to give separation roughly equivalent to three successive screenings on the Ro-Tap. It is apparent that more of the smaller particles (−325) accumulate during subsequent screenings with the burned oxide than was found with the hi-fired oxide.

Table 1.5 illustrates the results of shaking on the Cenco for 6 hr or on Ro-Tap for 75 min. The data indicate reasonable reproducibility from sample to sample for a given shaker and show much closer agreement between Cenco and Ro-Tap screen analyses. The differences between the analyses of Tables 1.4 and 1.5 pose the question of whether particle

Table 1.4. Screening Reproducibility of Burned U_3O_8, Batch I-3017

Sample Number	Size Fraction, %						
	+100	−100 +170	−170 +200	−200 +230	−230 +270	−270 +325	−325
			100 g in Cenco for 1 hr				
3	0.01	19.22	13.34	18.23	12.67	17.84	18.58
4	0.21	24.89	9.84	10.06	20.98	17.11	16.71
5	0.40	25.49	8.83	10.34	20.49	19.21	15.09
6	0.07	25.11	15.80	13.50	12.42	17.11	15.71
7	0.01	20.70	8.15	17.64	16.20	17.94	19.25
Average	0.14	23.08	11.19	13.95	16.55	17.84	17.07
			100 g in Ro-Tap for 15 min				
8	0.00	2.48	20.42	15.20	14.91	18.34	28.48
9	0.00	2.85	20.37	15.07	14.62	19.04	27.82
10	0.00	3.47	20.12	15.76	15.44	18.39	26.72
11	0.00	3.01	20.36	15.17	14.43	19.67	27.18
12	0.00	4.90	20.41	13.98	15.66	18.41	26.44
Average	0.00	3.34	20.33	15.03	15.01	18.77	27.33

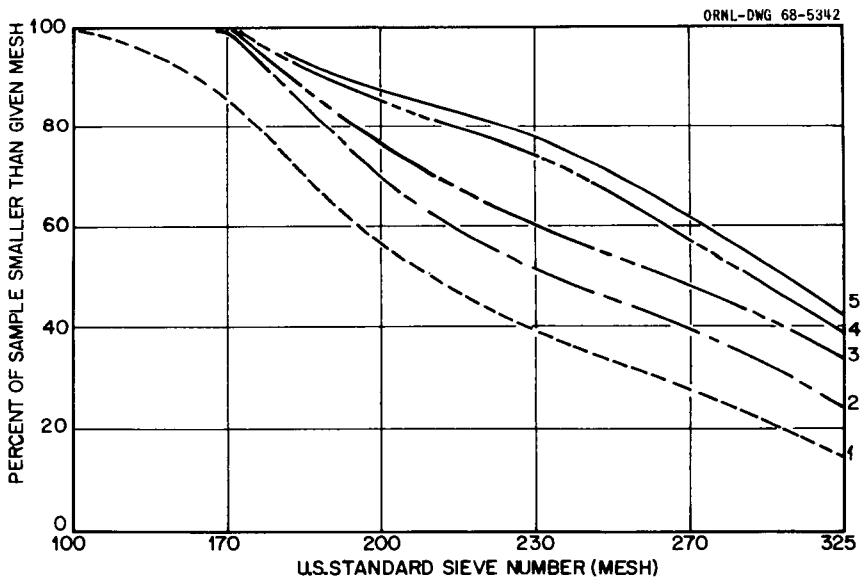

Fig. 1.2. Results of 100-g Samples of Burned U_3O_8 After Successive Cenco Screening for 1 hr.

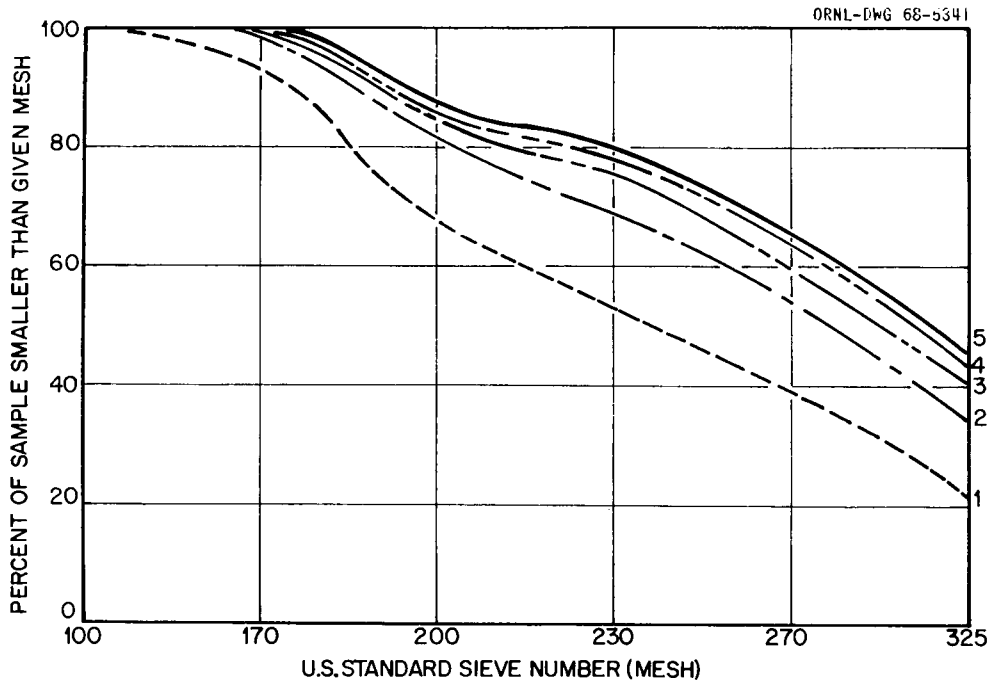

Fig. 1.3. Results of Successive Ro-Tap Screening 100-g Samples of Burned U_3O_8 for 15 min.

Table 1.5. Screening Reproducibility of Burned U_3O_8, Batch I-3017

Sample Number	Size Fraction, %						
	+100	−100 +170	−170 +200	−200 +230	−230 +270	−270 +325	−325
	100 g in Cenco for 6 hr						
1	0.02	0.38	19.58	12.18	10.31	13.17	44.02
2	0.00	0.31	16.65	11.66	9.51	15.32	46.37
3	0.05	0.49	18.51	9.51	11.32	15.09	44.81
4	0.02	0.58	18.22	11.07	10.00	16.42	43.42
5	0.03	0.56	21.61	11.83	11.42	11.88	42.46
	100 g in Ro-Tap for 1 1/2 hr						
1	0	0.41	11.97	8.30	14.05	18.12	46.86
2	0	0.60	11.80	8.31	14.78	16.78	47.54
3	0	0.46	12.66	8.23	13.50	18.01	47.06
4	0	0.61	12.17	8.18	13.65	18.41	46.86
5	0	0.68	11.86	8.29	13.81	18.48	46.17

breakup is occurring or whether the differences are simply due to incomplete separation of screen fractions.

In an attempt to resolve this question, individual 100-g samples were run on the Cenco shaker for periods of 1 and 5 hr and on the Ro-Tap for 15- and 75-min screenings. Surface area measurements were made on screen fraction from these runs and the results are shown in Table 1.6.

Table 1.6. Results of Screening Time on Surface Area

Screening Techniques (100-g Samples)	Surface Area, m^2/g, of Screen Fractions			
	−170 +200	−200 +230	−230 +270	−270 +325
Cenco, 1 hr	0.59	0.69	0.65	0.62
Cenco, 5 hr	0.49	0.56	0.58	0.56
Ro-Tap, 15 min	0.48	0.66	0.68	0.62
Ro-Tap, 75 min	0.44	0.45	0.44	0.57

If incomplete separation of particle size is the reason for the discrepancy between long- and short-time screenings, then one would expect a larger surface area measurement on the screen fractions from the short-time run, since they will contain unseparated small particles and fines. If, on the other hand, the particles are breaking up during the longer screenings, one would expect only a shift in particle-size distribution with small or no differences in surface area for a given size fraction. Table 1.6 shows that surface area goes down, but not greatly, for a given screen size with increased screening time. One can, therefore, conclude that 1 hr on a Cenco or 15 min on a Ro-Tap is not sufficient to give a true particle-size analysis for this material.

A sample of −325 fraction obtained from some of the tests above was run on a Sonic Sifter using precision screens. The particle-size distribution found was 57% 44 to 30 μm, 41% 30 to 20 μm, 1% 20 to 10 μm, and 1% less than 10 μm. The material tended to ball up during this screening and, consequently, the results may be suspect.

UAl_x Particle Preparation

M. M. Martin W. R. Martin

In the preparation of UAl_x, our immediate problem is the reduction of the arc-cast button to the desired particle size with production of a minimum of −325 mesh fines. The material crushed to date is UAl_3 containing about 75 wt % U. A distinguishing characteristic is that it burns and/or emits sparks when scratched or hammered in air. Previous work using crushing devices such as a diamond mortar and pestle or a rotating disk pulverizer yielded a minimum of 40% fines. In an attempt to decrease the yield of fines, we crushed this material with a hammer mill rotating at 3250 rpm. Table 1.7 records the size distribution determined by hand screening a sample from a 4000-g batch. Various combinations of (1) hole diameters from 0.250 to 0.020 in. for the internal mill screen and (2) size of feed particles to the mill were tried. Regardless of these crushing conditions, the mill produced mostly particles that were retained on a 140-mesh sieve. Of the material that passed through the 140-mesh sieve, the ratio of −140 +325 mesh fraction to fines was essentially 1.

Table 1.7. Particle-Size Distribution After Crushing +4 Mesh UAl_x in a Hammer Mill

Screen Size Number	Powder Distribution (wt %)
+4 (1027 μm)	0.0
+140 (105 μm) −4 (1027 μm)	78.5
+170 (88 μm) −140 (105 μm)	2.1
+200 (74 μm) −170 (88 μm)	2.7
+230 (63 μm) −200 (74 μm)	1.2
+270 (53 μm) −230 (63 μm)	1.3
+325 (44 μm) −270 (53 μm)	2.3
−325 (44 μm)	11.9
Total	100.0

To produce a sufficient quantity of UAl_x particles of the desired size, we utilized a 2.5-liter stainless steel rod mill to further crush the material. The advantage of this device in comparison to jaw, hammer, or ball mills is that the large particles supposedly hold the rods apart. Crushing of the smaller particles is therefore minimized until reduction of the larger sizes has occurred. Initially, rod milling of a small experimental batch of 300 g, however, gave little improvement; that is, the ratio of desired size to fines as determined for a 30-min screening with a Cenco shaker, remained essentially 1. We concluded that the yield of fines from hypostoichiometric UAl_3 does not depend primarily upon the crushing device used but upon the extremely brittle nature of the material.

To test this hypothesis, we annealed a small batch of UAl_x for 2 hr at 1000°C in an atmosphere of argon and then milled the conditioned material for 30 min in a rod mill. A sieve analysis using the Cenco shaking device for 30 min gave the following weight-to-size fractions: 7.5 g −325, 15.5 g −140 +325, and 275.0 g +140 mesh. Although the ratio of desired size to fines increased 100%, the vast majority of particles are still greater than +140 mesh.

Based on the results from the above 300-g batches, we annealed and then crushed an additional 3000 g of −4 +20 mesh UAl_x. The rod mill was charged with up to a maximum of 1755 g of the powder in a single run. Fourteen runs of 1- to 6-hr duration were required to obtain greater than 99.6% of −140 mesh particles. At the completion of each run, the material was screened on the Cenco shaker for 15 min; the successive run was charged only with oversized particles. After rod milling, a single Cenco sieve analysis indicated that the ratio of particles in the desired range to fines was approximately 2.

We then sieved 3000 g of the powder twice, using the Ro-Tap, and these results are shown in Table 1.8. In spite of the fact that we heat treated the material, the fines (< 44 μ) from the rod milling account for 52.4% of the distribution. Similar particle-size distributions for non-heat-treated material sieved using the Ro-Tap are not available. Therefore, we cannot yet assess the magnitude of the benefit derived from

Table 1.8. Particle-Size Distribution After Crushing −4 Mesh UAl_x in a Rod Mill

Screen Size Number	Powder Distribution (wt %)
+4 (1027 μm)	0.0
+140 (105 μm) −4 (1027 μm)	0.39
+170 (88 μm) −140 (105 μm)	12.18
+200 (74 μm) −170 (88 μm)	14.79
+230 (63 μm) −200 (74 μm)	5.83
+270 (53 μm) −230 (63 μm)	5.62
+325 (44 μm) −270 (53 μm)	8.81
−325 (44 μm)	52.38
Total	100.00

the heat treatment. We plan to further study the effect of heat treatment and also other crushing devices to minimize the generation of fines.

Fuel Plate Roll Bonding

M. M. Martin J. H. Erwin

The principal problem currently encountered in the fabrication of aluminum-base dispersion-type fuel plates at ORNL is nonhomogeneous deformation in the roll-bonding operation. The resultant defects in rolled plates may appear near the ends of the fueled region in the form of excessive core thickness, blister formation, and/or, in plane view, a gross departure of the core from the shape of a rectangular parallelepiped. The plate thickness is virtually independent of position, since the localized increase in the core is always affected by a corresponding decrease in the total cladding. We believe that the problem may stem from the following overlapping considerations:

1. characteristic differences in deformation between the fuel dispersion and the cladding,
2. either excessive or inadequate material to fill the picture-frame cavity,

3. inadequate control of rolling conditions to achieve uniform deformation throughout the billet per pass.

Table 1.9 illustrates the severity of this problem of localized increases in core thickness encountered in the fabrication of miniature

Table 1.9. Observations of Core Thickening in Miniature Fuel Plates Clad with Aluminum

Reference Plate Number	Fuel Dispersoid			Core Thickness[a]	
	Type	Core Concentration (wt %)	Loading of ^{235}U (g)	Average (mils)	Maximum Thickening[b] (%)
0-56-955	Hi-fired U_3O_8	50.2	2.75	19.8	21
0-3-892	Burned U_3O_8	44.8	2.21	19.6	22
0-56-876	Burned U_3O_8	51.0	2.75	21.2	23
0-24-958	Arc-cast UAl_x	48.6	2.20	20.6	26
0-57-879	Arc-cast UAl_x	58.5	2.76	20.7	55
0-57-962	Arc-cast UAl_x	58.9	2.75	19.7	52
0-57-966	Arc-cast UAl_x	58.8	2.75	19.9	66
0-57-972	Solid-state reaction UAl_3	57.4	2.75	19.9	56

[a]The desired fuel core thickness is 20 mils ±15%.

[b]Values based on average.

fuel plates. Maximum core thickening of 52 to 66% above the average thickness appears to be the rule for the UAl_x-bearing plates of highest loading. The UAl_x-aluminum composites of lower loading and also dispersions of both types of U_3O_8 in aluminum exhibit increases of only 21 to 26%.

Our initial efforts to elucidate the deformation behavior of advanced research reactor core materials will involve the determination of compression yield strength of U_3O_8- and UAl_x-aluminum powder compacts as a function of dispersoid concentration and temperature. The study will include both hi-fired and burned grades of U_3O_8 as well as two UAl_x intermetallics of 69 and 75 wt % U.

The fuels will be carefully characterized and fabricated into dispersion cylinders 0.5 in. in diameter by 0.5 in. high. The fuels have been prepared and characterized and fabrication of the cylinders is well under way.

Influence of Additives on the Swelling of UAl_x Dispersed in Aluminum

A. K. Chakraborty W. R. Martin

Additions of silicon, germanium, tin, and zirconium of different proportions stabilize the intermetallic compound UAl_3, which inhibits the formation of UAl_4 and thus reduces swelling. The mechanism of stability is not similar in all cases, since the existing phases present are not identical.

In order to study the swelling behavior, master alloys of uranium with zirconium, silicon, tin, and germanium were cast and then hydrided. These hydrided powders were blended with different proportions of uranium and aluminum powder, but in every case the combination of uranium plus added metal was kept constant at 74 wt %, it being assumed that any metal replaces uranium in UAl_3. The blended powders were cold pressed to pellets and the pellets in turn sintered at 1000°C in a graphite die for 1 hr to let the aluminum react while in the liquid phase.

These pellets were cooled slowly to room temperature and examined metallographically and with x-ray diffraction to identify the existing phases. In most cases the pellets consisted of UAl_2 + UAl_3 in varying proportions.

The uranium-aluminum compounds, thus made, were crushed to powder in a dry box and blended with 60 wt % Al in small bottles for each individual pellet. After 45 min of blending, these powders were pressed to 5-g pellets using 22 tsi. Compacts, prepared in the above way, were cleaned and the densities of the compacts were measured before and after heat treating for 1/2, 1, 2, 4, and 8 hr at 600°C.

The results of our experiments are tabulated in Table 1.10 and can be summarized as follows. In almost all cases a decrease in density was

Table 1.10. Isothermal Swelling of 40 wt % UAl_3 Dispersed in Aluminum and Annealed at 600°C

Alloy Addition		Phases Present (as hot pressed)	Percent Swelling Related to Initial Pellets During Heat Treatment at 600°C for				
Type	(wt %)		1/2 hr	1 hr	2 hr	4 hr	8 hr
Zirconium	1.48	UAl_2 + UAl_3	1.642	2.086	2.039	1.919	2.093
Zirconium	2.96	UAl_2 + UAl_3	0.784	0.826	0.863	0.822	1.042
Zirconium	4.44	UAl_2 + UAl_3	2.887	3.766	2.993	3.575	3.582
Zirconium	5.91	UAl_2 + UAl_3	4.011	4.346	4.629	4.644	5.219
14.0% Zr–31.0% Al-54.9% U[a]	14.0	UAl_3	0.219	0.542	0.060	0.261	0.360
Silicon	1.48		0.743	2.239	2.317	2.539	2.934
Silicon	2.96	UAl_2 + UAl_3	0.180	0.380	0.138	0.300	0.295
Silicon	4.44		0.119	0.366	0.098	0.060	0.236
Silicon	5.91		0.060	0.258	0.120	0.339	0.120
Germanium	1.48		0.243	1.485	1.432	1.709	1.729
Germanium	2.96		0.545	1.303	1.272	1.470	2.567
Germanium	4.44		0.246	0.385	0.061	0.201	0.200
Germanium	5.91		0.123	0.303	0.177	0.141	0.342
Tin	1.48		0.861	1.284	1.243	1.658	1.424
Tin[a]	3.77		0.110	0.306	−0.022	0.316	0.092
Tin[a]	4.44		2.650	2.840	2.593	3.659	3.029
Tin[a]	5.91		1.295	1.994	1.495	2.440	1.974

[a]Intermetallic prepared with raw materials.

found. Additions of zirconium and tin act in a similar way while those of germanium and silicon influence the swelling in a different manner. With the zirconium and tin content, the compacts swell at a rate which initially decreases with alloy content, but then increases with further additions. In the case of tin, the increase is greater than that for zirconium. With the increases of silicon and germanium content, swelling falls rapidly and approaches a constant value. A comparison of swelling behavior of zirconium and silicon is shown in Fig. 1.4. The swelling assumes, in all cases, a maximum value after 1 hr and does not change significantly even after a prolonged annealing of 8 hr, all values being included within the limits shown for each point.

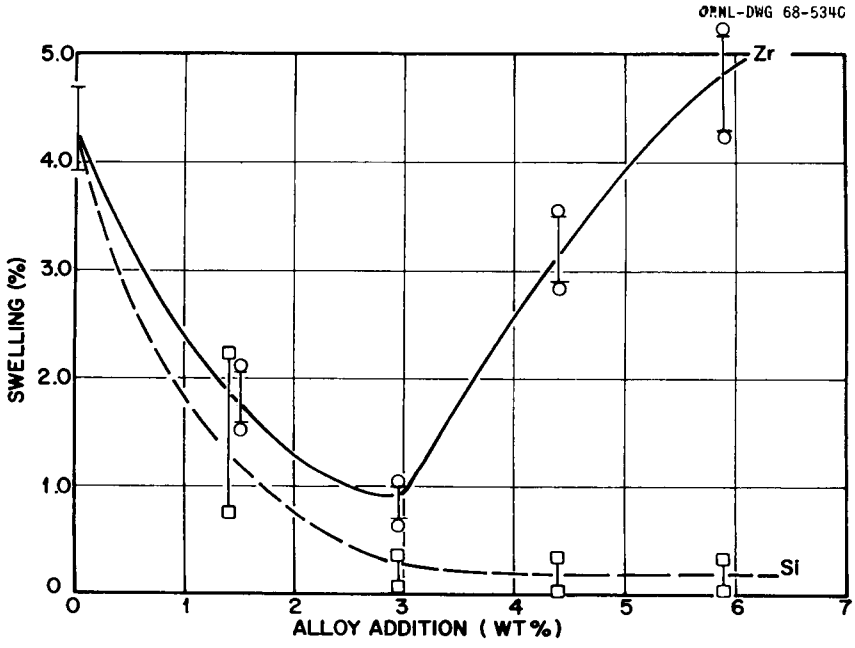

Fig. 1.4. Swelling Behavior of 40 wt % $U(Al,Si)_3$ and $U(Al,Zr)_3$ Intermetallic Fuel Compacts at 600°C. The compacts were heat treated for 1/2 to 8 hr in vacuum at 10^{-3} torr.

We then proceeded to identify the phases present in each sample before and after heat treatment. From the current data, it appears that silicon or germanium would be a useful addition for a wide range of compositions, whereas zirconium or tin additions would be restricted to approximately 3 wt %. Since silicon would be more practical than germanium, our initial efforts will be concentrated on characterizing the silicon system.

Plate Surface Studies

J. V. Cathcart

The buildup of corrosion product on aluminum fuel-element cladding in HFIR- and ATR-type reactors acts as a barrier to heat flow and limits the fuel loading that may be used. Our assignment is to devise a protective coating for the aluminum, and we have continued our efforts to develop an anodic film for aluminum alloys that will meet this need. Work during the last quarter was centered in two areas (1) flowing loop test and (2) investigations of the corrosion mechanism.

Flowing Loop Test

In order to test the protection afforded by an anodic coating on the 6061 aluminum alloys used in HFIR fuel elements, a test is being run in a flowing loop under heat flux conditions that simulate the reactor environment. The test is being conducted in cooperation with the Reactor Division. The test specimen, which is itself a part of the loop, is in the form of a slot with interior dimensions of $1 \times 6.5 \times 0.078$ in. We anodized the interior of the specimen in 1 wt % oxalic acid, the estimated thickness of the anodic film being approximately 0.0003 in. The test is currently in progress.

Investigations of the Corrosion Mechanism

Our previous work indicated that relatively thick anodic films formed on 99.999% Al provided excellent protection against corrosion in static, 200°C water for periods of several hundred hours. A reaction did occur, however, at the water-oxide interface which apparently involved primarily a slow conversion of the anodic film to Boehmite. Our subsequent work along these lines has been directed toward determining the rate of this reaction. We found that an anodic coating 2×10^{-5} in. thick provided very little protection; in a 24-hr test a significant fraction of the aluminum specimen itself was converted to Boehmite. A film 5×10^{-5} in. thick provided protection for approximately 75 hr, while a 25×10^{-5} in. film began to show signs of breakdown

after about 200 hr. A 50×10^{-5} in. film showed no signs of breakdown after 350 hr. The specimens were examined in cross section by electron microscopy after corrosion, and the previously described pattern of attack was evident in all cases.

Currently we are attempting to alter the corrosion properties of the anodic oxide by absorbing various inorganic ions in the pores of the films.

Irradiation Testing of Dispersion Plates

Irradiation Testing of Miniature Fuel Plates (M. M. Martin, A. E. Richt, W. R. Martin)

The six plates that bowed in the G-12 loop during ETR cycle 93A have been returned to ORNL and transferred into the hot cells for post-irradiation examination. As fabricated, these plates were 5.75 in. long by 1.25 in. wide by 0.050 in. thick. One plate contains a core of 53 wt % U_3O_8–Al while the remaining five have cores of 59 wt % UAl_x–Al. Our analysis will attempt to determine the reason for bowing after being exposed for only 567 Mwd in the loop.

The bowed miniature plates could not be easily removed from the irradiation holder. This is in marked contrast to the ease in which the samples were inserted into the holders prior to irradiation. Discolorations have been noted on the backside of the holder and at a position on the adjacent miniature plate that corresponds to one of three holes drilled into the holder prior to irradiation. As yet, we cannot attest to the significance of this observation. In addition, heavy surface markings or deep scratches on some of the fuel plates have been found. These markings may have occurred prior to, during, or after removal of the bowed plates from the reactor experimental facility. We shall continue our examination.

We have a set of 10 miniature irradiation plates similar to those previously described[1] now being irradiated in the G-12 loop during ETR cycle 94. These plates were inserted in the reactor late in February

---

[1]M. M. Martin and W. R. Martin, Fuels and Materials Development Program Quart. Progr. Rept. Dec. 31, 1967, ORNL-TM-2090, pp. 9–11.

and after a month of irradiation, the experiment is operating satisfactorily.

On March 11 and 12, 1968, personnel from INC and ORNL met in Idaho Falls, Idaho, to discuss fuel element fabrication programs. Irradiation experiments scheduled for the G-12 loop for FY 1969 were outlined as shown in Table 1.11. These experiments have been agreed upon by both organizations and represents a cooperative effort in research reactor fuel element development.

Flame Reactor Preparation of UO_2-Tungsten Dispersions

J. I. Federer W. R. Martin

Direct conversion of UF_6 to uranium oxides in a flame reactor has been demonstrated using hydrogen, oxygen, and UF_6 as reactants.[2] The powder product has been characterized in terms of phases present, purity, particle size, and sintering behavior. A preliminary economic evaluation of the flame reactor process has been made and the results compared favorably with the sol-gel[2] and ammonium diuranate production process. Especially, these data indicate that at product rates below 100 kg/day, the ADU product is less expensive. However, because of uncertainties in the economic evaluation, absolute cost values are most likely no better than ± 30%. Therefore, at this time we have seen no cost differences between the processes which we believe are significant. In recent experiments, powder mixtures of UO_2 and tungsten were prepared for thermal conductivity measurements, and attempts were made to prepare an assortment of other refractory materials.

The following conditions were used to obtain three powder mixtures of UO_2 and tungsten. The conditions were the same for the three experiments except that the amount of WF_6 was varied to obtain mixtures of different tungsten content. These conditions are shown on p. 23.

---

[2]J. I. Federer and W. R. Martin, Fuels and Materials Development Program Quart. Progr. Rept. Dec. 31, 1967, ORNL-TM-2090, pp. 14–18.

Table 1.11. Proposed ORNL and INC G-12 Loop Experiments for FY 1969

Table 1.11. Proposed ORNL and INC G-12 Loop Experiments for FY 1969

ETR Cycle	Type of Experiment for the Following Tiers					
	1	2	3	4	5	6
97	(INC) UAl alloy	(INC) UAl alloy	(INC) 6061 clad spherical UAl_x. Variable $^{235}U^x$ enrichment.	(INC) Fiber clad UAl_x	(INC) Al-Be clad UAl_x	(INC) Similar to tier 3
98 99 100	(ORNL) Effect of powder fines on the performance of hi-fired oxides (also burned if duplex plates are developed). Level of fines to be 3, 15, and 25 wt %.	(INC) Samples from tier 3, cycle 97 will be moved to this position (INC) Best of samples in tiers 2 and 1 of cycle 97 will be moved to this position.	(ORNL) Irradiation performance of burned U_3O_8 to 3×10^{21} at three loadings. 1. Present HFIR inner annulus 2. Advanced loading for HFIR outer annulus 3. 15% higher than (2) above	(INC) Performance of UAl_x to 3×10^{21} at three loadings. 1. 50 wt % 2. 60 wt % 3. Higher loading lower enrichment.	(INC) Samples from tier 6, cycle 97 will be moved to this position. (INC) 5-cycle experiment using UAl_x and U_3O_8. High loading to be taken to failure.	(ORNL) Irradiation of rolled plates with nonbond and/or lower interfacial grain growth. Use UAl_x or U_3O_8
101	(INC) Effect of irradiation on coarse UAl_x powders.	(INC) Borosilicate glass experiment in aluminum.	(INC and ORNL) U_3Si-Al; UAl_x with suppressant added.	Same as tier 3, cycle 101.		(INC) Effect of powder fines on the performance of intermetallic fuel. Level of fines to be 15, 25, and 40 wt %.
102 103	(ORNL) 2219-clad U_3O_8 with SAP as matrix	Same as tier 1, cycle 101				

Note: All instrumented plates to be supplied by ORNL. Another listing will set standards and type of materials to be used.

Flow rate of reactants, cm^3/min

H_2	2100
F_2	40 (400 cm^3/min used for ignition)
O_2	700
UF_6	25
WF_6	6 (FR-16); 28 (FR-17); 66 (FR-18)
Pressure, torr	15 to 30

The tugnsten content, x-ray and electron diffraction analyses, and particle sizes of the products are shown in Table 1.12. Both x-ray

Table 1.12. Analysis of UO_2-Tungsten Powder

	Powder Batch		
	FR 16-1	FR 17-1	FR 18-1
Tungsten, wt %	18.2	33.5	52.2
X-ray analysis[a]			
UO_2	S	S	S
Tungsten	NF	W	W
$W_{20}O_{58}$	W	M	S
Other	NF	NF	NF
Electron diffract on analysis[a]			
UO_2	S	S	
Tungsten	NF	NF	NF
$W_{20}O_{58}$	W	S	S
Other	NF	NF	NF
Appropriate particle size range, A	50–700	100–1000	150–1800

[a]Amounts of phases estimated from intensities of powder pattern lines: S – strong; M – medium; W – weak; NF – not found.

and electron diffraction showed the presence of UO_2 and revealed that tungsten was present mostly as the compound $W_{20}O_{58}$. No other compounds were detected. Electron microscopic examination showed a mixture of small

spherical particles and larger angular particles; the particle size range increasing with increasing tungsten content. As in the case of flame produced UO_2 powder, the UO_2-tungsten powders, along with UO_2 powder from previous experiments (FR 3-2 and FR 14-2) were sieved to obtain −200 mesh powder free of coarse agglomerates. These powder batches were heat treated at 1000°C for 16 hr in hydrogen containing 0.013 g water/liter. Samples from FR 3 and FR 17 were also heat treated at 600 and 800°C to evaluate the effect of temperature and wet hydrogen on fluorine removal. Uranium compounds, such as UF_4 and UO_2F_2, should react with water to form UO_2 or UO_3 and HF. The fluorine contents obtained for heat treated powder are shown in Table 1.13. Included also are the previously

Table 1.13. Fluorine Contents of Heat Treated UO_2 and UO_2-Tungsten Powder

Powder Batch	Temperature (°C)	Hydrogen Atmosphere	Fluorine (wt %)
FR 3-2[a]	600	Dry[b]	0.22
	800	Dry	0.091
	1000	Dry	0.032
FR 3-2[a]	600	Wet[c]	0.015
	800	Wet	0.034
	1000	Wet	0.005
FR 17-1[d]	600	Wet	0.015
	800	Wet	0.006
	1000	Wet	0.005

[a]As-prepared fluorine content, 4.7 wt %.

[b]Less than 10 ppm H_2O.

[c]0.013 g H_2O/liter H_2.

[d]As-prepared fluorine content, 3.3 wt %.

reported[2] fluorine contents obtained for powder heat treated in dry hydrogen (< 10 ppm H_2O). Table 1.13 shows that wet hydrogen was much more

effective at all temperatures in removing fluorine. However, fluorine contents ranging from < 5 to 33 ppm have been obtained in UO_2 powder heat treated at 1000°C in dry hydrogen,[3,4] an anomaly that cannot presently be explained. Defluorination at 1000°C also resulted in reduction of the compound $W_{20}O_{58}$ to tungsten.

Pellets were prepared from UO_2 and UO_2-tungsten powders by uniaxially pressing at 10,000 psi, followed by isostatic pressing at 50,000 psi, then sintering at 1750°C for 4 hr in dry hydrogen. Densities of the pellets, determined by the volume displacement method are shown in Table 1.14.

Table 1.14. Density and Electrical Resistance of Sintered UO_2 and UO_2-Tungsten Pellets

Pellet	Tungsten[a] (wt %)	Density, g/cm³		Resistance[c] (ohms)
		Determined	Theoretical[b]	
FR-14-2-1	0	10.23	10.9	600,000
-2	0	10.23	10.9	600,000
FR-16-1-1	18.2	11.18	11.8	50,000
-2	18.2	11.17	11.8	50,000
FR-17-1-1	33.5	13.45	12.8	0.2
-2	33.5	13.37	12.8	0.2
FR 18-1-1	52.2	15.24	14.3	0.05
-2	52.2	15.35	14.3	0.05

[a]Determined for as-prepared powder, may be higher in pellets.

[b]Assumes mechanical mixture.

[c]Approximate values determined by placing probes about 1/16 in. apart on pellet surface.

[3]J. I. Federer and W. R. Martin, Fuels and Materials Development Program Quart. Progr. Rept. Dec. 31, 1967, ORNL-TM-2090, p. 15.

[4]J. I. Federer and W. R. Martin, Fuels and Materials Development Program Progr. Rept. Sept. 30, 1967, ORNL-TM-2020, p. 41.

Theoretical densities, assuming a mechanical mixture of UO_2 and tungsten, are also shown in Table 1.14. Densities greater than calculated theoretical densities were obtained for pellets from powder batches FR 17-1 and 18-1, which indicates uncertainty in the tungsten contents of these pellets. The tungsten contents shown in Table 1.14 were determine for as-prepared powder, but sizing to −200 mesh may have enriched the powder in tungsten. The tungsten content of the pellets will be determined later.

Approximate electrical resistances are also shown in Table 1.14. As expected these decrease with increasing tungsten content. The thermal conductivities of pellets from powder batches FR 17-1 and 18-1 should be quite high.

Microstructures of the sintered pellets are shown in Fig. 1.5. The UO_2 shown in Fig. 1.5(a) contains some porosity and has a grain size of about 25 μm. The tungsten is readily observed as discrete particles in the pellet containing about 18% W [Fig. 1.5(b)], but in the pellets of higher tungsten content [Fig. 1.5(c) and (d)] the tungsten is present as a continuous phase, indicating that these pellets contain more tungsten than revealed by analysis of the as-prepared powder.

The pellets are are presently being ground to appropriate size for thermal conductivity measurements.

Vapor Fabrication of PuO_2 Powder from PuF_6

W. C. Robinson, Jr.

Recent interest in breeder reactors has led to consideration of techniques for the fabrication of PuO_2 and $(U,Pu)O_2$ composite fuels. Therefore, it was desirable to investigate the feasibility of converting PuF_6 to PuO_2 by chemical vapor deposition in a manner analogous to the UO_2 synthesis.

Several experimental runs have been made and plutonia bearing powder was produced.[5] We have proceeded to evaluate the powder product from these experiments.

---

[5]W. C. Robinson, Fuels and Materials Development Program Quart. Prog. Rept. Dec. 31, 1967, ORNL-TM-2090, p. 19.

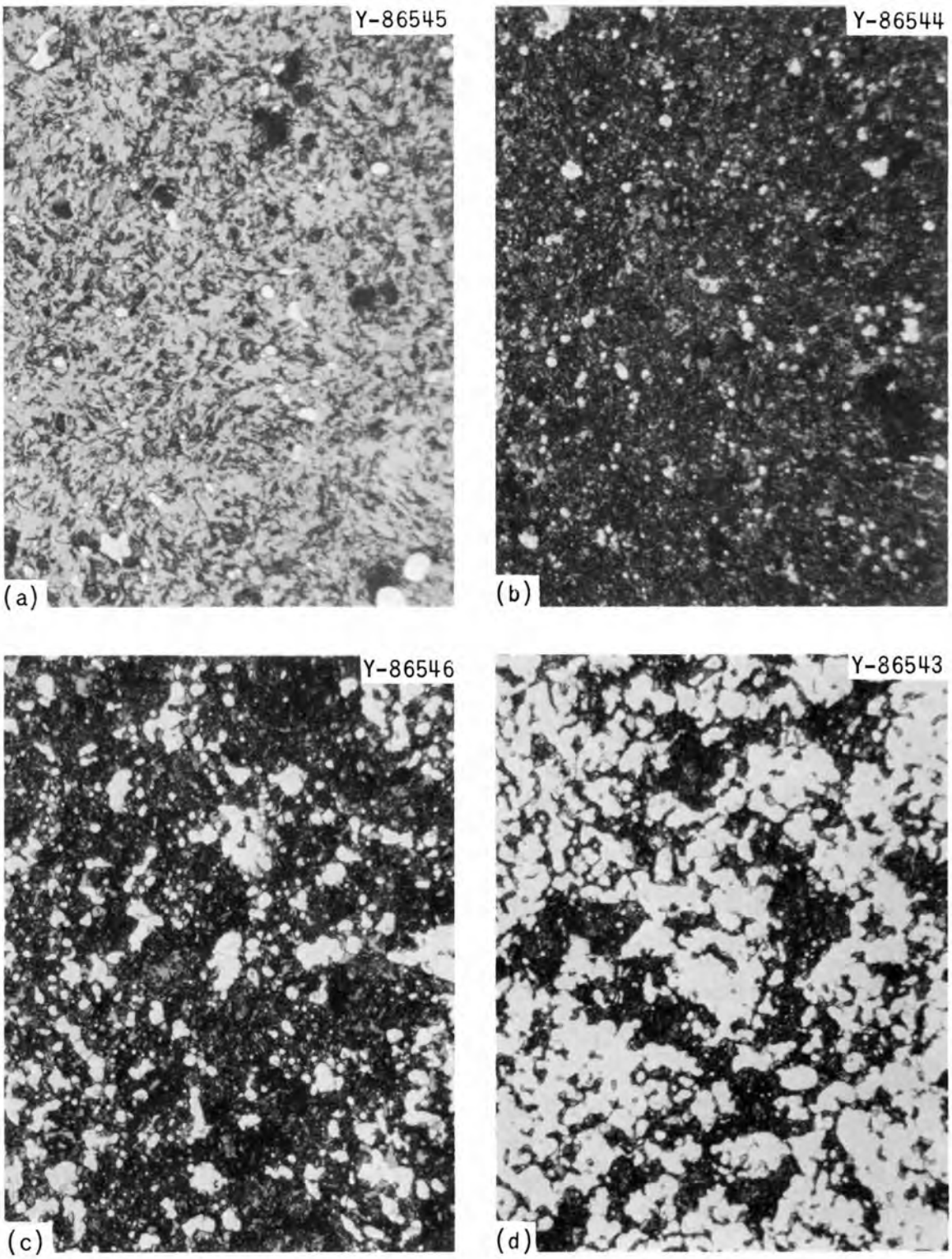

Fig. 1.5. Microstructure of UO_2-Tungsten Pellets Sintered at 1750°C for 4 hr in Hydrogen. (a) UO_2; (b) UO_2–18.2% W; (c) UO_2–33.5% W; (d) UO_2–52.2% W. Etchant: 70 parts H_2O, 20 parts H_2O_2, 10 parts HNO_3. 500×.

Much difficulty was encountered in mounting the powders for x-ray diffraction examination. The powder tended to float in the liquid araldite mounting epoxy. However, one powder sample from the second experiment (Pu-6) was mounted in a very thin layer of araldite, allowed to set for 3 hr and the composite then made. An x-ray diffraction pattern was taken of this sample. The observed lines and intensities of the pattern are shown in Table 1.15. Also shown is the pattern

Table 1.15. X-Ray Analysis of Product from the Pu-6 Experiment

Observed Values			X-Ray Data[a]		
2θ[b]	d	I	2θ	d	I
			28.62	3.115	14
33.0	2.71	13	33.18	2.698	7
47.56	1.91	29	47.62	1.908	12
56.4	1.63	28	56.51	1.627	15
			59.22	1.558	4
69.43	1.35	5	69.64	1.349	3
76.90	1.24	8	76.96	1.238	8
79.0	1.22	8	79.34	1.207	7
88.6	1.10	7	88.74	1.101	8
95.6	1.04	7	95.76	1.038	9
			107.70	0.954	4
115.2	0.913	8	115.24	0.912	14
117.4	0.901	4	117.86	0.899	8
			129.04	0.853	9
			138.78	0.823	10
			142.52	0.813	10
			162.96	0.779	6

[a] R.N.R. Mulford and C. E. Holley, Jr., Thermodynamic Properties of Plutonium Oxide, LADC-8266 (1966).

[b] Pattern starts and stops at 2θ values of 30 and 120°, respectively.

reported for PuO_2 by Mulford and Holley.[6] All of the lines observed on the CVD-powder pattern match the reported PuO_2 lines. All lines on our pattern are weak but the observed pattern agrees very well with the reported PuO_2 lines. It does not agree with any other plutonium compound. Therefore, we conclude that we have produced PuO_2 and definitely established the conversion feasibility.

The limitation of the vapor fabrication of PuO_2 in our experimental apparatus is not the conversion step from PuF_6 to PuO_2 but the fluorination step from PuF_4 to PuF_6. Since our task was visualized as the development of an apparatus and technique to convert an existing PuF_6 stream to PuO_2, we did not design or construct an efficient fluorination system. Prior to the optimization of conversion parameters, a different fluorination system will have to be constructed.

---

[6]R.N.R. Mulford and C. E. Holley, Jr., Thermodynamic Properties of Plutonium Oxides, LADC-8266 (1966).

2. JOINING RESEARCH ON NUCLEAR MATERIALS

G. M. Slaughter

A very important contribution to our welding research on high-nickel alloys and stainless steels is the work being performed under subcontract at the Welding Laboratory of Rensselaer Polytechnic Institute. Through the use of testing techniques conceived and developed there, we are able to pursue pertinent, but unusual, aspects of welding. This report will describe several interesting results of their recent research.

The last quarterly report[1] discussed the microstructural studies conducted at ORNL on synthetic weld heat-affected zones in experimental Incoloy-800 alloys. During this quarter we have begun weldability studies on experimental Inconel-600 (Ni–15.5% Cr–8% Fe) alloys. Preliminary hot-ductility results relating to the properties of weld heat-affected zones are described in this report.

Welding Studies at Rensselaer

W. F. Savage[2] C. D. Lundin[2]

Crack-Test Development

A second-generation VARESTRAINT-type device, nicknamed the "TIG-A-MA-JIG," has been designed to utilize the good points of its predecessor and to add several refinements.[3] Basic operation is similar to the VARESTRAINT in that an augmented strain is imposed on the sample while a gas tungsten-arc spot weld is being made. The number and length of cracks developed in the weld are then used as a measure of the material's weldability.

A series of specially contaminated type 304L stainless steel samples have been prepared to determine the sensitivity of the test to minor

---

[1]D. A. Canonico and W. J. Werner, Fuels and Materials Development Progr. Quart. Prog. Rept., Dec. 31, 1967, ORNL-TM-2090, pp. 157–164.

[2]Department of Materials Engineering, Rensselaer Polytechnic Institute, Troy, N. Y.

[3]W. F. Savage and C. D. Lundin, Fuels and Materials Development Program Quart. Prog. Rept., June 30, 1967, ORNL-TM-1941, pp. 74–75.

compositional changes. The TIG-A-MA-JIG master specimen is shown in Fig. 2.1(a). The special test sample compositions are made in the following manner: sintered powder shims containing the desired elemental additions are placed along the centerline of a 6-in. × 6-in. × 1/4-in. plate of stainless steel. A laterally oscillating low-current arc is then passed longitudinally along the shim insert, resulting in a wide weld zone of the desired chemical composition. This master sample yields five test samples [Fig. 2.1(b)] which are tested such that the weld zone and heat-affected zone of a stationary gas tungsten-arc spot weld are entirely contained within the previously prepared fusion zone.

Five master specimens were prepared, one control with an insert of type 304 stainless steel only and one each containing additions of sulfur, silicon, manganese, and phosphorus. The compositions of inserts and samples, together with recovery calculations, are shown in Table 2.1. The insert compositions are shown first, followed by the actual fusion-zone compositions. By measuring the area of the weld pad from a transverse section of the plate, it was possible to predict the fusion-zone composition. The comparison of these values with the actual values as determined by chemical analysis provides an indication of the percentage recovery of a particular element.

The phosphorus was 95% recovered; roughly one-fourth of the sulfur and silicon was lost; while manganese was reduced to nearly one-half of its original level.

The samples were tested using the following welding conditions:

Arc current, amp	108
Arc time, sec	55.5
Augmented strain, %	5

1/8-in. electrode, 3/32-in. arc gap, 25 cfh A

The data obtained are presented in Fig. 2.2. Note that the maximum, minimum, and average values of the total crack length are given for each series.

An analysis of these data shows that sulfur increases the hot-cracking sensitivity. Silicon appears to have a minor effect, and the effect of manganese, if any, is also minor. It is possible that the manganese effect is masked by the fact that most of the excess that

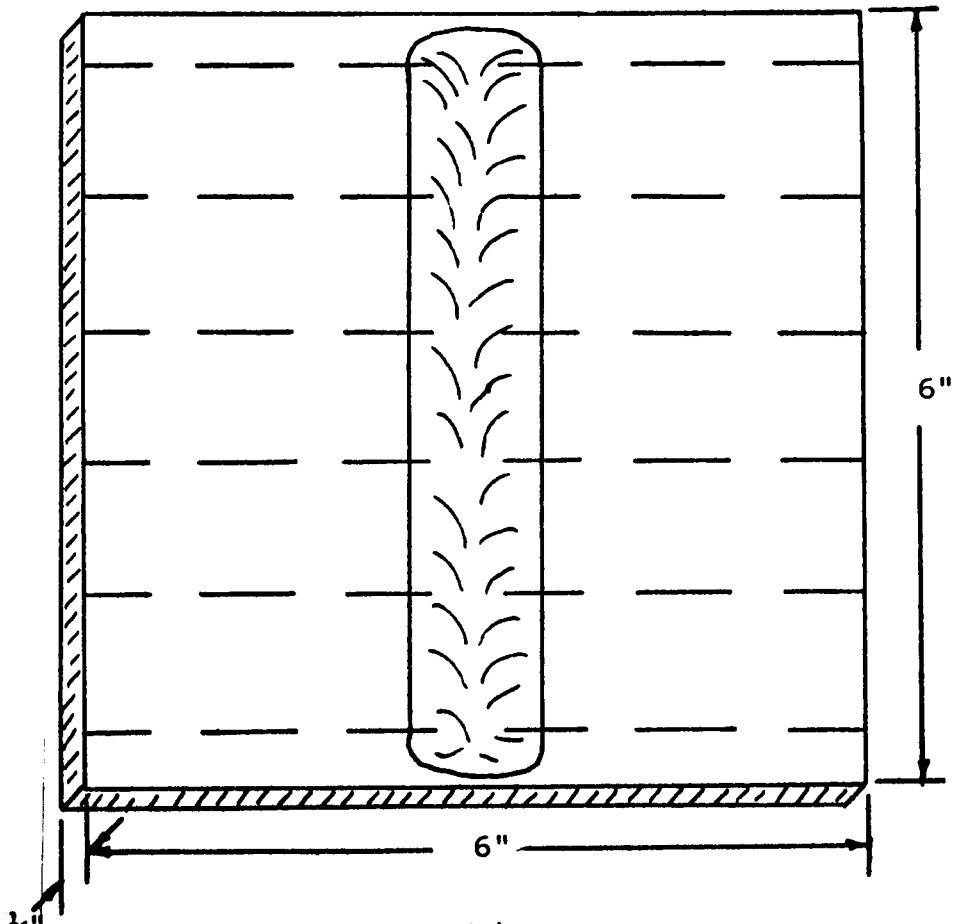

(a)

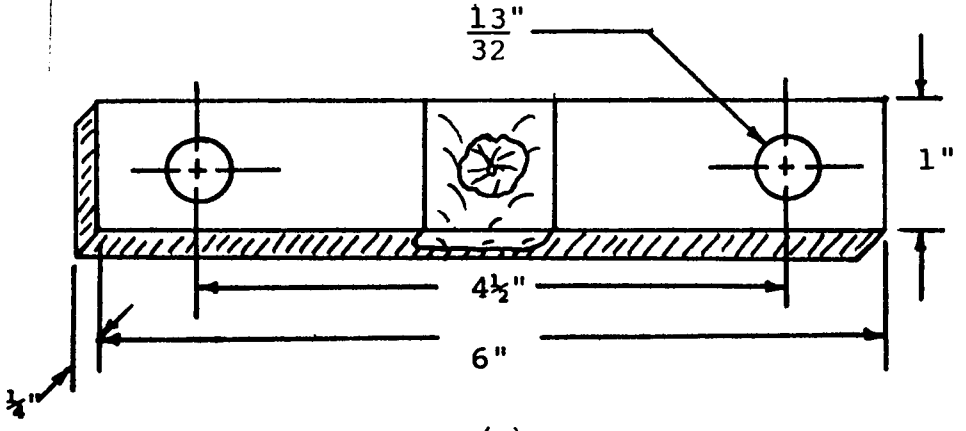

(b)

Fig. 2.1. TIG-A-MA-JIG Specimen (Rensselaer Polytechnic Institute Drawing). (a) Master specimen. (b) Test sample.

Table 2.1. Compositions and Recoveries of Type 304L Stainless Steel TIG-A-MA-JIG Samples

Specimen Number	Description	Composition, %							
		Fe	Cr	Ni	C	P	S	Mn	Si
		By Chemical Analysis							
1	Insert plus sulfur	66.6	17.8	10.1	0.060	0.018	0.156	0.80	2.19
2	Insert plus silicon	59.7	17.1	9.2	0.005	0.021	0.004	0.88	7.12
3	Insert plus manganese	56.3	16.7	8.7	0.064	0.014	0.020	14.7	1.88
4	Insert plus phosphorus	67.2	17.9	11.0	0.045	0.123	0.002	0.84	2.24
5	Control insert plus type 304 stainless steel	66.9	17.7	10.2	0.072	0.016	0.002	0.84	2.23
1	Fusion zone plus sulfur	69.2	18.1	10.6	0.016	0.016	0.027	1.34	0.84
2	Fusion zone plus silicon	68.8	18.1	10.5	0.012	0.013	0.021	1.40	1.16
3	Fusion zone plus manganese	68.5	18.1	10.6	0.013	0.012	0.019	1.45	0.81
4	Fusion zone plus phosphorus	69.0	18.0	10.6	0.014	0.022	0.020	1.50	0.78
5	Control fusion zone plus type 304 stainless steel	68.8	18.2	10.5	0.013	0.017	0.017	1.34	0.78
	Base material	68.5	18.4	10.5	0.017	0.012	0.020	1.43	0.67
		Calculated Recoveries							
Predicted fusion-zone						0.023	0.036	2.76	1.50
Actual Fusion-zone						0.022	0.027	1.45	1.16
Recovery						95.6	75.0	52.5	77.3

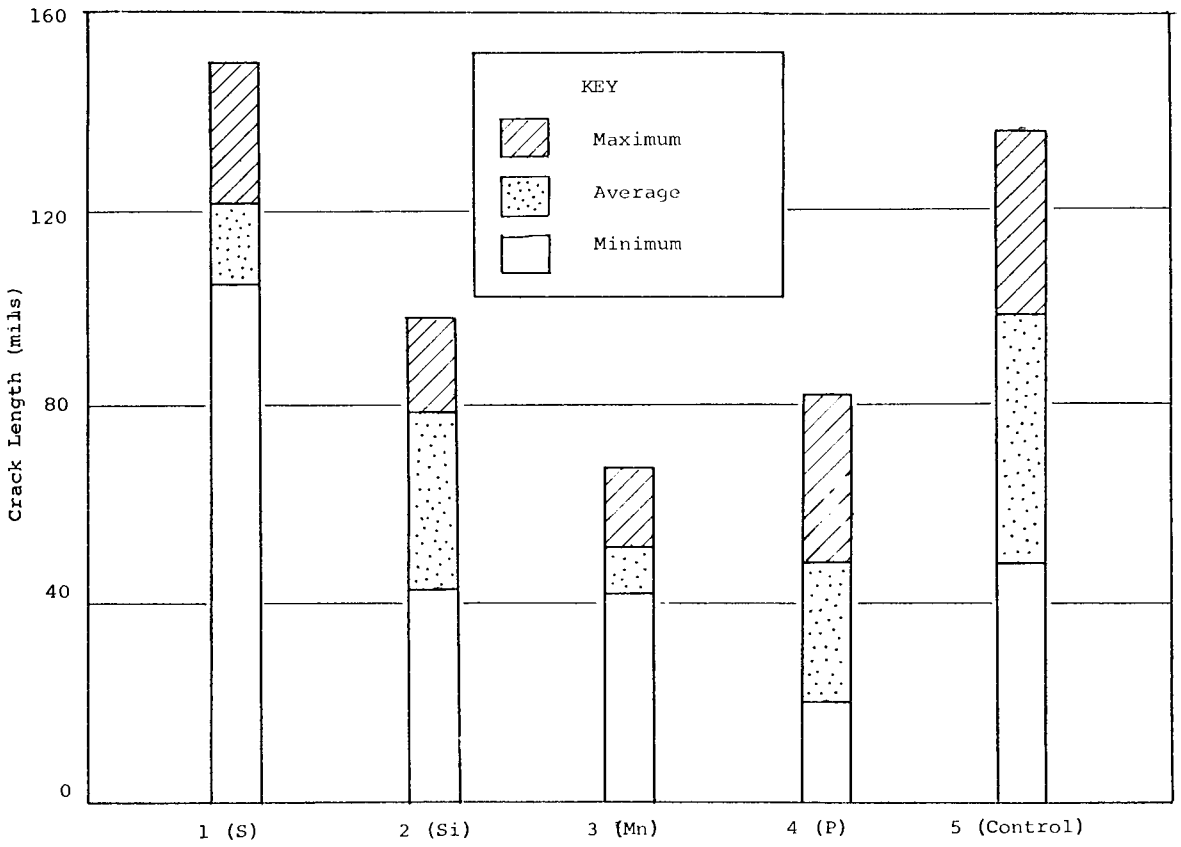

Fig. 2.2. Crack Length Versus Composition for Type 304L Stainless Steel TIG-A-MA-JIG Samples (Rensselaer Polytechnic Institute drawing).

was added was lost in the welding process. Note in Table 2.1 that the manganese content of all the fusion zones is nearly the same.

Contrary to what one would expect, phosphorus appears to have a beneficial effect on the cracking resistance of stainless steel. It is possible, however, that actually more cracks are produced under the influence of phosphorus, but that the cracks are back-filled with solute-rich liquid from the molten weld pool. This would be facilitated by the increased fluidity created by the phosphorus addition. Metallographic evidence supports this claim to a degree, but not conclusively.

It seemed logical that cracking data from TIG-A-MA-JIG samples might be complemented by performing subsequent tensile tests on the samples. Due to the strain distribution in the TIG-A-MA-JIG test, the largest and most commonly occurring cracks appear in a plane perpendicular to the longitudinal specimen axis, roughly coincident with the center of the weld nugget. Thus, the extent of this cracking should be reflected in

the effective cross-sectional area of the sample, and in the strength of the sample if pulled in tension.

To verify this hypothesis, thirteen TIG-A-MA-JIG samples were prepared from commercial Inconel 600. A weave bead was placed on six of the specimens, using the previously described technique with no impurity or powder insert added. Thus the only effect of the weave bead was to provide a segregated fusion-zone structure.

Seven of the samples were TIG-A-MA-JIG tested in the usual manner; four were strained 5%, while three were not strained.

All of the samples were then reduced in section as shown in Fig. 2.3 and tested to failure in a 50,000-lb hydraulic tensile testing machine. The results of this testing are in Table 2.2.

Table 2.2. Results of Tensile Testing of Commercial Inconel-600 Samples after TIG-A-MA-JIG Testing

Specimen	Ultimate Tensile Strength, psi	
	Individual Samples	Average
	$\times 10^3$	$\times 10^3$
No weave, not TIG-A-MA-JIG tested	85.7, 86.0, 85.8	85.8
No weave, tested at 5% strain	76.7, 76.8	76.8
No weave, tested at 5% strain	66.4, 62.5	64.4
Weave, not TIG-A-MA-JIG tested	84.1, 83.1	83.6
Weave, tested at 0% strain	67.4, 70.8	69.1
Weave, tested at 5% strain	65.0, 60.4	62.7

Note that the weave bead produces a slight reduction in strength. The TIG-A-MA-JIG test nugget, on the other hand, produces a fairly large drop in tensile strength, even in the case where the sample was not strained during the progress of the TIG-A-MA-JIG test. This is

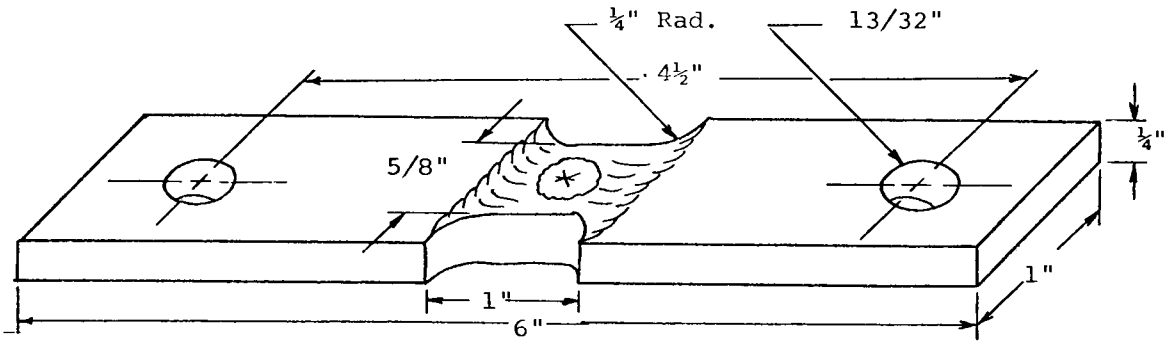

Fig. 2.3. Schematic of TIG-A-MA-JIG Tensile Test Sample. (Rensselaer Polytechnic Institute drawing)

probably due to crater cracks in the test nugget. An augmented strain of 5% results in a further decrease in the ultimate tensile strength as shown. Note that the scatter increases, indicating an increased variation in the amount of cracking.

Effect of Shielding Gas Composition on Welds in Commercial Inconel 600

During the preparation of the samples discussed in the previous section, it was noted that when argon gas cylinders were changed, a pronounced change occurred in the appearance of the weld puddle surface. This phenomenon was investigated using all of the argon cylinders on hand. Figures 2.4(a) and (b), photographs of the as-welded surface, represent the extremes in appearance obtained after tests with a large number of different argon gas cylinders. Note that the sample shown in Fig. 2.4(a) is badly oxidized, while the one in Fig. 2.4(b) is relatively clean and oxide free.

Mass spectrometer analyses of the gases used to produce these samples showed the impurity levels listed in Table 2.3.

No other impurities were detected, such as CO_2 or water vapor, the presence of which would indicate poor sampling technique. It is worthy of note that the overall purity in each case is well below the labeled purity of 99.995% Ar.

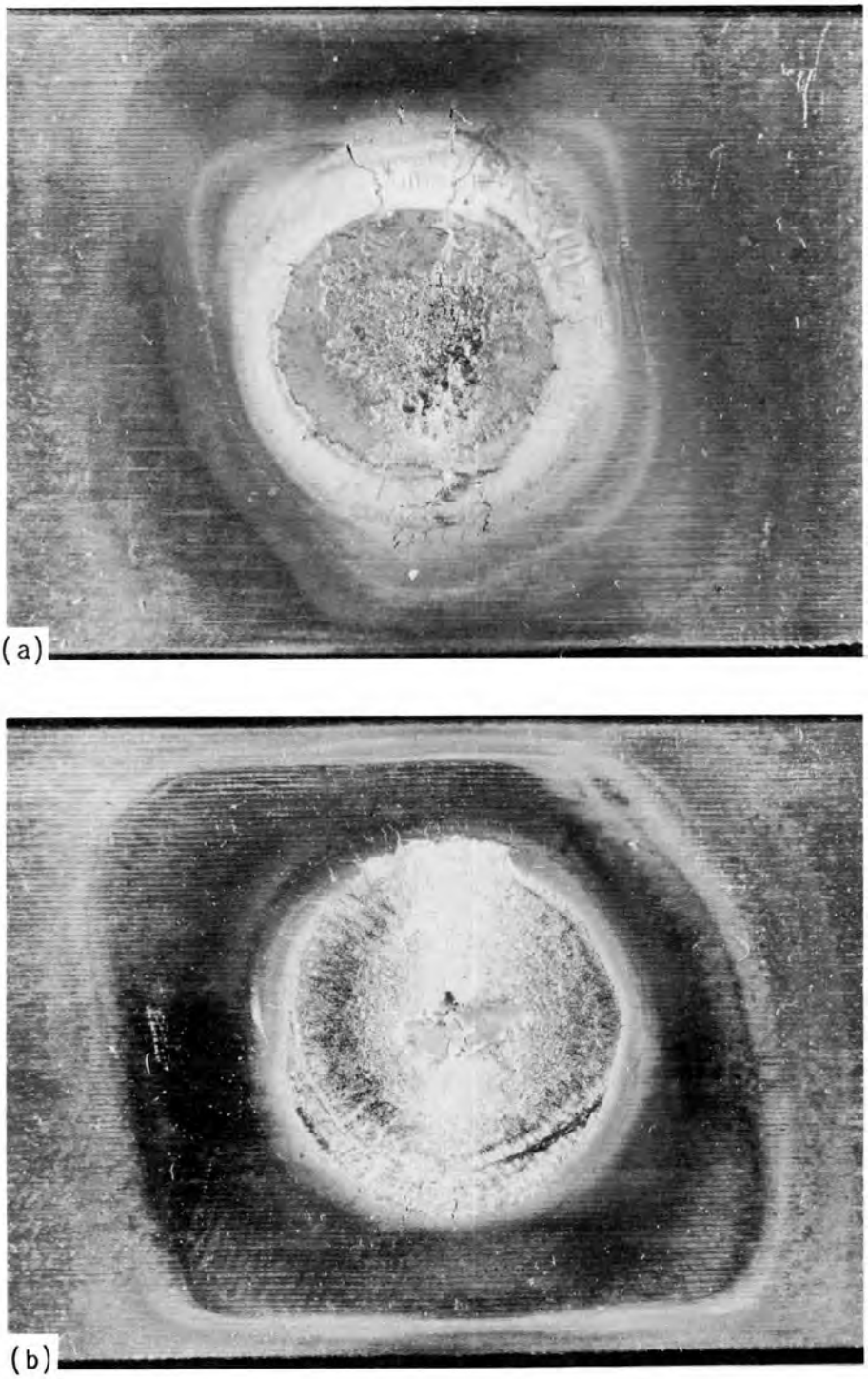

Fig. 2.4. As-Welded Surface of Inconel-600 TIG-A-MA-JIG Sample Tested with (a) "Dirty" Argon Shielding Gas, (b) "Clean" Argon Shielding Gas. 3.5×. More oxide on the weld surface is observed in (a). (Rensselaer Polytechnic Institute figures)

Table 2.3. Impurity Contents of Shielding Gases Used for Welding

	Impurities, ppm			
	N_2	O_2	Total	Purity (%)
Tank A [Fig. 2.4(a)]	1840	600	2440	99.756
Tank B [Fig. 2.4(b)]	450	240	690	99.931

A surprising result of this contamination is shown in Fig. 2.5. Figure 2.5(a) is a photomicrograph of a cross section of the sample shown in Fig. 2.4(a). Note that the penetration is roughly half the plate thickness. A photomicrograph of the cross section of the sample welded with the "clean" gas is shown in Fig. 2.5(b). Note that the penetration is complete. By approximate calculation, more than one-fourth more metal is melted with the "clean" gas than with the "dirty" gas.

A possible explanation for the gross difference in melting efficiency is proposed. It was observed during the welding process and may be seen from Fig. 2.4(a), that using the "dirty" argon caused a considerable portion of the puddle surface to be covered with a blanket of oxide. Therefore, a large percentage of the electrons arriving at the sample surface[4] would dissipate their energy on oxide rather than on liquid metal. Since metal oxides are in general better electron emitters than metals, it might be expected that more secondary electron emission would occur with the more heavily oxidized puddle. Thus, subsequent electrons from the cathode (electrode) would encounter a negative space charge in the vicinity of the puddle surface, decreasing their acceleration, and therefore decreasing the energy which they supply to the puddle surface.

[4]Straight polarity direct current was used in both instances.

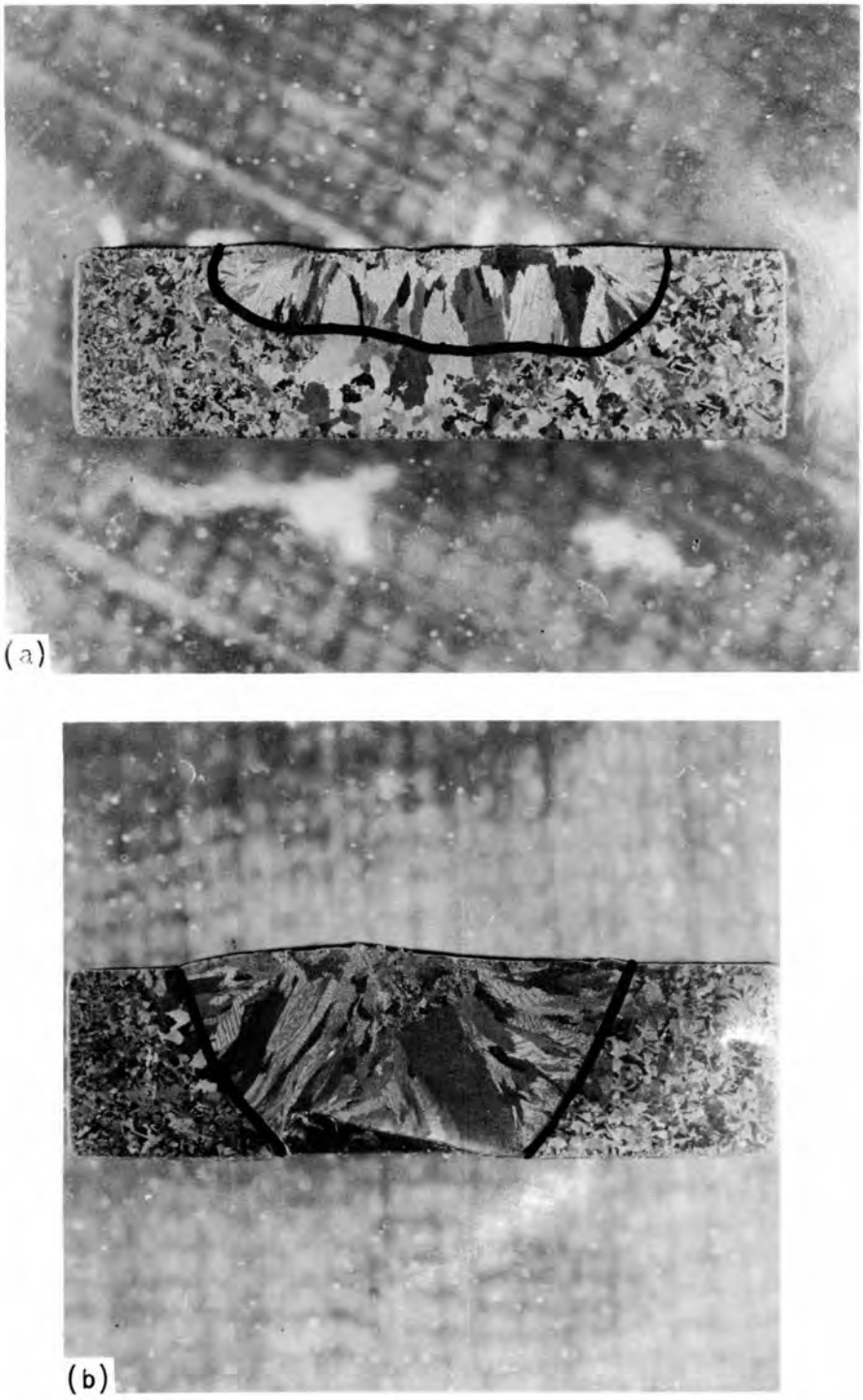

Fig. 2.5. Transverse Section of Inconel-600 TIG-A-MA-JIG Sample Tested with (a) "Dirty" Argon Shielding Gas, (b) "Clean" Argon Shielding Gas. 4×. Significantly greater weld penetration is observed in (b). (Rensselaer Polytechnic Institute figures)

It is also quite probable that the characteristics of the arc plasma itself are affected by the presence of the impurity gas ions, including the degree to which the energy in the plasma region is dissipated by radiation, convection, and conduction to the general surroundings. However, it is the effect of secondary emission on the anode drop which is probably of greatest import in this case.

Inconel 600 Weldability Studies

D. A. Canonico W. J. Werner

Studies to determine the behavior of weld heat-affected zones in experimental Inconel-600 (Ni–15.5% Cr–8% Fe) alloys have been initiated during this reporting period. Table 2.4 contains the desired and actual[5] chemical analysis of the alloys under study. The compositions studied include a pure ternary (600-1), a nominal commercial analysis (600-2), and nominal commercial analyses plus sulfur (600-3 through 600-5). As was the case with the Incoloy-800 alloys,[6] the starting stock, nickel, iron, and chromium, were all high purity (99.+ %).

Melting and fabrication were done in the Materials Processing Laboratory, and the product was supplied as 0.275-in.-diam rod. This rod was subsequently centerless ground to 0.250-in.-diam by 4-in.-long specimens for hot-ductility testing with the Duffer's Gleeble.[7]

Although the data obtained to date are preliminary, they do indicate a sulfur effect that is in line with that accepted for high-nickel alloys. Figure 2.6 is a graphical representation of the dramatic effect of sulfur on the "on heating" ductility (at 2400°F) of the five alloys studied. The pure ternary (600-1) and the nominal Inconel-600 without residuals had similar ductilities (in excess of 90%). The addition of

---

[5]It can be noted in Table 2.4 that the actual analyses closely approximated the desired analysis.

[6]W. J. Werner, D. A. Canonico, and R. E. McDonald, Fuels and Materials Development Program Quart. Prog. Rept., June 30, 1967, ORNL-TM-1941, pp. 69–73.

[7]Duffer's Associates, Inc., Troy, New York.

Table 2.4. Chemical Compositions of the Experimental Inconel-600 Alloys[a]

Alloy Identification	Chemical Composition (wt %)							
	Ni	Fe	Cr	C	Cu	Mn	Si	S
600-1	Bal	8.13	15.9	0.004	< 0.01	0.007	0.01	0.003
		(8.0)	(15.5)	(0)	(0)	(0)	(0)	(0)
600-2	Bal	8.55	16.1	0.028	0.026	0.11	0.2	0.002
		(8.0)	(15.5)	(0.03)	(0.04)	(0.20)	(0.20)	(0)
600-3	Bal	8.40	16.0	0.028	0.022	0.11	0.2	0.006
		(8.0)	(15.5)	(0.03)	(0.04)	(0.20)	(0.20)	(0.005)
600-4	Bal	8.04	15.5	0.025	0.029	0.15	0.2	0.010
		(8.0)	(15.5)	(0.03)	(0.04)	(0.20)	(0.20)	(0.010)
600-5	Bal	8.32	15.7	0.026	0.018	0.12	0.2	0.012
		(8.0)	(15.5)	(0.03)	(0.04)	(0.20)	(0.20)	(0.015)

[a](The desired analyses are in parentheses)

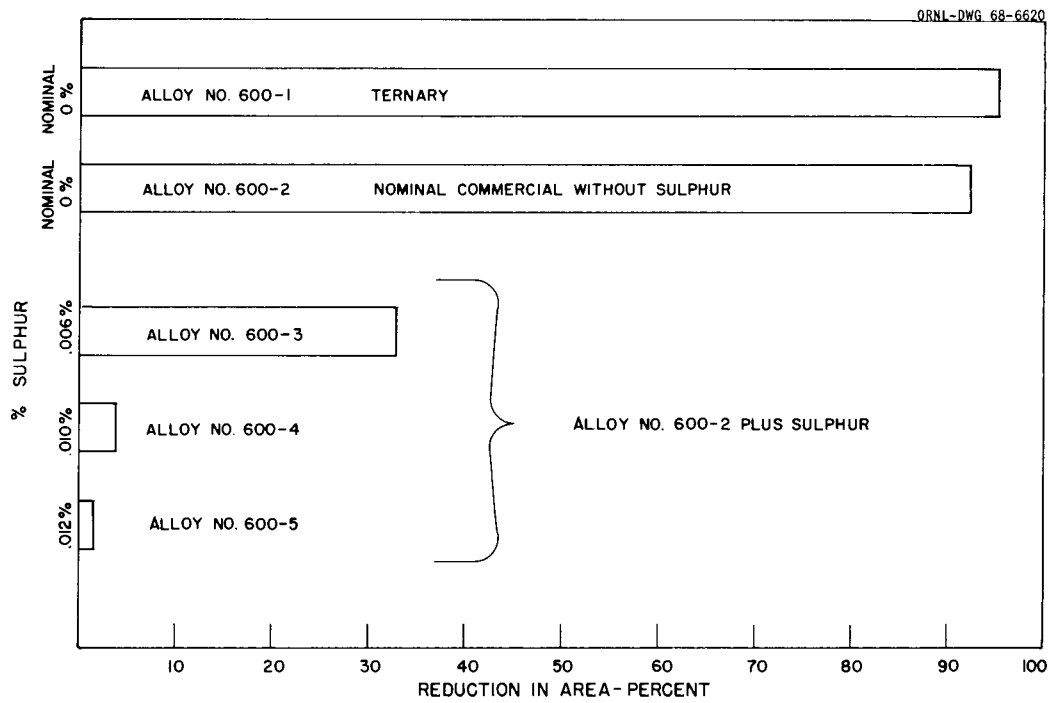

Fig. 2.6. The Effect of Sulphur on the "On-Heating" Ductility of Inconel at 2400°F.

sulfur caused a loss of ductility; 0.010% S decreased the reduction in area to 4% at 2400°F. This loss, which was not observed in the Incoloy-800 alloys, adds credence to the hypothesis that the sulfur in these alloys is being tied up by the titanium and/or aluminum.

The Inconel-600 series of alloys are being studied further and complete "on heating" and "on cooling" data are being accumulated.

3. MECHANICAL PROPERTIES RESEARCH AND LMFBR CLADDING AND STRUCTURAL MATERIALS DEVELOPMENT

J. R. Weir, Jr.

The objectives of these programs are to determine the effect of irradiation on the mechanical properties of alloys of interest as fuel cladding and to find a metallurgical condition or composition that produces the least effect of subsequent irradiation on the mechanical properties. To accomplish this, our study concerns the interaction of radiation-induced defects and the substructure of the alloys, the effect of irradiation temperature, postirradiation test variables, and neutron dosimetry in the facilities used in the irradiations. The materials being studied are types 304 and 316 stainless steel, Incoloy 800, and Hastelloy N, each containing various titanium additions, and a few vanadium alloys.

Development of Titanium-Modified Types 304 and 304L Stainless Steel

E. E. Bloom J. R. Weir, Jr.

Evaluation of the mechanical properties of two 1500-lb vacuum-induction melted heats of titanium-modified types 304 and 304L stainless steel is continuing. The compositions of these two alloys are given below:

	Composition, wt %	
Element	Heat 3756	Heat 60508
Carbon	0.012	0.05
Chromium	19.5	19.0
Nickel	11.2	10.0
Titanium	0.19	0.21
Manganese	1.0	0.65
Silicon	0.05	0.8
Phosphorus	0.006	0.013
Sulfur	0.013	0.002
Boron	0.0003	0.0027
Nitrogen		
Total	0.006	0.009
Soluble		0.003

Table 3.1 compares the as-annealed and postirradiation creep-rupture properties of the two alloys at a test temperature of 704°C. In each case the material was cold worked 50% prior to machining the test specimens. The pretest or preirradiation anneal was 1 hr at 925°C. Each alloy was irradiated at 650°C, but in separate irradiation experiments, thus, the neutron fluences are different and a direct comparison of properties is difficult. In the as-annealed condition the strength and ductility properties are approximately the same for the two carbon levels. For the low-carbon alloy there is a decrease in rupture life and increase in creep rate as a result of irradiation. Results of tests on unirradiated thermal control specimens indicate that the increased creep rate and thus some part of the reduced rupture life is a result of thermal aging. Ductility values for the irradiated specimens increase as the stress is reduced and for tests at 10,000 and 8,000 psi the values are significantly higher than the as-annealed specimens and slightly lower than the thermal controls.

Preliminary results on the high-carbon alloy indicate that the thermal aging effect is possibly less since creep rates of annealed and irradiated specimens are approximately the same. It should be noted that the irradiation time for these specimens was 1000 hr as compared to 2000 hr for the low-carbon specimens. A reduction in ductility is observed as a result of irradiation. However, ductility values are essentially independent of stress (or rupture life) for the conditions investigated to date.

Effect of Heat Treatment on the Creep-Rupture Properties of Types 304 and Titanium-Modified 304L Stainless Steel (R. T. King)

A number of types 304 and 0.2% Ti–304L stainless steel specimens have been cyclotron bombarded to a uniform concentration of

Table 3.1. Creep-Rupture Properties of Titanium-Modified Types 304 and 304L Stainless Steel at 704°C

Alloy	Stress (psi)	Unirradiated			Irradiated[a]		
		Rupture Life (hr)	Creep Rate (%/hr)	Total Elongation (%)	Rupture Life (hr)	Creep Rate (%/hr)	Total Elongation (%)
Type 304L stainless steel plus 0.2% Ti Heat 3756[b]	20,000	8.2	3.6	64.0			
	17,500	20.4	1.9	75.9			
	15,000	106.6	0.20	56.9	42.5 (59.2)	0.63 (0.64)	38.7 (63.0)
	12,500	372.7	0.11	53.2			
	11,250	366.1	0.08	60.5			
	10,000	1084	0.016	26.8	327.7 (738.2)	0.083 (0.044)	45.4 (51.1)
	8,000	4110	0.0038	20.8	688.0 (1460)	0.023 (0.02)	53.7 (66.2)
Type 304 stainless steel plus 0.2% Ti Heat 60508[c]	22,500	8.1	4.7	77.2			
	20,000	13.1	2.0	48.6	12.6	0.72	12.3
	17,500				23.9	0.40	12.1
	15,000	297.1	0.030	47.6	182.1	0.034	10.5
	13,500				220.3	0.030	9.7
	12,000				808.1		12.3
	10,000	1520.8	0.0037	20.4			

[a]Values in parentheses are for unirradiated thermal controls.

[b]Irradiated 2000 hr at 650°C to a neutron fluence of approximately 9×10^{20} neutrons/cm^2 (thermal) and 7×10^{20} neutrons/cm^2 ($E > 1$ Mev).

[c]Irradiated 1000 hr at 650°C, approximately 2.6×10^{20} neutrons/cm^2 (thermal) and 2×10^{17} neutrons/cm^2 ($E > 2.9$ Mev).

2×10^{-5} (atom fraction) of helium. The compositions of these steels are given as follows:

Element	Stainless Steel: Type 304 (Heat 71403)	Stainless Steel: 0.2% Ti–304L (Heat 3756)
Carbon	0.046	0.012
Manganese	1.77	1.0
Phosphorus	0.023	0.006
Sulfur	0.010	0.013
Silicon	0.62	0.05
Chromium	18.15	19.5
Nickel	9.60	11.2
Copper	0.25	
Titanium		0.19
Molybdenum	0.33	
Cobalt	0.03	

Both steels were finish cold rolled 50% to 0.010-in.-thick sheet material. Tensile and creep specimens with their gage length parallel to the rolling direction were machined to an 0.25-in. gage width and an 0.75-in. gage length. Specimens of each material were then annealed for 1 hr in argon at either 925 or 1038°C.

We are currently testing the nonbombarded control specimens at 500, 600, and 700°C. The series of tests at 700°C is reported below. All creep-rupture tests were performed under an argon atmosphere of approximately 10 psig. Table 3.2 lists the time to rupture, minimum creep rate, and fracture elongation for the types 304 and 0.2% Ti–304L stainless steel, respectively. Stresses ranged from 14,000 to 20,000 psi.

The results for the type 304 stainless steel indicate that over the range of stresses investigated, annealing for 1 hr at 925°C produces shorter rupture life, higher fracture elongation, and higher minimum creep rate at any given stress than annealing for 1 hr at 1038°C. Annealing the type 0.2% Ti–304L stainless steel for 1 hr at 925°C produces higher fracture elongations than annealing for 1 hr at 1038°C, but the rupture life and minimum creep rate parameters show no marked differences over the stresses tested.

Table 3.2. Creep-Rupture Properties of Type 304 Stainless Steel and Titanium-Modified Type 304L Stainless Steel

Heat Treatment	Stress (psi)	Time to Rupture, hr		Minimum Creep Rate, %/hr		Fracture Elongation, %	
		304	0.2% Ti–304L	304	0.2% Ti–304L	304	0.2% Ti–304L
	$\times 10^3$						
1 hr at 925°C	14	142.6	52.9	0.12	0.59	50	75
	16	72.3	29.3	0.37	1.26	72.3	75
	18	43.2	13.1	0.76	2.22	56.2	79.2
	20	27.6	7.2	1.22	5.55	69.3	83.3
1 hr at 1038°C	14	329.0	a	0.042	a	27.1	a
	15	255.0		0.058		27.1	
	15	262.5		0.066		23.0	
	16	181.2	42.7	0.13	0.77	39.6	50.0
	17	139.3		0.074		25.0	
	17	76.2		0.13		27.1	
	18	59.7	11.35	0.28	4.5	31.2	56.2
	20	36.2	5.1	0.74	9.2	39.6	56.2

[a]Bad test, no results.

Drawing of Stainless Steel Tubing

G. A. Reimann

Work has been in progress to produce tubing from the titanium-modified low-carbon grade of type 304 stainless steel. Ingots were obtained from Allvac Metals Company (heat 3756), and the analysis of the heat is 0.012% C, 0.013% S, 1.0% Mn, 19.5% Cr, 11.2% Ni, 0.19% Ti, bal Fe and 60 ppm N_2.

The ingot structure exhibits two phases (Fig. 3.1) plus a distribution of cubic crystals of titanium nitride. The second phase can be dissolved in the matrix by a 12-hr, 1200°C heat treatment, but the nitride particles are essentially unaffected by this treatment (Fig. 3.2). Microprobe analysis of the second phase showed concentrations of 32% Cr, 2% Ni, 0.3 to 10.0% Ti, and bal Fe. The presence of this phase would make tubing fabrication needlessly difficult and it was dissolved by heat treatment.

To convert the Allvac ingots into a configuration suitable for tubing manufacture, an ingot section was forged at 1200°C into a 4-in. round, machined into a billet, and extruded at 1200°C into a tube shell. After straightening and machining the outside and inside diameter to ensure concentricity, the tube shells were fabricated into tubing by swaging and drawing. Final sizes are as follows:
0.375-in. OD × 0.345-in. ID; 0.345-in. OD × 0.315-in. ID; and
0.250-in. OD × 0.218-in. ID.

Three separate approaches were investigated to determine their suitability as a fabrication technique for this grade of stainless steel – (1) plug drawing, (2) mandrel swaging, and (3) mandrel or rod drawing.

Plug Drawing

Plug drawing was unsatisfactory for tube-shell reduction, as severe circumferential cracks developed in the internal surface after 10 plug-draw passes (75% total reduction). It appears that the internal flaws were related to lubrication deficiency, and it is believed that the problem could be avoided by installing a lubrication system to pump

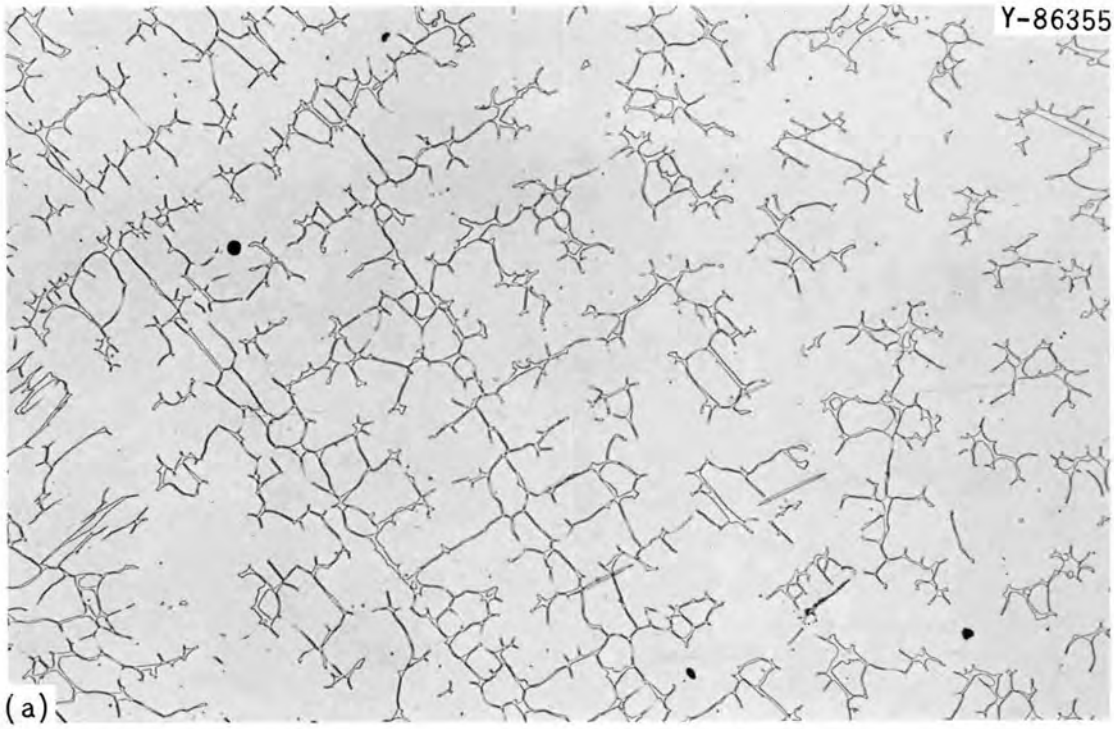

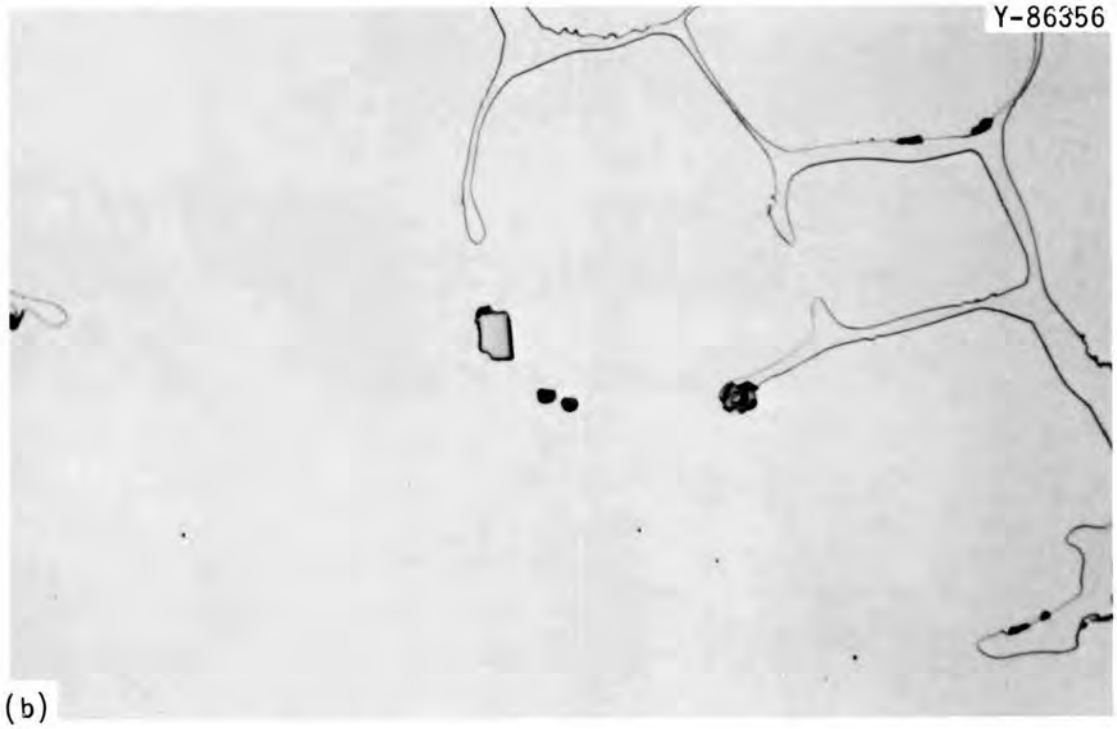

Fig. 3.1. Ingot Microstructure of Type 304L Stainless Steel Plus 2% Ti (heat 3756). Interdendritic phase is 30% Cr, up to 10% Ti, bal Fe, and cubic crystals are titanium nitride. (a) 100×. (b) 1000×.

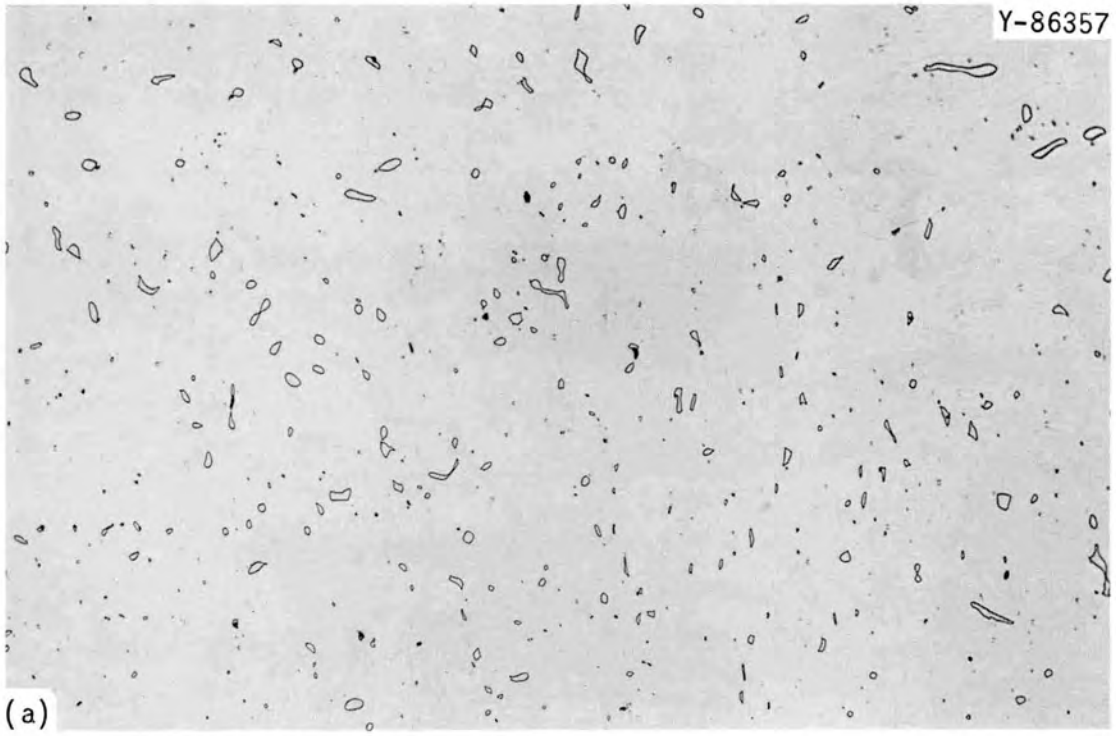

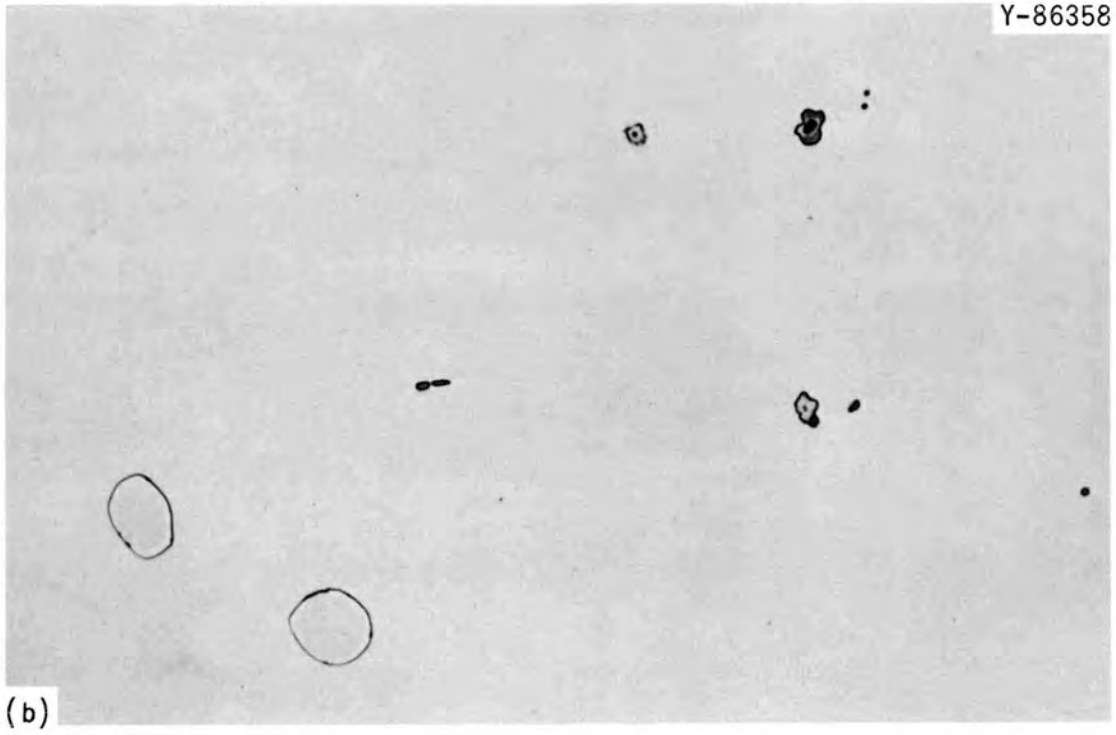

Fig. 3.2. Interdendritic Phase in Ingot Structure is Mostly Dissolved by 12-hr Treatment at 1200°C, but Cubic Crystals are Essentially Unaffected. (a) 100×. (b) 1000×.

chlorinated lubricating oil into the tube. The tube interior may have been contaminated by lubricant residue during anneals and, until this possibility is eliminated, the expense of a new lubrication system may not be justified.

Mandrel Swaging

Attempts to mandrel swage the tubing to size were more successful than plug drawing but even with 15% reductions between anneals, longitudinal cracks developed in the internal tube surface after 20 passes. Flaws of this nature developed from wrinkles caused by the swaging action and these flaws were subsequently ironed out as the internal surface of the tube deformed against the hard mandrel.

Mandrel Drawing

The final tube sizes were obtained by mandrel drawing; nondestructive testing did not disclose any flaws of the type described previously. Satisfactory tubing was produced in 28 to 32 passes of 15% reduction each. Tubing annealed for 20 min at 1200°C between each pass did not appear to differ from tubing annealed after two 15% passes (approx 27% total reduction). The flowsheet in Fig. 3.3 is based on the mandrel drawing approach and the four swaging passes were done only to reduce the tube cross section to be within the capacity of the drawbench.

The microstructure of the finished tubing is shown in Fig. 3.4. The nitride precipitates can be seen at 1000× and they appear to have been fractured into smaller particles and strung out in the direction of working. The matrix must flow around these particles during deformation and internal fissures may develop when the material is cold worked excessively.

Although nondestructive testing results are incomplete at this time, it appears that remaining problems in drawing can be solved by improvements in the drawbench technique.

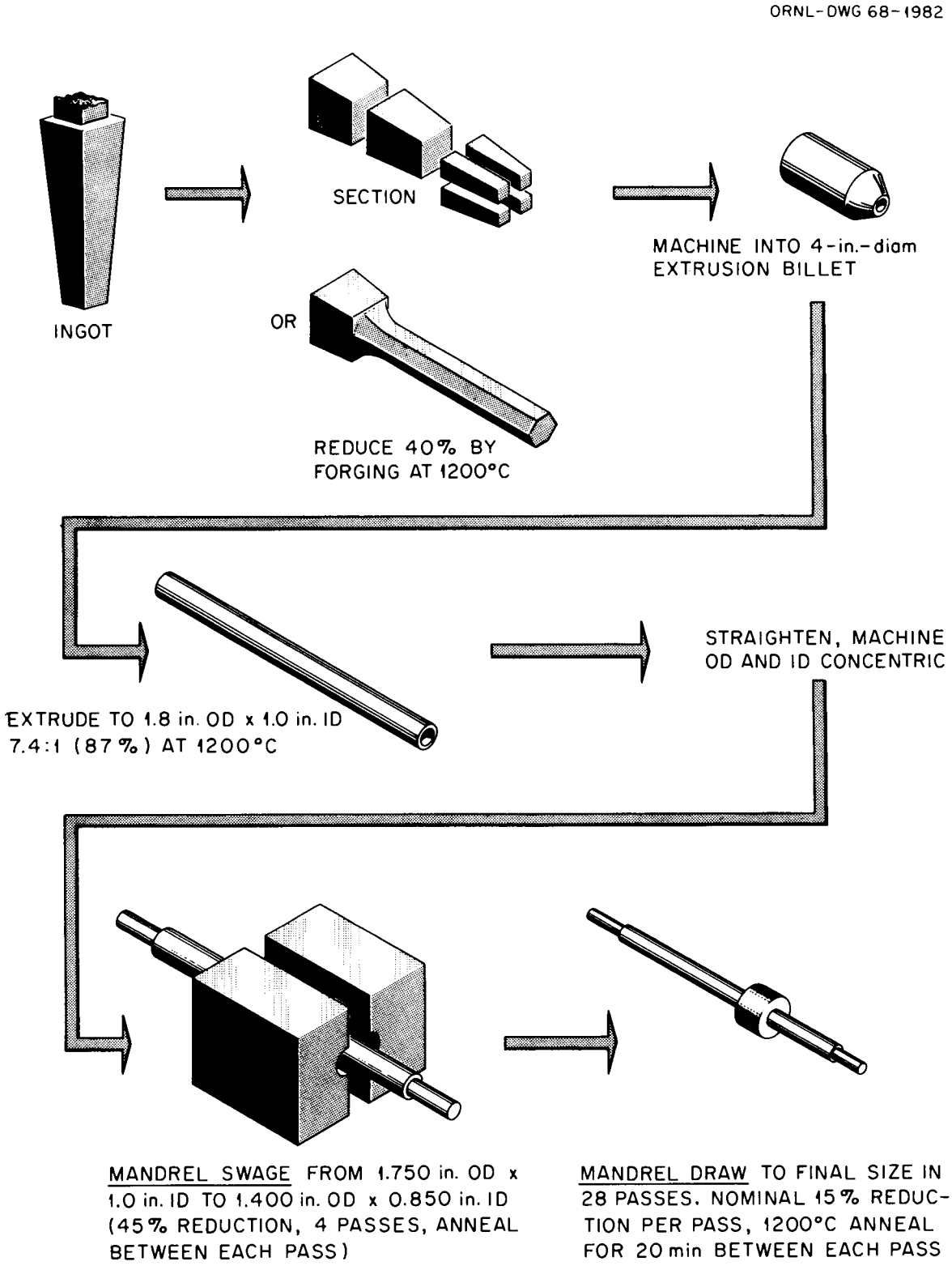

Fig. 3.3. Flowsheet Showing Mandrel Drawing Approach.

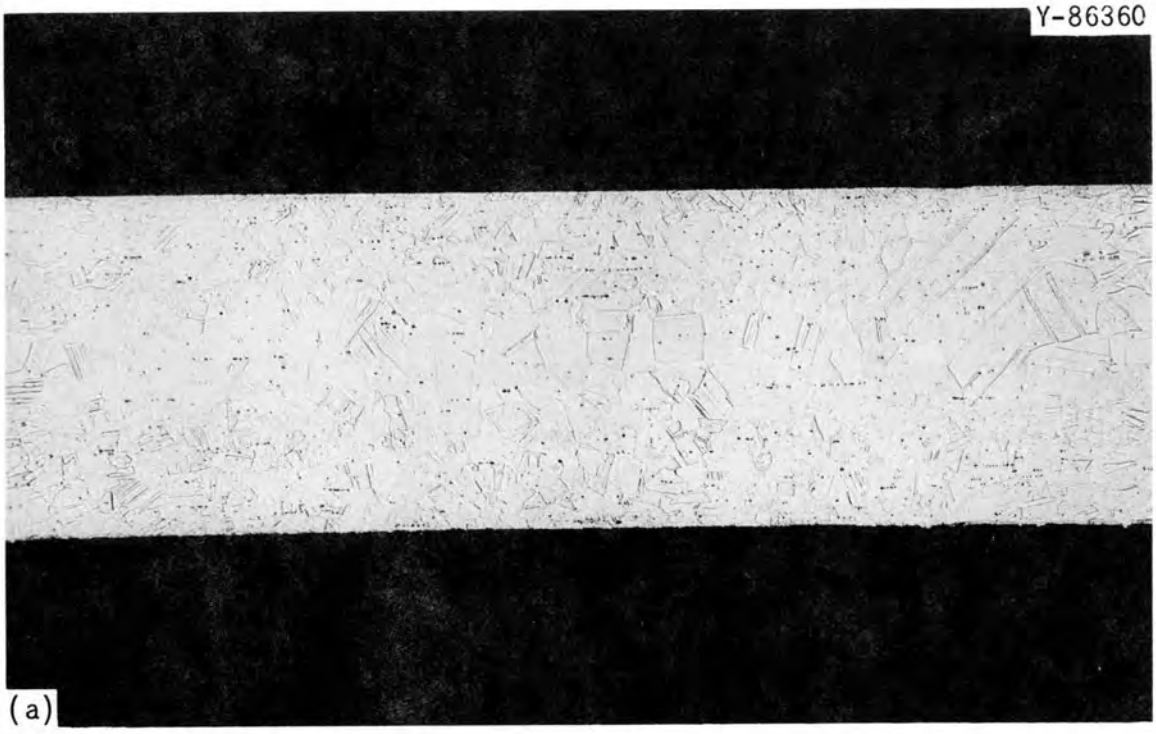

Fig. 3.4. Microstructure of Longitudinal Section of Finished 0.250-in. OD × 0.016-in. Wall Tube. Except for crushed nitride crystals, no second phase is evident. (a) 100×. (b) 1000×.

Effects of Neutron Irradiation on the Elevated-Temperature Mechanical Properties of Type 316 and Titanium-Modified Type 316 Stainless Steel

E. E. Bloom J. R. Weir, Jr.

An investigation of the effects of neutron irradiation on the mechanical properties of type 316 stainless steel and titanium-modified type 316 stainless steel is continuing. We have previously reported results for standard type 316 stainless steel (composition 0.068% C, 17.2% Cr, 12.5% Ni, 1.92% Mg, 0.51% Si, 0.004% S, 0.039% P, 2.06% Mo, and 0.0005% B) irradiated at temperatures of 550 and 750°C to neutron fluences of approximately 9×10^{20} neutrons/cm^2 (thermal) and 7×10^{20} neutrons/cm^2 ($E > 1$ Mev). It was shown that for test temperatures of 550, 650, and 750°C irradiation caused a significant decrease in the tensile ductility and that this decrease was independent of irradiation temperature in the range of 550 to 750°C. For annealing temperatures of 950, 1050, and 1150°C and for test temperatures of 650 and 750°C, maximum tensile ductility for both unirradiated and irradiated specimens (irradiated at 750°C) was obtained by annealing 1 hr at 1050°C (ref. 1).

A summary of the 650°C creep-rupture data on standard type 316 stainless steel is given in Table 3.3. Although the data available at this time are limited, several trends seem evident. Neutron irradiation causes a reduction in rupture life and total elongation to fracture of the alloy. In the range of 550 to 750°C these changes in properties are dependent on irradiation temperature. The ductility of specimens irradiated at 550°C is significantly lower than that of specimens irradiated at 750°C, yet with regard to rupture life the opposite is true. Creep rates of as-annealed specimens and those specimens irradiated at 550°C or aged for 2000 hr at 550°C are approximately the same, while the creep rate of specimens aged for 2000 hr at 650°C and those irradiated at 750°C are significantly higher. These data suggest that changes in properties result both from irradiation and from thermal aging effects.

---

[1]Fuels and Materials Development Program Quart. Progr. Rept. Dec. 31, 1967, ORNL-TM-2090, pp. 22–24.

Table 3.3. Creep-Rupture Properties of Type 316 Stainless Steel at 650°C

Heat Treatment and/or Irradiation Conditions	Stress (psi)	Rupture Life (hr)	Creep Rate (%/hr)	Total Elongation (%)	Reduction in Area (%)
Annealed 1 hr at 1050°C	40,000	28	0.35	36.2	39.2
	35,000	91	0.14	29.6	50.4
	32,500	117	0.029	25.1	44.9
	30,000	180	0.024	54.5	32.9
	27,500	1732	0.0046	31.4	52.6
	25,000	1311	0.0069	30.9	57.8
Annealed 1 hr at 1050°C,	30,000	15	0.085	3.2	9.0
irradiated approximately	25,000	252	~ 0.005	2.7	14.3
2000 hr at 550°C	20,000	5127		8.7	13.4
Annealed 1 hr at 1050°C	30,000	437		33.0	62.0
plus 2000 hr at 550°C	25,000	2305	0.0017	29.2	55.2
Annealed 1 hr at 1050°C,	25,000	92	0.12	14.8	17.4
irradiated approximately	20,000	137	0.064	9.3	6.7
2000 hr at 750°C	20,000	524	0.024	16.7	22.1
Annealed 1 hr at 1050°C	35,000	20	1.13	52.2	71.0
plus 2000 hr at 650°C	30,000	146	0.14	37.5	75.2

Additional tests are being conducted on specimens irradiated at 650°C and on thermal control specimens. Optical and transmission microscopy is also under way.

Specimens from two heats of vacuum-induction melted titanium-modified type 316 stainless steel were included in this irradiation experiment and are presently being evaluated. The compositions of the two alloys are given below:

	Composition, wt %			Composition, wt %	
Element	Heat 3765-3	Heat 3765-4	Element	Heat 3765-3	Heat 3765-4
Carbon	0.06	0.05	Titanium	0.22	0.33
Chromium	17	17	Manganese	0.5	0.4
Nickel	12	12	Silicon	0.4	0.4
Molybdenum	2.4	2.4	Boron	0.0007	0.0007

Tensile properties of standard type 316 stainless steel and the two titanium-modified experimental heats after irradiation at 550 and 750°C are listed in Table 3.4. Both of the titanium-modified alloys exhibit significantly higher yield and ultimate tensile strengths than the standard type 316 stainless steel alloy. Elongation values for the type 316 stainless steel plus 0.22% Ti alloy are approximately the same as the standard alloy and those of the type 316 stainless steel plus 0.33% Ti are approximately the same at 550°C, but tend to be slightly higher at test temperatures of 650 and 750°C. Results of postirradiation creep-rupture tests completed to date are listed in Table 3.5. Comparison of these test results with those listed in Table 3.3 indicates that both titanium-bearing alloys exhibit significant improvements in postirradiation stress-rupture life properties. Creep rates of specimens irradiated at 750°C were higher than those of specimens irradiated at 550°C suggesting that thermal aging effects are also important in these alloys. Elongation values are highest for the type 316 stainless steel plus 0.33% Ti alloy.

Postirradiation Properties of Incoloy 800

D. G. Harman

Our continuing work on experimental vacuum-melted heats of Incoloy 800 shows that this material is very responsive to grain-size treatments. Grain sizes can be controlled to less than 10 μ in diameter for both the 0.03 and 0.12% C alloys. Also the grain size resulting from a particular annealing treatment seems to be independent of the titanium content. (The aluminum level was approximately 0.22% for each of the alloys.) Figure 3.5 shows the fine structure at a magnification of 2000×.

We have tensile and creep tested several heats of both carbon levels after they were irradiated for two cycles in a core position of the ORR to an approximate thermal and fast fluence of 0.8×10^{21} neutrons/cm^2. The irradiation was carried out at controlled temperatures of 650 and 700°C for a duration of about 2300 hr.

Table 3.4. Tensile Properties of Type 316 and Titanium-Modified Type 316 Stainless Steel After Irradiation at 550 and 750°C

Alloy	Test Temperature (°C)	Irradiated at 550°C[a]			Irradiated at 750°C		
		Yield Stress (psi)	Ultimate Tensile Stress (psi)	Elongation (%)	Yield Stress (psi)	Ultimate Tensile Stress (psi)	Elongation (%)
Type 316 stainless steel, Heat 10542	550	17,300	60,400	32.9	19,900	63,100	29.7
	650	14,900	43,000	19.9	22,600	45,500	19.9
	750	14,800	29,300	13.2	17,500	26,200	14.8
Type 316 stainless steel plus 0.22% Ti, Heat 3765-3	550	22,900	119,700	31.7	28,200	74,900	22.6
	650	25,400	62,900	17.1	29,000	52,300	13.1
	750	15,100	36,700	17.9	19,700	29,200	11.7
Type 316 stainless steel plus 0.33% Ti, Heat 3765-4	550	26,500	78,800	29.9	28,200	70,100	22.6
	650	23,200	62,000	26.6	25,900	51,400	19.1
	750	25,700	37,000	20.0	21,900	29,300	20.5

[a]Irradiated for approximately 2000 hr to 7×10^{20} neutrons/cm^2 ($E > 1$ Mev) and 9×10^{20} neutrons/cm^2 (thermal); tensile tested at 0.002 min^{-1}.

Table 3.5. Postirradiation[a] Creep-Rupture Properties of Vacuum Melted Titanium-Modified Type 316 Stainless Steel at 650°C

Alloy	Heat Treatment and/or Irradiation Conditions	Stress (psi)	Rupture Life (hr)	Creep Rate (%/hr)	Total Elongation (%)	Reduction in Area (%)
Type 316 stainless steel plus 0.22% Ti, Heat 3765-3	Annealed 1 hr at 1050°C and irradiated at 550°C	40,000	50.5	0.156	1.3	3.2
		30,000	1053	0.0014	3.4	5.3
		25,000	> 1673		> 1.6	
Type 316 stainless steel plus 0.22% Ti, Heat 3765-3	Annealed 1 hr at 1050°C and irradiated at 750°C	35,000	15.6	0.58	10.6	14.9
		30,000	69.5	0.15	13.4	16.1
		25,000	250.7	0.09	30.0	13.3
Type 316 stainless steel plus 0.33% Ti, Heat 3765-11	Annealed 1 hr at 1050°C and irradiated at 550°C	40,000	75.8	0.022	5.2	11.6
		35,000	138.7	0.044	7.1	12.9
		30,000	557.9	0.005	4.8	
Type 316 stainless steel plus 0.33% Ti, Heat 3765-11	Annealed 1 hr at 1050°C and irradiated at 750°C	35,000	34.5	0.41	25.3	17.8
		30,000	132.8	0.074	17.6	19.4
		25,000	442.0	0.035	23.6	27.1

[a]Irradiated for approximately 2000 hr to 7×10^{20} neutrons/cm^2 (E > 1 Mev) and 9×10^{20} neutrons/cm^2 (thermal).

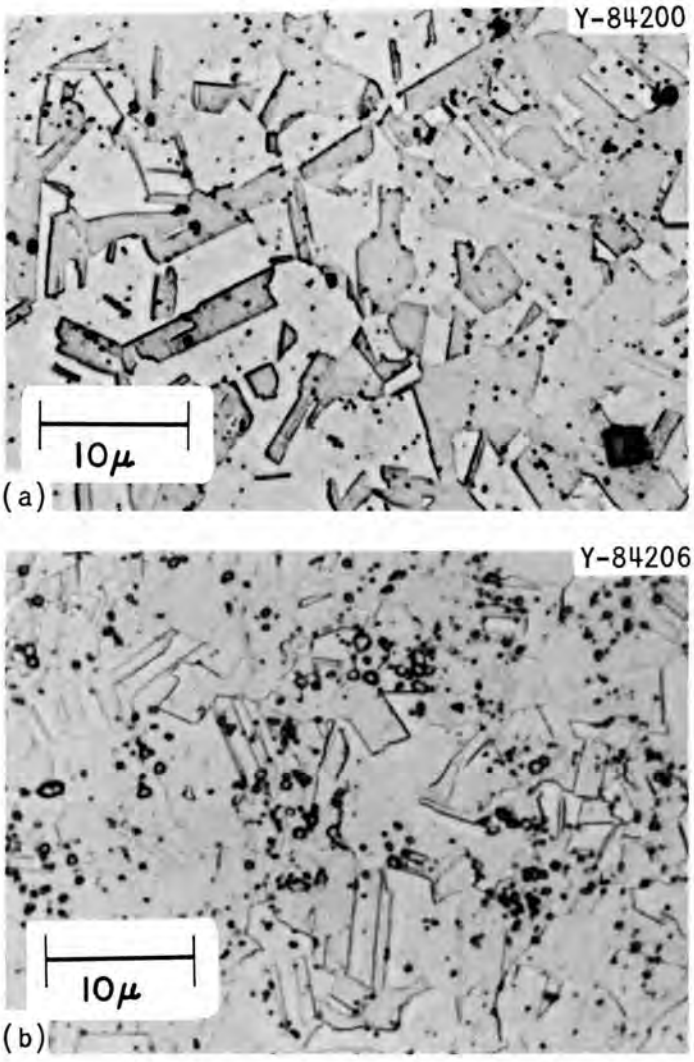

Fig. 3.5. Fine-Grained Microstructure of Incoloy 800. Representative microstructure of (a) 0.03% C and (b) 0.12% C with 0.1% Ti and 0.22% Al heat treated at 800°C for 10 min. 200×.

Calculations show that at least 90% of the boron (4 to 10 ppm for these alloys) would be burned up at this fluence.

Creep-elongation results at the 700°C test temperature are plotted as a function of titanium content for both carbon levels in Fig. 3.6. A distinct ductility peak for the 0.1% Ti level is evident. A similar compositional effect for creep elongation was reported previously[2] for

[2]D. G. Harman, Fuels and Materials Development Program Quart. Progr. Rept. Dec. 31, 1967, ORNL-TM-2090, pp. 29–39.

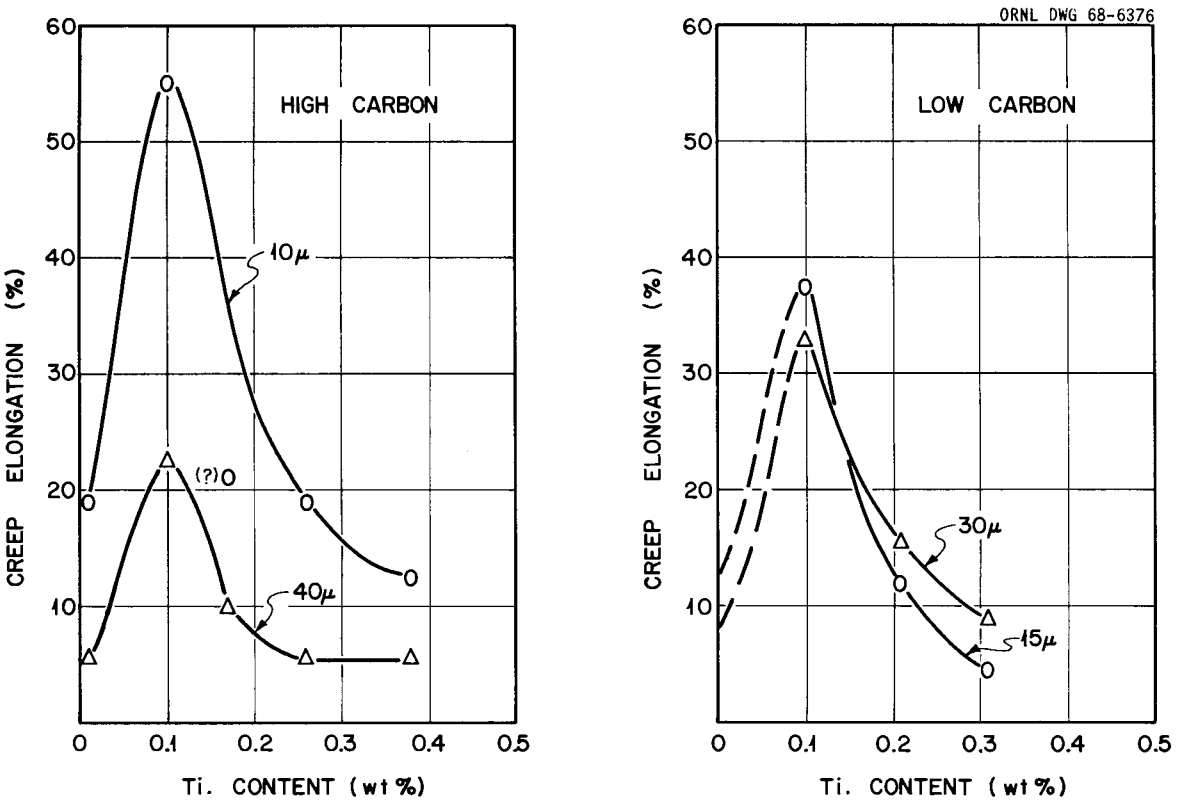

Fig. 3.6. Postirradiation Creep-Elongation of Incoloy 800 at 700°C. Irradiation was in core position of the ORR at 650 and 700°C for approximately 2300 hr to about 0.8×10^{21} neutrons/cm^2 (thermal and fast). Various grain sizes were attained using different annealing temperatures.

the test temperature of 760°C. Creep testing of Incoloy 800 is essential for postirradiation evaluation as tensile tests at both temperatures showed no ductility peak.

It is evident in Fig. 3.6 that the grain size is important to postirradiation creep ductility. Decreasing the grain size of the high-carbon 0.1% Ti alloy from 40 to 10 μ in diameter increased its ductility from 23 to 55% elongation. (See Fig. 3.6.) Figure 3.7 shows the data for two titanium levels plotted as a function of grain diameter and shows that the ductility may be independent of the carbon content. The expected longer rupture life for the larger grained material is illustrated by the rupture life versus grain diameter plot in Fig. 3.7.

We are currently conducting a more detailed study of grain size in an irradiation experiment at 700°C. Four alloys have been irradiated at 700°C in a poolside facility for one cycle [3 to 4 $\times 10^{20}$ neutrons/cm^2 (thermal)] after having been annealed for 30 min at temperatures that

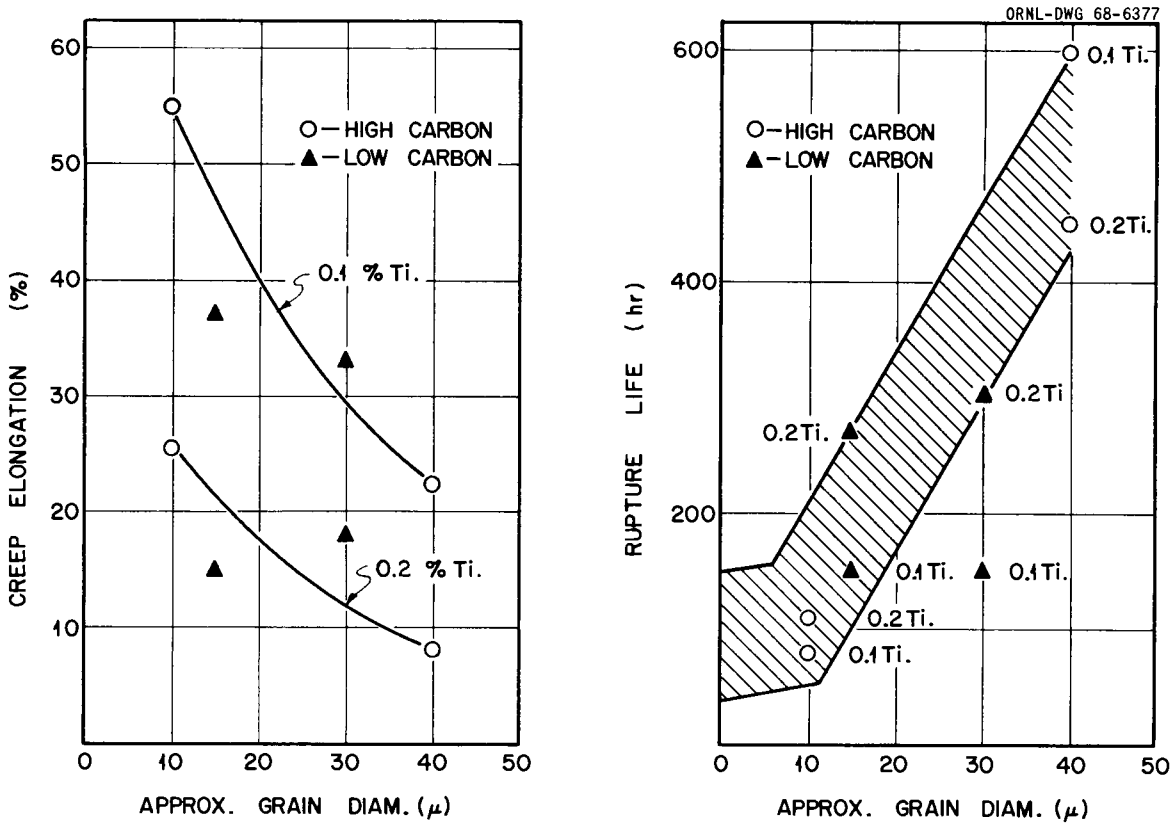

Fig. 3.7. Postirradiation Creep Properties of Incoloy 800 at 700°C. Irradiation was in core position of the ORR at 650 and 760°C for approximately 2300 hr to about 0.8×10^{21} neutrons/cm^2 (thermal and fast). Various grain sizes were attained with different annealing temperatures. The creep data are for 12,000 psi.

have been shown to produce desired grain sizes. Tensile and creep testing is being conducted at 700°C.

Creep tests at 12,000 and 10,000 psi completed on the 0.1 Ti–0.03% C alloy treated to fine-grain size showed 55 and 100% elongation, respectively. The specimen that elongated 100% was removed from the test just before rupture and is shown in Fig. 3.8 as compared with a specimen before test. Careful examination of the photograph shows the original specimen to be 1 7/8 in. long and the tested specimen to be 2 7/8 in. long. If all of this extension is assumed to have occurred within a 1-in. gage length, a 100% creep strain has occurred.

Our results so far on Incoloy 800 have shown that both material and testing parameters are very important. Creep-rupture testing is essential for postirradiation evaluation. A close control of titanium content

Fig. 3.8. Postirradiation Creep Specimen After Test. Buttonhead specimen near scale was creep tested nearly to failure at 700°C after 3 to 4 × 10^{20} neutrons/cm^2 at 700°C. Photograph compares the tested specimen to one before test. One-inch extension indicates 100% creep strain.

and grain size is imperative for postirradiation properties that are both desirable and predictable.

EBR-II Structural Materials Irradiation Experiments

E. E. Bloom J. R. Weir, Jr.

Two structural-materials irradiation experiments have been constructed and are to be inserted into the reactor at the beginning of run 28. The subassemblies have been designated X034 and X035 and are to be irradiated in rows 2 and 7 positions, respectively. ORNL materials included in the subassemblies are types 304, 304L, titanium-modified 304 and 304L, 316, and 316L stainless steel, Incoloy 800 (several compositions), V–20% Ti, and Nickel 270.

Specimens are contained in specimen holders as shown in Fig. 3.9. The experiments were designed on the basis of nuclear heating rates

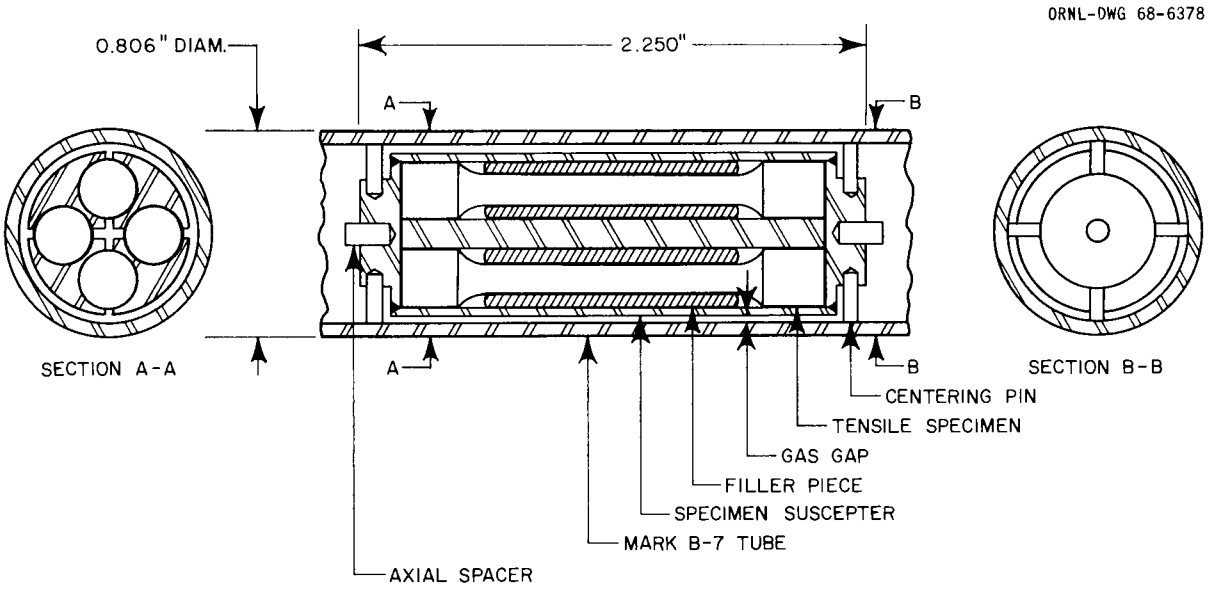

Fig. 3.9. Schematic of EBR-II Specimen Holder.

previously determined.[3] In the design of each tube of a subassembly a computer program was used to calculate the gas annulus between the surface of the specimen holder and the inner wall of the tube. Briefly the technique was:

1. The materials and desired irradiation temperature for each specimen holder within a given tube were determined.

2. This information, inlet sodium temperature, sodium flow rate, a sodium film coefficient, the fixed (cold) geometry, the material properties (such as, emissivity, density, thermal expansion coefficients and thermal conductivities as a function of temperature), and the nuclear heating rates as a function of axial position were input to the computer.

3. The computer was programmed to calculate the cold gas annulus required to attain the specified irradiation temperatures. Calculations for gas annulus were performed at three places (bottom, middle, and top) on each of the sixteen 2 1/4-in.-long specimen holders.

It was assumed that at steady state all heat transfer within the capsule tube was radial, and that the total heat transferred across the

[3]E. E. Bloom, A. F. Zulliger, and J. R. Weir, Fuels and Materials Development Program Quart. Progr. Rept. Dec. 31, 1967, ORNL-TM-2090, pp. 45-49.

gas annulus was the sum of that transferred by conduction and by radiation. Standard equations applicable to these conditions and geometry were used.

On the basis of initial computer calculations, the sodium flow rate to attain required outlet sodium temperature from the subassembly was determined. Subsequent calculations were then performed to determine the required gas annulus for each specimen holder within a given tube. Starting at the bottom of the tube, where the sodium inlet temperature is 370°C, heat was added to the sodium at each calculated position. The heat added included that generated within the tube and one-seventh of the heat generated in the sodium coolant within the subassembly and one-seventh of the heat generated in the stainless steel wrapper tube. The sodium coolant temperature at each calculated position was then determined and the calculation for the gas annulus was based upon the transfer of heat to sodium at this temperature.

In this experiment, the primary emphasis has been placed on an investigation of the variables of irradiation temperature, neutron flux and fluence. The effects of irradiation upon the properties of the various alloys will be determined by postirradiation tensile, stress-rupture, hot-hardness, density, and resistivity measurements. These data will be correlated with changes in microstructure as determined by optical and electron microscopy.

Irradiation temperatures will be checked by using silicon carbide monitors as described by Martin and Price.[3,4]

Examination of EBR-II Fuel Cladding

E. E. Bloom J. O. Stiegler J. R. Weir

We have recently started an electron microscope examination of the fuel cladding taken from EBR-II fuel element C-179-86. The cladding is type 304L stainless steel tubing with 0.174-in. OD and 0.009-in. wall

[4]W. H. Martin and A. M. Price, Determination of Irradiation Temperature in Graphite Irradiation Experiments Performed in the Dounreay Fast Reactor, UKAEA TRG Report 1117(C), 1966.

thickness. This particular fuel element was irradiated in a row-2 position to a peak fast neutron fluence of 1.4×10^{22} neutrons/cm^2.

To date we have examined specimens taken at intervals of approximately 3 in. along the length of the cladding. Two structural features, voids and dislocation loops, were present in all specimens. Table 3.6 lists the approximate irradiation temperatures, neutron fluences, and void densitites for each of the sections that have been examined.

Table 3.6. Irradiation Conditions and Void Density Measurements for EBR-II Fuel Cladding

Section Number	Irradiation Temperature (°C)	Fast Neutron Fluence (neutrons/cm^2)	Void Density (voids/cm^3)
		$\times 10^{22}$	$\times 10^{15}$
1	370	0.8	1.4
2	398	1.2	1.3
3	438	1.4	1.3
4	465	1.3	0.9
5	472	0.9	0.4

Void-density values are based on a count of the number of voids per unit area on a photomicrograph and upon the assumption of a foil thickness of 1000 A. A comparison of the results for sections 1 and 5 and 2 and 4 indicates that the void density decreases with increasing irradiation temperature. Figure 3.10 shows a histogram of the void sizes that were observed in section 3. On the basis of this void-size distribution and the number of voids per unit volume listed in Table 3.6, it is calculated that the cladding density is decreased 0.17% by the irradiation. Similar measurements are not available for the other sections; however, as can be seen from Fig. 3.11, the void size increases as the irradiation temperature increases.

The distribution of the voids was remarkably homogeneous. Variations observed between different micrographs probably reflect differences in foil thickness. It is significant, however, that no voids were present in the grain boundaries. In fact, the void density within about

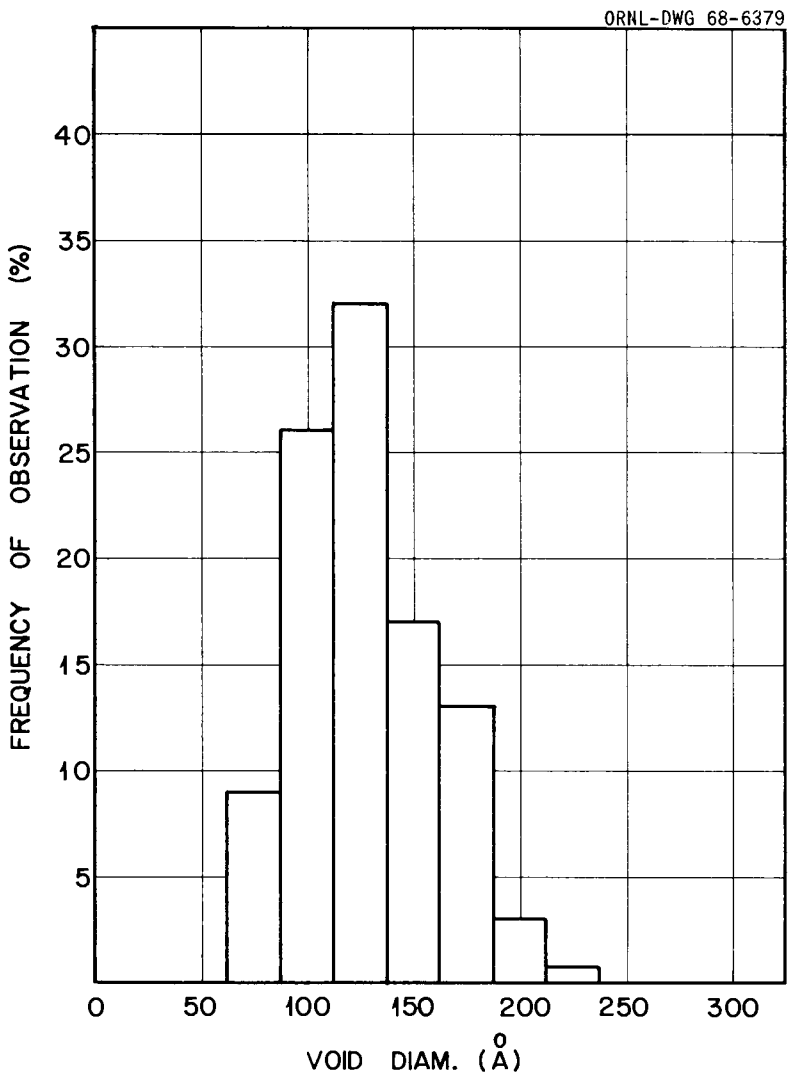

Fig. 3.10. Void-Size Distribution in EBR-II Cladding, Irradiated at 438°C to 1.4 × 10^{22} neutrons/cm^2.

0.1 μ of the boundary was reduced probably by annihilation of voids contacting the boundary.

A very complex dislocation substructure was present in each of the five sections. At the lower irradiation temperatures the structure was so complicated that individual loops could not be observed. At 472°C, however, well defined loops were resolved as shown in Fig. 3.12. These loops lie on {111} and appear faulted suggesting that they are Frank sessile loops formed by the collection of interstitial atoms. The loops ranged in diameter between 200 and 900 A and were present in a density of about 2 × 10^{15} loops/cm^3.

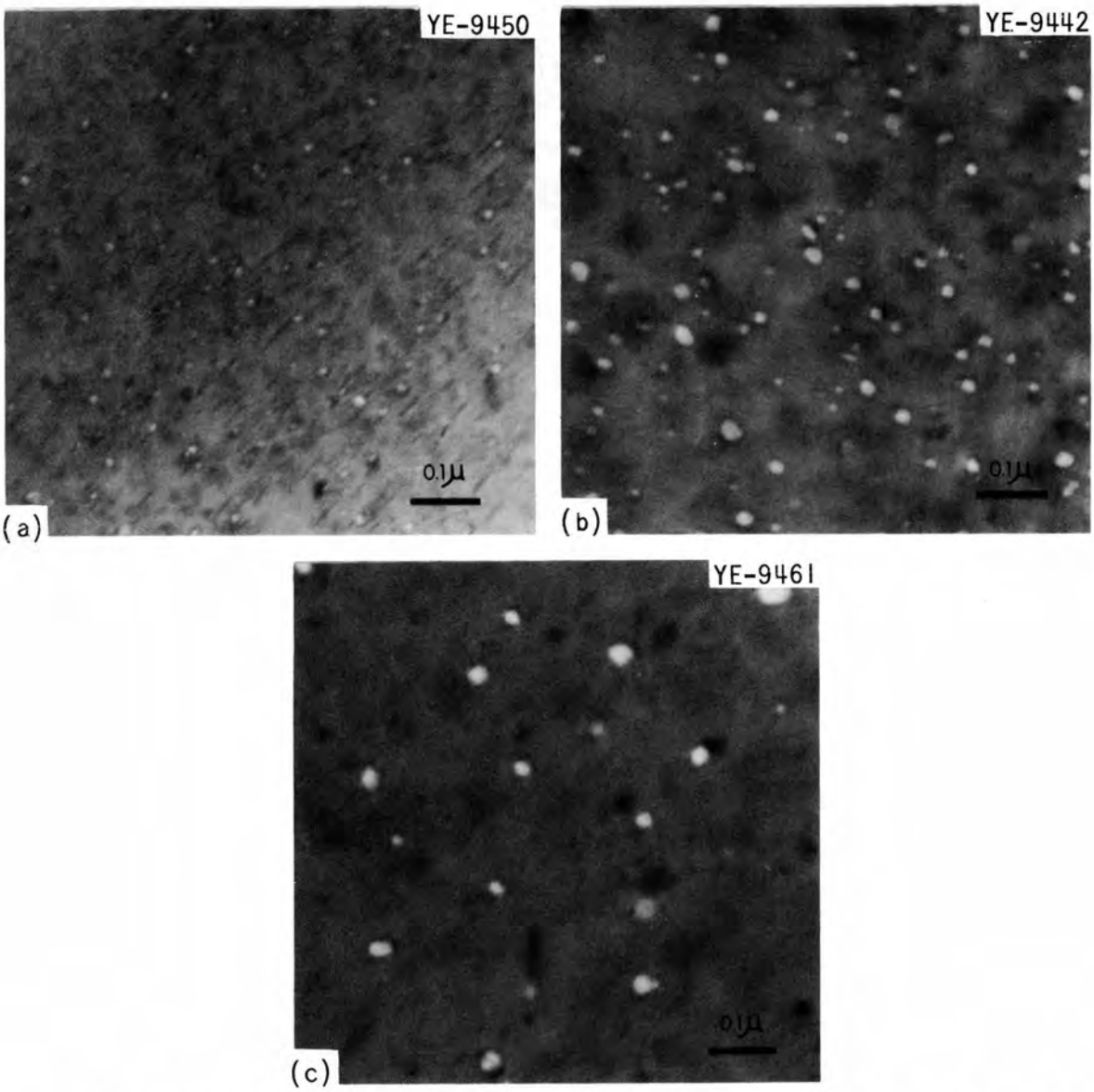

Fig. 3.11. Void Formation in Type 304L Stainless Steel Fuel Cladding from EBR-II. (a) 0.8×10^{22} neutrons/cm^2 at 370°C, 1.4×10^{15} voids/cm^3. (b) 1.4×10^{22} neutrons/cm^2 at 438°C, 1.3×10^{15} voids/cm^3. (c) 0.9×10^{22} neutrons/cm^2 at 472°C, 0.4×10^{15} voids/cm^3.

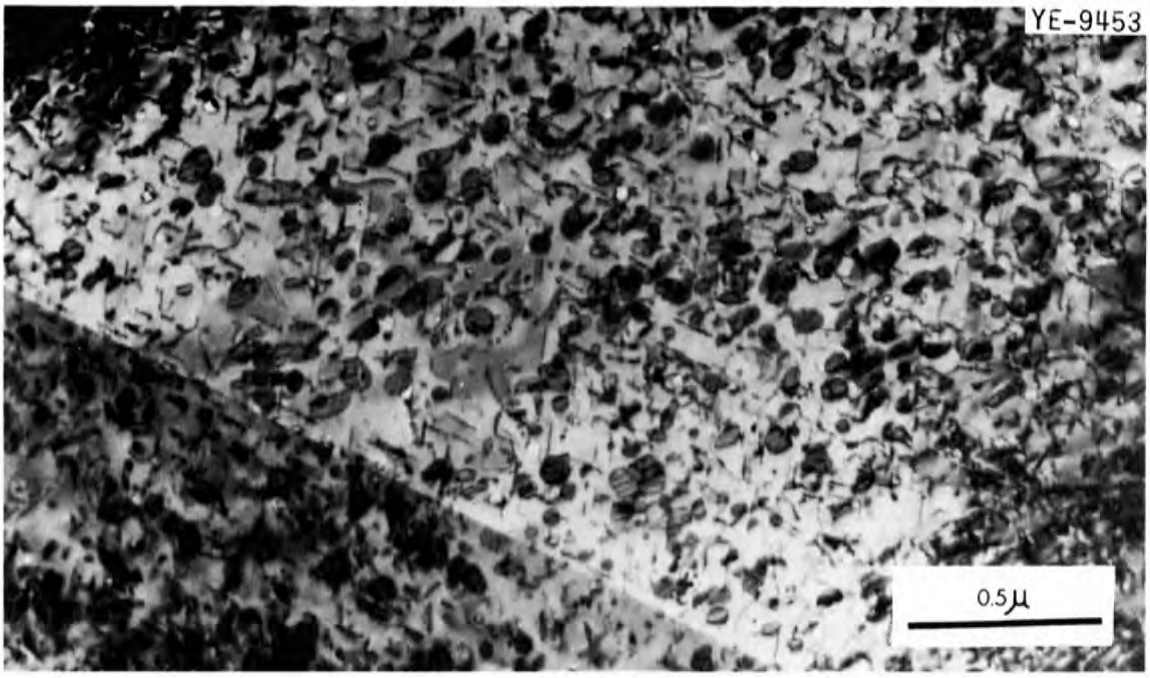

Fig. 3.12. Dislocation Loops Produced by Irradiation at 472°C.

4. MIXED NITRIDE FUELS DEVELOPMENT

J. L. Scott

Mixed (U,Pu)N continues to look attractive as fuel for advanced liquid-metal-cooled fast-breeder reactors. It has a very high theoretical density and good thermal conductivity.[1] Since stoichiometry control is easier than in the mixed carbide, a competitive fuel, compatibility problems should be less severe.

Our program for developing the mixed nitride includes fabrication studies, physical property determinations, compatibility work, and irradiation testing. Since our experimental facility for working with plutonium nitride is not yet available, our efforts are directed toward checking equipment and procedures with uranium nitride as a stand-in. We expect to have the facility operating within the next quarter. Since irradiation testing requires long lead times, preliminary work is already under way on this phase of the program.

Our continuing work on mixed UC-UN, which has the advantages of both UC and UN and also appears to have a very attractive fuel cycle since it can be produced readily from the oxide, will establish practical impurity limits of UC in UN or UN in UC depending on the application. Basic data on the UC-UN system will enrich our understanding of these rock-salt type compounds.

Fuel Cycle Sol Gel

T. B. Lindemer

The kinetics of the synthesis of uranium carbides, nitrides, and carbonitrides from sol-gel UO_2 is being considered in an effort to determine those factors that control the conversion reactions. This knowledge is fundamental to the eventual design of a fuel cycle for producing the desired reactor fuel material.

---

[1] J. L. Scott, Fuels and Materials Development Program Quart. Progr. Rept. Dec. 31, 1967, ORNL-TM-2090, p. 50.

We are studying the reaction of nitrogen with "UC_2" to produce U(C,N). During this quarter we relocated the experimental apparatus in order to use two idle induction furnaces, made some minor modifications to the equipment, and made the various necessary calibrations. One of the two significant modifications was the installation of a sampling device that lets us remove samples from the fluidized bed at any time without disturbing the rest of the material. This lets us obtain samples for a given time series of experiments at a given temperature in 20% of the time otherwise required. The second modification was a simple device for automatically controlling the nitrogen pressure in the experiment to ±1/4 torr at pressures from 5 to 760 torr.

The original parameters of the study included time, temperature, and particle size, but it has become apparent from the literature that the effects of nitrogen pressure, free carbon in the "UC_2," and the "age" of the "UC_2" are also important from both the fundamental and engineering viewpoints because they can alter the reaction rates quite significantly. We have established base-line data at a nitrogen pressure of 380 torr on unaged "UC_2" containing a given amount of free carbon; they appear to follow the predictions for a diffusion-controlled reaction to 100% completion, a condition necessary for the fundamental analysis of the reaction kinetics. We are attempting to study "fully aged" material to determine the increase in the reaction rate of this material over that for "unaged" material. It is exactly this kind of information that is critical in the designing of the most economical fuel cycle for producing U(C,N).

We are continuing the investigation of the new uranium compound observed when UO_2 is reacted in the presence of carbon and nitrogen.[2] A limited quantity of this has been produced and is being analyzed.

Synthesis and Fabrication of UN and U(C,N)

R. A. Potter

Since the continuing interest in UN and U(C,N) imposes on our synthesis and fabrication facility increasing demands for fabricated specimens,

[2]T. B. Lindemer, Fuels and Materials Development Program Quart. Progr. Rept. Dec. 31, 1967, ORNL-TM-2090, p. 62.

our efforts are now directed toward producing powder compositions and specimens to meet the current needs. Development of process techniques is mostly limited to expedient solutions of problems met during the routine preparation of materials and specimens. Recently, one such problem was the oxygen contamination of specimens formed isostatically for fundamental studies by methods essentially unchanged from those previously described.[3] Second-phase oxide contamination found in the first samples made it necessary to modify the bagging and debagging procedure. These are now done entirely within the glove box, whereas before this, samples were subjected to a short-time exposure to air which — since the change alleviated the problem — was apparently enough to allow measurable oxidation. Progressive deterioration of the atmosphere within the sintering furnace also aggravates the problem of oxygen contamination, but using finely divided UN powder as a getter during sintering overcomes this. Although the propensity of the material for oxygen remains the most important factor to control, other areas need to be watched. One such area is within the realm of material synthesis. Recently, we tried to fabricate a set of high-density (96% of theoretical) UN specimens for hot-hardness measurements. The five 3/4 × 1/4-in. disks were isostatically pressed to approximately 55% of theoretical density and sintered 2 hr at 2300°C and 1 atm N_2 pressure. Although densities of 95–96% are usually obtained readily under such conditions, the disks sintered to only 92%. Subsequent heat treatments totaling 9 hr at temperatures as high as 2400°C failed to densify them beyond 94%. Metallographic examination of the microstructures revealed clusters of open porosity throughout the structure (see Fig. 4.1). Results from a second set of specimens, carefully prepared with attention to details such as lubricant additions, were essentially the same. We concluded that the problem stems from the "as-synthesized" powder. The synthesis log showed powder preparation to be consistent with previous batches except that the temperature of dissociation from U_2N_3

[3]R. A. Potter, Fuels and Materials Development Program Quart. Progr. Rept. Dec. 31, 1967, ORNL-TM-2090, p. 63.

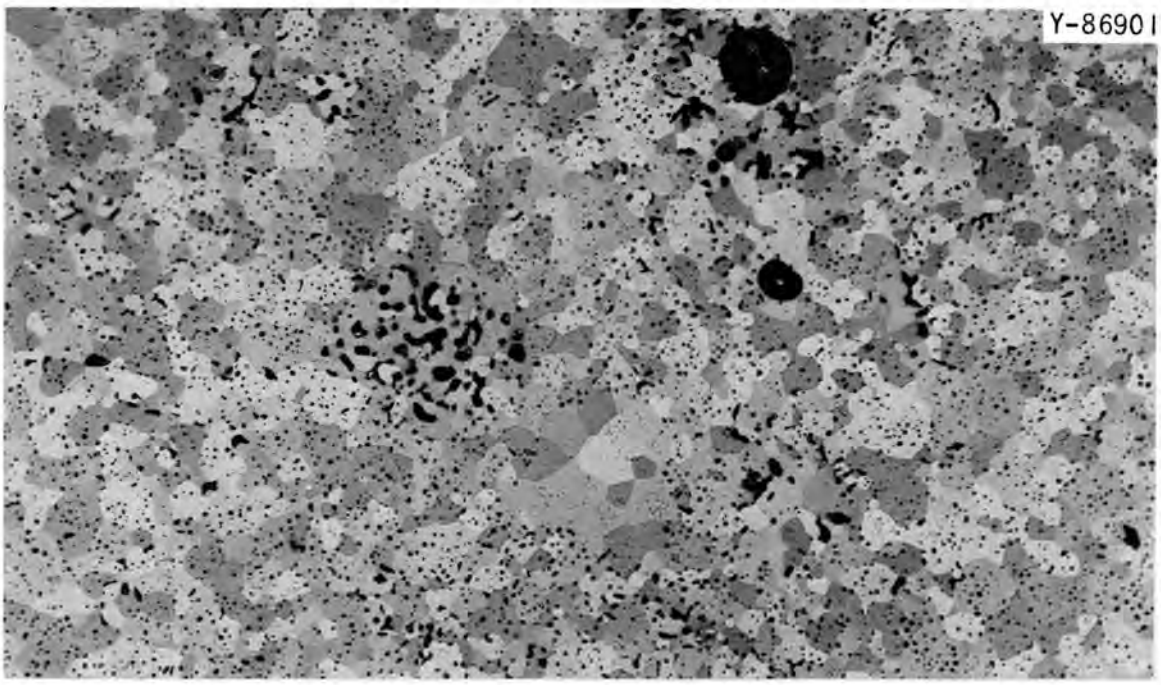

Fig. 4.1. Microstructure of UN Specimen Fabricated from Powder Containing Excess Nitrogen. Etchant: 30 lactic, 10 HNO_3, 1 HF. 100×.

to the lower nitride UN_x was 875°C rather than our usual 900°C. Apparently not enough nitrogen was removed from the material, and during sintering the exodus of the gas blew the structure apart. Chemical analysis for the nitrogen content of the original powder is pending. Such problems are exceptional, and with proper control measures, UN can be readily synthesized and fabricated into a variety of shapes.

During the report period, we successfully prepared high density, high purity, single-phase UN samples for diffusion and sintering studies and performed several heat treatments on specimens for fundamental studies. We also prepared a 1/2-kg batch of UN powder for NASA, Lewis Research Center, and a set of 50 sintered specimens now being ground to size. In our constant efforts to improve our facility, we isolated one glove box in which we hope to maintain an exceptionally clean atmosphere and equipped it with an argon purity meter.

Search for Grain-Boundary Segregation of Oxygen in Uranium Mononitride

J.D.L. Harrison

Westbrook[4] demonstrated that grain-boundary segregation of impurities takes place in several metal-oxide systems at impurity concentrations well below the solubility limits. Such segregation can influence greatly those properties of a polycrystalline material that depend on diffusion rates in and of the grain boundaries.

We plan to look for the possible segregation of oxygen in UN by autoradiography and grain-boundary microhardness measurements. Simple apparatus to oxidize fine UN powders with controlled amounts of ^{18}O vapor has been constructed and a specimen holder has been designed and made to hold the specimens sintered from the oxidized powder in a 3-Mev proton beam. This proton bombardment will produce ^{18}F in those areas containing ^{18}O, and the location of the ^{18}F, which decays by positron emission, will be found by thin film autoradiography to a resolution of ± 5 μm.

Measurements of the grain-boundary microhardness of arc-melted low-oxygen uranium nitride and of oxide-containing sintered nitride have not shown any significant differences from the bulk microhardness. It is possible that the effects of adsorbed surface water vapor obscured any differences. Later experiments have revealed both for UN and $U(N_{0.8}C_{0.2})$ that the observed microhardness increases when the surface is cleaned by cathodic etching and protected from subsequent gaseous contamination by toluene. Definitive work on grain-boundary microhardness in this system can probably not be done until better techniques for the cleaning and preservation of the surfaces have been devised.

---

[4] J. H. Westbrook, "Impurity Effects at Grain Boundaries in Ceramics," p. 263 in Science of Ceramics, Vol. III, ed. by G. H. Stewart, The British Ceramic Society, Stoke-on-Trent, England, 1967.

Study of the Compatibility of Uranium Mononitride with Cladding Alloys

J.D.L. Harrison

The object of this work is to observe the out-of-reactor interaction between nitrides of nominal compositions UN; $U(N_{0.95}C_{0.05})$; $U(N_{0.95}O_{0.05})$; $U(N_{0.90}C_{0.05}O_{0.05})$ with stainless steel types 316L, 304L, ORNL-modified 304, and with V–5% Ti–15% Cr. Sandwiches of each alloy and each nitride composition are to be placed in initially evacuated and welded stainless steel capsules. These are to be heated to 800 and 1000°C for 1000 hr and then examined by metallography and microprobe analysis.

The capsules have been designed and manufactured, as has the rig in which they will be heated. The steel samples have been prepared and the vanadium alloy ordered from Argonne National Laboratory. R. A. Potter is preparing the nitride samples.

The Hot Hardness of Uranium Carbonitrides

J.D.L. Harrison

Measurement of the hot hardness of compositions between UC and UN at temperatures up to 1200°C will provide some indication of the way high-temperature strength and creep vary with composition and will assist in the selection of the most appropriate compositions for more detailed irradiation creep experiments.

A diamond indenter that we designed for the Marshall hot-hardness machine is now due for delivery. Vacuum leaks in the machine have been repaired; the specimen support platform has been modified so that errors in temperature have been reduced from 100 to 6° at 800°C and from 30 to 10° at 1000°C. The mechanical load-applying mechanism transmitted vibration to the indenter and caused erroneously large indentations. Until a better loading system is installed, the loading mechanism is being operated by hand.

R. A. Potter is making high-density (> 96% of theoretical) specimens.

Studies in the U-C-N System

J. M. Leitnaker R. A. Potter
K. E. Spear

The importance of the U-C-N system in reactor technology has been discussed previously.[5] The work described here is an attempt to define the important compositional variables within the solid-solution range.

We have described the analytical procedures developed and the results of these procedures on single-phase U(C,N) samples.[5] We have now completed the analytical portion of the work. Samples containing excess uranium have been examined along with samples containing excess carbon. Results show that the UC-UN solid solution does not obey Vegard's law in the ranges studied and that the width of the phase is narrow.

Experimental

Many of the experimental details already have been reported.[5] We prepared samples in equilibrium with excess graphite by heating in the furnace described previously[6] UC, or UN mixed with spectrographic −325 mesh graphite, at desired temperatures and pressures of nitrogen.

Nine samples of monotonously increasing carbon content which were to be equilibrated with uranium were prepared initially as previously described for single-phase samples.[5] These samples were then heated in a dynamic vacuum (2×10^{-5} torr) at 1650°C for 9 hr. After this, samples 2, 4, 6, and 8 were crushed to −325 mesh, repressed, and reheated for 7 hr at 1650°C and 3×10^{-5} torr.

After the heat treatments, we examined the samples by x-ray, chemical analyses, and occasionally metallography. Details of the x-ray examination and the standards used are accurately described elsewhere.[6]

---

[5]J. M. Leitnaker, R. A. Potter, and K. E. Spear, Fuels and Materials Development Program Quart. Progr. Rept. Dec. 31, 1967, ORNL-TM-2090, pp. 87–98.

[6]J. M. Leitnaker, "The Ideality of the UC-UN Solid Solution," pp. 317–330 in Thermodynamics of Nuclear Materials, 1967, International Atomic Energy Agency, Vienna, 1968.

In view of the previously discussed difficulty[5] with analytical results, and because eight separate measurements had to be correlated on each sample (analyses for uranium, total carbon, free carbon, and nitrogen; plus measurement of temperature, pressure, and x-ray lattice parameter, and in some cases, an oxygen analysis), we performed our own analyses for uranium, total carbon, and free carbon and also obtained the same measurements from the Analytical Chemistry group. All of the analyses are rather standard procedures. Analytical Chemistry determined the nitrogen by heating samples in a sealed tube with HCl to 200°C. The nitrogen was then distilled as ammonia from a basic solution into saturated boric acid and titrated. Oxygen was determined, also by the Analytical Chemistry group, by a standard inert-gas fusion followed by conductimetric titration of the CO_2. We discussed our own analytical procedures previously.[5]

Results

Analyses and x-ray data for samples which were to be in equilibrium with uranium are reported in Table 4.1. Samples 3, 4, and 8 are suspect; they had a spread in the nitrogen-to-(N+C) ratio of 0.042, 0.085, and 0.0355, respectively. The largest spread in the other results was 0.016. The average values of these three agreed well with the other results of this series. From these data, again, one can calculate (C+N) and compare this with the total moles of uranium (see Table 4.2). In this case the average moles (C+N) is 0.3978 and the average moles of uranium is 0.3980. We conclude there is no significant difference in the metal to metalloid ratio between these samples and the single-phase samples reported previously. In Fig. 4.2 are photomicrographs taken at the outside edge of samples 3, 4, and 5. It is clear from the overall view that nitrogen is lost from the outside; the white areas in the gray matrix are uranium, clearly in the grain boundaries. The "blotchy" areas in the black mounting material are Al_2O_3 particles put in to preserve the edge during grinding and polishing. Free uranium was not visible in any of the samples richer in carbon than sample 5. Thus, we have really only demonstrated the results in equilibrium with uranium for the region from UN to this composition. But it seems reasonable to suppose that the rest

Table 4.1. Analyses of U-C-N Samples in Equilibrium with Uranium[a]

Sample	Analysis, wt %			Lattice Constant (A)
	U	C	N[b]	
1	94.706	0.448	4.846	4.89707 ± 12
2	94.569	0.839	4.592	4.90405 ± 7
3	94.652	1.347	4.001	4.91137 ± 12
4	94.662	1.668	3.670	4.91750 ± 14
5	94.70	2.010	3.290	4.92467 ± 7
6	94.784	2.390	2.826	4.93047 ± 13
7	94.738	2.727	2.535	4.93615 ± 15
8	94.950	3.014	2.036	4.94112 ± 10
9	95.046	3.420	1.534	4.94649 ± 19

[a]See text for preparation of samples and analytical procedures.

[b]Obtained by difference of 100% − %C − %U.

Table 4.2. Comparison of Total Metalloid Composition with Metal Composition in U(C,N) Samples in Equilibrium with Uranium[a]

Sample	Composition, moles			
	C	N	(C+N)	U
1	0.0373	0.3460	0.3833	0.3978
2	0.0698	0.3270	0.3968	0.3972
3	0.1121	0.2856	0.3977	0.3975
4	0.1389	0.2620	0.4009	0.3976
5	0.1673	0.2349	0.4022	0.3977
6	0.1990	0.2017	0.4007	0.3981
7	0.2270	0.1810	0.4080	0.3979
8	0.2509	0.1454	0.3963	0.3988
9	0.2847	0.1095	0.3942	0.3992
Average			0.3978	0.3980

[a]Data taken from Table 4.1 were normalized to 100 g for these calculations.

of the samples had nitrogen activities comparable to that in equilibrium with uranium at 1650°C. The grinding, repressing, and reheating of alternate samples for an additional 7 hr without significant change in composition versus lattice constant (see below) we take as evidence that the nitrogen activity was nearly constant across the samples. In none

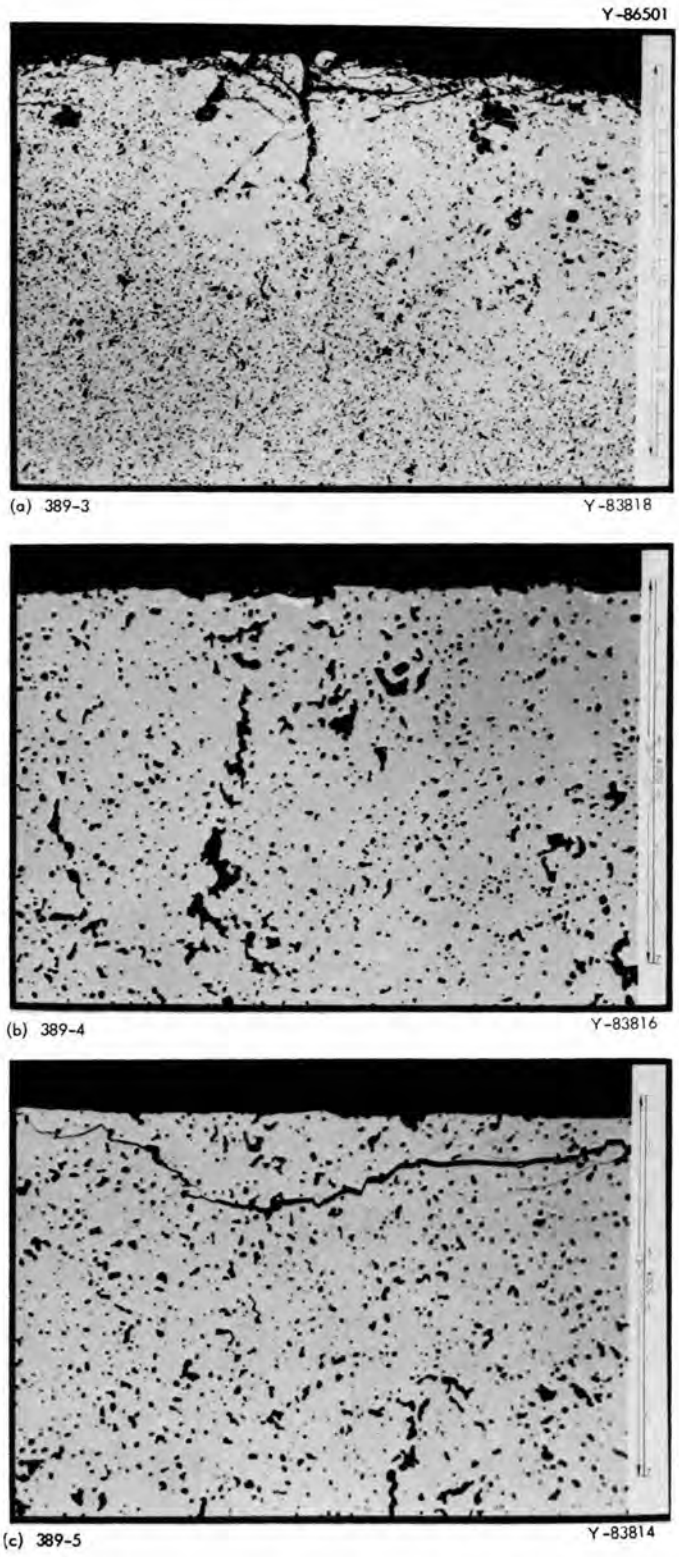

Fig. 4.2. Surfaces of Vacuum Heated U(C,N) Samples Showing Free Uranium. As polished.

of the samples did we take into account the amount of free uranium present. Note that we plot, subsequently, nitrogen-to-(N+C) and, furthermore, that the amount of free uranium present was very small compared to the total size of the sample. The smooth curve shown later in text seems to be evidence that equilibrium was attained in the first heating.

Analytical and x-ray data for samples intended to be in equilibrium with graphite are given in Tables 4.3 and 4.4. Table 4.3 shows data in which the starting material was UN plus spectroscopic grade graphite. These samples were, initially −325 mesh, mixed powders. These were reacted at the indicated temperatures by plunging them into the hot zone of the furnace at the indicated pressure of nitrogen as previously described.[6] After a 6-hr treatment, the sample was quenched, ground, and sieved through a 325-mesh screen in the dry box, and reheated for 6 hr.

Samples for which data are reported in Table 4.4 were obtained in a similar way except (a) the starting material was UC and (b) only the last two runs recorded were taken out and broken up.

By calculating the same quantities, as before, moles of uranium and moles of bound carbon plus moles of nitrogen, one sees that these results are less precise (see Tables 4.5 and 4.6). The average ratio of (C+N)-to-uranium is 0.9937 from Table 4.5 and 1.0176 from Table 4.6. The same ratio is 0.9962 from previously reported work[7] and is 0.9995 from Table 4.2. Within the accuracy of our experiments, there is really no detectable width to the U(C,N) — although it is somewhat comforting that our average ratios as calculated are greater on the carbon-rich side of the U(C,N) phase. The results in Table 4.4 (as seen via the aid of Table 4.6) are clearly the less precise of the two, perhaps because of the active state of the carbon precipitated from UC.

---

[7]J. M. Leitnaker, R. A. Potter, and K. E. Spear, Fuel and Materials Development Program Quart. Progr. Rept. Dec. 31, 1967, ORNL-TM-2090, p. 97.

Table 4.3. Data for UN Samples Reacted with Graphite

Sample[a]	Content, wt %					Lattice Constant[e] (A)	Temperature[f] (°C)	Pressure of Nitrogen[g] (torr)
	Uranium[b]	Total Carbon	Free Carbon	Nitrogen Difference[c]	Nitrogen[d]			
5077-54	90.53	4.54	4.13	4.93	4.78	4.89650 ± 5	1500 ± 2	607.8 ± 0.5
5077-100	93.536	3.548	1.428	2.916	2.83	4.92973 ± 10	1901 ± 3	393.3 ± 0.2
5077-104	94.060	2.824	0.806	3.116	3.00	4.92699 ± 6	1900 ± 3	597.3 ± 0.5
5077-108	93.630	3.562	1.322	2.838	2.73	4.93026 ± 13	1899 ± 3	389.9 ± 1.0
5077-114	92.423	3.594	2.334	3.983	3.97	4.91267 ± 6	1699 ± 2	390.7 ± 0.4
5077-118	92.976	2.862	1.734	4.162	4.03	4.90991 ± 7	1698 ± 2	590.0 ± 0.8
5077-124	92.203	3.581	2.678	3.581	3.53	4.91804 ± 11	1698 ± 3	187.3 ± 0.3

[a]All samples except 5077-54 were reacted on one day, reground to −325 mesh, and then subjected to an additional, identical heating. Otherwise, without a large excess of carbon, reaction was incomplete.

[b]All analyses are reported to one more figure than is believed significant. Each number is the average of at least two determinations.

[c]Obtained by subtracting weight percent total carbon and weight percent uranium from 100.

[d]Obtained by direct analysis.

[e]The error is the standard deviation as computed by the machine and the number means the error in the last one or two digits, as indicated. This error really serves as a measure of the quality of the pattern and, to the precision stated, bears only an accidental relationship to the lattice parameter of samples for which the analysis is reported.

[f]The stated error is the spread in recorded temperatures rather than an average value of deviation. The spread was assessed on the second day of heating.

[g]The stated error is the spread in recorded pressures rather than an average value of deviation. The spread was assessed on the second day of heating.

Table 4.4. Data for UC Samples Reacted with Nitrogen

Sample[a]	Content, wt %					Lattice Constant[e] (A)	Temperature[f] (°C)	Pressure of Nitrogen[g] (torr)
	Uranium[b]	Total Carbon	Free Carbon	Nitrogen Difference[c]	Nitrogen[d]			
5077-58[h]	90.492	4.547	4.16	4.854		4.89704 ± 5	1500 ± 3	583.4 ± 1.2
5077-62	85.981	9.499	9.08	4.52	4.40	4.89685 ± 12	1499 ± 2	594.6 ± 0.6
5077-64	86.266	9.564	8.601	4.170	4.16	4.90082 ± 12	1500 ± 3	194.2 ± 0.4
5077-66	86.566	9.558	8.201	3.876	3.79	4.91134 ± 9	1700 ± 3	389.0 ± 0.4
5077-78	91.994	4.368	2.828	3.638	3.46	4.91263 ± 10	1700 ± 3	387.3 ± 0.6
5077-82	91.532	4.394	3.308	4.074	3.98	4.90958 ± 7	1700 ± 5	583.7 ± 1.0
5077-92	92.719	4.352	2.112	2.929	2.80	4.92677 ± 14	1900 ± 2	590.7 ± 1.0
5077-96	92.794	4.488	2.034	2.718	2.52	4.93005 ± 11	1899 ± 3	391.3 ± 0.4

[a]Samples 5077-92 and 5077-96 were heated two days, as described in Table 4.3, Footnote a; others were heated one day only (about 6 hr).

[b]All analyses are reported to one more figure than is believed significant. Each number is the average of at least two determinations.

[c]Obtained by subtracting weight percent total carbon and weight percent uranium from 100.

[d]Obtained by direct analysis.

[e,f,g]See footnotes e, f, and g, Table 4.3.

[h]Sample run 22 hr.

Table 4.5. Comparison of Total Metalloid Content with Metal Content in Uranium Carbonitride Samples Containing Free Graphite[a]

Sample	Composition, moles				Ratio
	Uranium	Bound Carbon	Nitrogen Difference	(C+N)	(C+N)-to-Uranium
5077-100	0.3887	0.1765	0.2082	0.3846	0.9894
5077-104	0.3950	0.1680	0.2225	0.3905	0.9886
5077-108	0.3932	0.1865	0.2026	0.3891	0.9896
5077-114	0.3882	0.1049	0.2843	0.3892	1.0026
5077-118	0.3905	0.0939	0.2971	0.3910	1.0013
5077-124	0.3872	0.1280	0.2556	0.3836	0.9907

[a]Values taken from Table 4.3.

Table 4.6. Comparison of Total Metalloid Content with Metal Content in Uranium Carbonitride Samples Containing Free Carbon[a]

Sample	Composition, moles				Ratio
	Uranium	Bound Carbon	Nitrogen Difference	(C+N)	(C+N)-to-Uranium
5077-58	0.3801	0.0322	0.3467	0.3789	0.9968
5077-62	0.3611	0.0349	0.3227	0.3576	0.9903
5077-64	0.3623	0.0803	0.2977	0.3780	1.0433
5077-66	0.3636	0.1094	0.2767	0.3861	1.0619
5077-78	0.3864	0.1282	0.2597	0.3879	1.0039
5077-82	0.3844	0.0904	0.2908	0.3812	0.9917
5077-92	0.3894	0.1842	0.2091	0.3933	1.0100
5077-96	0.3897	0.2043	0.1940	0.3983	1.0221

[a]Values taken from Table 4.4.

In Fig. 4.3 (a through f) we compare results obtained in this study with those from various investigators.[8–12] To our data we added all published data available except the recent data of Naoumidis. We used end points of 4.9602 for UC and 4.8892 for UN and a least-squares technique to fit the data to a truncated power series. The equation used was

$$\frac{N}{C+N} = 1.00 + A(a_o - 4.8892) + B(a_o - 4.8892)^2 + D(a_o - 4.8892)^3 + E(a_o - 4.8892)^4 \quad . \tag{1}$$

We obtained these results:

$A = -13.2488$

$B = 42.5072$

$D = 2.13035 \times 10^2$

$E = -1.37677 \times 10^4$.

The term a_o is the lattice constant determined from the x-ray measurements for a given sample for which a composition is to be computed.

Our data are compared with the calculated line in Fig. 4.3a, b, and c. The data obtained with UN plus graphite as starting material in equilibrium with graphite are shown in a. These data lie just to the

---

[8]A. E. Austin and A. F. Gerds, The Uranium-Nitrogen-Carbon System, BMI-1272, p. 18 (June 23, 1958).

[9]J. Williams and R.A.J. Sambell, "The Uranium-Monocarbide-Uranium Mononitride System," J. Less-Common Metals 1, 217–226 (1959).

[10(a)]F. Anselin, "Preparation et Etude des Nitrures et Carbonitrures d'Uranium et de Plutonium," Tech. Rept. No. CEA-R 2988 (June 1966), Translation ORNL-tr-1722, by G. L. Boisvert, (b) F. Anselin, G. Dean, R. Lorenzelli, and R. Passard, "On the System (U,Pu)(C,N) as Applied to Sintered Carbides, Carbonitrides, and Oxycarbides," pp. 113–161 in Carbides in Nuclear Energy, Vol. 1, Physical and Chemical Properties/ Phase Diagrams (ed. by L. E. Russell et al.), Macmillan and Company, London, 1964.

[11]R. F. Stoops, J. V. Hamme, and G. S. Sheffield, Uranium Interstitial Phases, NCSC-2663-19, Joint USAEC-EURATOM, Research and Development Program, p. 43 (Dec. 1964), and private communication from G. S. Sheffield, Feb. 19, 1968.

[12]A. Naoumidis, Research in Uranium Nitrides and Carbonitrides, JUL-472-RW, p. 118 (March 1967).

Y-86558

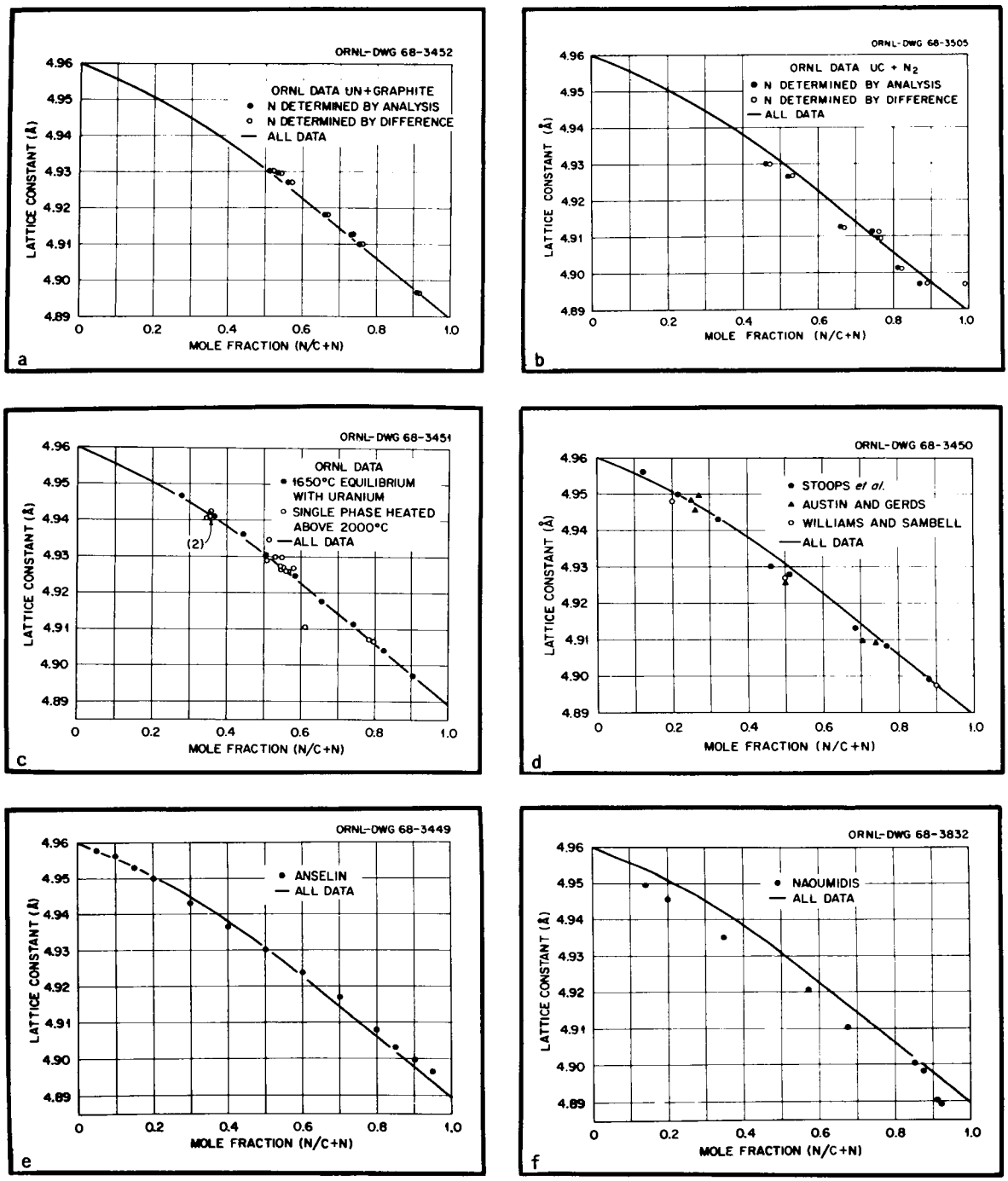

Fig. 4.3. Comparison of ORNL Data with Those of Other Investigators.

right of the line; and analyzed nitrogen-to-(N+C) compositions differ from the computed nitrogen-to-(N+C) [Eq. (1)] by an average +2%. The data from the starting material of UC + N_2, in the presence of excess carbon, are shown in b; these data scatter about the line but are not as smoothly consistent. The analyzed nitrogen-to-(N+C) values differ from that calculated by an average of −3.3%, and the nitrogen-to-(N+C) by difference is −1.0% from the line. The single-phase data and the data obtained in equilibrium with uranium — or low nitrogen activities — are shown in c. These data seem to bracket the line, but the average is somewhat above the line.

The data of other investigators are shown in the remainder of Fig. 4.3. The early investigators' data scatter considerably (d). The calculated curve agrees quite well with Anselin (e) from about N/(N+C) = 0.6 to pure UC. At higher nitrogen contents there is a deviation from the curve in the direction of higher a_o values for the same compositions. Anselin[10] indicates that samples of UN equilibrated with UO_2 at 1600°C have lattice parameters of 4.8925 ± 0.0005 A, while we use 4.8892 for the value of UN. Supposing a similar situation obtains with his U(C,N) samples as with his UN samples, for whatever reason, his deviation from the line is reasonably explained as a progressive increase in the effect from N/(N+C) = 0.6 to pure UN. However, Anselin[10a] also indicated that, "depending on how the sample was prepared, results for samples of identical composition could vary to ±10%, whereas the crystalline parameter remained constant to better than one ten-thousandth." We suspect that Anselin, in fact, observed the same difficulties in obtaining equilibrium that we experienced in the early portion of our work. The extent to which we have solved this problem can be seen most clearly in Fig. 4.3a, b, and c. We have approached equilibrium from several directions to obtain the results shown. We have used single-phase material, material in equilibrium with uranium, and material in equilibrium with graphite. Agreement among these three is excellent. Experimental temperatures have varied from 1500 to 2300°C, but we could find no effect of temperature on the lattice parameter-composition curve. Samples obtained from a UC starting material by reacting with nitrogen are very

likely not in true equilibrium, since they do not agree with the other three series.

It is most interesting to note, in agreement with Anselin's[10] earlier conclusion and in contrast with our own,[13] that the UC-UN solid solution does not obey Vegard's relationship over the range studied and that the width of the U(C,N) phase is so narrow. The data could provide an experimental basis for theoretical calculations on the difference between nitride and carbide bonding in uranium.

The practical significance of this work is that we provide a useful tool to indicate the degree of homogeneity of a U(C,N) sample. If analyses and lattice parameter measurements are not in agreement with Eq. (1), the system may be assumed to be inhomogeneous. We hesitate to say the converse is true, but one might hope that it is.

Thermodynamic Compatibility of Vanadium with LMFBR Fuels

K. E. Spear J. M. Leitnaker

Vanadium alloys are being actively considered for cladding LMFBR fuels. We have calculated equilibrium interactions of vanadium metal with uranium, plutonium, and mixed metal oxides, carbides, and nitrides with available thermodynamic data. In addition, we have begun an experimental program to determine the equilibrium phase behavior of the uranium-vanadium-nitrogen system.

Calculated Fuel-Vanadium Interactions

We have calculated the free energies of reactions representing possible interactions of vanadium metal and ceramic reactor fuels from available thermodynamic data; these are given below with their respective reactions. We believe these free energies are accurate within the error limits given up to at least 1500°C.

---

[13] J. M. Leitnaker, "The Ideality of the UC-UN Solid Solution," pp. 317–330 in Thermodynamics of Nuclear Materials, 1967, International Atomic Energy Agency, Vienna, 1968.

Oxides

$$4V + O(UO_{2+x}) = V_4O;\ \Delta G < 0 \text{ for } x > 0 . \quad (2)$$

$$4V + O(UO_{2-x}/U) = V_4O;\ \Delta G > 0 . \quad (3)$$

$$4V + O(PuO_{2-x}/Pu_2O_3) = V_4O;\ \Delta G < 0 . \quad (4)$$

$$4V + O(Pu_2O_3/Pu) = V_4O;\ \Delta G > 0 . \quad (5)$$

$$4V + O[(U_{1-x}Pu_x)O_{2-y}] = V_4O;\ \Delta G < 0 \text{ for } x > 2\left(y^{+0.02}_{-0.00}\right) . \quad (6)$$

Carbides

$$2V + UC = V_2C + U;\ \Delta G = (-10 \pm 2) + T\ (3 \pm 3)/10^3, \text{ kcal} . \quad (7)$$

$$2V + UC = V_2C + U(l);\ \Delta G = (-4 \pm 2) - T\ (1 \pm 3)/10^3, \text{ kcal} . \quad (8)$$

$$2V + PuC = V_2C + Pu;\ \Delta G = (-21 \pm 5) + T\ (5 \pm 5)/10^3, \text{ kcal} . \quad (9)$$

$$2V + PuC = V_2C + Pu(l);\ \Delta G = (-19 \pm 5) + T\ (1 \pm 5)/10^3, \text{ kcal} . \quad (10)$$

$$2V + (U_{0.8}Pu_{0.2})C = V_2C + (U_{0.8}Pu_{0.2});\ \Delta G = (-12 \pm 4) + T\ (3 \pm 4)/10^3, \text{ kcal} . \quad (11)$$

$$2V + (U_{0.8}Pu_{0.2})C = V_2C + (U_{0.8}Pu_{0.2})(l);\ \Delta G = (-7 \pm 4) - T\ (1 \pm 4)/10^3, \text{ kcal} . \quad (12)$$

Nitrides

$$2V + UN = V_2N + U;\ \Delta G = (+13 \pm 4) + T\ (3 \pm 3)/10^3, \text{ kcal} . \quad (13)$$

$$2V + UN + V_2N + U(l);\ \Delta G = (+19 \pm 4) - T\ (1 \pm 3)/10^3, \text{ kcal} . \quad (14)$$

$$2V + PuN = V_2N + Pu;\ \Delta G = (+19 \pm 4) + T\ (2 \pm 4)/10^3, \text{ kcal} . \quad (15)$$

$$2V + PuN = V_2N + Pu(l);\ \Delta G = (+21 \pm 4) - T\ (2 \pm 4)/10^3, \text{ kcal} . \quad (16)$$

$$2V + (U_{0.8}Pu_{0.2})N = V_2N + (U_{0.8}Pu_{0.2});\ \Delta G = (+14 \pm 5) + T\ (3 \pm 5)/10^3, \text{ kcal} . \quad (17)$$

$$2V + (U_{0.8}Pu_{0.2})N = V_2N + (U_{0.8}Pu_{0.2})(l);\ \Delta G = (+19 \pm 5) - T\ (1 \pm 5)/10^3, \text{ kcal} . \quad (18)$$

We assumed the activities of the metals, oxides, carbides, and nitrides were equal to unity. We calculated the activities of oxygen in oxide fuels to determine if they were higher or lower than that for the reaction

$$4V + 1/2\ O_2(g) = V_4O\ . \qquad (19)$$

If the activity (or pressure) of oxygen in the fuel is higher than that for reaction (19) then vanadium can react with the fuel to form V_4O; if it is lower, V_4O cannot form.

The Uranium-Vanadium-Nitrogen System

Vanadium cannot reduce uranium nitride to uranium metal according to the calculations reported in the previous section. We have begun experiments designed to test this prediction as well as to fix other equilibrium tie lines in the ternary uranium-vanadium-nitrogen phase diagram.

Mixtures of uranium nitride and either vanadium metal or vanadium nitride were pressed into pellets and heated at 1400 to 1600°C in dynamic vacuums of 10^{-6} torr or in nitrogen pressures up to 600 torr for 2 to 60 hr. The pellets were placed on a vanadium metal plate in a tungsten crucible for heating. The samples are being examined by x-ray and metallographic techniques.

A detailed analysis of the results has not been completed, and we are planning more experiments. However, a preliminary conclusion from the results is that vanadium metal will not reduce UN to uranium metal at 1400 to 1600°C. In (UN+V) samples contaminated with oxygen, small amounts of UO_2 and another phase were observed metallographically along with the UN and vanadium. The overall reaction may have been

$$UN + O_2 + 2V = UO_2 + V_2N\ . \qquad (20)$$

We have not, however, positively identified the V_2N phase.

Chemical Effects of Nuclear Burnup on Mixed Nitride Fuels

K. E. Spear J. L. Scott J. M. Leitnaker

The ability to predict and understand the equilibrium chemical interactions of a fuel in a reactor environment requires, among other things, a knowledge of the effects of nuclear burnup on the fuel. We have begun calculating these effects on nitride fuels.

The preliminary calculation below shows the atom distribution after 10 heavy atom percent burnup.

Zero Percent Burnup	Distribution of Atoms after Burnup
100 atoms nitrogen	100 atoms nitrogen
80 atoms ^{238}U	72 atoms ^{238}U
20 atoms ^{239}Pu	18 atoms ^{239}Pu (10 initial Pu) (8 from ^{238}U)
	20 atoms fission products

Nitrogen-14 will be lost because of burnup, but the amount is less than 1% and has been neglected in the present calculations.

The distribution of bound nitrogen is as follows:

Zero Percent Burnup	Distribution of Bound Nitrogen after 10 Heavy Atom Percent Burnup
0 atoms nitrogen as U_2N_3	9–15 atoms nitrogen as U_2N_3
80 atoms nitrogen as UN	66–62 atoms nitrogen as UN
20 atoms nitrogen as PuN	18 atoms nitrogen as PuN
0 atoms nitrogen as fission-product nitrides	7–5 atoms nitrogen as fission-product nitrides

The uncertainties in the distribution of bound nitrogen after burnup are due to the uncertainities in the stabilities of intermetallic compounds that could form. Effects of fuel and/or fission-product interactions with possible cladding materials have not been considered, nor has the effect of temperature gradients.

Our calculations show that 9 to 15 at. % N will be in the form of U_2N_3 after about 10 heavy atom percent burnup of a $(^{238}U_{0.8}{}^{239}Pu_{0.2})N$

fast-reactor fuel. Similar calculations for a ^{235}UN fuel indicate about 3 at. % N as U_2N_3 after the same burnup.

Available thermodynamic data indicate that U_2N_3 can nitride possible clad elements Cr, V, Nb, Ti, and Zr. Therefore, the elimination of U_2N_3 that could form as a result of fuel burnup would eliminate one possible source of compatibility problems.

We are considering two general approaches for prohibiting the formation of U_2N_3; both involve chemically tailoring the fuel. The first approach is to add another component such as vanadium to the fuel, either in the form of the metal or as hypostoichiometric VN_{1-x}. This additional component would take up the excess nitrogen resulting from burnup and thus eliminate the formation of U_2N_3. The second approach is to investigate the possibility of using a carbonitride fuel. While the abundant fission product molybdenum will not form a stable nitride (relative to U_2N_3), it does form a stable carbide. The reaction

$$(U,Pu)C_{soln} + 1/2\ N_2(g) + 2\ Mo(s) = (U,Pu)N_{soln} + Mo_2C\ (s) \qquad (21)$$

would proceed from left to right as burnup occurs. In other words, the carbonitride fuel would become richer in nitrogen as burnup occurs, and the carbon that is eliminated would react with the molybdenum.

5. NONDESTRUCTIVE TEST DEVELOPMENT

R. W. McClung

This program is intended to develop new and improved methods of nondestructively evaluating reactor materials and components. To achieve this we are studying various physical phenomena, developing instrumentation and other equipment, devising application techniques, and designing and fabricating reference standards. Among the methods being actively pursued are electromagnetics (with major emphasis on eddy currents), ultrasonics, penetrating radiation and holography. These and other methods are being evaluated for both normal and remote inspection.

Electromagnetic Test Methods

C. V. Dodd

Analytical Studies

We continued research and development on both analytical and empirical bases. In our analytical research, we are continuing to derive integral equations for problems of interest and we are using our computer programs to generate numerical solutions having direct applicability to actual eddy-current tests.

We have determined that the signal due to a defect can be expressed as a product of a "defect sensitivity factor" and a "flaw factor." The defect sensitivity factor is a mutual or self-inductance function and depends only on the coil system, frequency, conductivity and location in the metal. The flaw factor depends only on the volume, shape and orientation of the flaw.

We have derived the integral equations for the defect sensitivity factor for the following cases:

1. both single and differential coils inside a tube,
2. both single and differential coils encircling a tube,
3. a coil above a plane of one metal clad on another,

4. a reflection probe coil (such as used with the phase sensitive eddy-current instrument) above a plane of one metal clad on another.

We now need to program these integral equations for numerical solutions on a computer.

We have applied our computer programs to the analysis of eddy-current techniques using the phase-sensitive eddy-current instrument. Figure 5.1 shows the variation in calculated phase shift as a function of thickness for type 347 stainless steel. This was calculated for a coil similar to that used on our portable instrument at a frequency of 50 khz. Figure 5.2 shows the manner in which phase varies with lift-off (coil-to-metal spacing) for the same coil for a specific thickness (0.0635 in.). These calculations agree in general with measurements performed on the portable phase-sensitive eddy-current instrument.

We have also applied our computer program to determine the optimum frequency to obtain the maximum phase shift for a given coil and metal thickness. The results are shown in Fig. 5.3. The thickness is scaled in terms of mean coil radius.

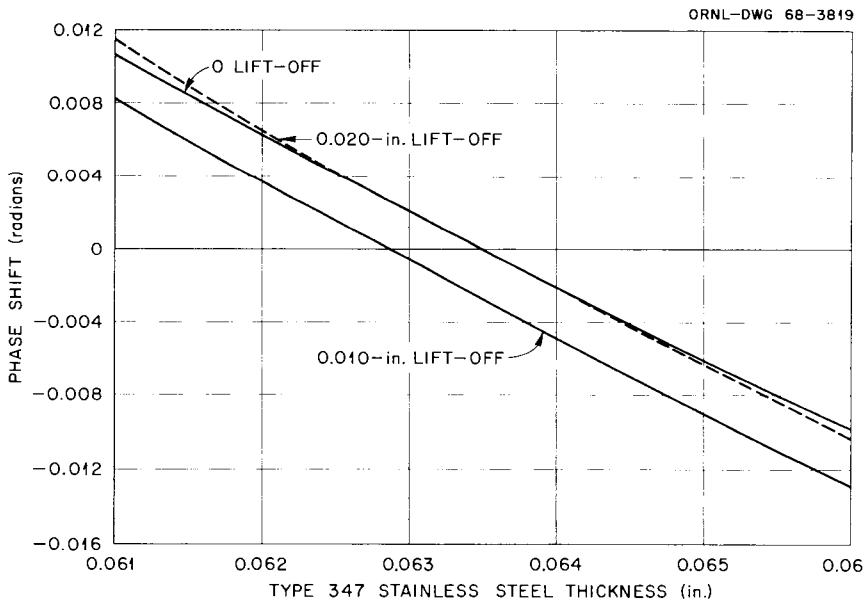

Fig. 5.1. Eddy-Current Phase Shift Versus Thickness of Type 347 Stainless Steel for Lift-Off Values of 0, 0.010, and 0.020 in.

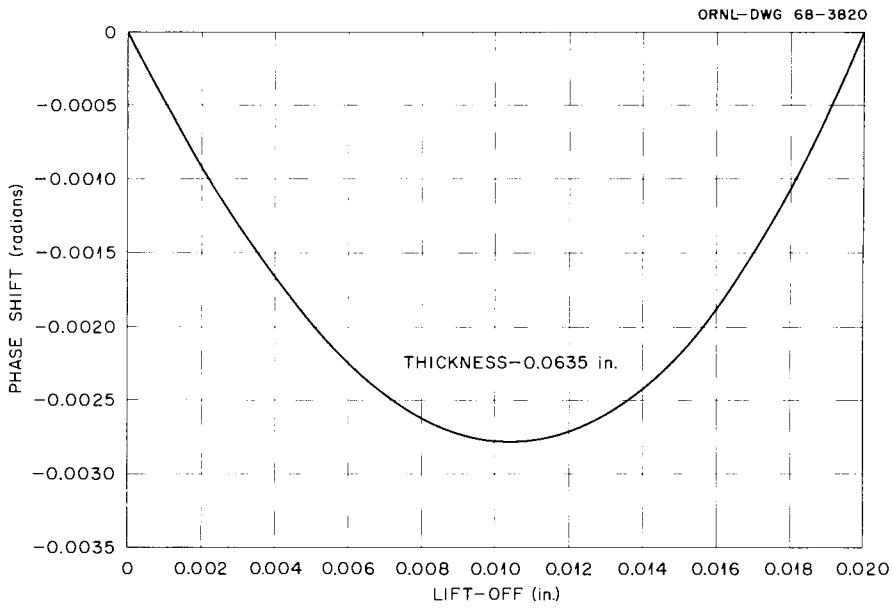

Fig. 5.2 Eddy-Current Phase Shift Versus Lift-Off for a 0.0635-in.-thick plate of type 347 stainless steel.

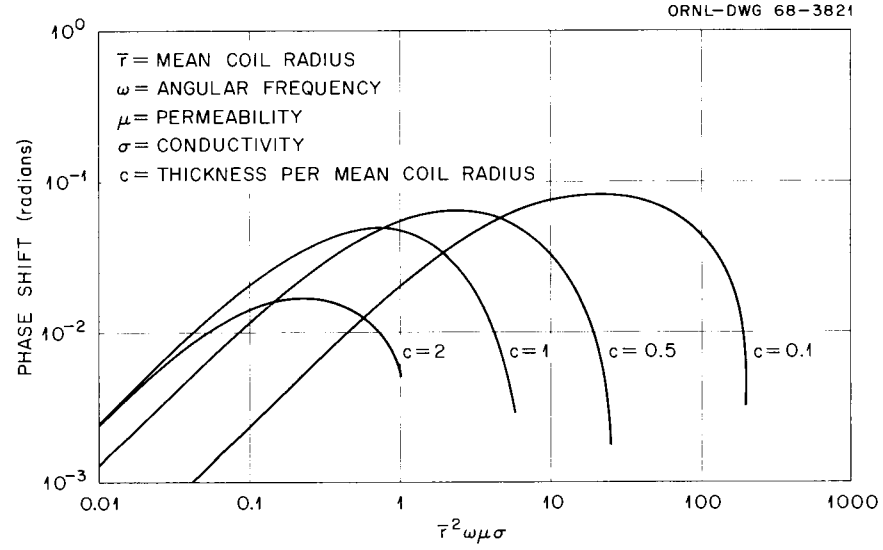

Fig. 5.3. Curves of Eddy-Current Phase Shift for Determination of Optimum Frequency and Coil Dimensions for Various Thicknesses of Metal.

With these curves and a knowledge of the capabilities of our instrument, we can select the optimum frequency for a given test application. These curves will be used to improve the eddy-current techniques performed with the phase sensitive eddy-current instrument.

Ultrasonic Test Method

K. V. Cook, H. L. Whaley

Optical Visualization of Ultrasound

Minor mechanical and optical changes have been made in the schlieren system to allow more effective imaging of ultrasonic energy. The present system is providing valuable information, but the restricted viewing area has prevented its application in several areas of interest. For this reason, a modified system using parabolic mirrors to increase the viewing area by a factor of nine has been designed. Necessary hardware to mount new optical components is currently being fabricated.

Frequency Analysis

Additional investigation of the electronic characteristics of the ultrasonic frequency analysis system has been made resulting in improvements of the signal-to-noise ratio for low level signals. The method of data recording has been improved by modifying the system to allow use of an X-Y recorder. Formerly, it was necessary to make polaroid photographs of the CRT display of the analyzer. Plots of relative amplitude versus frequency can now be quickly made, allowing cataloging of information for reference.

Spectra have been recorded from ultrasonic pulses reflected from front and back surfaces and flat-bottomed drilled holes (simulated flaws) in aluminum test blocks. These spectra have been found to possess characteristic shapes (for a given transducer) which enable one to determine whether the pulse was reflected from the front surface, back surface, or the drilled hole.

Holography

B. E. Foster

Studies were continued on the making of high quality reflection-type holograms. This work is directed toward the use of holography for evaluation of surface as well as subsurface discontinuities in metals and ceramics.

Some difficulty has been encountered in maintaining an efficient ratio of intensities between the reference and object beams of laser light. This inhibits the ability to achieve qualitative comparison between holograms made with different design angles or different subjects. Of course, the difficulty is somewhat worse since we cannot visually observe the laser beam due to the associated eye hazard. We hope to resolve this problem when the fabrication is completed on an intensity measuring device. The system will utilize a photo-sensitive field effect transistor and an associated power supply, multiplier resistors and a micro-ammeter.

6. SINTERED ALUMINUM PRODUCTS DEVELOPMENT

W. R. Martin

Dispersion-strengthened aluminum alloys prepared by powder-metallurgy techniques are commonly referred to as SAP, sintered aluminum products. Our objective has been to examine the primary billet fabrication techniques for SAP and to establish a process that will produce a billet that has uniform and reproducible properties at a strength level equivalent to that of commercial SAP 895.

Powder Consolidation

G. L. Copeland M. M. Martin

The completion of topical reports that are in preparation will conclude our development program. This final account relates process reproducibility and the effects of iron and carbon impurities in SAP to the magnitude and thermal stability of its mechanical properties at 450°C.

We have developed procedures for ball-milling and consolidating SAP powders for a SAP-billet process specification. As evaluated from extruded billets 4 in. in diameter, our billet-processing techniques produce SAP rods of strength reproducible within ±10% at a confidence level of 30. Compared to commercially available SAP 895, ORNL's material of comparable oxide content is significantly stronger at test temperatures from 25 to 550°C. The problem of limited ductility remains.

Iron

Small iron particles from mill and ball wear contaminate SAP powder during ball-milling. Later, during processing at high temperatures, these particles react with aluminum. Electron microprobe analysis indicates qualitatively that the reaction product is composed of iron and aluminum in the proportions of $FeAl_3$. We processed and evaluated five SAP rods of varying tramp-iron content to determine if this reaction had any effect on the stability of mechanical properties.

To produce various levels of iron contamination, we blended controlled amounts of ball-milled iron powder with ORNL's SAP powder. Each mixture was heated to 600°C in vacuum and consolidated into an 80% dense billet 4 in. in diameter. The billets were vacuum annealed at 600°C for 17.5 hr and then immediately extruded through shear dies for reduction in area ratio of 5.2. Two sections from each of these primary extrusions were extruded through conical dies for a total reduction ratio of 156. To determine the thermal stability of the rods, we compared the tensile strength as extruded to the strength after annealing 40 hr in vacuum at 600°C. The results of these tests are given in Table 6.1. The changes in strength upon annealing are statistically insignificant with respect to iron content. Uniform elongation consistently decreases which is usual even for SAP of low impurity content. We conclude that iron contamination of up to 3 wt % has no significant effect on the magnitude or thermal stability of the tensile properties of SAP rods. However, all the iron added during ball-milling can be removed by magnetic-separation techniques. Generally, our processing technique yields less than 0.5 wt % Fe content.

Carbon

The carbon in SAP results from the organic materials used in ball-milling and is mainly in the form of small inclusions, which are beleived to be Al_4C_3 based on electron microprobe analysis. Since aluminum carbide decomposes readily in contact with water to produce acetylene, the effect of the carbide inclusions in SAP on thermal stability is of concern where moisture is present. We produced five rods of varying carbon content by blending finely powdered Al_4C_3 with portions of a batch of ORNL-milled flake powder. The technique for processing the powders into extruded rods was identical to that used for the rods of varying iron contents. Sections of the rods were annealed at 600°C for 40 hr in vacuum and in air with a 11°C dew point. The results are given in Table 6.2 of tensile tests performed on the extruded rod and after the stability tests. The changes observed after the annealing are normal variations and are random with respect to carbon content. We conclude that carbon content up to 2 wt % as Al_4C_3 inclusions is not detrimental

Table 6.1. Effect of Iron on Stability of Extruded Rods

Rod Number	Chemical Composition[a]				Mechanical Properties[b] at 450°C			
	Fe	C	Al_2O_3	H_2	Ultimate Tensile Strength (psi)		Uniform Elongation (%)	
	(wt %)			(wt ppm)	As Extruded	Change Upon Anneal[c]	As Extruded	After Anneal[c]
					$\times 10^3$	$\times 10^3$		
276	0.26	0.25	9.80	2.0	13.97	−0.07	0.78	0.69
272	0.57	0.21	8.23	1.8	12.48	+0.18	0.72	0.62
273	0.81	0.19	8.95	2.6	13.15	−0.39	0.78	0.57
274	0.97	0.25	8.84	2.4	13.10	−0.16	0.65	0.59
275	3.48	0.25	9.40	2.8	12.50	+0.04	0.57	0.37

[a]Chemistry samples taken adjacent to tensile specimens along length of rods. Al_2O_3 determined by gaseous HCl analysis.

[b]Strain rate of 0.002 min^{-1}. Values represent average of six determinations along the length of two extruded sections.

[c]Specimens annealed in vacuum after machining. Conditions: 600°C; 10^{-3} to 10^{-4} torr; 40 hr.

to the mechanical properties or thermal stability of SAP rods. However, with our process, carbon contents are generally less than 0.3 wt % in the extruded alloy.

Process Evaluation

To determine the overall reproducibility of the ORNL process, we examined extrusions from nine billets produced under the same conditions. Nine 27-lb batches of MD-101 powder were ball-milled for 20 hr by the reference process. A 4-in.-diam by 4-in.-long billet from each batch was consolidated and extruded by the same processing conditions described on p. 97 for the rods of varying iron content. Three specimens from each of two secondary extruded billets cut from along the length of the two rods were tensile tested at 450°C. These results and the

Table 6.2. Effect of Carbon on Stability of Extruded Rods

Billet Number	Chemical Composition[a]				Mechanical Properties[b] at 450°C					
	C	Fe	Al_2O_3	H_2	Ultimate Tensile Strength (psi)			Uniform Elongation (%)		
	(wt %)			(wt ppm)	As Extruded	Change Upon Anneal		As Extruded	After Anneal in	
						Vacuum[c]	Air[d]		Vacuum[c]	Air[d]
					$\times 10^3$	$\times 10^3$	$\times 10^3$			
277	0.14	0.29	9.46	3.7	13.58	−0.18	−0.16	0.80	0.65	0.77
278	0.27	0.33	9.38	3.3	13.15	+0.07	−0.17	0.70	0.50	0.85
279	0.42	0.35	9.88	6.5	12.10	+0.70	+0.18	0.64	0.51	0.59
280	0.58	0.34	9.17	3.9	13.71	−0.37	−0.20	0.58	0.53	0.78
281	1.97	0.30	11.5	7.8	12.55	+0.61	−0.07	0.55	0.49	0.49

[a] Chemistry samples taken adjacent to tensile specimens along length of rods. Al_2O_3 determined by gaseous HCl analysis.

[b] Strain rate of 0.002 min^{-1}. Values represent average of six determinations along length of two secondary extruded sections per billet.

[c] Specimens annealed in vacuum after machining. Conditions: 600°C; 10^{-3} to 10^{-4} torr; 40 hr.

[d] Specimens annealed in moist air after machining. Conditions: 600°C; 1 atm of air with 11°C dew point; 40 hr.

chemical composition of the rods are in Table 6.3. The strength within any particular billet was uniform, the maximum range observed being less than 2% of the mean. This amount of variation is similar to that observed in short, secondary extruded sections of SAP 895.

The expected variations (3 σ) among billets is ±10% of the mean ($\bar{X}$). This degree of process reproducibility appears to be due to differences in milling, since the average strength correlates well with the oxide content. We believe that further improvement in ORNL's billet-to-billet strength variations depends upon better control of the as-milled oxide content. Although comparable data have not been found for SAP 895, the allowed oxide range of 9 to 12% would indicate strength variations similar to those observed in Table 6.3. The minimum strength value observed in the ORNL reproducibility study was 12,940 psi.

Table 6.3. Chemistry and Strength from Reproducibility Study Rods

Rod Number	Ball-Mill Run Number	Chemical Composition				Mechanical Properties[a] at 450°C	
		Fe	C	Al_2O_3	H_2	Ultimate Tensile Strength (psi)	Uniform Elongation (%)
		(wt %)			(wt ppm)		
						$\times 10^3$	
276	23	0.26	0.25	9.80	2.0	13.97	0.78
277	27	0.29	0.14	9.46	3.7	13.58	0.80
282	20	0.28	0.22	10.1	1.7	14.64	0.54
283	21	0.22	0.24	9.48	1.7	14.13	0.58
284	22	0.30	0.30	9.35	2.4	13.80	0.62
285	28	0.32	0.26	8.35	2.3	13.11	0.60
286	29	0.40	0.22	9.70	2.1	14.23	0.70
287	30	0.33	0.32	8.50	2.2	13.30	0.68
σ, estimate of standard deviation				0.58		0.47	0.089
$\bar{X}$, mean				9.32		13.83	0.67

[a]Strain rate of 0.002 min^{-1}; values represent the average of six determinations along the length of two secondary extruded billets.

Figure 6.1 shows the ORNL material to be stronger than SAP 895 from room temperature to 550°C with similar uniform elongation. Note that each datum point in Fig. 6.1 represents a single determination except that at 450°C, which is an average of six specimens tested at an earlier date.

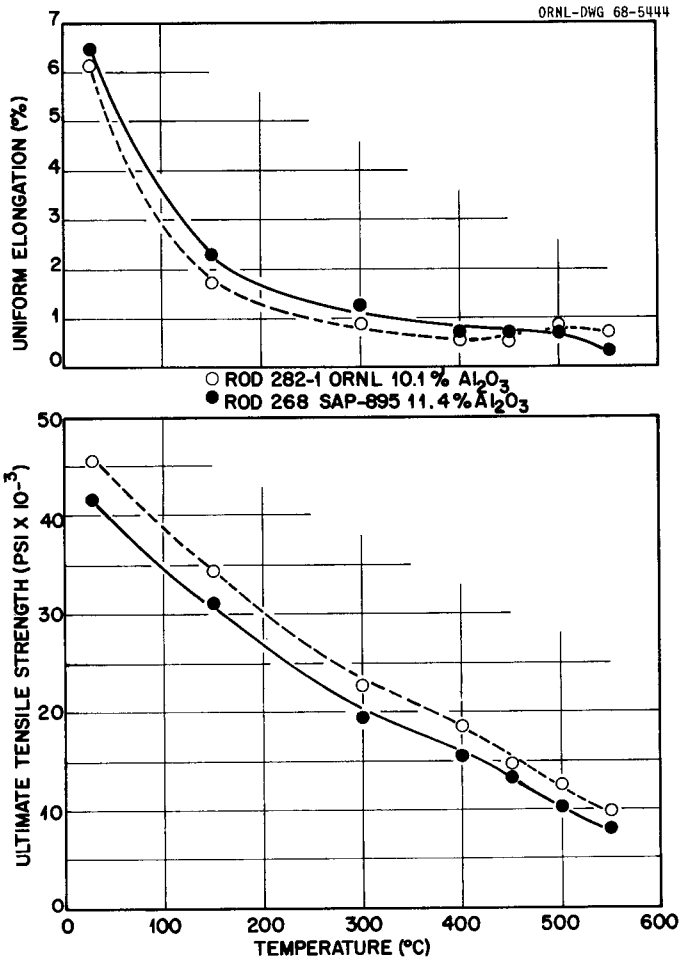

Fig. 6.1. Strength and Uniform Elongation of ORNL-SAP and Commercial SAP-895 at 0.002 min^{-1} Strain Rate.

The internal structures of ORNL material and SAP 895 may be compared from conventional metallography in Fig. 6.2 and from transmission electron microscopy in Fig. 6.3. In viewing the photographs, one should be aware that SAP 895 has received a total reduction ratio of approximately 510 in comparison to 156 for the ORNL material. This additional hot working

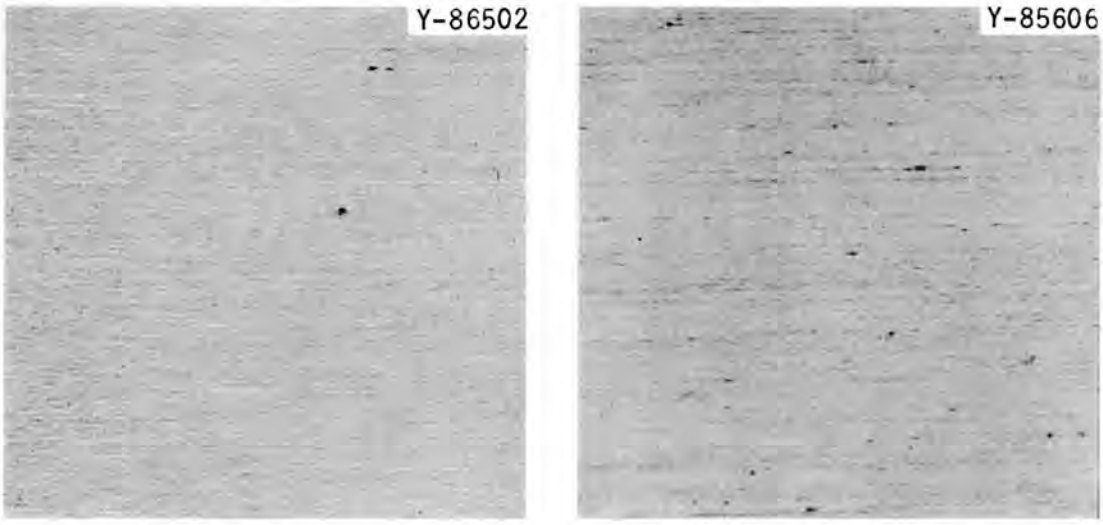

Fig. 6.2. Comparison of Microstructure of ORNL-10% Al_2O_3-Material (right) with SAP 895 (left). Etchant: 1 vol % HF. 100X.

should have resulted in slightly improved oxide distribution and corresponding increase in strength.[1] The excellent uniformity and closer spacing of the oxide in the ORNL material accounts for its higher strength at a given oxide concentration. We believe that the better oxide distribution results from the elimination of intentional agglomeration of individual particles during ball-milling. Commercial SAP milling practice welded the particles together,[2] whereas, in the ORNL milling sufficient surfactant and milling vehicle are added to maintain individual flake particles.

Development of Ductile Dispersion-Strengthened Aluminum

G. L. Copeland

The objective of this phase of the program is to improve the high-temperature ductility of SAP products through alloy modifications. These

---

[1]T. M. Nilsson, p. 110, this report.

[2]D. Gualandi and P. Jehenson, "Powder Metallurgy of Al-Al_2O_3 Composites (SAP) for Nuclear Applications," Modern Developments in Powder Metallurgy, Vol. 3, H. H. Housner, ed., Plenum Press, New York, 1966.

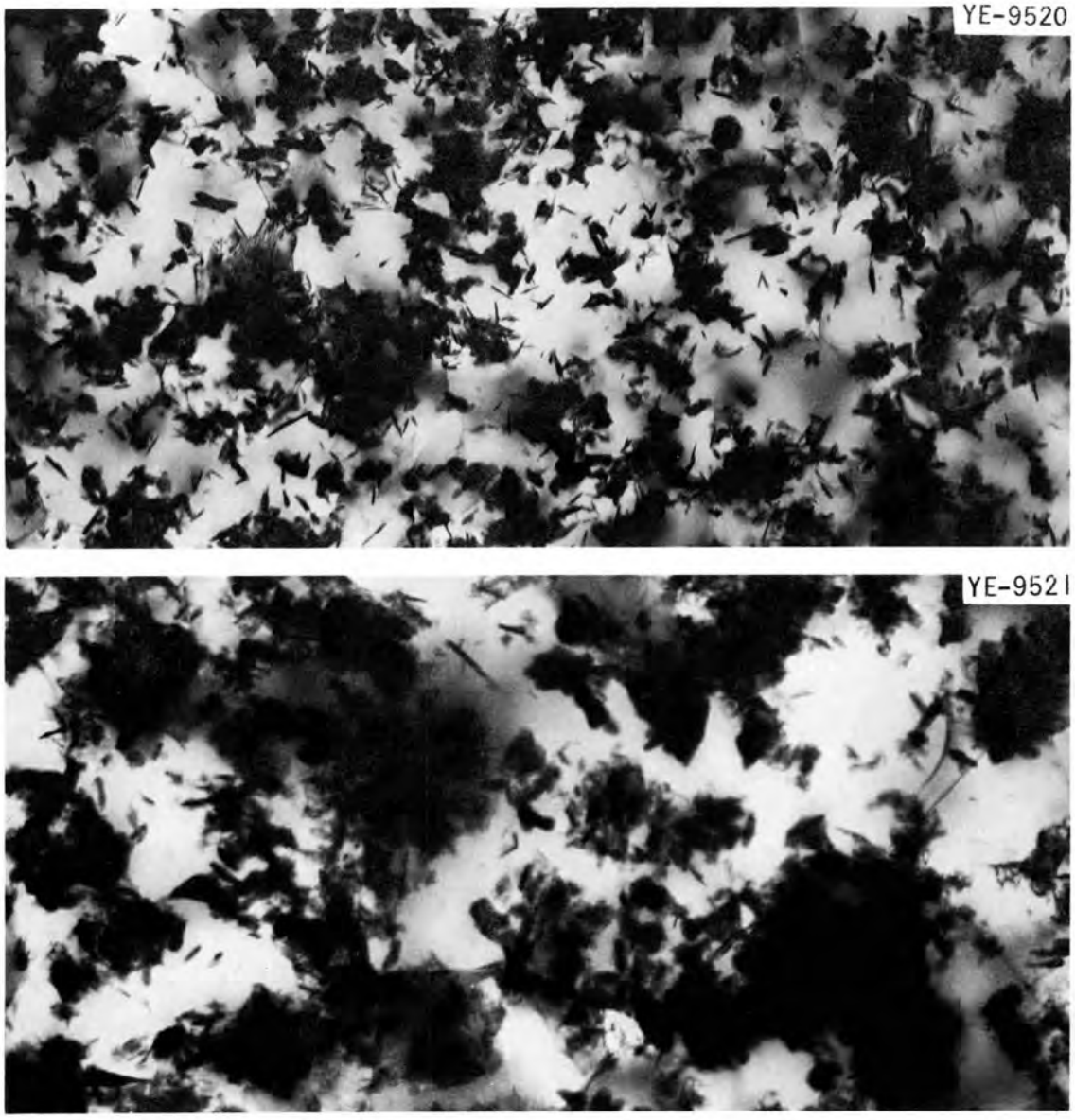

Fig. 6.3. Comparison of Transmission Electron Microstructure of ORNL-10% Al_2O_3-Material (Top) with SAP-895 (Bottom).

alloys will be referred to as dispersion-strengthened aluminum (DSA) to distinguish them from the pure aluminum–aluminum oxide (SAP) materials.

Work is continuing on the atomization development of alloyed powders at the Illinois Institute of Technology Research Institute (IITRI). The work performed there during this report period is summarized in Table 6.4. Melts weighing 10 lb were atomized in the 100-gal chamber used previously. Due to a coil failure, about 5 lb of run 2 were poured prematurely. The balance of the charge was atomized under slightly different conditions after the coil had been repaired. A tundish freeze-up occurred near the end of run 7 (Al–2% Mo–4% Zr). This and the lower yields of –100 mesh material probably result from the increase in the melting temperature of the alloy caused by the zirconium. A higher pouring temperature should remedy these problems. Some unmelted stock observed after pouring runs 4 through 8 indicates incomplete alloying. The optimum tundish orifice appears to be 1/4 in. in diameter. No nozzle clogging occurred during any of the runs. These atomizing conditions will be used with 20- to 30-lb melts of Al–4% Mg and Al–4% Mo–2% Zr in the 500-gal chamber to ensure that nozzle clogging does not occur.

The powders listed in Table 6.4 have been received from IITRI and are presently being characterized. Portions of each run are being ball-milled to three different oxide contents and consolidated by vacuum-hot-pressing. When compaction of this series is complete, these billets, along with those already pressed, will be vacuum annealed and extruded (at a reduction in area ratio of 30) in preparation for evaluation.

Effects on Mechanical Properties of Work Applied in Various Directions on Commercial Extruded SAP 895

T. M. Nilsson

This report concludes the quarterly progress reports on secondary working of SAP. A topical report that is in preparation will describe the results we obtained.

Table 6.4. Atomization Data for Aluminum Alloy Powders[a]

Run Number	Alloy	Water Level[b] (in.)	Pouring Temperature (°C)	Weight of Material, lb		Sieve Analysis of Atomized Powder, wt %			Remarks
				Melt	Atomized Product	+40 Mesh	−40 +100 Mesh	−100 Mesh	
1	2% Mg	16	1000	8.67	8.30	6.7	22.1	71.2	
2	4% Mg	16 24	750 900	4.91 5.05	4.65 4.44	17.2	29.5	53.3	Coil failure – half of melt poured prematurely
3	6% Mg	24	1000	8.82	8.25	32.0	33.5	34.5	3/8 in. tundish orifice
4	6% Mo–2% Zr	16	1020	9.36	6.82	11.6	29.2	59.2	
5	6% Mo–2% Fe	16	1025	10.86	7.99	c	21.4[d]	76.6	
6	4% Mo–4% Fe	16	1000	9.93	7.74	7.5	10.0	82.5	
7	2% Mo–4% Zr	16	1050	9.51	7.15	34.5	16.6	48.9	Tundish freeze-up
8	2% Mo–2% Fe–2% Zr	16	1000	10.12	6.56	36.2	25.2	38.6	

[a]Air pressure at gas inlet, 350 psi; adjustable nozzle ring 5 turns out; tundish orifice except for run 3, 1/4 in. in diameter.

[b]Distance from nozzle tip to water surface.

[c]Not determined.

[d]+100 mesh.

Transverse Swaging

The effects on mechanical properties of transverse extruding a SAP 895 billet have been described.[3] Also, SAP 895 billets have been hot swaged in the transverse direction at 600°C. The samples were initially annealed for 1 hr in vacuum at 600°C and again for 10 min during working before each new 10% reduction. The hot-swaged material was tensile tested at 450°C in the new working direction. The mechanical properties determined in this experiment are presented in Table 6.5. The results, in general, show the same trend found by transverse extrusion.[3] After little transverse working, strengths are low because of

Table 6.5. Mechanical Properties of SAP 895 as a Function of Transverse Reduction by Hot Swaging[a]

Reduction Ratio	Elongation, %		Strength, psi	
	Uniform	Total	Ultimate Tensile	Yield 0.2% Offset
			$\times 10^3$	$\times 10^3$
1	0.50	1.20	8.55	8.05
1.6	0.35	0.50	10.45	10.4
2	0.32	0.40	9.9	9.8
4.2	0.36	0.60	10.7	10.6
8	0.71	0.91	12.25	11.7
30.5	0.94	1.5	12.4	11.7
	0.43[b]	1.44[b]	11.0[b]	10.8[b]

[a]Temperature, 450°C; strain rate, 0.002 min^{-1}; direction of testing, parallel to the swaging direction. Longitudinal and transverse properties (i.e., transverse reduction ratio of 1) of the original bar are also given for comparison. Values are averages of five tests.

[b]Original longitudinal values.

[3]T. M. Nilsson, Fuels and Materials Development Program Quart. Progr. Rept. Dec. 31, 1967, ORNL-TM-2090, p. 115.

the unfavorably aligned structure. Ductility is lower in this case than in the original transverse direction because of localized yielding and failure. The striated fracture surface indicates a very brittle fracture mode. Further transverse working realigned the structure sufficiently to restore the mechanical properties to their original longitudinal level and to exceed this level because of the improved dispersion. The most remarkable result of transverse swaging is the large increase in uniform elongation. An increase of more than 100% is found after a transverse reduction ratio of 30. This seems to be connected with the complicated alignment of the structure resulting from transverse swaging (see Fig. 6.4). Apparently, the formation and growth of voids, which usually lead to a concentration of stress after small amounts of deformation,[4] are more difficult in such a structure since the uniform elongation is higher than in normally aligned SAP structures.

Some samples were also cold swaged in the transverse direction. Cold work was only possible up to reductions of about 30%. At higher reductions, cracking occurred along the oxide bands. The initial straight alignment becomes bent during transverse working. Because of the poor cohesion between the brittle oxide particles and the ductile aluminum matrix, cracks nucleate and grow very easily along the aligned bands of oxide particles, as shown in Fig. 6.5. Some of the cold swaged material was annealed in vacuum at 600°C. Results of tensile tests on SAP 895 as a function of cold work and annealing are shown in Table 6.6. The results are divided into three sections, groups A, B, and C.

Group A shows the influence of cold swaging followed by vacuum heat treatment at 600°C on the high-temperature properties. Strength properties correspond closely to the initial transverse level. The uniform elongation is surprisingly high, especially when compared to the results from hot swaging at low transverse reduction. The total elongation corresponds to the level of the initial bar.

Groups B and C show the influence of cold swaging alone and cold swaging followed by vacuum annealing at 600°C, respectively, on room-temperature properties. The alignment only changes slightly as a result

---

[4]D. G. Harman and T. A. Nolan, Fracture Initiation in XAP-001 SAP Alloy, to be published.

Fig. 6.4. Cross Section of Extruded SAP 895 After Transverse Swaging, Secondary Reduction. Etched 45 sec in a 1 vol % HF solution at room temperature. 38X.

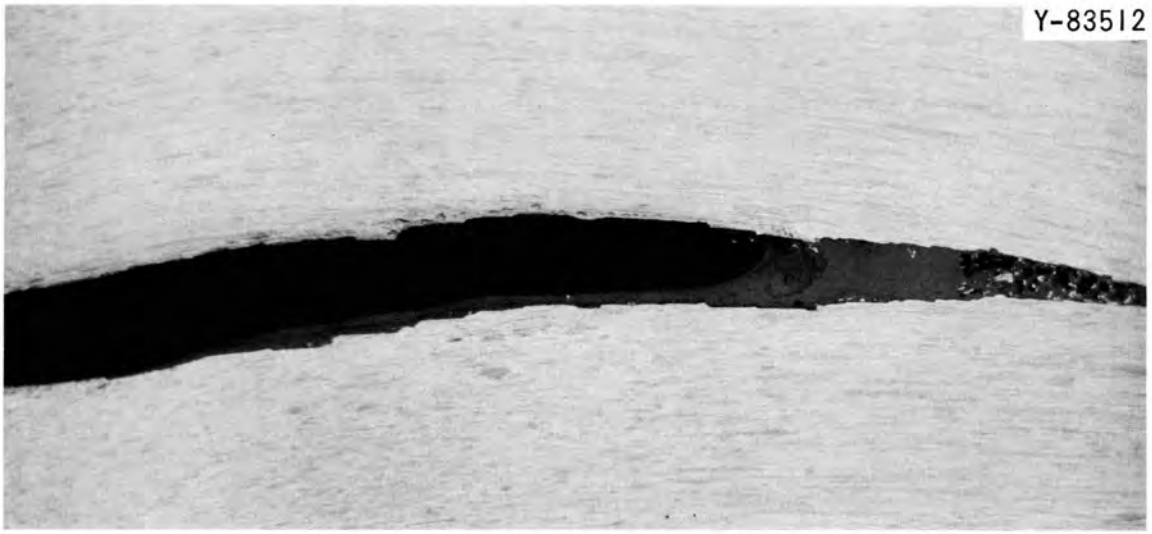

Fig. 6.5. Sample of Extruded SAP 895 Cold Swaged About 55%. The swaging direction is vertical. Etched 45 sec in a 1 vol % HF solution at room temperature. 12X.

Table 6.6. Mechanical Properties of SAP 895 as a Function of Transverse Reduction by Cold Swaging

Number of Specimens	Transverse		Elongation, %		Strength, psi	
	Reduction Ratio[a]	Percent Cold Work	Uniform	Total[b]	Ultimate Tensile	Yield
					$\times 10^3$	$\times 10^3$
	Group A[c] Tested at 450°C and 0.002 min^{-1}					
	1	0	0.50	1.20	8.55	8.05
4	1.16	13.5	0.90	1.4	8.4	7.9
4	1.27	21	0.90	1.4	8.45	8.0
3	1.39	28	0.89	1.1	8.5	8.1
			0.43[d]	1.4[d]	11.0[d]	10.8[d]
	Group B Tested at Room Temperature and 0.02 min^{-1}					
	1	0	6.8	6.9	35.7	25.5
2	1.16	13.5	2.9	3.5	41.0	37.7
2	1.27	21	2.3	3.0	41.6	38.2
2	1.39	28	2.1	2.2	41.1	38.4
			8.7[d]	11.0[d]	40.9[d]	30.7[d]
	Group C[c] Tested at Room Temperature and 0.02 min^{-1}					
2	1.16	13.5	4.4	4.8	40.6	34.8
2	1.27	21	3.6	3.8	40.8	35.8
2	1.39	28	3.6	3.8	41.0	36.8
			8.7[d]	11.0[d]	40.9[d]	30.7[d]

[a]The reduction ratio of 1 corresponds to the transverse properties of the original extruded bar.

[b]Gage length equals to 10 times the diameter.

[c]Cold swaging was followed by vacuum heat treating 24 hr at 600°C.

[d]Original longitudinal values.

of small amounts of cross working (see Fig. 6.5). Properties, excluding any effect of work hardening, should therefore correspond to the initial transverse properties when the cold worked material is tested in the new working direction. Table 6.6 shows that cold working increases the ultimate tensile strength from 35,700 to 41,000 psi, or 15%, practically

uninfluenced by the annealing treatment. The yield strength increases 40 to 50% depending on whether or not the cold swaging is followed by heat treatment. The ultimate tensile strength of the swaged material reaches the same level as in the original longitudinal direction, whereas the yield strength is higher than the initial longitudinal value. The ductility, however, is quite low even after annealing.

Our conclusions from the cold-swaging experiment are that high-temperature strength properties are low after cold swaging and annealing, whereas uniform elongation is favorably high. Cold swaging, even followed by heat treatment at 600°C, raises the room-temperature strength considerably but lowers the ductility. These conclusions (except for the ones concerning uniform eleongation, for which no comparative results are available) are qualitatively in agreement with cold-working experiments in the longitudinal direction of SAP 895 (ref. 5, 6).

Longitudinal Extrusion

Samples of the initial SAP 895 billet, extruded at Montecatini to a reduction ratio of 20, were further extruded in the longitudinal direction to determine the effects of total extrusion ratio on properties. We used an extrusion temperature of about 500°C and conical dies with and entrance angle of 45°. The schedule of the actual extrusions is shown in Table 6.7 together with high-temperature tensile properties as a function of extrusion ratio. Table 6.7 shows that the strength generally increases with increasing extrusion ratio, but increase is only 7% for an increase in extrusion ratio from 20 to 1740. The ductility is practically constant. The very slight changes that occur in the mechanical properties as a function of extrusion ratio after a reduction ratio of 20 is surpassed confirmed our experiments with an experimental SAP alloy containing 6.6 wt % Al_2O_3 (ref. 7). Hansen[8] found no changes in

[5]R. J. Towner, Trans. Met. Soc., AIME 230, 505 (April 1964).

[6]E. G. Hess, Z. Metallk. 55(3), 123 (1964).

[7]T. M. Nilsson, Fuels and Materials Development Program Quart. Prog. Rept. Dec. 31, 1967, ORNL-TM-2090, p. 124.

[8]N. Hansen, Dispersion-Strengthened Aluminum Products, Risö Report No. 113, (May 1966).

Table 6.7. Schedule of Actual Extrusions Performed and Mechanical Properties[a] of SAP 895 as a Function of Extrusion Ratio

Diameter Reductions During Extrusion (in.)	Extrusion Ratio		Elongation, %		Strength, psi	
	Additional	Total	Uniform	Total[b]	Ultimate Tensile	Yield 0.2% Offset
					$\times 10^3$	$\times 10^3$
	1	20	0.50	1.3	12.8	12.65
2.39 → 1.27	3.55	71	0.51	1.3	12.25	12.1
2.39 → 1.27, 1.22 → 0.52	19.6	392	0.42	1.2	13.4	13.25
2.39 → 1.27, 1.22 → 0.25	87	1740	0.49	1.4	13.85	13.6

[a]At a test temperature of 450°C and a strain rate of 0.002 min^{-1}. Testing direction parallel to the extrusion direction. The values are averages of five tests.

[b]Gage length equals to 10 times the diameter.

mechanical properties of an Al–7 wt % Al_2O_3 alloy by increasing the extrusion ratio from 15 to 75. Schwartzwelder[9] found increases in strength and ductility at 315°C by increasing the extrusion ratio to 13; however, no trend was evident at higher reductions.

Comparison Between Properties of Extruded SAP 895 After Longitudinal and Transverse Working

The billet used for the longitudinal extrusion experiment was different from the one used for the study of anisotropy and of the effects of transverse extrusion and swaging. As had been shown at ORNL,[10] properties within one billet are practically constant, whereas properties between assumedly identical billets may vary to a greater extent, ±10%. Therefore, only relative variations will be compared. High-temperature ductility as a function of reduction and direction during secondary

[9]J. H. Schwartzwelder, Intern. J. Powder Met. 3(3), 53 (1967).

[10]G. L. Copeland and M. M. Martin, p. 100, this report.

working is shown in Fig. 6.6. During transverse working the variations are large because of the realignment of the oxide particles, whereas the ductility values are practically unchanged by further longitudinal extrusion. At the highest transverse reductions, both uniform and total elongations improved over the original longitudinal properties. Quantitatively, the variations in ductility at a secondary reduction ratio of 30 are shown in Table 6.8 as a function of working direction. Especially noteworthy is the more than 100% improvement in uniform elongation brought about by transverse swaging. The variations in tensile strength as a result of the various ways of secondary working are shown in Fig. 6.7. Strength properties improve slightly by longitudinal working, whereas they improve strongly by transverse working from the initial transverse level until at the highest transverse reductions the initial longitudinal strength level is surpassed. The quantitative improvements in strength after a secondary reduction ratio of 30 are also shown in Table 6.8. Transverse working seems to increase strength properties more effectively than further longitudinal extrusion. Table 6.8 shows that the best mechanical properties of SAP 895 at high temperature are achieved by transverse swaging, which gives especially great improvement in uniform elongation.

The large variations in strength occurring during transverse working (Fig. 6.4) emphasize the importance of the way the oxide particles are distributed. The average distribution improves during the additional working, since the oxide particles diminish in size and particle clusters break up. Consequently, assuming a random distribution, an increase in strength would be expected. However, not until a sufficient realignment has taken place (i.e., at a transverse reduction ratio of about 8) are the strength properties restored to their original level. At further transverse reduction the strength improves over the original level because of the improved alignment and dispersion of oxide particles. The microstructural parameters at the highest secondary reduction ratio are shown in Table 6.9. Considering the microstructural variations as compared to the improvements in strength (Table 6.8) we find qualitative agreement in that the structure with the finest dispersion (i.e., after transverse swaging, shows the highest strength improvement and vice versa).

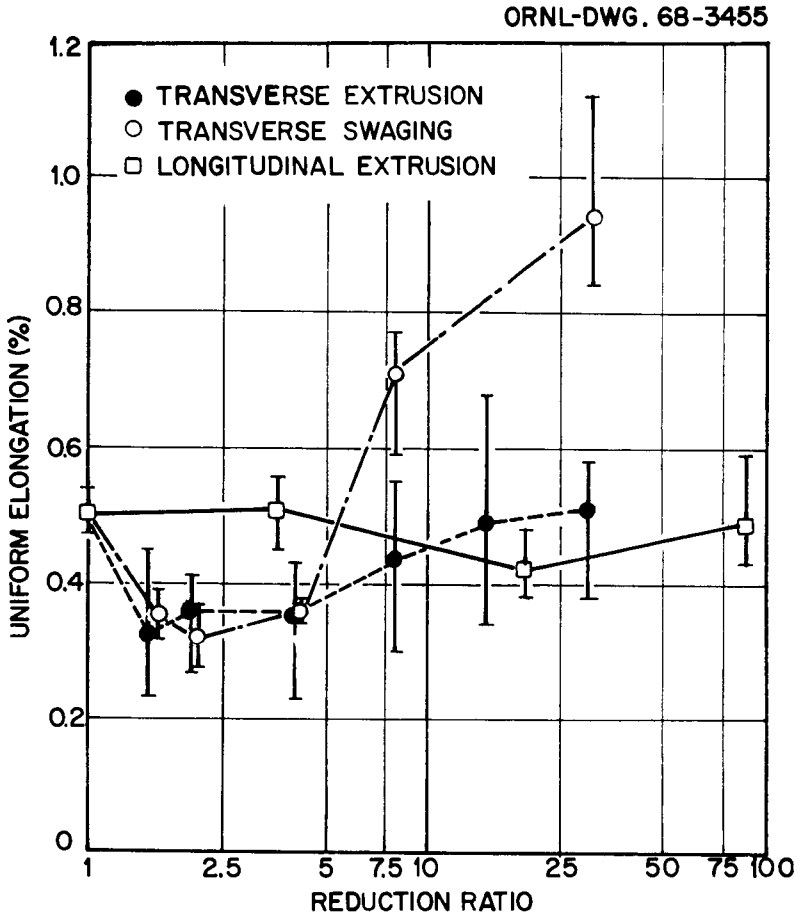

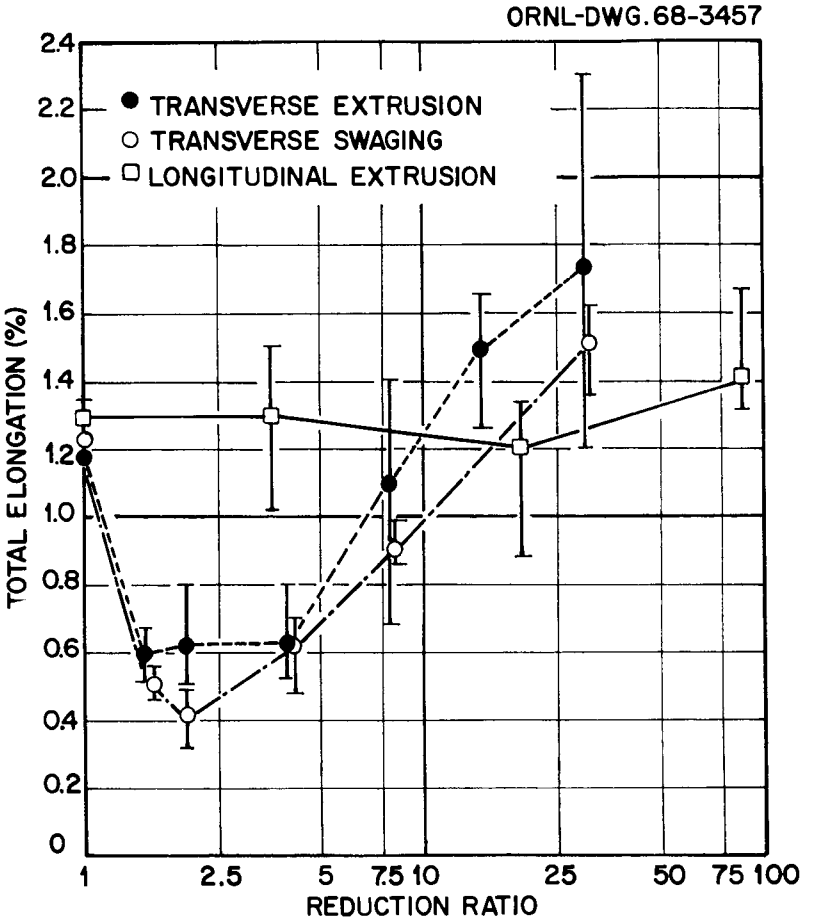

Fig. 6.6. Ductility at 450°C of SAP 895 as a Function of Reduction and Direction During Secondary Working.

Table 6.8. Effect of Additional Workings[a] in the Longitudinal and Transverse Directions on the 450°C Tensile Properties of Extruded SAP 895

Condition	Elongation, %				Ultimate Tensile Strength (psi)	Relative Variation (%)	Yield Strength 0.2% Offset (psi)	Relative Variation (%)
	Uniform	Relative Variation	Total[b]	Relative Variation				
					$\times 10^3$		$\times 10^3$	
Initial longitudinal	0.43		1.44		11.04		10.84	
Transversely extruded	0.51	+18	1.75	+22	12.2	+10	12.0	+10
Transversely swaged	0.94	+118	1.5	+4	12.4	+12	11.7	+8
Initial longitudinal	0.50		1.3		12.8		12.65	
Longitudinally[c] extruded	0.50	0	1.35	+4	13.55	+6	13.3	+5

[a] Secondary reduction ratio of 30.

[b] Gage length equals to 10 times the diameter.

[c] Averaged values from Fig. 6.3.

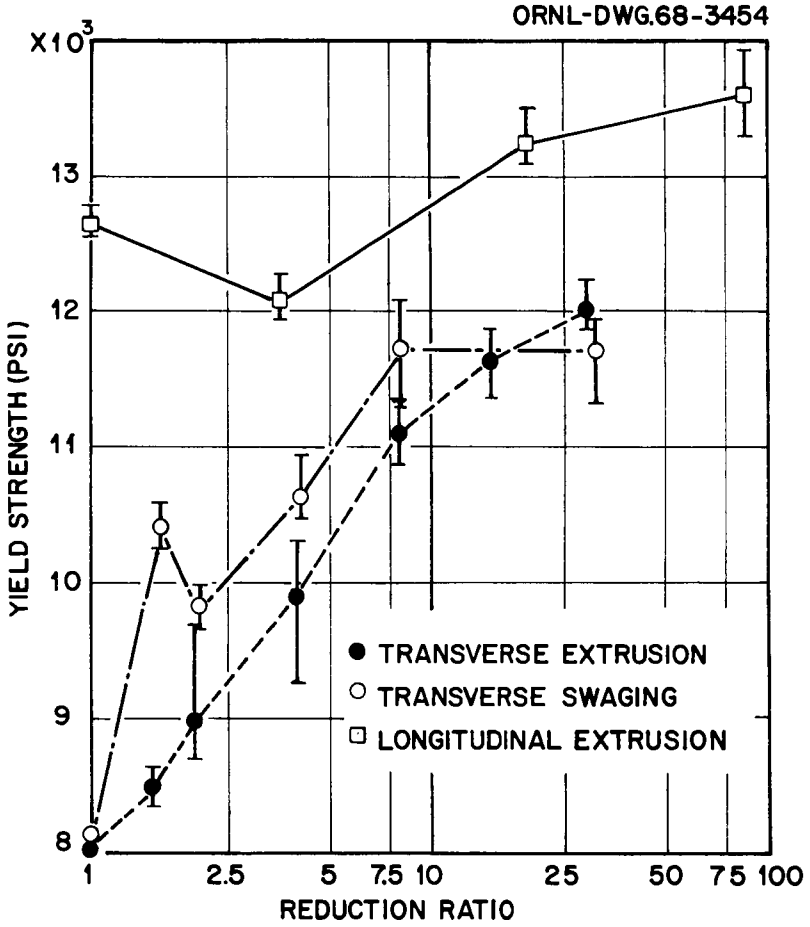

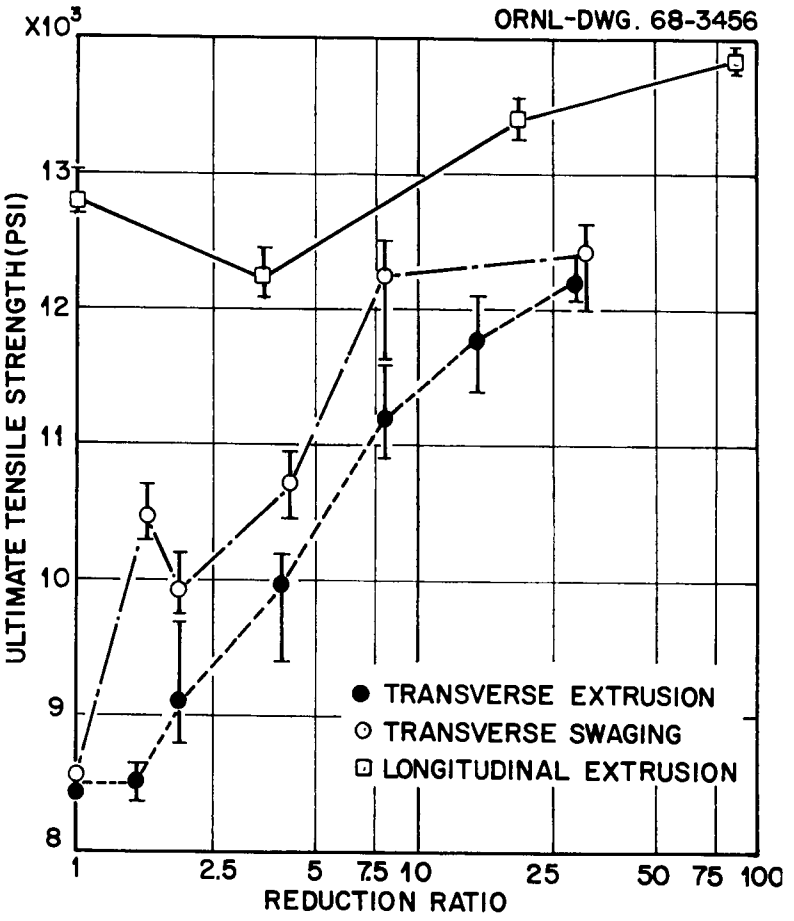

Fig. 6.7. Strength at 450°C of SAP 895 as a Function of Reduction and Direction During Secondary Working.

Table 6.9. Average Microstructural Parameters of SAP 895 After Different Types of Secondary Working

Condition	Secondary Reduction Ratio	Oxide Particle Parameters,[a] Å		Subgrain Size (μ)
		Diameter	Thickness	
As extruded	1		100	0.65
Transverse extruded	30	545	100	0.45
Transverse extruded	30	525	100	0.40
As extruded	1	1100	100	0.65
Farther longitudinally extruded	87	660	100	0.53

[a]Particle diameters and subgrain sizes were determined from both longitudinal and transverse micrographs, which gave nearly the same values. Particle thickness was measured on transverse electron micrographs.

Quantitatively, however, greater improvements would be expected. Calculations assuming a random distribution of the particle show an expected increase in yield strength of 40% as compared to the 5 to 10% found (Table 6.8).

7. SOL-GEL FAST REACTOR FUELS

A. L. Lotts

The objective of the Sol-Gel Fast Reactor Fuels program is to assess the potential of sol-gel-derived $(U,Pu)O_2$ fuel for use in primarily liquid metal-cooled fast breeder reactors and the Fast Flux Test Facility. The task areas of the programs are:

1. the preparation of $(U,Pu)O_2$ fuel by the sol-gel process,
2. out-of-reactor testing to characterize the sol-gel product,
3. the development of fabrication procedures for incorporating the mixed oxide fuel into a suitable fuel rod component,
4. the irradiation testing of the fuel.

The activities now include (1) the preparation of a variety of $(U,Pu)O_2$ products; (2) the completion of the plutonium equipment for out-of-reactor characterization of material and for additional fabrication methods; (3) the development of procedures for packing $(U,Pu)O_2$ microspheres and for making $(U,Pu)O_2$ pellets from sol-gel-derived material; and (4) the irradiation of uninstrumented capsules in the ETR to test Sphere-Pac $(U,Pu)O_2$, the irradiation of instrumented capsules in the ORR, the design and construction of experiments and capsules for transient testing, and the design of irradiation experiments for the EBR-II.

In the program for investigation of the behavior of sol-gel $(U,Pu)O_2$ fuel under conditions simulating accidental power excursions in the TREAT facility, we have done preliminary reactor physics and heat transfer calculations to support the capsule design and other analyses which have to be completed in order to accomplish the TREAT experiments. The program has been revised so that Series I tests will use nominally (0.8% U–0.2% Pu)O_2 fuel rather than the (0.75% U–0.25% Pu)O_2 fuel initially planned. A proposal for approval in principle of the Series I EBR-II sol-gel fuels irradiation tests was submitted to the Experimental Review Committee at Argonne National Laboratory.

Plutonium Ceramic Facilities

J. D. Sease E. S. Bomar W. H. Pechin
M. K. Preston[1] C. F. Sanders

Our plutonium ceramic facilities are being equipped to examine and prepare ceramic nuclear fuels that contain alpha-active materials. Glove-box facilities are being provided for fuel preparation and characterization and for fabrication of fuel rods and irradiation test capsules.

The facilities, which are in two locations due to the scarcity of available alpha laboratory space, are being developed to complement each other. The equipment in Building 3019 is to contain most of the equipment for developing sol-gel mixed-oxide fabrication processes, facilities for assembling and welding irradiation capsules and fuel elements, and a complete alpha metallography facility. The equipment in Building 4508 is directed mainly toward developing preparation techniques for reactive materials such as mixed uranium-plutonium nitrides and the characterization of fuels with respect to structure, composition, and thermal characteristics. Because of the possible presence of reactive materials, all of the boxes for 4508 will be designed for high-purity inert-atmosphere operation. This inert atmosphere will be supplied initially by a one-pass purge system, but this will be replaced eventually with a closed loop and purifier. In Building 3019, the metallography boxes and a few of the other boxes will be supplied with inert-atmosphere purge capabilities. We have received all of the glove boxes and equipment that were ordered, and we are currently either operating or installing this equipment. The status of the work in the two buildings follows.

Building 3019 Facilities

The Interim Alpha Facilities contain three laboratories approximately 24 × 24 ft each. Initially our equipment was confined to laboratories 1 and 2; however, we recently obtained space in laboratory 3 for the installation of a pellet-sintering facility.

---

[1]General Engineering Division.

The layout of the 3019 Interim Alpha Laboratory and the principal equipment associated with the glove boxes are shown in Fig. 7.1. Glove boxes 1 through 4, 10 through 12, and 24 are primarily for oxide fabrication; glove boxes 5 and 6 are for irradiation capsule assembly and welding; boxes 7 and 8 are for pyrolytic carbon coating of plutonium-bearing microspheres; box 9 is for microsphere microradiography; boxes 13, 14, and 15 are for deposition of mixed $(U,Pu)O_2$ from the fluoride vapors, and boxes 16 through 23 are for metallographic preparation and examination.

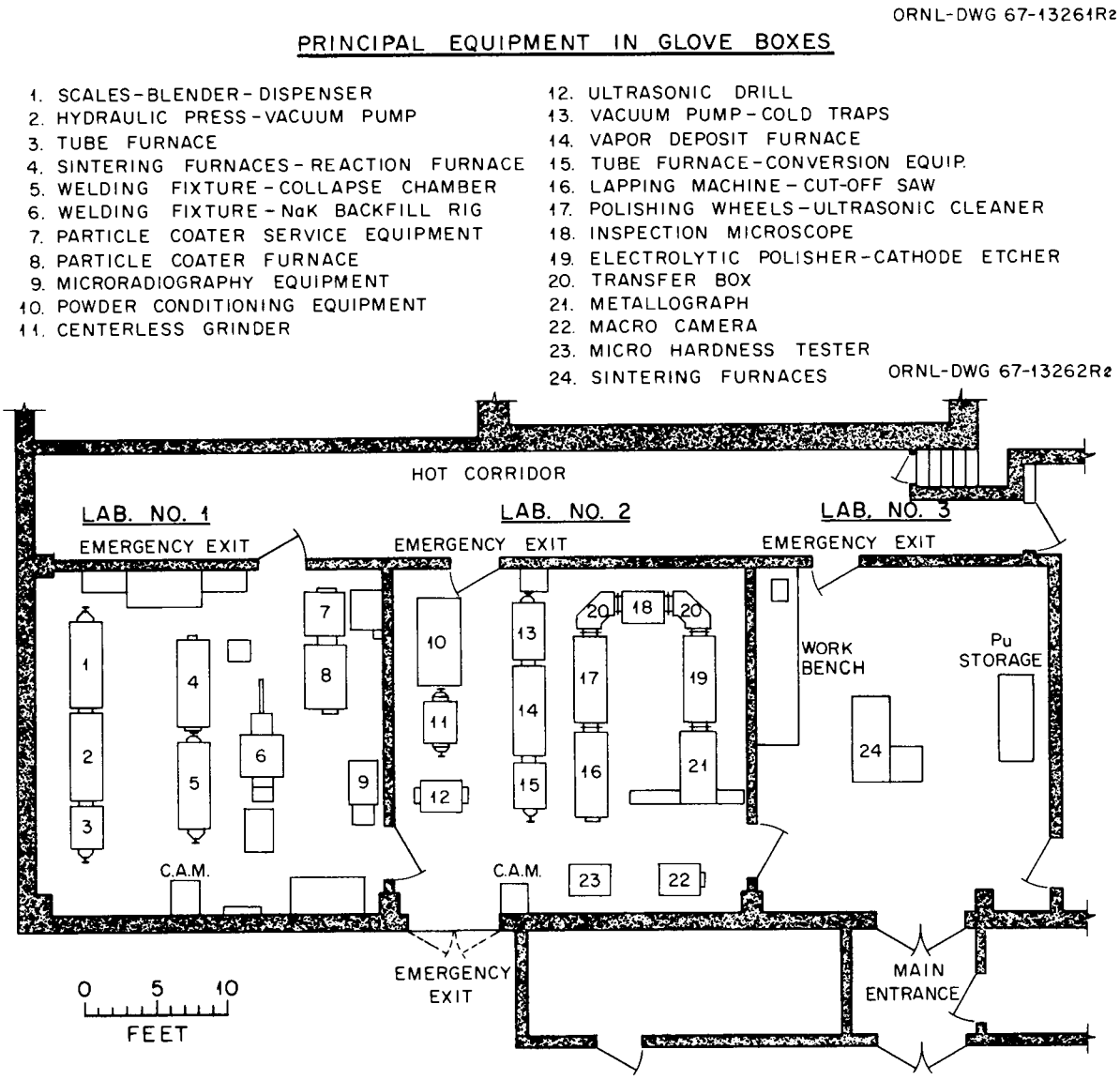

Fig. 7.1. Layout of Interim Alpha Laboratory Located in Building 3019.

With the exception of boxes 12, 22, 23, and 24, all of the glove boxes shown on the layout are installed and are either operating or in the final stages of check-out.

The principal work this quarter has involved the equipment installation and check-out of the metallography line, the completion of the argon distribution system, and the design and modification of an existing molybdenum resistance furnace for installation in laboratory 3.

Oxide Fabrication. All of the boxes in laboratories 1 and 2, except the ultrasonic drill glove box, have been installed and are in operation. During the quarter, glove boxes 1 and 2 were installed, leak checked, and placed in operation. The centerless grinder glove box was also placed in operation after receiving approval from the Radiochemical Plants Review Committee.

Because of the irradiation test schedule requirements for pellets (and later extrusions), we decided to install a large sintering furnace in the 3019 alpha facility. Additional space was requested and obtained from Chemical Technology Division in laboratory 3. The pellet-sintering furnace that will be installed is an existing molybdenum heating element type furnace with a hot zone of approximately 7 1/2 × 14 × 8 in. and capable of 1650°C continuous operation. In addition to the pellet furnace, provisions were made for the later installation of a large microsphere sintering furnace in the same glove box. A standard mild steel 6-in. glove box was obtained. The design for the incorporation of these furnaces into the glove box and modification to the glove box have been completed along with installation of services in laboratory 3. Final installation and check-out should be finished before the end of April.

Metallography. Seven of the nine metallography glove boxes were installed, all service connections completed, and leak checking and preoperational check-out are now well under way. An overall view of the metallography line as installed in the 3019 facility is shown in Fig. 7.2. The microcamera and microhardness tester glove boxes are not shown; however, they have been completed and are now undergoing extensive cold check-out. They are shown individually in Figs. 7.3 and 7.4. These boxes will be installed when the two old TRU-type metallography glove boxes, which we are currently operating to maintain plutonium metallography, are removed from the space these two boxes are to occupy.

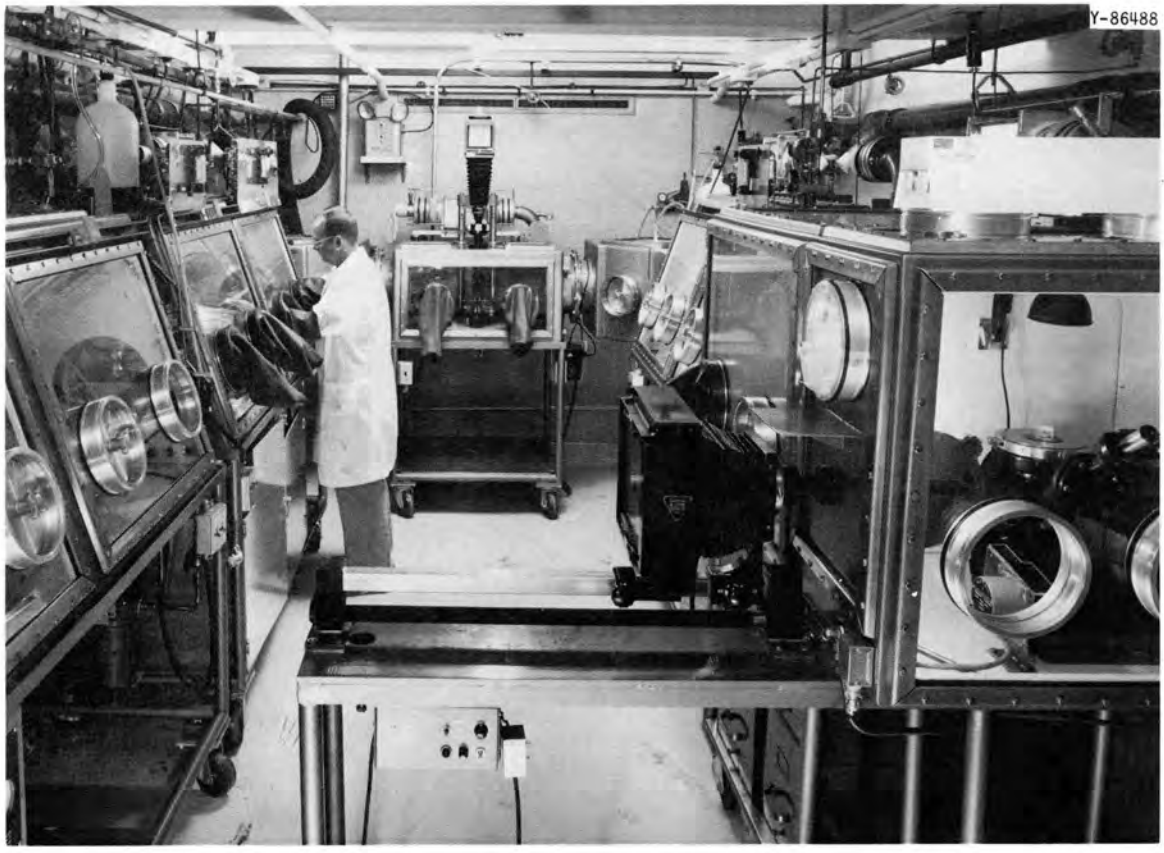

Fig. 7.2. Metallography Glove-Box Line Located in Building 3019 Facility.

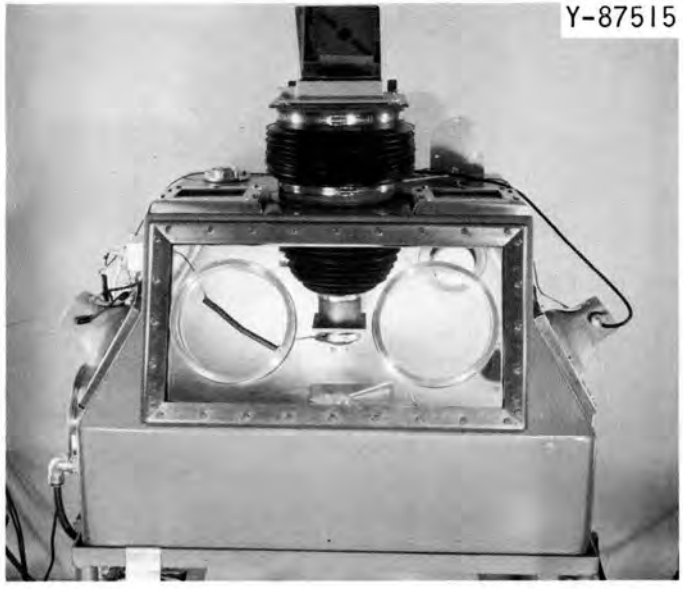

Fig. 7.3. Microcamera Located in the Plutonium Metallography Facility.

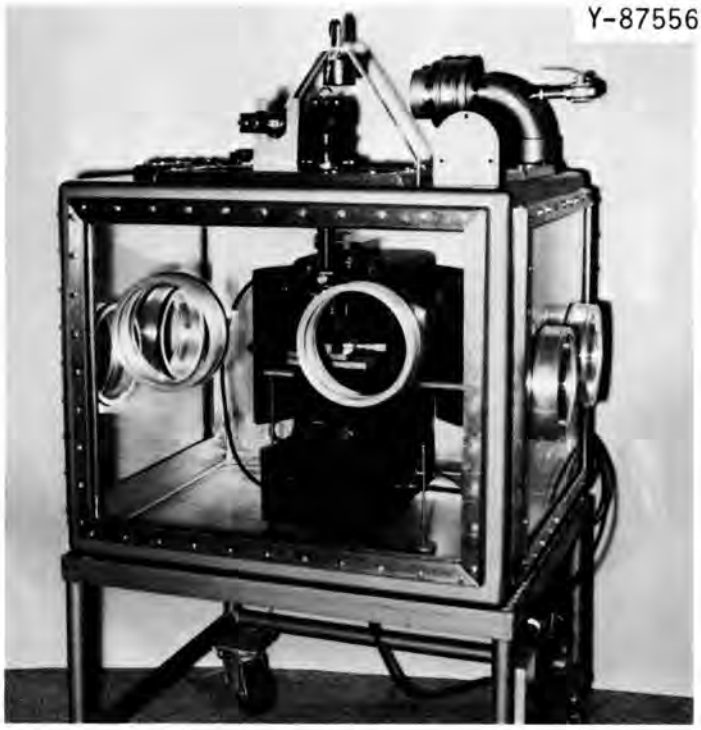

Fig. 7.4. Microhardness Tester Glove Box in the Plutonium Metallography Facility.

Design has been started on the cathodic etcher and the vapor deposition equipment which are to be located in each of the transfer boxes (No. 20).

Building 4508 Facilities

The layout of the 1700-sq-ft, 4508 Interim Plutonium Laboratory and the principal equipment associated with each glove box are shown in Fig. 7.5. The boxes are grouped according to purpose:

Group	Purpose
1, 19, 20, 21	Fuel characterization
2, 3, 4, 5, 8	Nitride synthesis and fabrication
6, 7	Pellet examination
9, 10	Short-term compatibility studies
11, 12, 13	Thermal conductivity measurement
14	Fuel rod density scan
15, 16, 17	X-ray diffraction studies
18	Vapor pressure measurement
22	Arc melting
23	Isothermal grain growth
24	Creep measurement

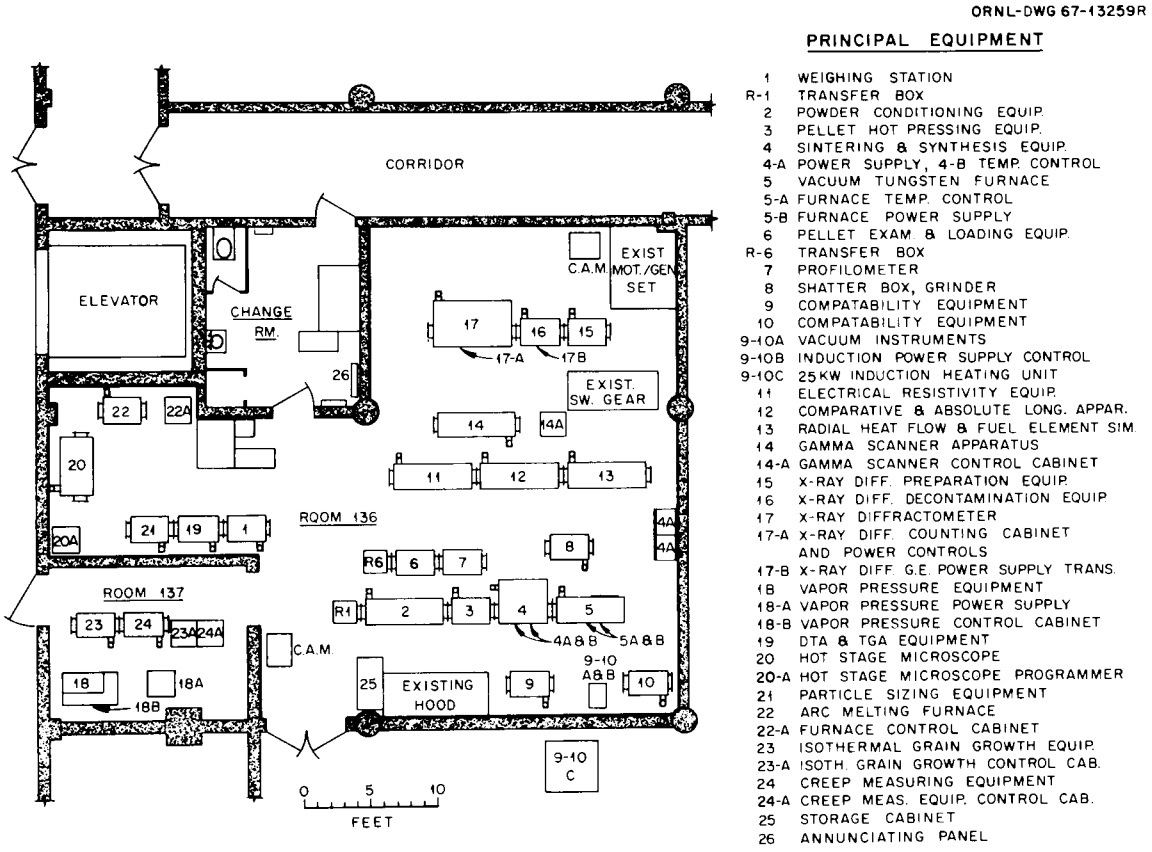

Fig. 7.5. Layout of Interim Plutonium Laboratory Located in Building 4508.

Only 14 of the boxes will be set up initially; these boxes are 1 through 4, 6, 8 through 10, 14 through 17, 19, and 20. These boxes are essentially completely installed and are now in various stages of cold check-out. The safety analysis and operating procedures for the area were completed and the laboratory reviewed by the ORNL Radiochemical Plant Review Committee in late March. Review of the facility by a review committee from the local operations office of the AEC is scheduled for the middle of April. We expect to begin hot operation of the laboratory shortly after this review.

Box Argon Purge-Exhaust System. The boxes are all being equipped to operate with a high-purity (< 50 ppm total impurities) argon atmosphere, initially with a once-through purge and later with an argon purification-recirculation system. This quarter a large percentage of the work has involved the installation of safety devices, such as

emergency power, and the evacuation and fire alarm systems. Leak checking and preoperational check-outs are now in progress. A brief summary and status of each major equipment group follow.

The argon purge supply for reducing the bulk argon supply from 30 psig to 20 in. water for supply to the glove boxes was completed, checked out, and placed in operation. The individual glove box purge-exhaust systems were leak checked and placed in operation. The overall glove box exhaust system was placed in operation after modifying the emergency power supply to the system to meet safety criteria.

Purchase specifications for the argon purification and recirculation system were completed and preliminary bids for the unit are now being obtained. Capital funds are currently not available for this unit.

Fuel Characterization. The group of boxes includes the analytical balance box, DTA-TGA box, hot-stage microscope box, and particle-size analysis equipment. All of this equipment except the particle-size analysis equipment has been initially installed, and we are in the final stages of cold check-out. In Fig. 7.6 the analytical balance glove box is shown in (a) and the DTA-TGA glove box is shown in (b). The hot-stage microscope glove box is shown in Fig. 7.7.

Nitride Synthesis and Fabrication. All of the equipment except the high-temperature tungsten furnace has been installed or is being fabricated. A purchase requisition for the tungsten furnace was let to the Richard D. Brew Company with delivery expected in August. During the quarter the hot press frame was completed and installed in its glove box. An overall view of the hot press glove box is shown in Fig. 7.8. The induction furnace for the hot press is now being fabricated.

The sintering and synthesis glove box, which contains two 1 5/8-in.-diam Marshall tube furnaces capable of operating up to 1750°C in a vacuum or with an oxidizing, neutral, or reducing atmosphere, has been installed and checked out. An overall view of this box is shown in Fig. 7.9.

The "Shatterbox" grinder has been installed in its glove box and checked out. The pellet press and other related equipment are installed and ready for operation.

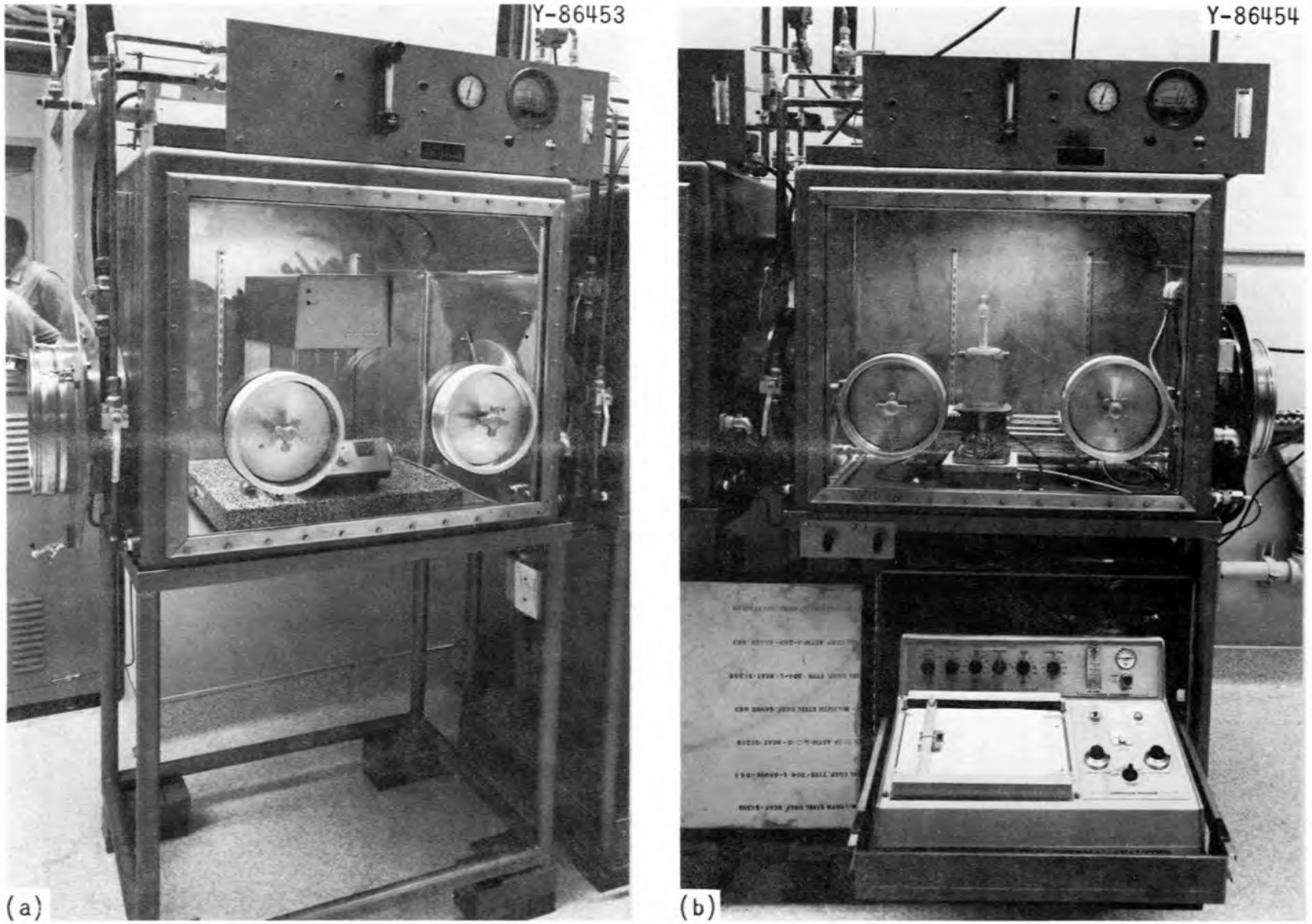

Fig. 7.6. Analytical Balance Glove Box (a) and DTA-TGA Glove Box (b) Located in the Interim Plutonium Laboratory.

Fig. 7.7. Hot-Stage Microscope Glove Box Located in the Interim Plutonium Laboratory.

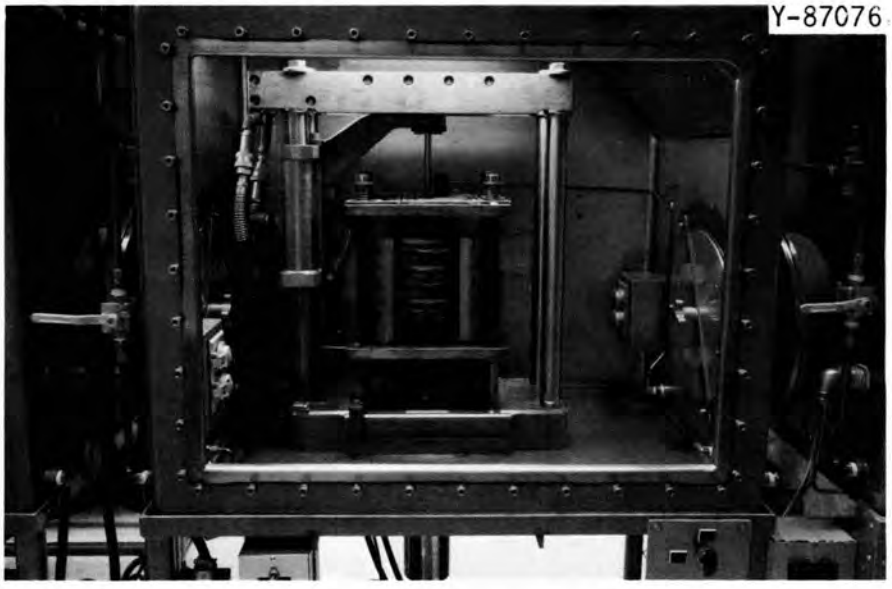

Fig. 7.8. Hot Press Glove Box Located in the Interim Plutonium Laboratory.

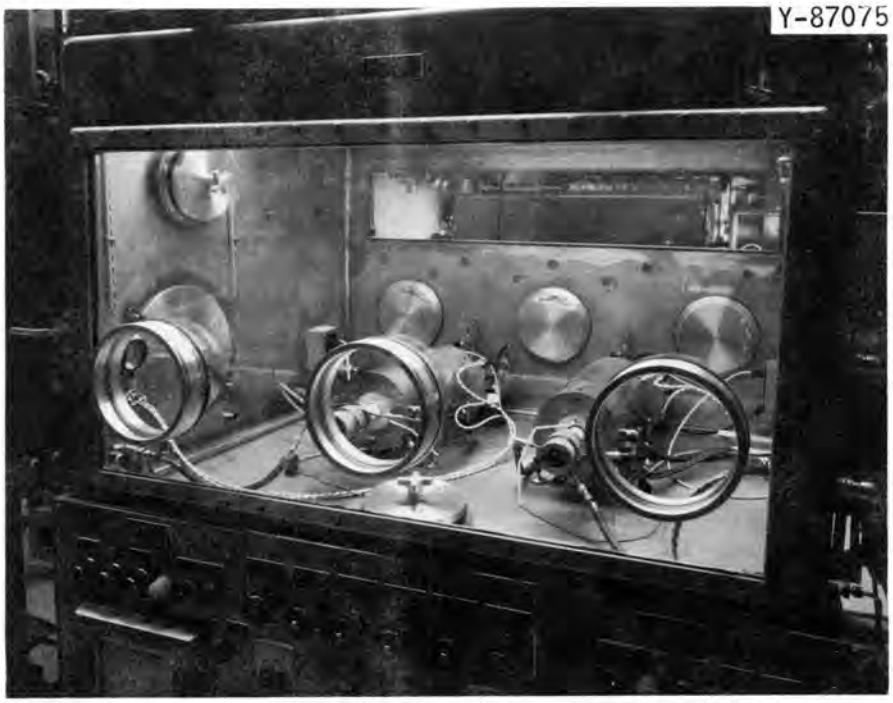

Fig. 7.9. Sintering and Synthesis Glove Box Containing Two Marshall Tube Furnaces.

Compatibility. Installation of this box and its related equipment has been completed and checked out. A view of the compatibility box is shown in Fig. 7.10.

X-Ray Diffraction. The three boxes for x-ray diffraction have been set up in their operating positions, the x-ray power supply and counting circuits installed, and unit is now ready for cold check-out. An overall view of the x-ray diffraction setup is shown in Fig. 7.11.

Thermal Conductivity Measurement. Design of the glove boxes for the thermal conductivity line has been completed and is ready for procurement. Design of the radial heat flow apparatus has been initiated. Capital funds are not available for the procurement of these items.

Vapor Pressure Measurement. The design of the vapor pressure measuring system and its related glove box has been essentially completed. This system consists of a high-vacuum system, microbalance, a tungsten mesh furnace, residual gas analyses, and associated hardware. The equipment is either on hand, ordered, or in the process of being ordered.

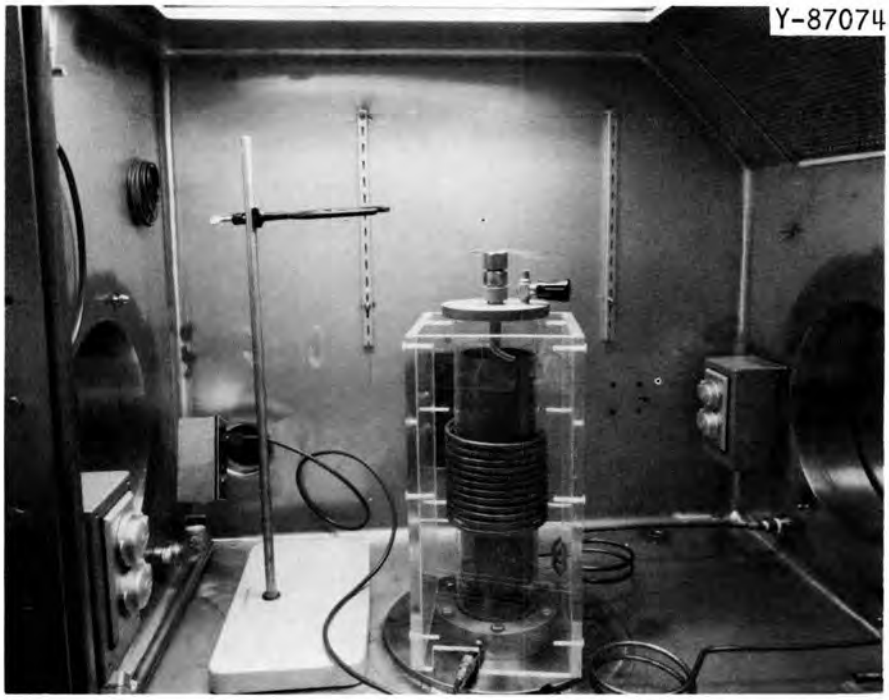

Fig. 7.10. Compatibility Box Located in Building 4508 Interim Plutonium Laboratory.

Fig. 7.11. X-Ray Diffraction Glove Box Line Located in Building 4508 Interim Plutonium Laboratory.

Preparation of $(U,Pu)O_2$ Sol-Gel Material

W. T. McDuffee[2]

The sol-gel work reported in this section is part of a larger program on sol-gel process development and demonstration supported at ORNL. The work reported here is that being carried out in the Chemical Technology Division Pilot Plant. During the past quarter, 485 g of PuO_2 was prepared as aqueous sol for use in fuel fabrication studies. This sol was to be mixed with UO_2 sol, also prepared for this program. About 500 g of UO_2–20% PuO_2 microspheres was prepared for use in fuel evaluation studies. About three-fourths of the spheres were 300 to 400 μ in diameter; the remainder were under 44 μ in diameter.

Development of Urania-Plutonia Fabrication Techniques

J. D. Sease R. A. Bradley R. B. Fitts
R. L. Hamner J. Komatsu W. L. Moore
A. R. Olsen

Various techniques are being investigated for fabricating sol-gel-derived urania-plutonia into fuel for LMFBR applications. Current activities are directed toward developing a process for pressing and sintering pellets for loading into fuel rods for irradiation tests. Pellets with controlled densities at various levels between 86 and 96% of theoretical and with oxygen-to-metal ratios of 1.94 or 1.98 are required for the irradiation tests.

Sphere-Pac, a method for loading fuel rods directly with dense microspheres by low-energy vibratory compaction, is also being investigated. Future development work will include extrusion of fuel rods from urania-plutonia "clay" produced from sol-gel material.

---

[2]Chemical Technology Division.

Pellet Development (R. A. Bradley, R. L. Hamner, W. L. Moore)

Summary of Previous Experience. Hamner and Robbins[3] conducted a preliminary investigation of the pelletization of sol-gel-derived urania. They demonstrated that pellets with densities in the range of 70 to 92% of theoretical could be produced from various forms of sol-gel-derived material, with the density depending on the powder preparation, the pressure used in forming the pellet, and the sintering conditions. In our previous work with urania-plutonia, we produced 93% dense pellets from powder prepared by crushing and sieving microspheres.[4] Those pellets were pressed at 30,000 psi and sintered in Ar–4% H_2 at 1450°C.

Material Preparation. We are investigating methods for converting mixed urania-plutonia sols into powder suitable for pressing and sintering into dense pellets. We prepared mixed urania-plutonia sol by blending UO_2 and PuO_2 sols in a Waring Blendor for 5 min, then dried the sol in an argon-purged stainless steel tray. In each tray-drying experiment the water was removed with no difficulty, yielding dark, friable granules, 1/8 in. in diameter and smaller. The drying conditions used in four preliminary experiments with UO_2 sol and one with mixed $(U,Pu)O_2$ sol are given in Table 7.1. The BET surface area, bulk density, crystallite size, and heavy metal content of the products are also given in Table 7.1.

The dried gel was ground into a fine powder in a Gem-T Research Model jet mill, a fluid energy mill which comminutes the material by the impact action of particles carried in opposing jet streams. The tray-dried material must be ground to –60 mesh to provide suitable feed material for the jet mill. Several grinding experiments were performed with UO_2 to investigate the effects of the position of the opposing jets, the feed rate, and the argon pressure on the ground product. Since we could not obtain a particle size distribution analysis on plutonium-bearing materials, we used green and sintered density to evaluate the jet-milled

[3]R. L. Hamner and J. M. Robbins, Fuels and Materials Development Program Quart. Progr. Rept. Sept. 30, 1967, ORNL-TM-2020, pp. 9–16.

[4]R. A. Bradley and R. L. Hamner, Fuels and Materials Development Program Quart. Progr. Rept. Dec. 31, 1967, ORNL-TM-2090, pp. 140–143.

Table 7.1. Description of Drying Conditions and Characterization of Product from Tray-Drying Experiments

Dried Material Batch No.	Drying Conditions	Characterization of Product			
		Surface Area (m^2/g)	Bulk Density (g/cm^3)	Crystallite Size (A)	Heavy Metal Content (wt %)
UO_2-TD1	Volume of sol: 1.74 liters; bed depth: 7/16 in.; argon purge: 0.2 cfm; temperature: 95°C for 24 hr, 170°C for 6 hr	65	4.8–6.1 Av 5.3	65	U, 82.3
UO_2-TD2	Volume of sol: 3.14 liters; bed depth: 3/4 in.; argon purge: 0.5 cfm; temperature: 95°C for 1 hr, 170°C for 12 hr	68	5.0–5.6 Av 5.3	77	U, 83.72
UO_2-TD3	Volume of sol: 3 liters; bed depth: 3/4 in.; argon purge: 0.5 cfm; temperature: 180°C	36.4	6.06	a	U, 83.91
UO_2-TD4	Volume of sol: 3 liters; bed depth: 3/4 in.; argon purge: 0.5 cfm; temperature: 230°C	36.8	6.06	a	U, 83.95
PuU-TD1	Volume of sol: 2.7 liters; bed depth: 3/4 in.; argon purge: 0.5 cfm; temperature 170°C	59.8	6.41	a	U, 69.03; Pu, 18.3

[a]Results not received.

powder. This material, which had a bulk density of about 55% after tray drying, could be pressed at 40,000 psi into pellets which had green densities of about 47%. The conditions used in jet milling 10 batches of material and the densities obtained from each batch are given in Table 7.2. The pellets were sintered according to schedule 1, shown in Table 7.3. Since the best green densities were obtained on Batches UO_2-TD3-C and UO_2-TD4-C, the jet milling conditions used for those materials were used to grind mixed urania-plutonia.

Pressing and Sintering. We performed a series of experiments to investigate the effect of forming pressure and sintering temperature on the density of sol-gel urania-plutonia. Powder prepared by jet milling tray-dried urania-plutonia (Batch PuU-TD1) was pressed at 20,000, 30,000,

Table 7.2. Description of Conditions Used in Grinding Tray-Dried Urania by Jet Mill and the Densities of Pellets Pressed from the Material

Jet Mill Batch No.	Jet Mill Conditions			Forming Pressure (psi)	Density, Percent of Theoretical	
	Feed Venturi	Opposite Venturi	Argon Pressure		Green	Sintered
				$\times 10^3$		
UO_2-TD3-A	Variable	Variable	Variable	20	40.7	68.1
				30	43.4	80.5
				40	46.8	85.2
UO_2-TD3-B	1/4 in. out	In	80	20	40.4	80.4
				30	43.7	83.2
UO_2-TD3-C	3/8 in. out	In	80	20	44.2	76.2
				30	46.2	80.0
				40	47.8	82.1
UO_2-TD3-D	1/4 in. out	3/8 in. out	80	20	44.2	76.2
				30	45.8	76.1
				40	47.4	79.4
UO_2-TD3-E	1/4 in. out	In	50	20	43.2	74.5
				30	45.7	77.9
				40	47.6	77.3
UO_2-TD4-A	1/4 in. out	In	80	20	42.0	73.4
				30	44.5	77.7
				40	46.6	78.2
UO_2-TD4-B	3/8 in. out	In	80	20	43.3	78.8
				30	45.4	78.6
				40	47.1	77.4
UO_2-TD4-C	1/2 in. out	1/2 in. out	80	20	44.1	72.2
				30	45.9	79.9
				40	47.7	80.2
UO_2-TD4-D	1/2 in. out	In	50	20	43.3	79.1
				30	45.9	79.9
				40	47.7	80.2
UO_2-TD4-E	1/2 in. out	In	30	20	43.7	75.9
				30	45.6	80.0
				40	47.5	79.6

Table 7.3. Description of Sintering Schedules Used in Sintering Urania and Urania-Plutonia Pellets

Schedule Number	Heating Rate	Atmosphere
1	25 to 1450°C at 250°C/hr Hold at 1450°C for 100 min	20 to 700°C – argon with steam 700 to 1450°C – dry Ar–4% H_2
2	25 final temperature at 250°C/hr; hold at final temperature for 100 min	Dry Ar–4% H_2
3	25 to 425°C at 100°C/hr 425 to 450°C at 25°C/hr 450 to 550°C at 10°C/hr 550 to 600°C at 25°C/hr 600 to 1000°C at 100°C/hr 1000 to 1450°C at 250°C/hr Hold at 1450°C for 100 min	Dry Ar–4% H_2

or 40,000 psi and sintered at 1350, 1450, or 1550°C according to schedule 2, shown in Table 7.3. The forming pressure, sintering temperature, and densities of these pellets are given in Table 7.4. From a graph of sintered density versus green density (Fig. 7.12), it appears that there is a quadratic relationship between green and sintered density and that the sintering temperature has no effect in the range 1350 to 1550°C.

Table 7.4. Forming Pressure, Sintering Temperature, and Densities of Pellets Made from Tray-Dried and Jet-Milled Urania-Plutonia[a]

Sintering Schedule	Forming Pressure (psi)	Sintering Temperature (°C)	Number of Pellets	Density, Percent of Theoretical	
				Average Green	Average Sintered
	$\times 10^3$				
2	20	1450	3	43.8	73.4
	30	1450	12	45.0	78.2
	40	1450	3	46.8	79.7
	25	1350	3	44.6	76.5
	35	1350	3	46.0	79.5
	25	1550	3	45.2	78.4
	35	1550	3	46.9	79.5
3	20	1450	3	42.2	81.2
	30	1450	3	44.1	83.88
	40	1450	3	46.0	86.1

[a]PuU-TD1-A.

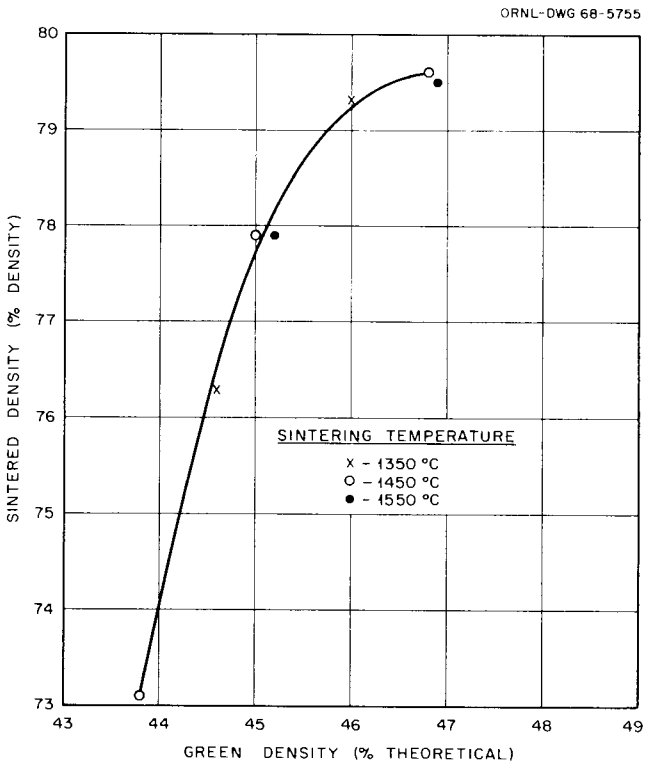

Fig. 7.12. Relationship Between Green and Sintered Density of $(Pu_{0.20}U_{0.80})O_2$ Pellets Pressed from Tray-Dried Jet-Milled Powder (PuU-TD1-A) and Sintered at Various Temperatures.

Since the sintered densities obtained in the above experiments were all lower than those obtained previously with crushed microspheres sintered by a slower sintering schedule, pellets pressed from tray-dried jet-milled material were sintered according to schedule 3, shown in Table 7.3. This schedule differs from schedule 2 in the slower heating rate from room temperature to 1000°C. The pressing conditions and densities of the pellets are given in Table 7.4. The densities of pellets pressed at 40,000 psi increased from 80% for schedule 2 to 86% for schedule 3, although the final temperature was 1450°C in both cases. This indicates that the heating rate up to 1000°C is very important in the densification process.

In order to compare the densification behavior of tray-dried jet-milled powder with that obtained from crushed microspheres, pellets were pressed from each material and sintered together using the sintering cycle used previously for sintering pellets made from crushed microspheres. The densities of the pellets pressed at 40,000 psi were about 90% of

theoretical while those pressed at the same pressure from tray-dried jet-milled powder were only 84.5%. We are attempting to learn more about the surface characteristics of both of these materials in order that we might understand the difference in their densification behavior.

Work will be continued to establish a process that will reproducibly yield pellets of the required density and oxygen-to-metal ratio.

Low-Energy Microsphere Packing (Sphere-Pac) (R. B. Fitts, A. R. Olsen, J. Komatsu)

High-density microspheres of $(U,Pu)O_2$ produced by the ORNL sol-gel process are ideally suited for fuel rod fabrication by the Sphere-Pac process. We are developing the Sphere-Pac fabrication process to produce fuel rod loadings with smear densities in the range of 80 to 90% of theoretical.

Studies of binary packing have verified the results of earlier workers in this field, provided practical evidence of the simplicity and reproducibility of the binary Sphere-Pac beds, and yielded samples, at around 85% of packing density, for characterization and irradiation testing.

We have continued to investigate Sphere-Pac, and in particular we are attempting to form sphere beds in the higher density range (88% and higher). We have investigated the effectiveness of blending two sizes of large spheres to form the initial poured bed prior to infiltration. The blending studies were carried out by placing about 60 g of coarse- and medium-size spheres in a 3.5-cm-diam 120 cm^3 bottle, rolling the bottle at 275 rpm for times up to 5 min, pouring the blended spheres into a 1.07-cm-ID graduated tube, and packing the unrestrained bed by vibrating for from 1 to 120 min. Blending was found to be complete after about 1 min and the poured bed was fully settled after about 1 min of vibration on a syntron vibrator. The conditions of vibration were 60 cps with about 7 g horizontal and 2 g vertical acceleration of the bed.

The first data on blending were obtained using 50% coarse and 50% medium spheres to determine the general trend in bed densities to be obtained by blending of various size spheres and to examine the problem of segregation of the size fractions. Figure 7.13 presents these data

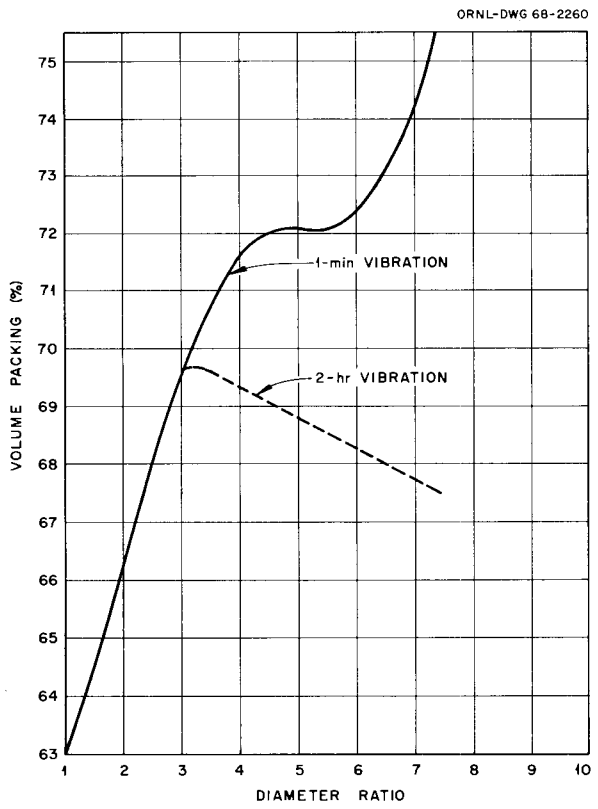

Fig. 7.13. Volume Packing for 50:50 Mixture of Two Sizes of Spheres and Effect of Vibration after Mixing.

A definite increase in bed density is obtained with increasing sphere diameter ratios; an unrestrained bed will begin to segregate during vibration when this ratio exceeds about 3.5. The blended bed density lacks reproducibility at higher diameter ratios. This effect is probably due to segregation during blending and might be reduced by the use of better, more sophisticated blending techniques. All of our work to date has employed the simple rolled bottle blending technique.

Figure 7.14 illustrates our results on blended bed volume packing (P_V) as a function of the volume percentage coarse and medium spheres for three sphere diameter ratios. These results agree well with those obtained by McGeary[5] and extend them to lower diameter ratios and smaller size spheres. The data obtained from the maximum density point (approx 65% coarse and 35% medium) on these curves may be used to calculate the

[5]R. K. McGeary, J. Am. Ceram. Soc. 44(10), 513–522 (1961).

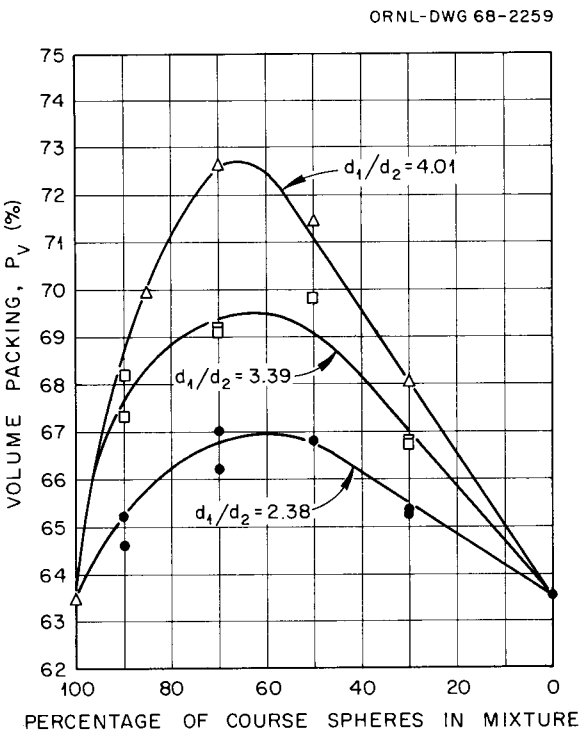

Fig. 7.14. Volume Packing of Blended Spheres of Two Sizes for Various Diameter Ratios.

efficiency (P_E) of the medium-size spheres in filling the void available to them around the coarse spheres. In order to calculate this efficiency on a uniform basis we assume an artificial packing efficiency for the coarse spheres of 63.5%. This is the limit for packing efficiency of a single size sphere in a large tube as presented by Ayre.[6]

Using this basis for the packing efficiency of smaller spheres in a packed bed of large spheres, the data in Fig. 7.15 was obtained. Some data from the work of McGeary and Ayre are also shown in this figure. The agreement is excellent for diameter ratios up to 8 or 10. Above this range Ayre's work deviates significantly from our findings and those of McGeary.

Using this information on blended bed densities and packing efficiencies we have developed a graphical construction which may be used to correlate and generalize all of our information relating to the Sphere-Pac fabrication procedure. This is shown in Fig. 7.16 where the horizontal

[6]J. E. Ayre and F. E. Soppet, J. Am. Ceram. Soc. 44(4), 180–183 (1965).

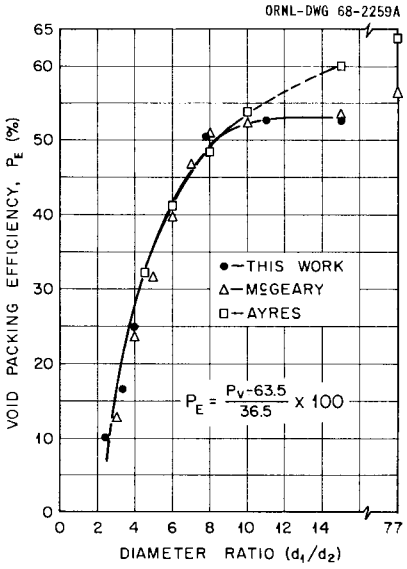

Fig. 7.15. Packing Efficiency of Small Spheres in a Packed Bed of Large Spheres.

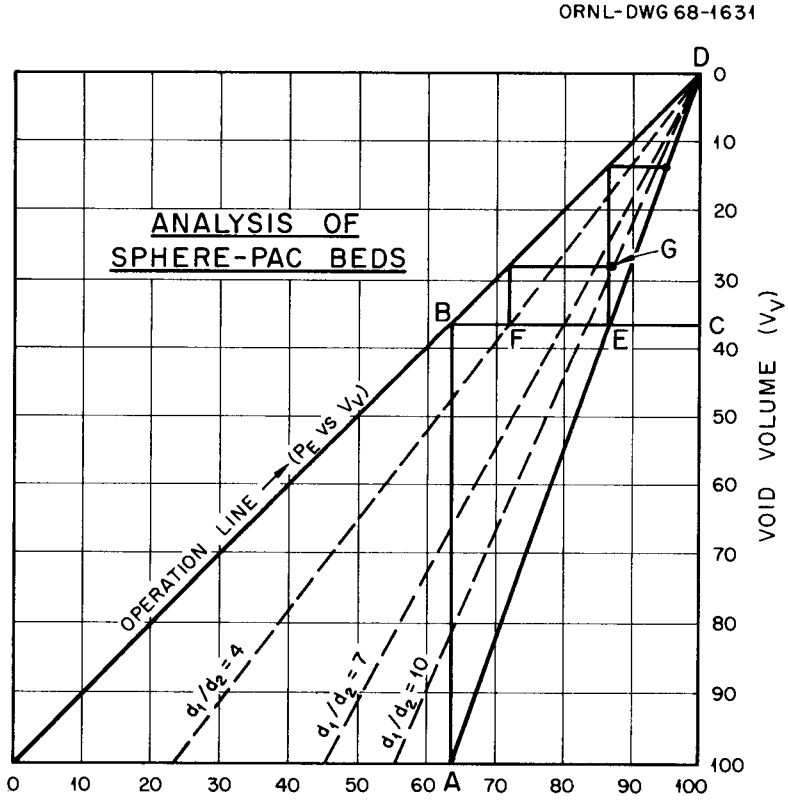

Fig. 7.16. Void Packing Efficiency (P_E).

axis represents the volume packing of spheres in a container or bed (packing efficiency) and the vertical axis represents the void volume associated with this volume packing. If a 45° operation line is established between the two zero points of the axes then the void volume associated with any packed volume may be determined by reading up and then across (line A-B-C). If we now construct a line joining the volume packing efficiency of a given size sphere (percent of available void volume filled by spheres) to the void volume zero point, the horizontal distance between this line and the operation line is always proportional to the packing efficiency multiplied by the void volume associated with that packed bed density. Thus the line A-D represents the packing of a single size sphere in a large tube or in a packed bed (according to Ayre) where the diameter of the sphere is less than approximately 1/25 that of the smallest sphere in the packed bed.

This curve may be used to illustrate the effect of serial infiltrations with spheres having d_1/d_2 greater than 25. We will obtain 63.5% packing with the coarse spheres. If we then infiltrate a small size sphere at this same efficiency we would obtain, from point E, an 87% dense bed, and a second infiltration produces a 95% dense bed. This type of line must also be plotted for the packing of spheres of varying diameter ratio with respect to the bed. These data are shown by the dotted lines for spheres of 1/4, 1/7, and 1/10 the size of the spheres in the bed and are obtained from the plot of P_E vs d_1/d_2 (Fig. 7.16).

We may now see the effects of using a blended bed, or the effect of infiltration at less than the optimum 63.5% packing efficiency. If a d_1/d_2 ratio of 4.0 is used for a blended bed the bed density (volume packing) is increased to 72%, point F. Infiltration with spheres 1/10 the size of the medium fraction produces an 88% dense bed, point G. This is exactly the density that we have obtained and reproduced by this technique. We have also produced 86.5% dense beds by infiltration of a blended bed ($d_1/d_2 = 3.4$) with the 10-to-1 size ratio of medium to small. This is the density predicted by the graphical correlation for these conditions.

From the above discussion it may be seen that to produce a 90% dense fuel we must use either a double infiltration with very carefully

controlled sphere sizes or a blended bed at d_1/d_2 of about 5.8, followed by a single infiltration. This requires investigation of the behavior of beds blended at this diameter ratio. They tend to segregate, as was shown in Fig. 7.13. We are presently studying this segregation and techniques for controlling it.

Characterization of Sol-Gel $(U,Pu)O_2$ Fuels (W. H. Pechin)

The development of the various sol-gel fuel fabrication processes requires various characterization tests to determine those properties that influence irradiation behavior. Equipment is just now becoming available for accomplishment of many phases of this work; therefore, we do expect to expand it considerably in the near future. Recently, we have concentrated on analytical chemistry techniques and the design of a system for radial heat flow measurements.

Hot-Stage Microscopy. – (Ji Young Chang) We intend to use hot-stage microscopy in conjunction with differential thermal and thermogravimetric analyses and x-ray crystallite size determinations for studies involving the characterization and sintering behavior of mixed fuels, particularly sol-gel mixed oxide microspheres.

We now have the capability for hot-stage microscopy at temperatures up to 1300°C in controlled atmospheres. Other major features of the equipment are (1) automatic programming of the heating, soaking, and cooling cycles, (2) observations by transmitted and reflected light, and (3) automatic equipment for sequence photography.

We have checked the equipment by making shrinkage measurements of 465-μ ThO_2 sol-gel microspheres during heating. Figure 7.17 shows that photographs of the microspheres were made by transmitted light during a heating schedule arbitrarily selected; the shrinkages were calculated by measurements of the photographs.

The equipment has been installed in a glove box in our Interim Plutonium Facility, and we expect to be able to begin studies of mixed oxide and mixed nitride fuels soon.

ORNL DWG. 68-3913

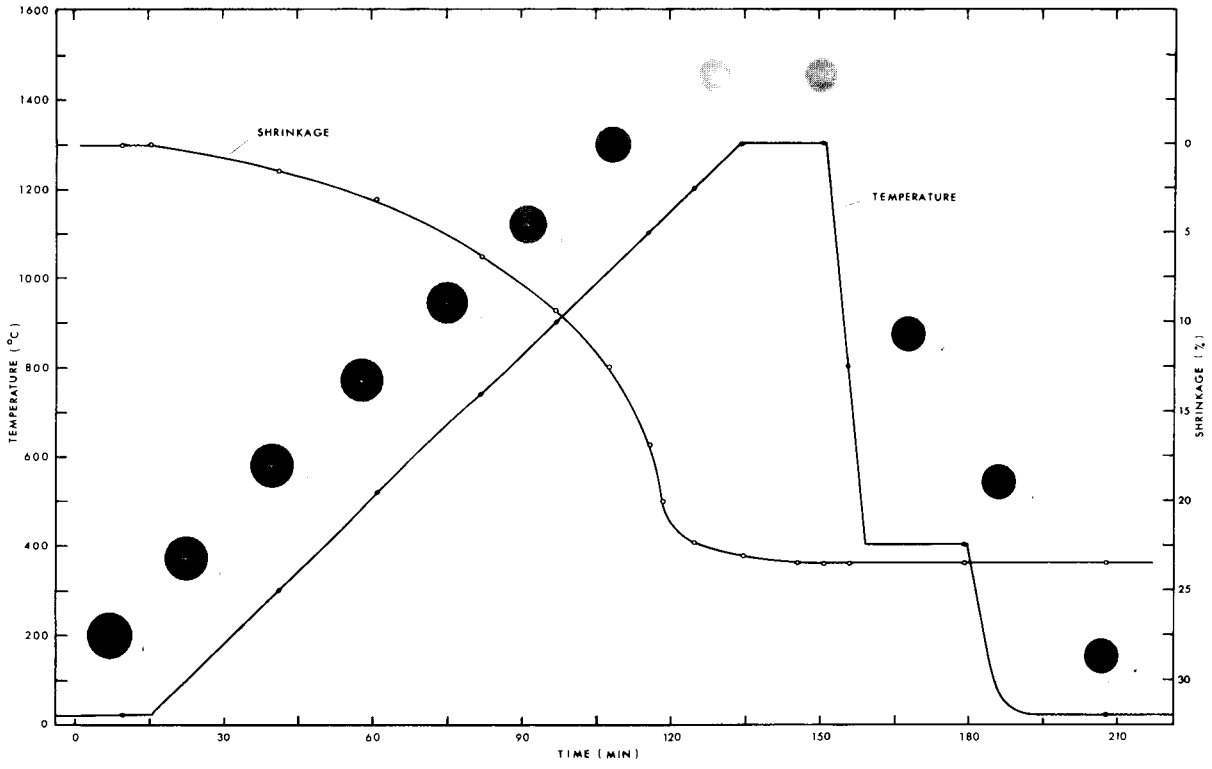

Fig. 7.17. Shrinkage of Sol-Gel ThO_2 Particle During Heating in Air.

Oxygen-to-Metal Ratio Control and Measurement (R. A. Bradley, W. H. Pechin)

We are investigating methods of determining the oxygen content of urania-plutonia. The NITROX method and a thermogravimetric technique[7] are currently being studied.

In a preliminary evaluation of the NITROX method, urania pellets were analyzed by both the NITROX method and the well-established polarographic method, which has been used in the past for determining oxygen-to-uranium ratios. The results of these analyses are given in Table 7.5. It appears that the oxygen-to-uranium ratio as determined by the NITROX method is about 0.9% lower than that determined by the polarographic technique.

[7]W. L. Lyon, The Measurement of Oxygen-to-Metal Ratio in Solid Solutions of Uranium and Plutonium Dioxides, GEAP-4271 (May 31, 1963).

Table 7.5. Oxygen-to-Uranium Ratios as Determined by the NITROX Method and the Polarographic Method

Analytical Method	Oxygen-to-Metal Ratio		
	Analysis 1	Analysis 2	Analysis 3
Polarographic	2.001	2.002	2.002
NITROX	1.977	1.990	1.984

The oxygen contents of seven urania-plutonia pellets sintered under various conditions were analyzed by the NITROX technique. The oxygen-to-metal ratios and nitrogen contents determined by duplicate analyses on each pellet are given in Table 7.6. An analysis of variance was performed to obtain an estimate of the analytical error and to test the significance of treatment effects. Assuming there is no real variation in oxygen-to-metal ratio within a pellet and that all the variation in the duplicate analyses is due to analytical error, the standard deviation due to analytical error, with seven degrees of freedom, was found to be 0.027. The treatment effects were not significant at the 95% confidence level.

Table 7.6. Oxygen-to-Metal Ratios of Urania-Plutonia Pellets Determined by the NITROX Method

Treatment Number	Forming Pressure (psi)	Sintering Temperature (°C)	Nitrogen Content (ppm)	Oxygen-to-Metal Ratio		
				Analysis 1	Analysis 2	Average
	$\times 10^3$					
1	20	1450	< 50	2.007	2.067	2.037
2	30	1450	< 50	1.943	1.971	1.957
3	40	1450	< 50	1.973	2.002	1.987
4	25	1350	< 50	1.977	1.996	1.987
5	35	1350	< 50	1.990	1.958	1.974
6	25	1550	< 50	1.925	1.986	1.955
7	35	1550	< 50	1.954	1.954	1.954

We are attempting to reduce the analytical error in the NITROX method. The thermogravimetric technique will be studied and compared with the NITROX method.

Thermal Conductivity (Peter Spindler)

The thermal conductivity of plutonium-bearing materials as function of temperature (300 to 1300°K) and gas pressure (1 to 4 atm) is to be measured in a radial heat flow apparatus, located in a glove box.

For proof-tests, a similar system that is to be operated without contamination with specimens of known thermal conductivity was designed. The components of the system are the stainless steel sample chamber, the molybdenum-wound nickel tube outside the heater and the molybdenum-wound nickel-top and -bottom heaters, the water-cooled stainless steel pressure vessel, and the brass base plate for instrumentation penetration.

Tests will be carried out on all components during the next quarter. After that, thermal conductivity of the following materials will be measured: MgO, sol-gel thoria microspheres, thoria (tungsten-coated), and ThO_2–8% UO_2 at three densities.

Irradiation Testing of Sol-Gel $(U,Pu)O_2$ Fuels

A. R. Olsen

The final evaluation of sol-gel-derived $(U,Pu)O_2$ fuels will be based upon their irradiation performance. The irradiation testing program is concentrating on comparative tests of the fabrication forms -- Sphere-Pac, pellets, and extrusions. The program includes tests in both thermal reactors and fast reactors. The thermal flux irradiations permit the use of instrumented capsules and the achievement of high-burnup levels in relatively short periods of time. These tests will provide supplemental information essential to the analysis of the fast-flux irradiation tests where the radial fission-rate distribution and fuel temperature profiles are more typical of anticipated LMFBR operating conditions. The test program also includes transient tests to investigate fuel performance under off-normal operating conditions. The development of mathematical models to predict fuel behavior and computer programs to perform the associated calculations is an integral part of the irradiation test program.

Uninstrumented Thermal Flux Irradiation Tests (A. R. Olsen, R. B. Fitts, J. Komatsu, W. H. Pechin)

A limited number of uninstrumented capsules designed for screening-type irradiations and fuel swelling determinations are being irradiated in the Engineering Test Reactor. The capsule design, described previously,[8] permits the simultaneous irradiation of four test rods, each containing a 3-in. fuel column.

Examination of the first two capsules in this series, ORNL 43-99 and -100, is complete. There were some failures in the (U–20% Pu)O_2 fuel rods because of overpower operation as reported previously.[9] A final report on these tests is being written.

Postirradiation examination of the third capsule, ORNL 43-112, which contained Sphere-Pac (^{238}U–15% Pu)O_2 fuels, is continuing. Preliminary results of the examination were discussed in the last quarterly report.[9] Since the primary reason for removing experiment 43-112 after an exposure of only one reactor cycle was to obtain experimental confirmation of our fission-rate calculation techniques using the ANISN computer code,[10] we have concentrated on the burnup analysis of these fuels. The radiochemical analyses as reported previously agree quite well with the ANISN predictions.[9] The results of the calculation of burnup by changes in isotopic analysis and fuel composition have pinpointed a need for precise analytical results. A preliminary error analysis for low-burnup fuels indicates that errors in the plutonium analyses will have a tenfold effect on the calculated burnup. Therefore, repeat analyses were requested for the 43-112 burnup samples. The repeat plutonium analyses were made by coulometric titration, which has greater precision than the former technique of alpha counting. The calculated burnup values based on these analyses are listed in Table 7.7 along with the radiochemical average values and the ANISN predictions. These results confirm the reliability of the ANISN predictions. We are continuing our attempts to

[8]R. B. Fitts and A. R. Olsen, Fuels and Materials Development Program Quart. Progr. Rept. Sept. 30, 1967, ORNL-TM-2020, pp. 19–24.

[9]A. R. Olsen, R. B. Fitts, and J. Komatsu, Fuels and Materials Development Program Quart. Progr. Rept. Dec. 31, 1967, ORNL-TM-2090, pp. 143–147.

[10]W. W. Engle, Jr., A User's Manual for ANISN, K-1693 (March 1967).

Table 7.7. Comparison of Burnup Determinations with ANISN Predictions

Fuel Rod Sample	Fuel Burnup, Percent FIMA		
	Isotopic Analysis	Radiochemical Analysis[a]	ANISN Predictions
43-112-1B	0.34	0.46	0.49
43-112-2B[b]	0.61	0.66	0.71
43-112-3B	0.67	0.65	0.69
43-112-4B	0.57	0.51	0.54

[a]Average of ^{137}Cs, ^{144}Ce, and ^{89}Sr analyses.

[b]Initial fuel was UO_2 enriched to 20% ^{235}U; all others were (0.85% ^{238}U–0.15% Pu)O_2.

improve the accuracy and reliability of both our analytical techniques and our burnup calculational procedures.

ORR Instrumented Tests (R. B. Fitts, V. A. DeCarlo[11])

The ORR instrumented capsule irradiation tests will be used to investigate the basic in-reactor characteristics of sol-gel-derived $(U,Pu)O_2$ fuels. Since a knowledge of the fuel temperatures is fundamental to the analysis and understanding of fuel behavior, the capsule has been designed to monitor fuel-central and cladding-surface temperatures and fuel rod heat generation rates. In the overall program the primary characteristics to be investigated include thermal conductivity, fuel restructuring, and fission-gas release The influence of fuel composition, stoichiometry, density, fabrication history, and burnup on these temperature-sensitive properties will be investigated.

The first series of these tests has two primary objectives: (1) The characteristic temperatures for microstructural changes will be determined for sol-gel Sphere-Pac and pellet fuels. These data are needed for the analysis of uninstrumented tests. (2) The fuel central temperature will be investigated as a function of heat generation rate and fuel rod surface

[11]Reactor Division.

temperature and this information will be used to develop and refine a mathematical model for the in-reactor thermal conductivity of sol-gel fuel.

The first capsule, designated SG1-OF-2, has been fabricated and is scheduled for installation in an ORR poolside position during the April 5, 1968, shutdown. The fuel rods were fabricated by the Sphere-Pac process with the same fuel (^{238}U–15% Pu)O_2 used in three of the uninstrumented ETR capsules. The fuel has been loaded to an average smear density of 8.8 g/cm^3.

Although some useful characteristic information will be obtained from this test, the primary purpose is to test the capsule design described previously.[12] Therefore, this capsule will not be operated in a manner to optimize the determination of fuel characteristics, but rather to determine capsule performance limits.

Transient Testing of Sol-Gel-Derived (U,Pu)O_2 Fuel (C. M. Cox, J. D. Jenkins,[13] M. K. Preston[14])

Preliminary reactor physics and heat transfer calculations have been performed and are being refined in support of the capsule design, Preliminary Proposal, and Hazards Analysis for the ORNL Series I TREAT experiments described previously.[15] The program has been revised so that the Series I tests will use nominally (0.8% U–0.2% Pu)O_2 fuel rather than the (0.75% U–0.25% Pu)O_2 fuel initially planned.

The work during the last quarter has concentrated on three interrelated areas: reactor physics calculations, heat transfer calculations, and capsule design and fabrication.

Reactor Physics Calculations. The quantitative results needed from reactor physics calculations are the fuel pin power profile, pin power relative to the TREAT total power, and the neutron energy spectra at

---

[12] R. B. Fitts and V. A. DeCarlo, Fuels and Materials Development Program Quart. Progr. Rept. Dec. 31, 1967, ORNL-TM-2090, pp. 147–148.

[13] Reactor Division.

[14] General Engineering Division.

[15] C. M. Cox, Fuels and Materials Development Program Quart. Progr. Rept. Dec. 31, 1967, ORNL-TM-2090, pp. 149–152.

various positions in the experimental capsule. The capsule design for the Series I experiments will be a modified version of the GE-APO capsule used in their Series C2 TREAT experiments.[16] We have performed a series of one-dimensional neutron transport theory calculations with the ANISN code,[10] using S_4 angular segmentation and P3 scattering, to investigate the use of neutron filters in the capsule. Eighteen group cross sections were prepared for each case considered using the GAM-2 library for energies greater than 1.86 ev and the THERMØS library for lower energies. The neutron spectrum hardening resulting for each case is indicated roughly by the epithermal-to-thermal flux ratios given in Table 7.8 for an 81-cm radius TREAT core with a core temperature of 20°C and a fuel specimen temperature of 1000°C. The calculated power profiles are still under evaluation; however, it appears that it may be possible to flatten significantly the fuel pin power profile while maintaining a specimen power-to-TREAT power ratio sufficient to melt the fuel. The final evaluation of these filters will be made on the basis of the shape of calculated temperature profiles for each case.

The preliminary estimates of fuel pin power densities relative to TREAT power indicated in Table 7.8 are based on an estimated TREAT peak-to-average axial power ratio of 1.19 (ref. 17) and an energy release of 200 Mev/fission. The fuel pin power calculated in this manner for the unfiltered case is reasonably close to the GE C2 series values for essentially the same geometry but with 9.95 g/cm^3 fuel smear density. They have reported a calculated value of 1.12×10^{-4} and measured values of 0.79×10^{-4} and 0.96×10^{-4} w cm^{-3} w^{-1} (ref. 16).

In addition to completing the analyses of fuel pin power profiles, we will extend the calculations to consider an 87-cm core radius and a core temperature of 200°C.

Heat Transfer Calculations. The planning and analysis of the TREAT experiments will depend largely on transient heat transfer calculations.

---

[16] J. E. Hanson, J. H. Field, and S. A. Rabin, Experimental Studies of Transient Effects in Fast Reactor Fuels Series II — Mixed Oxide (PuO_2-UO_2) Irradiations, GEAP-4804 (May 1965).

[17] G. A. Freund, P. Elias, D. R. MacFarlane, J. D. Geier, and J. F. Boland, Design Summary Report on the Transient Reactor Test Facility, TREAT, ANL-6034, p. 89 (June 1960).

Table 7.8. Preliminary Results from ANISN Calculations TREAT Capsule TR-1 with 8.96 g/cm^3 Smear Density (0.8% U–0.2% Pu)O_2[a,b]

Case	Epithermal-to-Thermal Neutron Flux Ratio[c]		Average Specimen Power Density TREAT Power (w cm^{-3} w^{-1})
	Capsule Surface	Fuel Cladding	
			$\times 10^{-4}$
No filter	2.30	5.16	0.843
0.0025 in. Cd	2.66	6.44	0.368
0.005 in. Cd	2.75	7.09	0.271
0.0115 in. boral[d]	2.79	8.58	0.308
0.023 in. boral[d]	2.95	14.0	0.185

[a] Natural uranium; assumed plutonium isotopic by weight: 0.91 ^{239}Pu, 0.082 ^{240}Pu, 0.008 ^{241}Pu.

[b] Clad with 0.250-in.-OD × 0.016-in.-thick type 304 stainless steel tubing.

[c] Thermal ≡ ≤ 1.86 ev; epithermal ≡ > 1.86 ev.

[d] Assumed natural boron content: 5.124×10^{22} atoms/cm^3.

In a typical Series I experiment the inner-fuel capsule will be heated first to approximately 430°C, to simulate typical coolant temperatures, and then the fuel will be pulsed severely in a TREAT transient to obtain various degrees of fuel melting in some 2 to 4 sec.

A lower limit on the specimen energy release required to melt all the fuel can be estimated for adiabatic conditions as $\int_{700}^{3073} C_p\,dT$. Assuming the melting point of the fuel to be approximately 3073°K and extrapolating Ogard's equation[18] for the specific heat of (0.8% U–0.2% Pu)$O_{1.98}$ yields $\int_{700}^{3073} C_p\,dT \cong 330$ cal/g. Combining this required energy input with the conversion factor in Table 7.8 for the unfiltered case gives a minimum integrated TREAT power pulse of 148 Mwsec to increase the fuel temperature to the melting point. Adding

[18] A. E. Ogard, Advanced Plutonium Fuels Program Quarterly Status Report for April 1 through June 30, 1967, LA-3745-MS, p. 43 (Aug. 30, 1967).

the heat of fusion, approximately 85 cal/g (ref. 19), brings the minimum integrated TREAT power to completely melt the specimen to approximately 186 Mwsec.

The deviation from an adiabatic process can be estimated from the GE-APO data recently reviewed by Thomas and Field,[20] in which they reported the volume percentage of fuel melted in several experiments with $(U,Pu)O_2$ fuel. These data are based on a measured molten boundary radius, which is somewhat nebulous in terms of microstructural appearance. It will be assumed here for this illustration that, due to the short duration of these transients, the heat of fusion must be included in the specimen energy release for such a structure to form. Comparing the actual energy release E in calorie per gram and the observed volume percentage melt V_m with our estimated adiabatic energy release to give the molten structure, 415 cal/g, an adiabatic process efficiency η_a is defined such that $\eta_a = 415\ V_m/E$, assuming uniformly dense fuel. For the data summarized by Thomas and Field, η_a varies from approximately 62 to 79%, apparently being influenced somewhat by the initial TREAT period. The heating of these fuel specimens during a TREAT transient thus approaches but is not adequately described by an adiabatic process.

This simple approach will not suffice for the design and interpretation of transient tests in which failure thresholds and mechanisms are to be investigated. Our initial Series I experiments will be designed based on transient heat transfer calculations with the TOSS computer program.[21] TOSS is limited in that it does not allow temperature-dependent physical properties and does not account for phase transformations; on the other hand, it is quite flexible in terms of geometry and initial and boundary conditions.

---

[19]J. G. Reavis and C. W. Baker, Quarterly Status Report on the Advanced Plutonium Fuels Program for October 1 through December 31, 1967, LA-3880-MS, p. 19 (Feb. 20, 1968).

[20]G. R. Thomas and J. H. Field, "Response of Axially Restrained Pellet Fuel to Transient Overpower," Trans. Am. Nucl. Soc. 10(2), 707 (1967).

[21]D. Bagwell, TOSS — An IBM-7090 Code for Computing Transient or Steady-State Temperature Distribution, K-1494 (December 1961).

Capsule Design and Fabrication. The TREAT capsule design for the Series I experiments basically will follow the GE-APO design, with the possible addition of a neutron filter. Capsule materials specifications are currently being prepared.

Fast Flux Irradiation Tests of Sol-Gel $(U,Pu)O_2$ Fuels (A. R. Olsen)

A proposal for approval-in-principle of the Series I EBR-II sol-gel fuels irradiation tests has been submitted to the experimental review committee at Argonne National Laboratory.

The primary objective of the Series I test group is to obtain comparative performance information on sol-gel fuels fabricated by pelletizing and Sphere-Pac processing. Duplicate fuels will be irradiated in the instrumented capsules in a thermal flux in the ORR pool-side facilities. The EBR-II uninstrumented fuel rods will be encapsulated and installed in a standard Mark A 19-rod subassembly. Preliminary information indicates that this subassembly will be assigned a position in row 6, the outermost core position.

Table 7.9 lists the Series I fuel rod parameters. All fuel will be derived from the sol-gel process and fabricated in our facilities. With a composition of 20% Pu and the uranium enriched to 93% ^{235}U we calculate peak linear heat ratings in the range 9 to 12 kw/ft in the EBR-II row 6 position, using the recent Table of Radial Fission Distributions at the Reactor Midplane, supplied by the EBR-II Irradiation Tests coordinator.

We propose to start the Series I tests with capsules I-1 through I-19 in the subassembly. Eight of these capsules will be removed after achieving a burnup level of approximately 2% FIMA (approx 20,000 Mwd/MT). Six of these will be replaced by capsules I-20 through I-25. The specific fueling of the two additional capsule locations has not yet been defined. If the sol-gel extrusion process is sufficiently well developed, we will load extruded fuel of the same composition and similar smear density in these two capsules.

We are proceeding with the detailed design and hazard analysis for the Series I tests with the objective of having the capsules ready for insertion in the EBR-II by October 1968.

Table 7.9. Proposed EBR-II Encapsulated Irradiation Tests of Sol-Gel $(U,Pu)O_2$

Series I

Capsule Number[a]	Fuel Form	Density, Percent of Theoretical		Oxygen-to-Metal Ratio[b]	Scheduled Burnup (% FIMA)
		Fuel	Smeared Fuel		
I-1	Pellet	93	88	A	10
I-2	Pellet	93	88	A	2[c]
I-3	Pellet	93	88	A	2
I-4	Pellet	93	88	B	10
I-5	Pellet	86	81	A	10
I-6	Pellet	86	81	A	2[c]
I-7	Pellet	86	81	A	2
I-8	Pellet	86	81	B	10
I-9	Annular pellet	96	85	A	10
I-10	Annular pellet	96	85	A	2
I-11	Annular pellet	96	85	B	10
I-12	Sphere-Pac	98	81–83	A	10
I-13	Sphere-Pac	98	81–83	A	2[c]
I-14	Sphere-Pac	98	81–83	A	2
I-15	Sphere-Pac	98	81–83	B	10
I-16	Sphere-Pac	98	87–88	A	10
I-17	Sphere-Pac	98	87–88	A	2
I-18	Sphere-Pac	98	87–88	A	8
I-19	Sphere-Pac	98	87–88	B	10
I-20	Pellet	93	88	A	8[c,d]
I-21	Pellet	86	81	A	8[c,d]
I-22	Sphere-Pac	98	81–83	A	8[c,d]
I-23	Pellet	93	88	A	8[d]
I-24	Pellet	86	81	A	8[d]
I-25	Sphere-Pac	98	81–83	A	8[d]

[a]Each rod to contain a 13.5-in. fuel column with an insulator pellet at each end. The fuel cladding to be 0.250-in. OD × 0.016-in.-thick tube of type 304 stainless steel modified by the addition of titanium. The fuel pin is to be wire wrapped and immersed in sodium in the secondary capsule containment.

[b]The approximate oxygen-to-metal ratios will be: A = 1.980 ± 0.005; B = 1.940 ± 0.005.

[c]These rods subsequently will be tested in TREAT.

[d]These rods will be installed in the EBR-II spaces vacated by the 2% FIMA burnup rods.

8. ZIRCONIUM METALLURGY

P. L. Rittenhouse

The present generation of nuclear reactors makes use of a number of zirconium alloys as fuel cladding, pressure tubes, and channels. Although these alloys have relatively low neutron cross sections, there is continuing pressure to reduce the mass of all nonfissionable material associated with the reactor core. We hope, by controlling the texture of zirconium alloy tubing and, thereby, its anisotropy of properties, to permit the use of thinner tubes and cladding. This will be done without loss in safety factor and will result in more economic nuclear power.

Tubing Test Program

P. L. Rittenhouse

Biaxial testing at a tangential-to-axial stress ratio of 2 has been completed for all lots of Zircaloy tubing but the data have not as yet been analyzed. Tests are now proceeding at a stress ratio of 1/2. All tests of the material on hand should be completed before the end of FY-1968. The external pressure system will then be used to perform experiments in the compression-compression quadrant of the yield surface (stress ratios from -1 to $-\infty$). Other materials will be tested when received.

Correlation of Texture with Properties

E. Tenckhoff P. L. Rittenhouse

In our overall program of texture control of Zircaloy tubing it is necessary that we correlate crystallographic texture with uniaxial and biaxial mechanical properties. Also, polarized light examination of this tubing shows that texture gradients often exist across the wall thickness. Techniques are now being developed to allow us to measure these textures by x-ray diffraction.

Reflection measurements with our texture goniometer require a flat surface about 0.4 × 0.4 in. This can be obtained by thinning to 1 to 2 mils and then bending these foils elastically. A comparison of different preparation methods has led to the following technique. First, the tubes are machined in such a manner that a 10-mil ring containing material from the outer, inner, or center section of the tube wall is obtained. This, then, is thinned to 2 mils or less by chemical machining. The textures measured on these foils will be representative of material 3 to 4 mils under the outer surface or the inner surface and the center of the tube wall.

The specimens for 15 lots of tubing are prepared, and experiments have begun.

Tubing Fabrication Study

T. M. Nilsson P. L. Rittenhouse

The scope and objectives of this study have been described previously.[1] During this quarter we have planned the fabrication schedules in detail and have begun fabrication. A forged 4-in.-diam billet of Zircaloy-4 was machined into eight tube shells 3.9-in. OD × 1.0-in. ID. These shells were extruded (Materials Processing Group of the Metals and Ceramics Division) into tubes 1.5-in. OD × 1-in. ID. The material was heated in a neutral salt bath (E. F. Houghtons Liquid Heat 980) at 1450°F prior to extrusion. The layer of molten salt adhering to the surface functioned as the extrusion lubricant. About 75 ft of extruded tubes was produced.

Sixty feet of these tubes has been shipped to Wah Chang Corporation, Albany, Oregon, for tube reduction (rocking). Part of this material will be taken to the final desired size, 0.59-in. OD × 0.52-in. ID, by several combinations of reduction and reduction ratio. The effect of reversibility (reversing the lead end of the tube on successive passes) will also be studied. Some of the schedules will be repeated to estimate the

[1] P. L. Rittenhouse, Fuels and Materials Development Program Quart. Progr. Rept. Dec. 31, 1967, ORNL-TM-2090, pp. 169–171.

reproducibility of texture development. The remainder of the tubes will be reduced to intermediate sizes to furnish starting material for drawing experiments.

To establish techniques for cold drawing at ORNL we have performed several experiments. Annealed Zircaloy-4 tubes 0.86-in. OD × 0.73-in. ID were used in all cases. The tubes were first pickled in a nitric-fluoric acid bath and then coated in a sodium-phosphate solution. The drawing lubricant was G. Whitfield Richards 31-S diluted with 10-30 Texaco oil. After lubrication the tubes were drawn through tungsten carbide dies using stationary mandrel rods. The tubes were cold worked up to 55% with no intermediate anneals and no cracking was apparent. The maximum reduction per pass was 15%. After about 40% cold work the tubes began to deform unevenly. Because of this, all material processed in the future will be annealed after each 30% cold work.

An important factor in obtaining tubes with a satisfactory surface is the condition of the coating used as the lubricant base. It will be necessary to renew the coating after each pass. Therefore, a closed pickling and coating tank has been designed and built to handle 7-ft lengths of tubing. A special tank is necessary because large amounts of acid fumes are evolved during the pickling.

Circumferential Texture Variations in Zircaloy Tubing

D. O. Hobson P. L. Rittenhouse

We are continuing our investigation into the cause of texture variations in fabricated tubing. A new x-ray device was designed to aid in the analysis of circumferential texture variations in tubing. Plots of intensity variation versus tube rotation were shown in a previous report of this series.[2] These data were for a single circumferential scan of the tubing surface and gave no indication of the texture variation down the length of the tubing. The new device is capable of both rotating and translating the tube so that the x-ray scan covers the surface of the tube.

[2]P. L. Rittenhouse and D. O. Hobson, Fuels and Materials Development Program Quart. Progr. Rept. Sept. 30, 1967, ORNL-TM-2020, pp. 85–89.

Figure 8.1 illustrates a typical plot of data obtained with this device. Tube rotation is plotted on the abscissa and length down the tube on the ordinate. The contour lines represent reflected intensity of basal planes parallel to the surface of the tube. These data were taken from a tube that necked down to a square cross section in a uniaxial tensile test and can be compared to the data reported last quarter.[3] This device will be used in conjunction with standard pole figure techniques in studying tubing texture variations.

Texture Development in Single-Crystal Zirconium

D. O. Hobson

This is a continuation of work reported earlier[4] in which the effects of specific fabrication operations on various orientations of single crystals were studied. We found that the crystals responded predictably and formed the final stable textures that were expected. The next step is to apply these findings to polycrystalline material. A reasonable assumption to make is that each grain in a polycrystalline matrix behaves as if it were a single crystal and deforms according to its immediately surrounding stress field. The problem is to determine or calculate the stress field surrounding a grain within a matrix of other grains. This field will depend upon the stress-transmitting characteristics of the surrounding grains and, in turn, upon the deformation systems that operate in each grain. The Schmid factor calculations discussed previously[5] gave an indication of the operative systems in a biaxial rolling situation. The data, unfortunately, were not amenable to unambiguous plotting. R. O. Williams[6] has developed a method for

---

[3]P. L. Rittenhouse and D. O. Hobson, Fuels and Materials Development Program Quart. Progr. Rept. Sept. 30, 1967, ORNL-TM-2020, Fig. 6.2, p. 86.

[4]D. O. Hobson, Fuels and Materials Development Program Quart. Progr. Rept. Dec. 31, 1967, ORNL-TM-2090, pp. 174–177.

[5]D. O. Hobson, Fuels and Materials Development Program Quart. Progr. Rept. Sept. 30, 1967, ORNL-TM-2020, pp. 89–92.

[6]Group Leader, Deformation of Crystalline Solids Group, Metals and Ceramics Division.

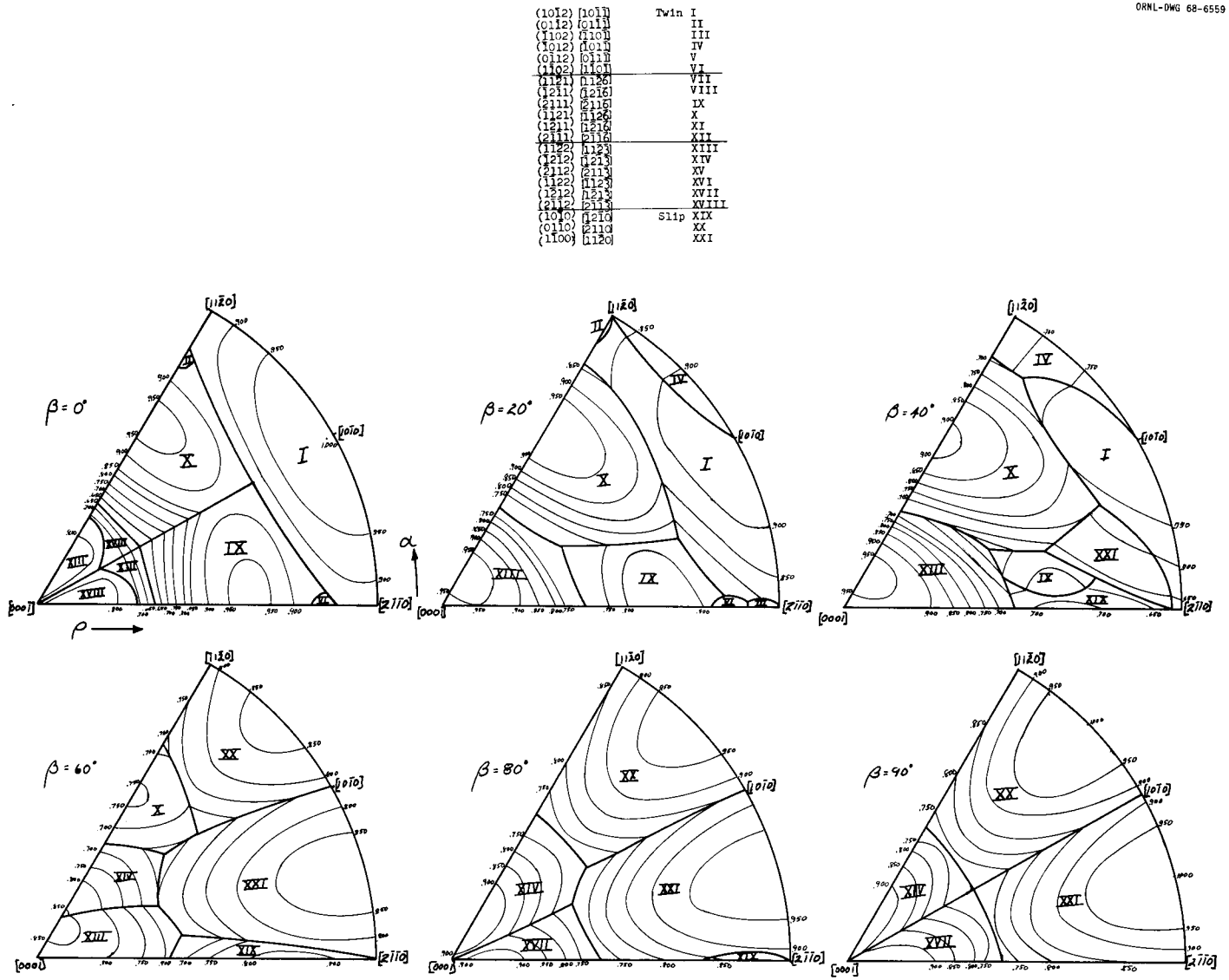

Fig. 8.1. Circumferential Texture Variation of the (0002) Plane in the Surface of a Zircaloy Tube.

plotting biaxial texture data that can be used to plot the Schmid factor data.[7] He has also developed a computer program for recalculating the data to make them easier to plot. The plotting procedure consists of locating the compressive stress which lies parallel to the rolling plane normal, σ_N, within a standard $[11\bar{2}0]$-$[0001]$-$[2\bar{1}\bar{1}0]$ triangle and locating the tensile stress which lies in the rolling direction, σ_R, by means of the angle β measured counterclockwise from the equator around σ_N. Figure 8.2 shows the coordinate system used and Fig. 8.3 illustrates representative biaxial Schmid factor plots for zirconium, where the angle β is represented as 20° increments between successive triangles. Each triangle is divided into regions that show the operative deformation system for any orientation of the stress axes. Although these data are accurate geometrically, they do not correspond exactly to the actual situation during deformation of a grain or a crystal.

[7] R. O. Williams, "The Representation of the Textures of Rolled Copper, Brass, and Aluminum by Biaxial Pole Figures," Trans. Met. Soc. AIME 242, 105–115 (January 1968).

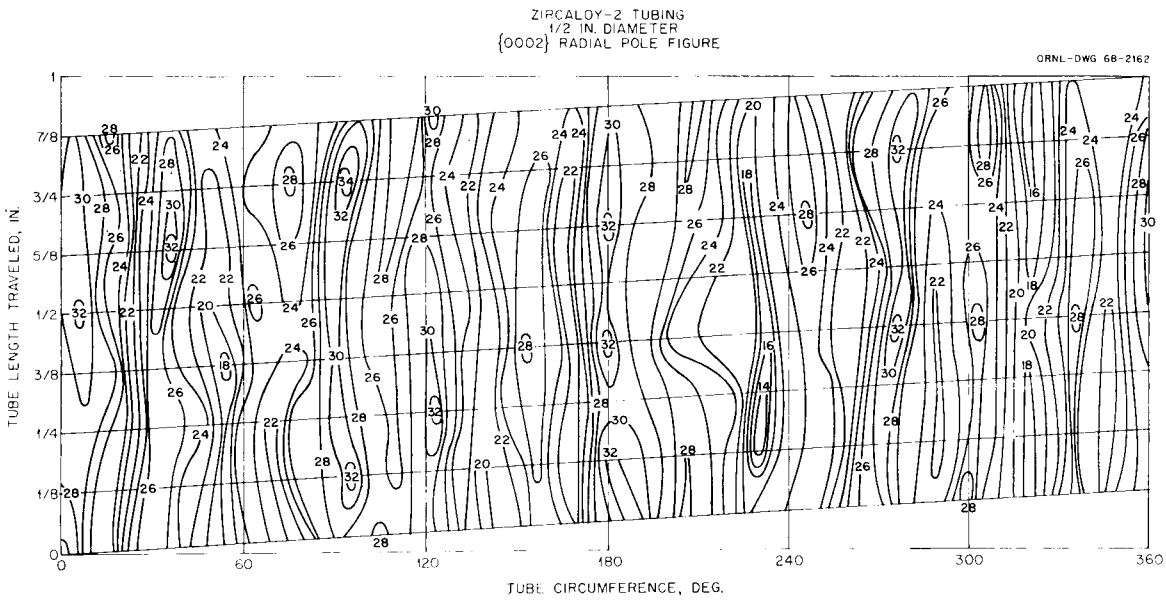

Fig. 8.2. Coordinate System for the Biaxial Plot of the Schmid Factors for Zirconium.

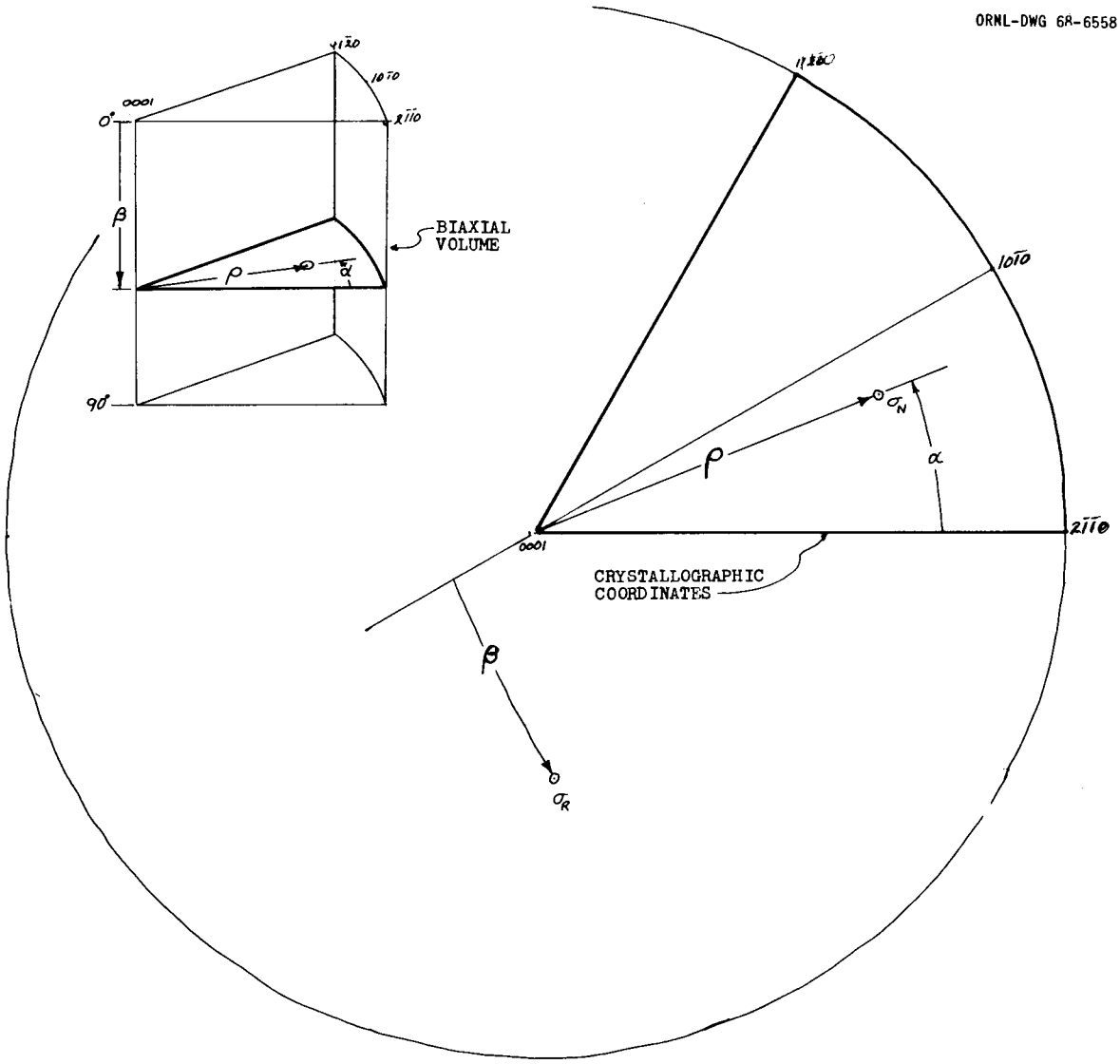

Fig. 8.3. Biaxial Schmid Factor Plot for Zirconium.

Slip is much easier to initiate than twinning (slip has a lower critical resolved shear stress) and, therefore, the regions in which slip is favored would be larger than shown and would encroach into the adjacent deformation regions. The plot is of great usefulness, however, in that it shows the geometrical relationships among the four deformation modes in zirconium and allows the approximate prediction of the operative systems in an actual rolling situation. This will help in attempting to analyze the polycrystalline rolling situation. The plot

is also useful as a tool for studies of critical resolved shear stress (CRSS) for twinning. A series of specimens biaxially tested in orientations that span the sets of boundaries between slip, whose CRSS is known, and twinning, with unknown CRSS, should enable the determination of the CRSS for twinning. An analogous plot could be made for the uniaxial stiuation. To the author's knowledge Schmid factor data have never been represented in the manner described above for either the biaxial or the uniaxial situation.

Deformation of Zirconium at Elevated Temperatures

E. Tenckhoff

The rolling texture of zirconium has a spread of the basal poles in the transverse direction. This texture sharpens and stabilizes with increasing deformation.[8] The formation of this texture cannot be explained on the basis of prism slip alone, although a sequence of several twinning operations does give an explanation. This, however, has been proven only at room temperature.

As rolling of zirconium is done at elevated temperatures, it seems both reasonable and necessary to look at its deformation system at elevated temperatures (up to 850°C). In this field very little work has been done. We know that at higher temperatures, especially above 500°C, twinning is reduced, kinking develops, and new slip systems are more likely as the critical resolved shear stress is lowered.[8–10] Possibly we can find here an easier explanation for the texture development of zirconium.

---

[8]M. L. Picklesimer, "Deformation, Creep, and Fracture in Alpha-Zirconium Alloys," Electrochem. Technol. 4, 289 (1966).

[9]R. E. Reed-Hill, "Role of Deformation Twinning in the Plastic Deformation of a Polycrystalline Anisotropic Metal," pp. 295–330 in Deformation Twinning, Gordon and Breach, New York, 1964.

[10]A. Seeger, Moderne Probleme der Metallphysik, Vol. 1, Springer-Verlag, Berlin, 1965.

Single crystals of zirconium will be stressed by pure shear in defined planes and directions. A shear specimen similar to that used by Parker and Washburn[11] fulfills our requirements as well as possible. The deformation experiments will be undertaken in vacuum.

---

[11]E. R. Parker and J. Washburn, "Deformation of Single Crystals," p. 186 in Modern Research Techniques in Physical Metallurgy, American Society for Metals, Metals Park, Ohio, 1953.

[redacted]

Part II

REACTOR CHEMISTRY DIVISION

[redacted]

FISSION-GAS RELEASE AND PHYSICAL PROPERTIES OF FUEL MATERIALS DURING IRRADIATION

R. M. Carroll
G. M. Watson
R. B. Perez
J. G. Morgan
O. Sisman

High Burnup Studies

Details of the 48%-enriched single-crystal UO_2 specimens were given in the preceding report.[1] In brief, an enriched UO_2 crystal was sliced into cubes and then ground into spheres, 0.0997 cm in diameter. We placed 36 of these spheres into a tungsten holder so that they formed a hollow cylinder of 12 spheres in circumference and 3 spheres deep (Fig. 1).

It was necessary to keep the specimens small to prevent thermal-stress cracking. We then needed at least 36 specimens to give sufficient volume for good temperature measurements. The small specimens released a great deal of fission gas so that we were unable to operate at temperatures in excess of 1300°C because of the radioactivity limitations of the experiment.

The specimens are still in the reactor but are scheduled to be removed soon; a total burnup of about 4.7% U will have been achieved. The data are still in the process of evaluation. Swelling measurements will be made in postirradiation examination of the fuel, and these will help in the interpretation of the gas-release data. Our preliminary evaluation is given below.

The Effect of Fission Density on Fission-Gas Release

It has often been assumed that the fractional fission-gas release, release rate to birth rate (R/B), from UO_2 is not affected by fission density. This assumption is based on the premise that either a diffusion or a coupled diffusion-trapping process controls the gas release and neither process is changed by fission density (fission cm^{-3} sec^{-1}).

---

[1] Fuels and Materials Development Program Quart. Progr. Rept. Dec. 31, 1967, ORNL-TM-2090, pp. 184–187.

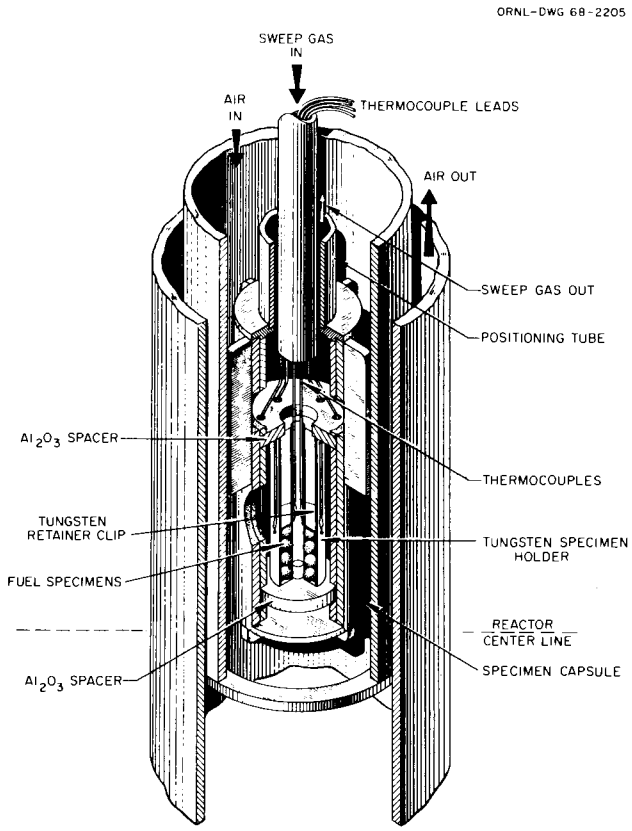

Fig. 1. Schematic of Capsule

In our early work we found that an increase of fission density will cause the fractional release to decrease when the UO_2 temperature remains constant.[2] This observation led us to postulate a defect-trap model wherein the gas was released by a coupled diffusion-trapping process where the equilibrium number of defect traps was a function of the fission density and the temperature.[3,4] It is clear that the fission-generated traps will have little effect at low fission densities in comparison to the natural traps (such as grain boundaries). Also, at very high fission densities the fission tracks will annihilate traps created by previous fissions.[2]

---

[2]R. M. Carroll and O. Sisman, "In-Pile Fission-Gas Release from Single-Crystal UO_2," Nucl. Sci. Eng. 21, 147 (1965).

[3]R. M. Carroll and O. Sisman, "Fission-Gas Release During Fissioning in UO_2," Nucl. Appl. 2(2), 142 (1966).

[4]R. B. Perez, "A Dynamic Method for In-Pile Fission-Gas Release Studies," Nucl. Appl. 2(2), 151 (1966).

These earlier experiments were performed in the range of fission densities from 1.8 to 9.0×10^{12} fissions cm^{-3} sec^{-1}. Within this range an increase of fission density lowered the fractional fission-gas release. Work by Soulhier, where fission densities were in the range 1.8 to 3.8×10^{11} fissions cm^{-3} sec^{-1}, showed no change of fractional fission-gas escape with a change of fission density.[5] He suggested that our different results could be explained by the different fission densities.

The experiments with the single-crystal spheres of enriched UO_2 allowed us to obtain much higher fission densities. At the higher fission densities we find that the fission-gas release is accelerated (rather than retarded) as the fission density is increased.

Using the data reported by Soulhier and our own data, we have constructed the fractional release rate versus density relation shown in Fig. 2. The initial flat portion of the curve shows that the effects

---

[5]R. Soulhier, "Fission-Gas Release from UO_2 During Irradiation Up to 2000°C," Nucl. Appl. 2(2), 138 (1966).

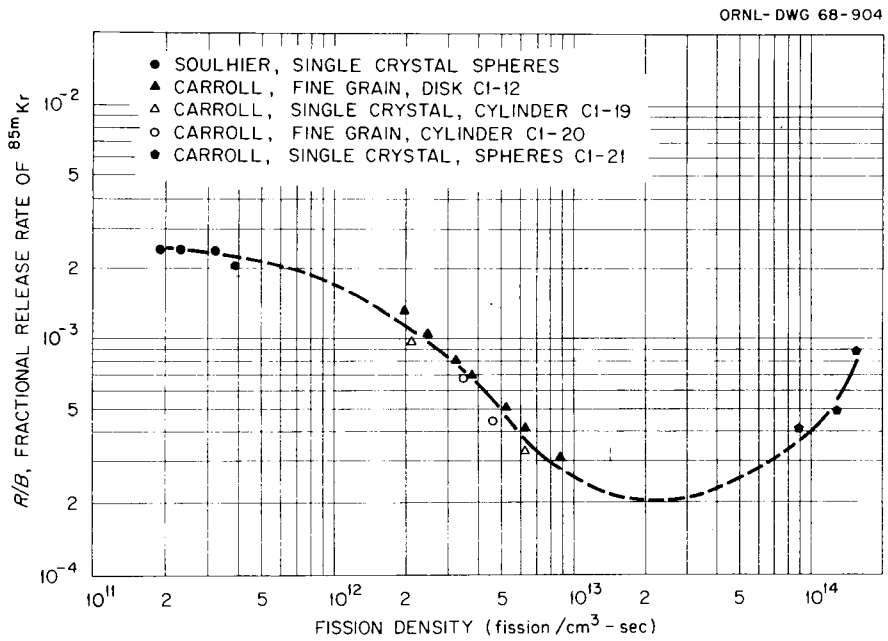

Fig. 2. Fractional Release of ^{85m}Kr from High-Density Stoichiometric UO_2 During Irradiation at 1400°C.

of fission-created traps are insignificant at fission densities of less than 3×10^{11} fissions cm^{-3} sec^{-1}. The next data points begin at 2×10^{12} fissions cm^{-3} sec^{-1} and the effect of fission density obviously becomes significant at some intermediate point. In this range the fractional fission-gas release decreases smoothly as fission density increases to a fission density of 9×10^{12} fissions cm^{-3} sec^{-1}, our highest point using natural enrichment UO_2. Using enriched specimens we obtained an order of magnitude higher fission density, starting at 9×10^{13} fissions cm^{-3} sec^{-1}. At this level the fission-created traps became less effective, and an increase of fission rate increased the fractional release. We have no data for the dashed portion of the curve, but it is likely that the minimum fractional fission-gas release would be around 2×10^{13} fissions cm^{-3} sec^{-1} fission density.

All the data shown in Fig. 2 are for specimens being irradiated at 1400°C. For our single-crystal spheres, we extrapolated from 1300°C, knowing the temperature dependence of the gas release. Another factor influencing the fractional gas release is the surface-to-volume ratio of the specimen. All the data were normalized to the same geometric surface-to-volume ratio as Soulhier's single-crystal sphere specimens, which by coincidence had the same surface-to-volume ratio as our fine-grain disk specimens, 23 cm^{-1}. All specimens were stoichiometric UO_2 of high density (> 99% of theoretical) except specimen C1-20 which was 98.4% of theoretical density; see Fig. 2.

Most of the UO_2-fueled, water-cooled power reactors operate in the fission density region where the fractional fission-gas release rate is decreasing or constant with an increase of fission rate; for example, Dresden approximately 6.5×10^{12} fissions cm^{-3} sec^{-1}; Yankee approximately 1.5×10^{13} fissions cm^{-3} sec^{-1}. However, some gas-cooled and fast sodium-cooled reactors are planned to operate in the fission density range above 2×10^{13} fissions cm^{-3} sec^{-1}, where the fractional release will increase with higher fission densities. Any reactor design using oxide fuels operating in the 10^{14} fissions cm^{-3} sec^{-1} range should consider that the fission-gas release rate will be accelerated as the fission density is increased.

Effect of Burnup on Fission-Gas Release

As with most of our previous specimens, the fission-gas release rate decreased during the initial portion of the irradiation. We think this decrease of gas-release rate is because the surface of the specimen is smoothed and possibly recrystallized by surface fissions.

The gas release did not increase with burnup until after 1.9% U burnup. At that time the gas-release rate increased smoothly. The increased rate did not appear to be caused by the specimen breaking, since this causes a step increase of gas release.

The reactor was shut down for a week just after the increase of release rate occurred at 1.9% U burnup. After the startup, the specimen was operated at low temperatures and fission rates to obtain surface-fission release data. At the start of the low-temperature irradiation, the fission-gas release was characterized by small spontaneous pips superimposed on the steady-state release.

We have seen this type release pattern when UO_2 specimens were irradiated at temperatures above 1600°C. We believe that when the gas is mobile enough at high temperatures it can form bubbles just beneath the surface of the specimen. The bursting of these bubbles can cause the pips.

The low-temperature pips of gas release cannot be explained in this way. Possibly the single-crystal specimen became strained enough by the 1.9% burnup to develop small cracks. Or possibly, the higher fission density allowed the fuel matrix to become sufficiently mobile to allow the formation of the bubbles before the reactor shutdown. Postirradiation examination will resolve this point.

The increase of gas-release rate would be expected to occur at a higher burnup than 1.9%. However, these were small single-crystal specimens which did not contain much internal void space to store fission products. When the specimen was again operated at higher fission densities and temperatures, the gas release was much higher than before the low-temperature runs.

The effect of burnup on fission-gas release to date is shown in Fig. 3. The irradiation has almost been completed so we do not expect

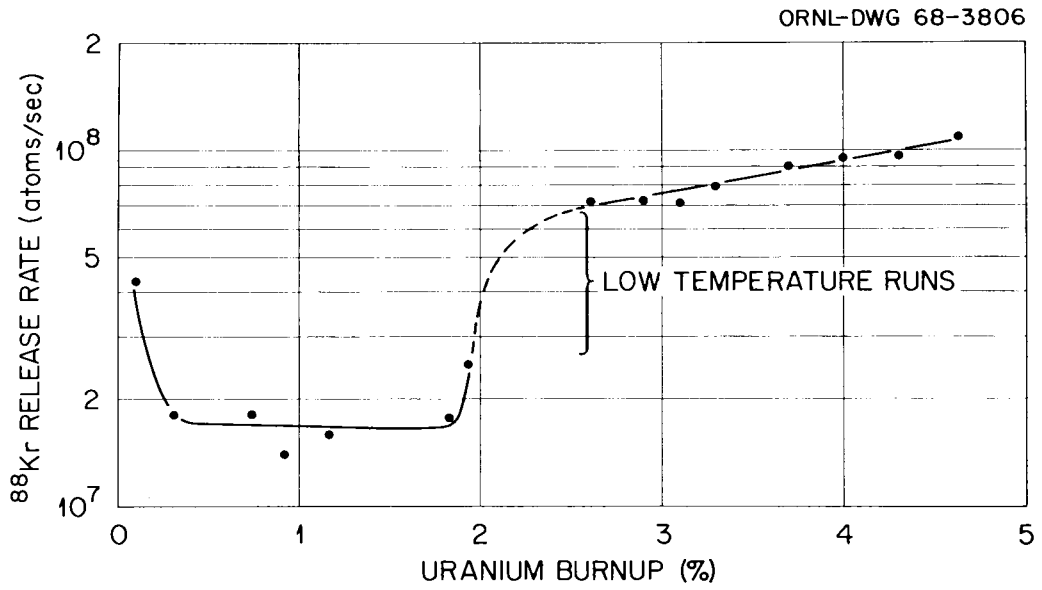

Fig. 3. Krypton-88 Release from Single-Crystal UO_2, Normalized to 820°C and 1.5×10^{14} fissions cm^{-3} sec^{-1} as a Function of Uranium Burnup.

the additional data to change the pattern of Fig. 3. To make Fig. 3, the measured data were corrected for the effects of fission density (see Fig. 2) and temperature. The data were normalized to a temperature of 820°C and a fission density of 1.5×10^{14} fissions cm^{-3} sec^{-1}.

Thermal Conductivity During Irradiation

We have constructed an experiment to determine the amount of heating from gamma-ray and neutron absorption in comparison to fission heating in the C-1 position of the ORR Reactor. This knowledge is necessary to obtain accurate thermal diffusivity measurements on fuel materials.

The capsule assembly consists of a cylinder of pure copper suspended within a brass holder. The experimental method will be to move the specimen or change the air-cooling rate and then measure the time dependence of the temperature changes to determine the amount of heat being generated in the copper cylinder. By using argon activation techniques, we will be able to measure the nonnuclear heating and the neutron flux simultaneously.

[redacted]

Part III

SOLID STATE DIVISION

[redacted]

RADIATION METALLURGY

D. S. Billington and M. S. Wechsler

INTRODUCTION - M. S. Wechsler

The Radiation Metallurgy Section is studying radiation damage, hardening, and embrittlement in the body-centered cubic metals. Despite a fairly large body of research results,[1] many important aspects of these phenomena are not well understood. For example, although the hardening and embrittlement are known to be due to radiation-produced defect clusters, the structure and size range of clusters most effective in increasing the strength and decreasing the ductility of metals have not been determined. While the questions of defect clusters and their effect on plastic deformation and fracture may seem to some to be only of academic interest, they are at the core of the problem of the radiation embrittlement of reactor pressure vessel steels.[2] The failure of a reactor pressure vessel could have catastrophic consequences to the public safety, and letters[3,4] from the Advisory Committee on Reactor

---

[1] M. S. Wechsler, "Radiation Embrittlement of Metals and Alloys," in The Interaction of Radiation with Solids, edited by R. Strumane et al., North Holland Publishing Co., Amsterdam, 1964, 296-345.

[2] M. S. Wechsler, "Radiation Damage to Pressure Vessel Steels," Nucl. Safety, 8, 461, (1967).

[3] J. P. Blakely, "ACRS Comments on Reactor-Safety Research," Nucl. Safety, 8, 277, (1967).

[4] "Text of ACRS Letter to AEC," Nucleonics, 24, 17, (1966).

Safeguards to the Chairman of the Atomic Energy Commission have emphasized the advisability of certain research and development programs to develop pertinent information. The program of the Radiation Metallurgy Section[5] is based on the premise that an assessment of the danger to reactor systems by virtue of the radiation embrittlement of structural metals and the ability to minimize this danger in the future are aided by a better understanding of the nature of the phenomenon itself. This requires a broad investigation that embraces fundamental and applied aspects of the problem.

The principal metals under investigation are pressure vessel steels, iron and iron alloys, niobium, and vanadium. As is characteristic of body-centered cubic metals, these metals exhibit a ductile-brittle transition and the ductile-brittle transition temperature (DBTT) is increased upon irradiation. The question arises as to whether this radiation embrittlement is chiefly a consequence of the radiation hardening or whether a change in the cleavage stress required to initiate a running cleavage crack is also important. To test this point for the pressure vessel steels we are conducting tensile and impact tests on samples from the same heat of steel irradiated under identical conditions. The results described below suggest that the increase in the DBTT can be correlated with the intersection of the yield curve (lower yield stress vs test temperature) and a critical cleavage stress.

---

[5]M. S. Wechsler, The Program of the Radiation Metallurgy Section, Solid State Division, Oak Ridge National Laboratory, ORNL-TM-2059, (1968).

The correlation does not require a decrease in the critical cleavage stress upon irradiation. However, it is necessary to assume that the degree of stress triaxiality at the point of cleavage fracture initiation is reduced in the irradiated steel.

The annealing characteristics of irradiated steel are also described below. The shape of the stress-strain curve (e.g., whether a yield drop is observed or not) is shown to depend on whether a short time-low temperature or a long time-high temperature annealing treatment is applied. This observation suggests that the annealing process occurs in several stages, and we deduce from the changes in the shape of the stress-strain curve during annealing that rearrangements in the distribution of interstitial elements are involved. Interstitial elements are also responsible for strain-aging effects, and thus, it was of interest to investigate the effect of neutron irradiation on strain aging in these steels. The results described below indicate that the strain aging is reduced after irradiation, probably due to the trapping of carbon and nitrogen at radiation-produced defect clusters.

One of the ACRS letters[3] commented on the importance of research into thick-section and higher-strength steels and a Heavy Section Steel Technology Program[6] is underway with the purpose of evaluating the application of such steels to nuclear pressure vessels. Under this program, some initial results have been obtained on samples from a 12-inch-thick plate of ASTM A-533-B steel.

---

[6] F. J. Witt, Heavy Section Steel Technology Program Progress Report, ORNL-4176, (1968).

The notion of trapping of interstitial elements in irradiated BCC metals has received support from measurements of internal friction and electrical resistivity in irradiated niobium. The internal friction measurements are especially helpful since they are selective, i.e., from the frequency and temperature at which the internal friction is observed, one can deduce the amount of a particular interstitial element in solid solution. In this way, a fairly unambiguous determination was made of the trapping at about 150°C of oxygen in neutron-irradiated niobium.[7] In this report, additional experiments are described in which the annealing was taken to higher temperatures at which the oxygen becomes dissociated from the traps and returns again to solid solution.

Vanadium is chemically similar to niobium and the trapping of interstitial elements at radiation-produced defects is also being investigated for this BCC metal. The results to date indicate that oxygen and nitrogen are trapped at temperatures between 150°C and 300°C, but the temperature range for the dissociation of the interstitials from defect traps has not yet been determined.

We have mentioned that the structure and size of the defect clusters that are critical to the radiation hardening have not yet been established. To help clarify this matter, an investigation is underway into the correlation between the size distribution of clusters in niobium observed by transmission electron microscopy and the changes in yield

---

[7] J. M. Williams, W. E. Brundage, and J. T. Stanley, "The Effect of Oxygen on 'Stage III' Annealing in Neutron-Irradiated Niobium," to be published in Metals Science Journal.

stress upon irradiation and upon post-irradiation annealing. The observed initial increase in yield stress upon irradiation is found to be consistent with a hardening model in which the radiation-produced defect clusters observed in the electron microscope are the hardening agents. However, the further increase in yield stress upon annealing cannot be accounted for by the size distribution of defect clusters and, therefore, it is suggested that interstitial carbon atoms migrate to the clusters and form even stronger barriers to dislocation motion. Also, the fluence dependence of the hardening indicates that the rate of hardening decreases with increasing fluence more rapidly than would be predicted by a dispersed barrier model. This "saturation effect" has been observed for other metals and remains one of the difficult questions in the understanding of radiation hardening.

The effect of radiation on the temperature dependence of yielding has been presented earlier for tensile tests on single crystals of niobium oriented for {110} <111> slip.[8] In the present report, compression tests are reported for irradiated single crystals of the same orientation but somewhat higher purity. The irradiation appears to have introduced more temperature dependence for the higher purity samples, but this point needs further confirmation.

Finally, several aspects of our work on the preparation and evaluation of niobium sample material are described below.

---

[8] S. M. Ohr, R. P. Tucker, and M. S. Wechsler, "Radiation Hardening in B.C.C. Metals Niobium and Iron," in Proceedings of the International Conference on Strength of Metals and Alloys, Japan Inst. of Metals, (1968).

The Temperature Dependence of Yielding in an Irradiated Pressure-Vessel Steel and the Relationship Between Radiation Hardening and Embrittlement

M. S. Wechsler, N. E. Hinkle, R. G. Berggren, and W. J. Stelzman

Introduction

It is commonly recognized that yield and fracture in metals are intimately inter-related. Among other things, this is suggested by the fact that the ductile-brittle transition phenomenon is exhibited by the BCC metals which are the very materials that show strong temperature dependence of yielding. The exact nature of the relationship between flow and fracture is complicated by many material and testing variables. Nevertheless, a useful first approximation to the relationship was expressed over a quarter-century ago by the principles formulated by Mesnager, Ludwig, Davidenkov, and Wittman (cf. Orowan,[9] Tetelman and McEvily[10]). These principles, illustrated in Fig. 1, suggest that the ductile-brittle transition occurs at the temperature where the appropriate yield stress, σ_y, and fracture stress, σ_c, curves intersect. It is emphasized that σ_y and σ_c are quantities appropriate to the material and type of test. For example, for the ductile-brittle transition temperature (DBTT) obtained by Charpy V-notch impact tests on a pressure-vessel steel, the σ_y should refer to the yield stress under the actual conditions of strain rate and stress state of the impact test and the σ_c should be

---

[9] E. Orowan, "Classical and Dislocation Theories of Brittle Fracture," Fracture, Wiley, New York, 147, (1959).

[10] A. S. Tetleman and A. J. McEvily, Fracture of Structural Materials, John Wiley and Sons, New York, (1967).

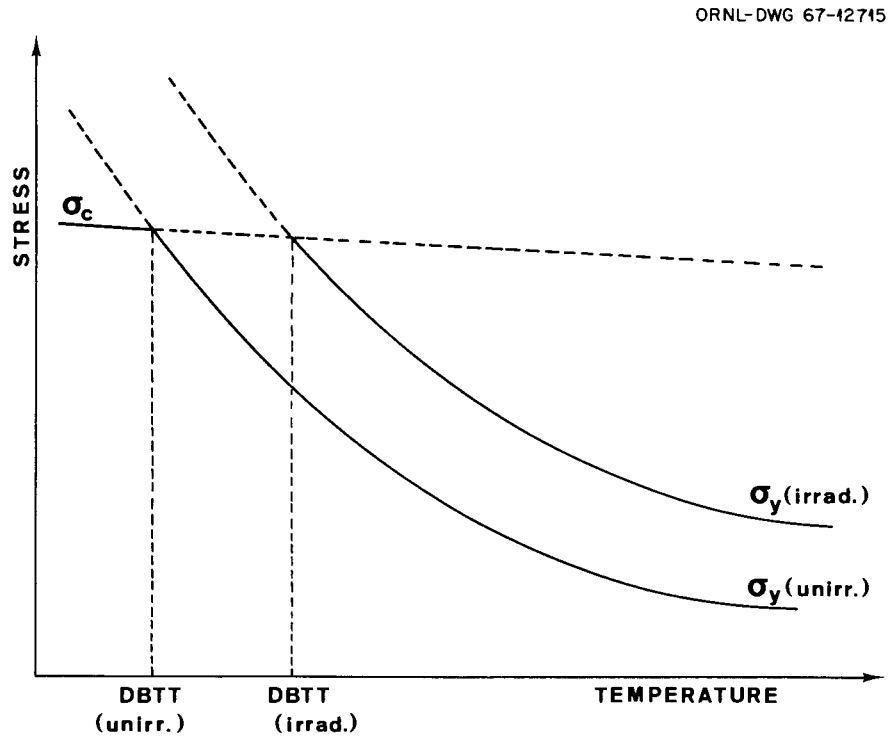

Fig. 1. Schematic Illustration of the Relationship Between the Increase Upon Irradiation of Yield Stress (σ_y) and Ductile-Brittle Transition Temperature (DBTT).

the effective cleavage fracture stress of the material, given all its eutectoid decomposition products, inclusions, and the like. Armstrong[11,12] has applied these ideas to the influence of grain size on the DBTT of steels and has expressed the DBTT analytically in terms of experimentally determined quantities. Also, Hendrickson, Wood, and Clark[13,14]

---

[11] R. W. Armstrong, "On Determining the Ductile-Brittle Transition Temperature," Phil. Mag., 9, 1063, (1964).

[12] R. W. Armstrong, "Stress-Grain Size Analysis of the Brittle Fracture Transition of Steel," ARPA E 38, February (1967).

[13] J. A. Hendrickson, D. S. Wood, and D. S. Clark, "The Initiation of Brittle Fracture in Mild Steel," Trans. ASM, 50, 656, (1958).

[14] J. A. Hendrickson, D. S. Wood, and D. S. Clark, "Prediction of Transition Temperature in a Notched Bar Impact Test," Trans. ASM, 51, 629, (1959).

have conducted notch-tensile and notch-impact tests on a mild steel as a function of test temperature and strain rate. Their results constitute an experimental verification of the concepts, since they found that a necessary and sufficient condition for the occurrence of brittle fracture was the attainment of a critical tensile stress, σ_c, before yielding occurred across the specimen.

This approach provides a useful clue to the understanding of the origin of radiation embrittlement. As is illustrated in Fig. 1, since the yield stress of irradiated metals is increased, the point of intersection between σ_y and σ_c is shifted upwards on the temperature scale, thus increasing the DBTT. The question arises as to whether the increase in σ_y is in itself sufficient to account for the ΔDBTT upon irradiation assuming no change in σ_c, or whether the σ_c is also changed in the irradiated material. In most discussions of the problem along these lines (cf. Armstrong,[11,12] Tetelman and McEvily[10]), σ_c is assumed to be rather independent of temperature and strain rate. Hendrickson, et al.[13,14] concluded from their experiments that σ_c is independent of temperature and strain rate, whereas Wilshaw and Pratt[15] observed some variation. However, little is known concerning the effect of radiation on σ_c. Based on criteria described below, we find a slight increase in σ_c upon irradiation.

A strict test of these ideas is difficult to make because of the necessity of doing tests as a function of temperature, strain rate, and

---

[15]T. R. Wilshaw and P. L. Pratt, "The Effect of Temperature and Strain-Rate on the Deformation and Fracture of Mild-Steel Charpy Samples," Proc. First International Conference on Fracture, 2, 973, (1966).

stress state on materials identical in every respect except the irradiation treatment. In this report, we describe an attempt to do this on unirradiated and irradiated ASTM A-212-B pressure-vessel steel on which tensile and impact tests were performed as a function of temperature and, to a limited extent, strain rate. The results are interpreted in terms of Fig. 1 on the assumption that σ_c is independent of temperature and strain rate. The observations suggest that the σ_c is increased slightly by the irradiation and the degree of triaxiality reached in the Charpy test at the point where cleavage is initiated is decreased slightly. When these changes are taken into consideration, the DBTT's for smooth tensile and notch impact tests are predicted reasonably well on the basis of the Mesnager-Ludwig-Davidenkov-Wittman approach.

Experimental Details

The material for this study was taken from the quarter thickness plane of a 2 3/4 inch plate of ASTM A-212-B pressure vessel steel. This plate, originally fabricated for the EGCR pressure vessel, was rolled from an aluminum-treated heat of steel melted according to fine-grain practice. The mill chemical analysis and specifications are given in Table 1. The plate was normalized at about 900°C (1650°F), water-spray cooled to 260°C (500°F), and stress relieved at 650-680°C (1200-1250°F). The ferrite grain diameter was about 20 micron (ASTM grain size No. 9).

The tensile samples were machined to a gage length of 1.25 inch and a gage diameter of 0.177 inch. The tensile tests were performed on an Instron testing machine. The tensile samples were held in slotted-type grips with the load exerted on the smooth fillets at the ends of

TABLE I

Mill Report on ASTM A-212 Grade B Steel Plate

SSD Item No.	157
Heat No.	A-2056
Thickness	2 3/4 in.
Carbon	0.27%
Maganese	0.70%
Phosphorus	0.012%
Sulphur	0.032%
Silicon	0.20%
Yield Strength	45,200 psi
Ultimate Tensile Strength	75,900 psi
Elongation in 2"	28%

the gage length. The test temperatures from room temperature to 77°K (-196°C) were obtained by spraying liquid nitrogen or cold nitrogen gas uniformly over the sample, grips, and pull rods. The low temperature tensile apparatus used in this study was an adaptation of the system used by Spreadborough, et al.[16] The test chamber consisted of a series of small diameter tubes arranged parallel to and equally spaced around the pull rods, and a styrofoam insulating shell around the spray tubes. Each tube had small holes drilled through the surface facing the pull rods such that nitrogen forced through the tubes was sprayed toward the pull rods. Below 77°K, liquid helium was forced through a vacuum insulated tube and sprayed over the sample after precooling the assembly to 77°K. Temperatures above room temperature were obtained by placing

[16] J. Spreadborough, et al, "The Effect of Radiation on the Ductile-Brittle Transition in Pressure Vessel Steels," Final Report EUR-2354E, EURAC 1394, (1965).

a ceramic clam-shell furnace insert around the sample and grips. Temperatures were measured with copper-constantan thermocouples attached to the sample and the grips. The thermocouples were calibrated at liquid nitrogen and liquid helium temperatures. National Bureau of Standards tables of emf vs. temperature were used for temperatures above 77°K. Below 77°K, a computed table of emf vs. temperature compiled by Adams and Davisson[17] was used.

The impact samples were prepared from the same heat of steel as the tensile samples (Table 1) and conformed to ASTM specifications for standard Charpy V-notch impact tests. The impact machine was equipped with a temperature conditioning chamber containing carbon electrodes for resistance heating, a liquid nitrogen line for cooling, and a spring-loaded contact thermocouple for temperature measurement. The samples were transferred from the chamber to the test position by a pneumatic cylinder and located in test position by three pneumatic cylinders. Interlocks prevented dropping of the pendulum hammer until transfer and locating devices were retracted. The elapsed time from time of removal from the temperature chamber to the time of impact was less than three seconds.

The irradiations were performed at the poolside facility of the Oak Ridge Research Reactor where the fluence rate was (2-3) x 10^{12} n/cm^2·sec (E > 1 Mev). The tensile and impact samples were irradiated at 60°C to fluences of 10 and 9.8 x 10^{18} neutrons/cm^2 (E > 1 Mev), respectively.

---

[17] R. K. Adams and E. G. Davisson, "Smoothed Thermocouple Tables of Extended Significance (°C)," 2, Section 2.11, Constantan Copper Cryogenic Thermocouples, ORNL-3649, 2, March (1965).

Results

A. Tensile Tests

The tensile samples were tested at two strain rates, 2.7×10^{-4} and 2.7×10^{-2} sec.$^{-1}$ At 2.7×10^{-4} sec^{-1} the testing temperatures covered the range from about 20°K to 473°K for the unirradiated samples. Fewer tests were conducted below 77°K for the irradiated samples, and the maximum temperature was 373°K. The irradiated samples exhibited the usual increase in yield stress, decrease in rate of work hardening, and decrease in uniform and fracture elongations, as is seen in Fig. 2 showing load-extension curves taken at 77, 133, and 299°K.

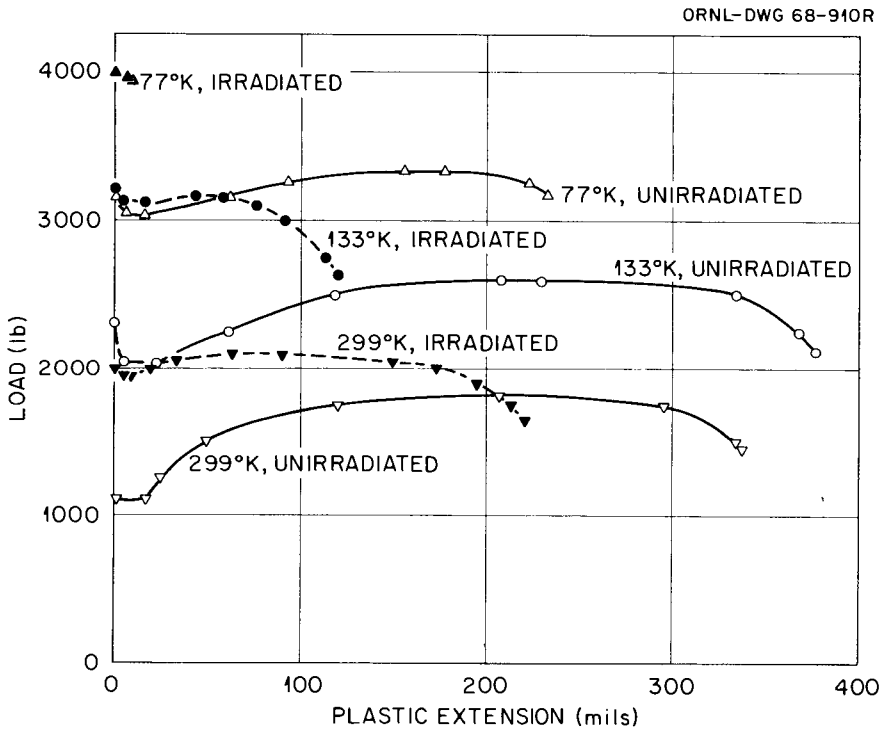

Fig. 2. Load-Extension Curves for Unirradiated and Irradiated ($\Phi = 1.0 \times 10^{19}$ n/cm^2, 60°C) A-212-B Steel Tested at 77, 133, and 299°K at Strain Rate of 2.7×10^{-4} sec^{-1}.

The effect of irradiation on the yield properties as a function of test temperature is shown in Fig. 3. With decreasing test temperature, the unirradiated yield stresses increase quite rapidly and the rate of work hardening decreases as is suggested by the approach of the UTS curve toward the LYS and UYS curves. The increase in yield stress upon irradiation to 1 x 10^{19} n/cm^2 (E > 1 Mev) is largely independent of temperature from 373°K to 60°K. This was also observed by Chow, McRickard, and Gurinsky[18] for A-212-B tensile samples irradiated to 2 x 10^{18} n/cm^2 (E > 1 Mev) and tested over a comparable range of temperatures and by Fearnehough[19] for a variety of notched steel bars irradiated to 10^{19} - 10^{20} n/cm^2 and tested down to about 190°K. The true fracture stress shows a sharp decrease at 70-80°K for the unirradiated steel, similar to that observed by Hahn, et al.[20] At this temperature they observed that the frequency of microcracks in the microstructure begins to rise. Thus, we may use the intersection of the fracture stress (FS) and lower yield stress (LYS) curves in Fig. 3 as a measure of the DBTT for uniaxial tension of smooth samples. This occurs at the intersection of arrows A and B giving 56°K for the DBTT under these conditions and 153 kpsi for the cleavage fracture stress, σ_c. At temperatures below about 60°K the lower yield is never reached, the sample

---

[18]J. G. Y. Chow, S. B. McRickard, and D. H. Gurinsky, "Mechanical Properties of Irradiated Iron and Iron Alloys," in Symposium on Radiation Effects on Metals and Neutron Dosimetry, ASTM-STP-341, American Society for Testing and Materials, Philadelphia, 46, (1963).

[19]G. D. Fearnehough, "The Strain Rate Sensitivity of the Yield Stress of Steels," in The Physical Basis of Yield and Fracture, Oxford, Institute of Physics and Physical Society, 88, (1966).

[20]G. T. Hahn, B. L. Averbach, W. S. Owen, and M. Cohen, "Initiation of Cleavage Microcracks in Polycrystalline Iron and Steel," in Fracture, Oxford, Institute of Physics and Physical Society, 91, (1966).

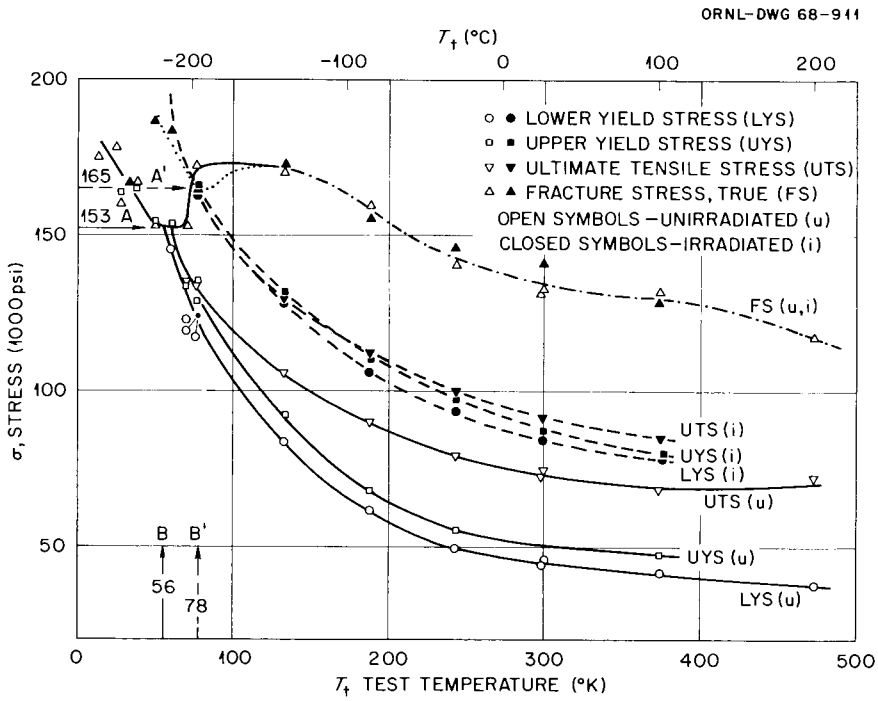

Fig. 3. Stress vs Test Temperature for Unirradiated and Irradiated (Φ = 1.0 x 10^{19} n/cm^2, 60°C) A-212-B Tested at Strain Rate of 2.7 x 10^{-4} sec^{-1}.

exhibiting brittle fracture at or slightly after the UYS is reached or even prior to reaching the upper yield point.

The FS for the irradiated material does not show the large decrease as the DBTT is approached, although fewer points are available to define its shape in the lower temperature region. However, as suggested in Fig. 3 it appears that the FS and LYS curves intersect at 78°K and 165 kpsi, thus defining the DBTT and σ_c corresponding to those discussed above. It is interesting that the FS curves for the unirradiated and irradiated steel do not appear to differ significantly at temperatures above the transition. However, Fig. 3 does show the reduced rate of work hardening in the irradiated material in that the UTS curve lies quite close to the curves for LYS and UYS.

Another measure of the transition from ductile to brittle behavior is the reduction of area (RA) at fracture. This is shown in Fig. 4 as a sharp drop near the DBTT. Extrapolating the RA curves to the abscissa, we can identify the DBTT's as 70°K and 81°K for the unirradiated and irradiated samples, respectively, in fair agreement with the temperatures 56 and 78°K determined in Fig. 3. Fig. 4 also shows that RA curves for unirradiated and irradiated conditions approach each other as the test temperature is increased.

The curves in Fig. 5 show the transition behavior of the uniform strain. For the unirradiated samples, the transition temperature is fairly well defined at 62°K, but the points for the irradiated samples are not as plentiful and we can only state that the irradiated transition is above 77°K and below about 130°K.

A number of authors have commented on the shape of the LYS curve as a function of test temperature. We find that an adequate fit to the observations is given by an equation of the form discussed by McKinsey, et al.,[21] namely,

$$\sigma = \sigma_o + \frac{B}{T_t} \qquad (1)$$

A least-squares fit to the LYS for unirradiated samples gives σ_o = 21.5 $\pm$ 2.2 kpsi and B + (7.5 $\pm$ 0.2) x 10^3 kpsi·deg K; the comparison with observed values is shown in Fig. 6. For the irradiated samples, the parameters in Eq. (1) were chosen in two ways: (1) for best general fit as for the unirradiated samples; this gives σ_o = 59.4 $\pm$ 3.7 kpsi and

---

[21] C. R. McKinsey, A. L. Mincher, W. F. Sheely, and J. L. Wilson, "Investigation of Tungsten-Tantalum-Columbium-Base Alloys," ASD Technical Report 61-3, July (1961).

B = (8.3 ± 0.5) x 10^3 kpsi·deg K, and (2) best fit assuming no change in the temperature dependence upon irradiation, i.e. assuming B = 7.5 x 10^3 kpsi·deg K as before; this gives σ_o = 64.0 kpsi. The curves for cases (1) and (2) are also plotted in Fig. 6. It would appear that B is increased slightly upon irradiation, but the increase is barely outside experimental error. This may be seen in Fig. 6 in that curves (1) and (2) appear to be almost equally good fits to the experimental points.

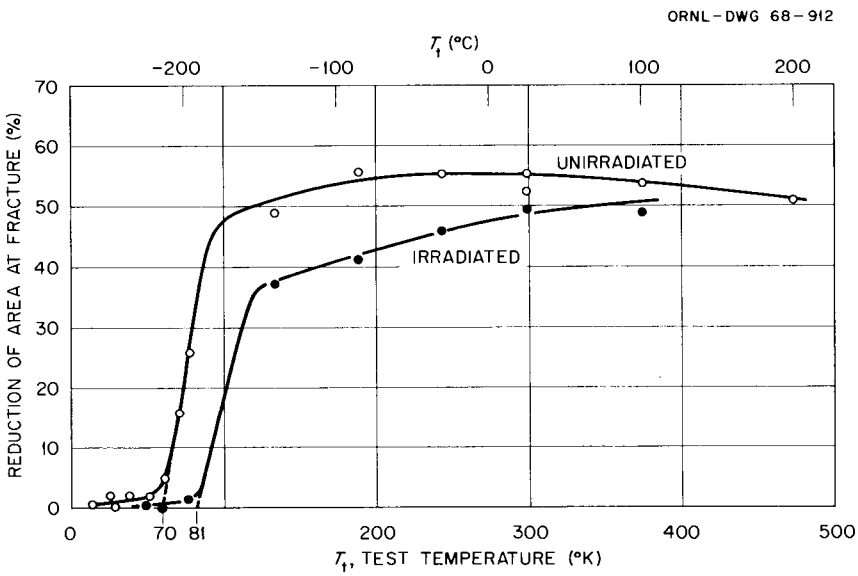

Fig. 4. Reduction of Area at Fracture vs Test Temperature for Unirradiated and Irradiated (Φ = 1.0 x 10^{19} n/cm^2, 60°C) A-212-B Steel Tested at Strain Rate of 2.7 x 10^{-4} sec^{-1}.

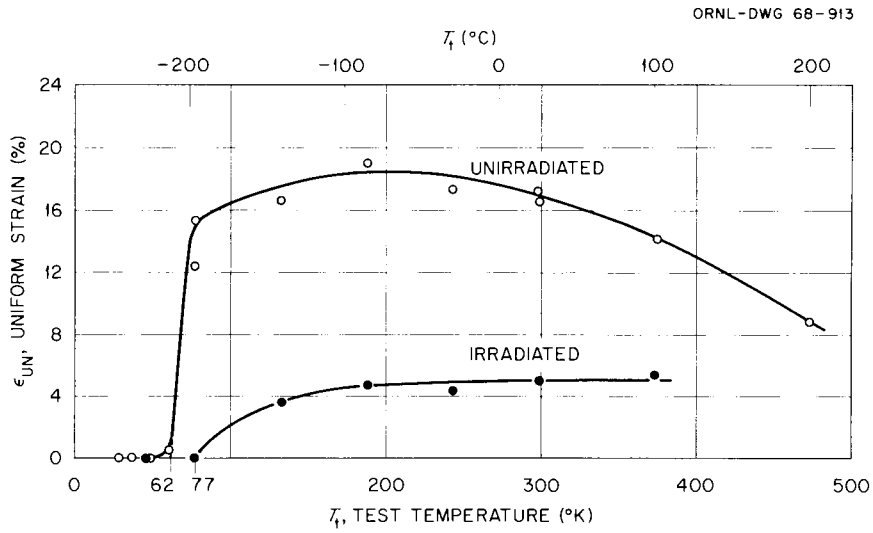

Fig. 5. Uniform Strain vs Test Temperature for Unirradiated and Irradiated (Φ = 1.0 x 10^{19} n/cm^2, 60°C) A-212-B Steel Tested at Strain Rate of 2.7 x 10^{-4} sec^{-1}.

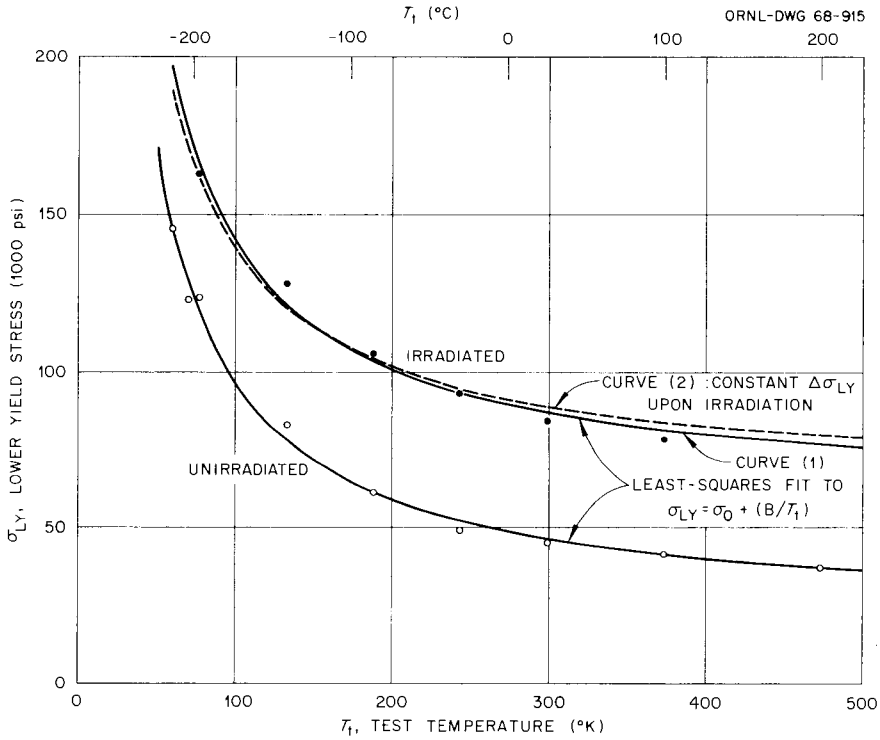

Fig. 6. Lower Yield Stress vs Test Temperature for Unirradiated and Irradiated (Φ = 1.0 x 10^{19}n/cm^2, 60°C) A-212-B Steel Tested at Strain Rate of 2.7 x 10^{-4} sec^{-1}. Illustration of the fit to $\sigma_{LY} = \sigma_o + (B/T_t)$.

It is of course of interest to know at what microstructural feature or features the cracking is initiated at low temperatures. Figures 7 and 8 show photomicrographs at 1000X and 2000X for an unirradiated sample tested to fracture at 28°K. The photographs indicate cracks in the longitudinal section near the fracture surface. The fracture path is oriented in a variety of ways relative to grain boundaries, pearlite colonies, and twin bands, and these photographs do not appear to suggest a special significance to any one type of feature.

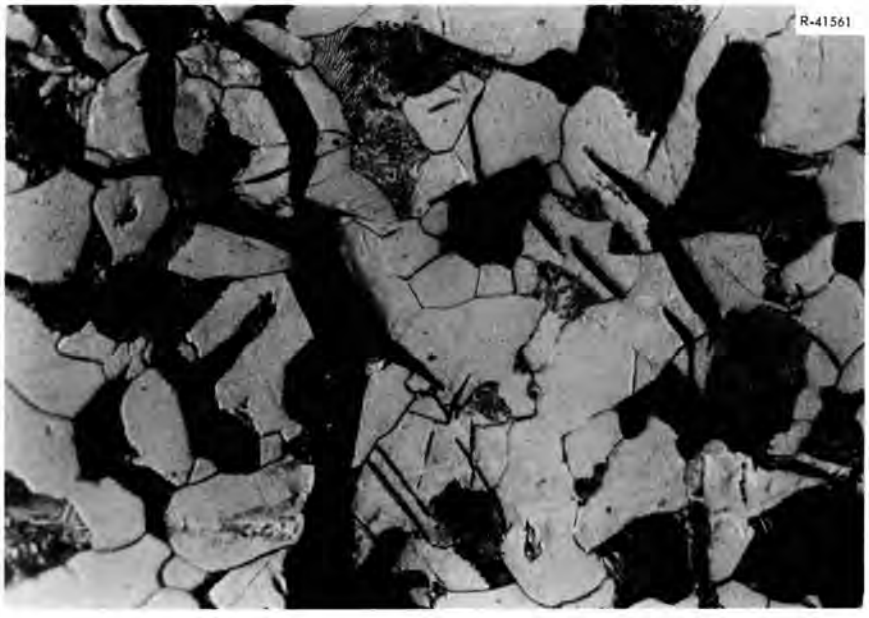

Fig. 7. Photomicrograph at 1000X of Longitudinal Section (Stress Axis Vertical) of Unirradiated sample of A-212-B Steel Tested to Fracture at 28°K. Nital (2%) Etch.

A

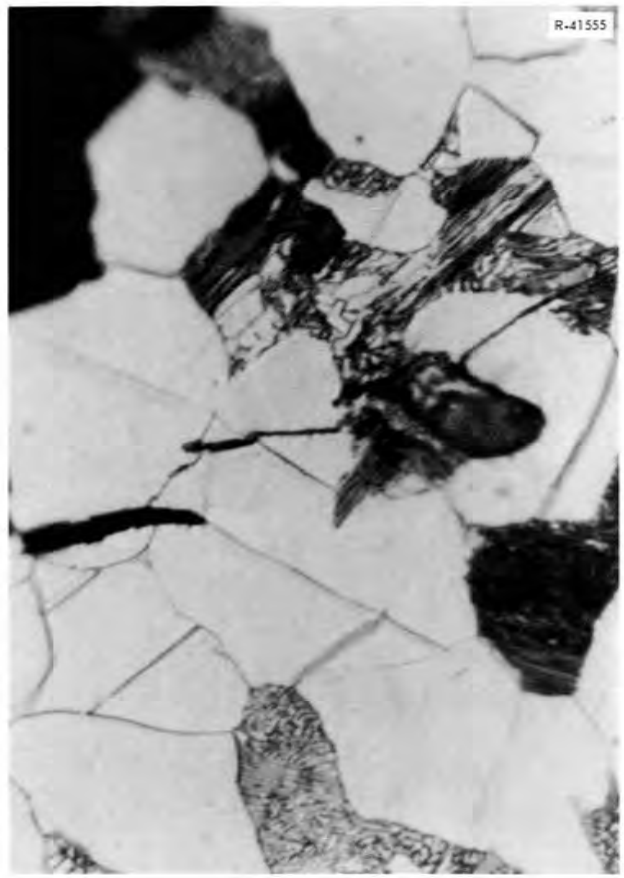

B

Fig. 8. Photomicrographs at 2000X of Longitudinal Section (Stress Axis Vertical) of Unirradiated Sample of A-212-B Steel Tested to Fracture at 28°K. Nital (2%) Etch. (a) Oblique Light; (b) Direct Light.

A limited number of tensile tests were conducted on unirradiated samples at a strain rate of 2.7×10^{-2} sec^{-1} in the temperature range between 77 and 299°K. However, in what follows we shall refer only to measurements at 188, 243, and 299°K. This is done in the Discussion section below.

B. Impact Tests

The impact tests were conducted over a range of temperatures from -75°C (198°K) to 175°C (448°K) and the results were expressed in terms of the fracture energy and the fracture appearance. Figure 9 indicates that the irradiation to 9.8×10^{18} neutrons/cm^2 (E > 1 Mev) increased the DBTT under notched-bar impact conditions from 5°C to 108°C on the basis of a 20 ft-lb fracture energy criterion and from -30°C to 65°C based on the criterion of nil fibrous fracture appearance. The latter criterion appears more in accord with the reduction-in-area criterion (Fig. 4) adopted for the smooth tensile samples; therefore in the discussion that follows, we will use -30°C (243°K) and 65°C (338°K) for the unirradiated and irradiated notched-bar impact DBTT's, respectively, as determined from the fracture appearance curves in Fig. 9 and listed in Table 2.

Discussion

As was mentioned in the Introduction, our object is to see to what extent it is possible to apply the simple concept enunciated by Mesnager, Ludwig, Davidenkov, and Wittman (Fig. 1) to the radiation embrittlement of pressure vessel steels. At the outset, an effective cleavage stress,

σ_c, must be adopted. Based on the intersection of the yield stress and fracture stress curves (Fig. 3), values of σ_c = 153 kpsi and 165 kpsi were chosen for the unirradiated and irradiated material, respectively. The DBTT's under low-strain-rate, smooth-tensile conditions deduced from Fig. 3 were 56°K (unirradiated) and 78°K (irradiated). These agree reasonably well with the DBTT's of 70°K (unirradiated) and 81°K (irradiated) observed for the reduction of area at fracture (Fig. 4 and Table 2) and the DBTT's of 62°K (unirradiated) and 77-130°K (irradiated) observed for the uniform strain (Fig. 5 and Table 2).

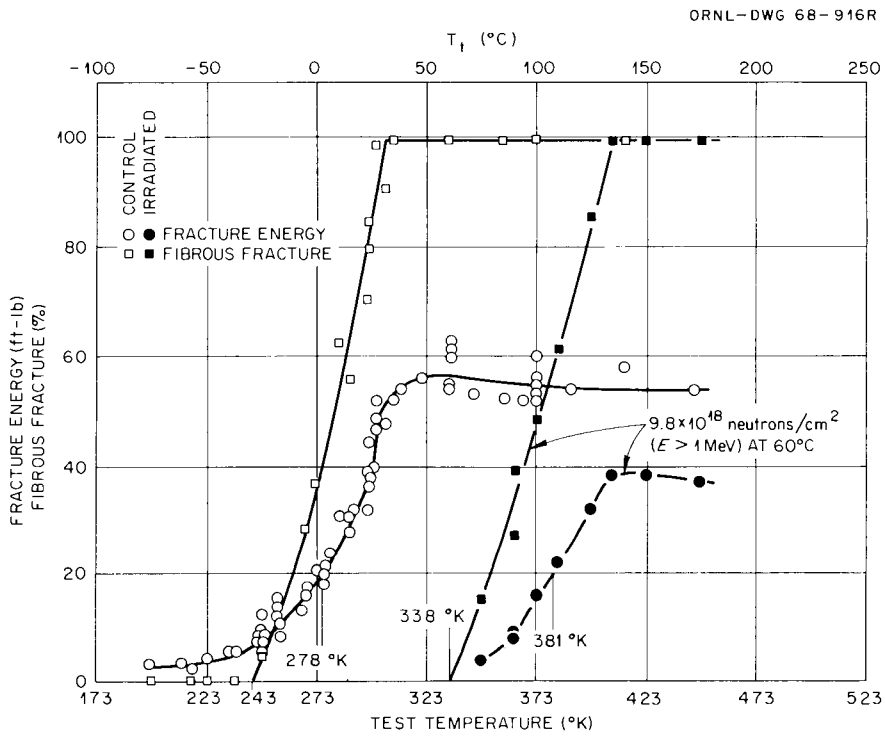

Fig. 9. Effect of Neutron Irradiation on Charpy V-Notch Impact Tests on Unirradiated and Irradiated (Φ = 9.8 x 10^{18} n/cm^2, 60°C) A-212-B Steel.

Table 2. Ductile-Brittle Transition Temperatures (DBTT) for Unirradiated and Irradiated (Φ = 1.0 x 10^{19} n/cm^2, 60°C) A-212-B Steel

Criterion and Type of Test	DBTT Unirrad.	DBTT Irrad.
1. Intersection of fracture and yield curves, smooth tensile, $\dot{\epsilon}$ = 2.7 x 10^{-4} sec^{-1} (Fig. 3)	56°K	78°K
2. Nil reduction of area at fracture, smooth tensile, $\dot{\epsilon}$ = 2.7 x 10^{-4} sec^{-1} (Fig. 4)	70°K	81°K
3. Nil uniform strain, smooth tensile, $\dot{\epsilon}$ = 2.7 x 10^{-4} sec^{-1} (Fig. 5)	62°K	77-130°K
4. Fracture appearance, Charpy impact (Fig. 9)	243°K	338°K
5. Intersection of fracture and yield curves, notch impact, $\dot{\epsilon}$ = 2 x 10^{3} sec^{-1} (Fig. 10)	223°K (K = 2.1)	338°K (K = 1.74)*

*K adjusted to give DBTT = 338°K.

On the assumption that σ_c is independent of temperature, the DBTT for a given type of test should occur where the appropriate yield curve, corrected for strain rate and triaxiality, reaches the value 153 kpsi or 165 kpsi for unirradiated or irradiated material, respectively. In Fig. 10 the yield and cleavage stress curves are shown for the unirradiated and irradiated steel. The observed unirradiated lower yield stress is shown at Curve (A) for $\dot{\epsilon}$ = 2.7 x 10^{-4} sec^{-1} and at Curve (B) for $\dot{\epsilon}$ = 2.7 x 10^{-2} sec^{-1}. In order to derive the DBTT (unirradiated) under notch impact conditions, these curves must be corrected for the strain rate and triaxiality at the point of fracture below the root of the

notch. The notch-impact strain rate is estimated to lie in the range $(1.0 - 2.3) \times 10^3$ sec^{-1} and we shall use the value 2×10^3 sec^{-1} given by Wilshaw and Pratt.[22] To make the extrapolation to this strain rate we apply a constant strain-rate-sensitivity factor, $\Delta \sigma / \Delta \ln \dot{\epsilon}$, as determined from the measurements at 2.7×10^{-4} and 2.7×10^{-2} sec^{-1}. The extrapolated curve appropriate to unirradiated material at 2×10^3 sec^{-1} is labelled (C) in Fig. 10. At room temperature the measured yield stress at 2.7×10^{-4} sec^{-1} is 46 kpsi and this is calculated to be increased to 60 kpsi at 2×10^3 sec^{-1} or an increase of 14 kpsi. This may be compared with the results given by Fearnehough (Ref. 19, Fig. 4) for the dynamic increase in yield stress as a function of the static yield stress. For a static yield stress of 46 kpsi (32 kg/mm^2), the increase in yield stress obtained from his instrumented Charpy tests is given as 15 kpsi (11 kg/mm^2).

A triaxiality correction must also be applied since the yielding is governed by the maximum shear stress, τ, whereas the cleavage fracture depends largely on the longitudinal stress, σ_{yy}, below the root of the notch. In the absence of triaxiality

$$\sigma_{yy} = 2\tau = \sigma_{LY}$$

whereas when the stress state is triaxial

$$\sigma_{yy} = K\, 2\tau$$

where K is the plastic stress concentration factor. The maximum possible value of K for a Charpy bar is 2.18 (Ref. 10, p. 296), and Wilshaw and

---

[22] T. R. Wilshaw and P. L. Pratt, "The Effect of Temperature and Strain-Rate on the Deformation and Fracture of Mild-Steel Charpy Samples," Proc. First International Conference on Fracture, 2, 973, (1966).

Pratt[22] obtained 2.05 ± 0.05 experimentally. Hence, for the unirradiated material we apply a triaxiality correction of 2.1; that is, we raise Curve (C) in Fig. 10 a factor of 2.1 to bring it to Curve (D). Curve (D) intersects the horizontal σ_c = 153 kpsi line at 223°K. Thus, the predicted DBTT (unirradiated) for notch-impact loading is 223°K to be compared with the observed value of 243°K deduced from the fracture appearance curve in Fig. 9. In view of the approximations inherent in the analysis, this may be considered to constitute reasonable agreement.

For the analysis of results for the irradiated samples, the same strain-rate correction was applied as for the unirradiated samples, bringing Curve (A') to (C') in Fig. 10. This seems reasonable in view of the slight change in temperature dependence upon irradiation (Fig. 6).

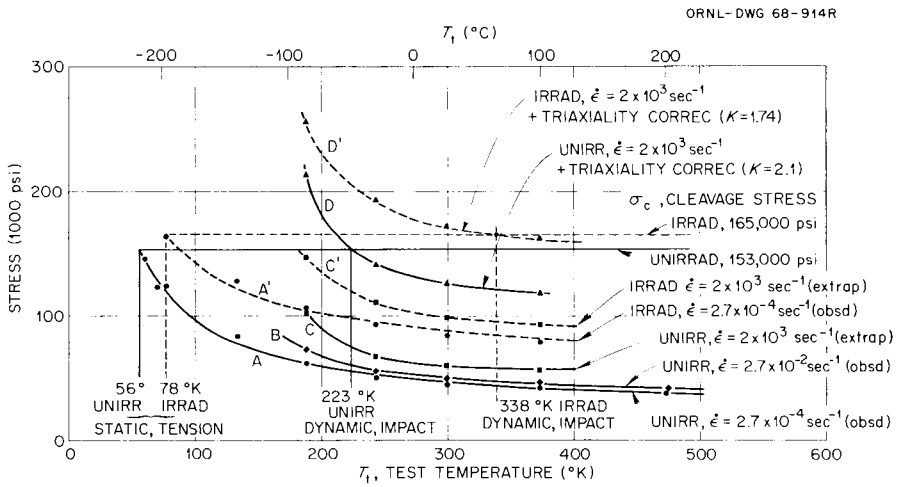

Fig. 10. Stress vs Test Temperature for Unirradiated and Irradiated (Φ = 1.0 x 10^{19} n/cm^2, 60°C) A-212-B Steel.

Also, Campbell and Harding[23] and Fearnehough[24] observed little change upon irradiation in the rate sensitivity of steels tested from 10^{-3} to 10^{3} sec^{-1}. Figure 10 indicates that if the full triaxiality correction of 2.1 were applied to the irradiated case the predicted increase in DBTT upon irradiation would be too large. However, a decrease in the triaxiality correction from K = 2.1 to K = 1.74 allows the point of intersection of Curve (D') with the σ_c = 165 kpsi line to fall at 338°K, the DBTT obtained from the impact tests. The stress concentration factor is given in terms of distance, x, below the notch by [25,22]

$$K = 1 + \ln\left(1 + \frac{x}{r}\right)$$

where r is the root radius, 0.25 mm. A decrease in K from 2.1 to 1.74 corresponds to a decrease in $\frac{x}{r}$ from 2.0 to 1.1.

Observations of the shapes of yield zones in steels[22,23,26] by etching techniques have revealed the succession of events that takes place as deformation spreads from the surface across the specimen. At first the deformation is confined to a small plastic zone or wedge just below the notch root. But then a point of plastic instability is

---

[23] J. D. Campbell and J. Harding, "Effect of Grain Size, Strain Rate, and Neutron Irradiation on Tensile Strength of α-Fe," in Response of Metals to High Velocity Deformation, 51, Interscience, N. Y. (1961).

[24] G. D. Fearnehough, "The Strain Rate Sensitivity of the Yield Stress of Steels," in The Physical Basis of Yield and Fracture, Oxford, Institute of Physics and Physical Society, 88, (1966).

[25] A. S. Tetleman and A. J. McEvily, Fracture of Structural Materials, John Wiley and Sons, New York, (1967).

[26] J. R. Griffiths and A. H. Cottrell, "Notch Effects on Slip, Twinning and Fracture in Silicon-Steel," J. Mech. Phys. Solids, 15, No. 2, 125-133, March, (1967).

reached at which far-reaching arcs or "hinges" of deformation sweep suddenly across the entire specimen section. A lower value of K associated with the DBTT (irradiated, notch impact) at 338°K in Fig. 10 implies that this plastic instability is reached closer to the surface for the irradiated material where the triaxiality is 1.74 instead of 2.1. Possibly this could be due to intensification of strain in the plastic zone due to the coarsening of slip characteristic of irradiated metals. On the other hand, it may be that the σ_c increases with temperature (and perhaps strain rate) in the irradiated steel. To account for the DBTT at 338°K using K = 2.1 as for the unirradiated case, the σ_c would have to increase from 165 kpsi at 78°K and 2.7×10^{-4} sec^{-1} to 200 kpsi at 338°K and 2×10^{3} sec^{-1}. If a similar increase in σ_c were permitted for the unirradiated steel, the DBTT would be decreased only slightly (from 223°K to 210°K). The relative insensitivity of the DBTT (impact, unirradiated) to variations in σ_c is a consequence of the fact that Curve (D), Fig. 10, is rising fairly steeply in the region of 200-250°K. On the other hand, for the DBTT (impact, irradiated) the slope of Curve (D') near 340°K is quite low and small changes in σ_c have a considerable effect upon the point of intersection with the yield curve, i.e. upon the DBTT.

One of the puzzling features of radiation embrittlement in the pressure vessel steels is the large variability in the increase in DBTT from one steel to another or even from heat to heat.[27] The origin

---

[27]M. S. Wechsler, "Radiation Damage to Pressure Vessel Steels," Nucl. Safety, 8, 461, (1967).

of this variability may lie in the fact that the temperature dependence of the yield curve is small at temperatures near the irradiated DBTT.

Post-Irradiation Annealing of ASTM A-212-B Steel

R. G. Berggren, W. J. Stelzman, T. N. Jones, and M. S. Wechsler

We have previously reported[28,29] the results of post-irradiation annealing studies on several heats of ASTM A-212-B carbon-silicon steel. The post-irradiation annealing of Charpy V-notch impact transition temperature was reported[28,29] for specimens irradiated at 55 to 70°C and 233 to 474°C. The post-irradiation annealing of tensile properties was reported[28] for specimens irradiated at 230 to 300°C. The results of post-irradiation annealing studies presented in this report are from tensile tests of specimens irradiated at about 60°C in the Oak Ridge Research Reactor. These tensile test specimens were from the quarter thickness location of a 2 3/4-inch-thick plate from Lukens heat no. A-2056 (SSD Item 157).[28] All the tests were conducted at 27°C and a strain rate of 2.7×10^{-4} sec^{-1}.

The degree of recovery of radiation-induced increase of lower yield stress is shown in Fig. 11. In previous work, the times for 50% recovery were shown to decrease with decreasing irradiation temperature in the range 94 to 290°C (cf Ref. 30). The present work is consistent with that trend, since for our irradiation temperature of 60°C the annealing times are shorter than for the higher irradiation temperatures of the previous work.

---

[28] R. G. Berggren, W. J. Stelzman, and T. N. Jones, "Radiation Effects on Pressure Vessel Steels," Radiation Metallurgy Section Solid State Division Progress Report for Period Ending July, 1966, ORNL-4020, 1, (1966).

[29] R. G. Berggren, W. J. Stelzman, and T. N. Jones, "Radiation Effects on Pressure Vessel Steels," Radiation Metallurgy Section Solid State Division Progress Report for Period Ending July, 1967, ORNL-4195, 4, (1967).

[30] N. E. Hinkle, N. K. Smith, and M. S. Wechsler, "Tensile Tests on Irradiated Iron," Radiation Metallurgy Section Solid State Division Progress Report for Period Ending Feb. 1966, ORNL-3494, 22, (1966).

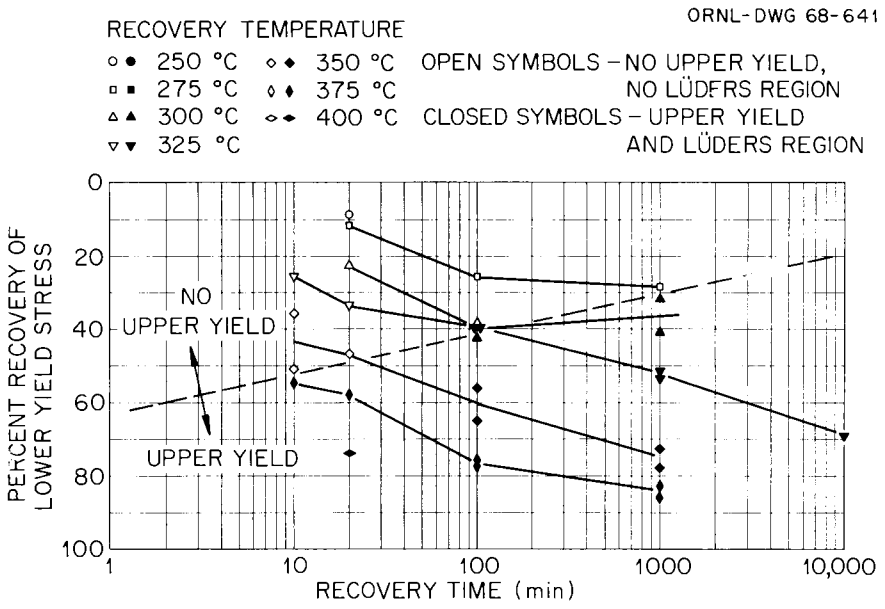

Fig. 11. Recovery of Yield Stress in Irradiated ASTM A-212-B Steel (1×10^{19} n/cm^2, E > 1 Mev, 60°C). SSD Item 157.

During the annealing studies, we observed consistent changes in the shape of the stress-strain curves of this irradiated steel. Specimens tested in the as-irradiated condition exhibited an upper yield point and a Lüders extension. The upper yield point was rounded as often observed in irradiated steels. After post-irradiation anneals at time-temperature combinations lying above the dashed line in Fig. 11, no upper yield point or Lüders extension were observed. The activation energy for this annealing range was about 1.0 to 1.5 ev. After post-irradiation anneals at higher temperatures and/or longer times (combinations lying below the dashed line of Fig. 11) the upper yield point and Lüders extension were observed and were very similar to the behavior of the unirradiated steel. The activation energy for this annealing range was about 2.5 to 3.5 ev. This change in yielding behavior is illustrated in Fig. 12 for 100 minute annealing times at the indicated temperatures.

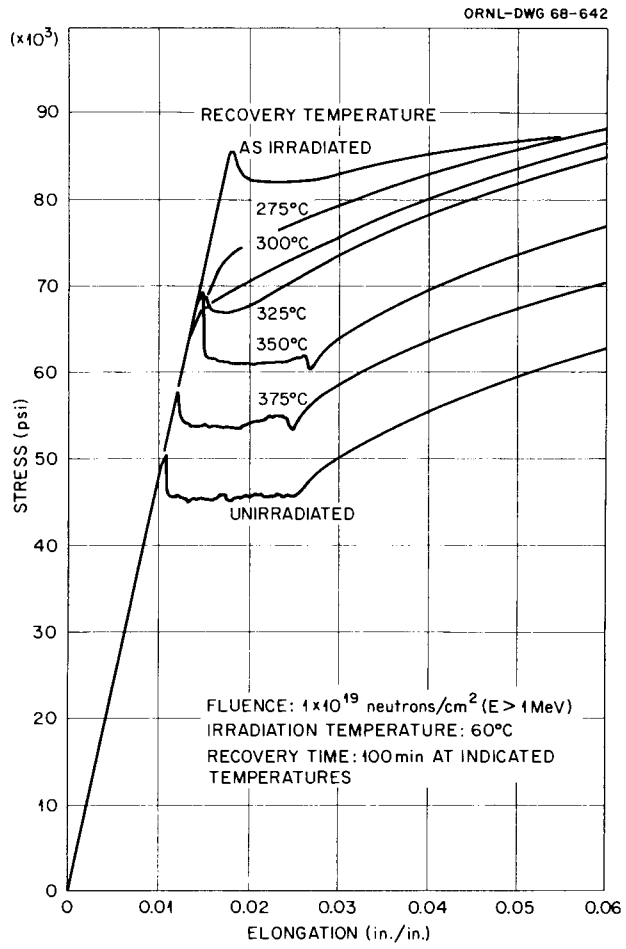

Fig. 12. Recovery Behavior of Irradiated ASTM A-212-B Steel (SSD Item 157).

The following qualitative interpretation emerges. The irradiation temperature was sufficiently high (50°C) for interstitial solutes to be mobile and therefore be trapped at radiation-produced defect clusters. In this condition the defect clusters give rise to a modified, somewhat weakened, yield point effect, as observed for the as-irradiated steel. Upon low temperature annealing (e.g. 275°C for 100 minutes), the trapped interstitial solutes dissociate from the defect clusters, the defect clusters may begin to anneal out, and very small nitride or carbide particles are formed, which do not contribute to a yield point phenomenon.

Finally, in the longer-time, high-temperature region (e.g. 350°C for 100 minutes) the smaller particles are dissolved, the interstitials return to solid solution, and the normal upper yield point and Lüders extension return.

Strain Aging of Neutron Irradiated Steel

W. J. Stelzman, R. G. Berggren, and J. T. Stanley

The term "strain aging" applies to processes which occur upon aging following plastic deformation, chiefly the gradual return of the upper yield point and Lüders strain and the increase in flow stress. The articles by Wilson and Russell[31,32] provide a description of the phenomena as well as a number of references to other work. Various workers in this field are in general agreement that strain aging in steel is produced by the segregation of interstitial impurities such as carbon and nitrogen to dislocations where they form atmospheres or precipitates and thus prevent dislocation motion. Wilson and Russell and also others conclude that for a commercial steel slow-cooled and tempered at 200°C for 2000 min., the strain aging effects are caused by nitrogen since carbon atoms are all precipitated as stable carbides. Strain aging also increases the ductile-brittle transition temperature of steel, and it has been determined that the effects of strain aging and neutron irradiation are additive in increasing the ductile-brittle transition temperature.[33]

---

[31]D. V. Wilson and B. Russell, "The Contribution of Atmosphere Locking to the Strain-Aging of Low Carbon Steels," Acta Met., 8, 36, (1960).

[32]D. V. Wilson and B. Russell, "The Contribution of Precipitation to Strain Aging in Low Carbon Steels," Acta Met., 8, 468, (1960).

[33]M. Grounes and H. P. Myers, "Irradiation Effects in Strain-Aged Pressure Vessel Steel," Nature, 193, 468, (1962).

The interaction of interstitial impurities with radiation-produced defects undoubtedly influences the mechanical properties of irradiated iron and steel. There have been several studies[34,35] using physical properties which show that both carbon and nitrogen interact strongly with radiation-produced defects, and there have been some studies which indicate that these interactions exert a profound influence on the mechanical properties.[36] These studies have been confined to relatively pure iron and their applicability to steel is somewhat indirect. The experiments described below constitute a preliminary investigation of the behavior of interstitial carbon or nitrogen in irradiated pressure vessel steel using the strain aging phenomena.

Experimental Procedures and Results

Specimens were strained in an Instron tensile machine located in a hot cell. The strain rate was 2.7×10^{-4} sec^{-1}. Annealing was carried out in a vacuum furnace at a pressure of 10 μ.

Figure 13b shows load-elongation curves for two specimens of ASTM A-212-B steel and illustrates the strain aging technique used in these experiments. The specimen given the strain aging treatment was pulled to a strain greater than the Lüders strain, unloaded, annealed at the temperature shown, and then re-strained. The effect of strain aging is apparent in Fig. 13 where the load-elongation curve of the strain

---

[34] A. C. Damask, "Effect of Neutron Irradiation on Precipitation of Carbon in Alpha Iron," Diffusion in Body Centered Cubic Metals, 24, 317, ASM, Metals Park, Ohio, (1965).

[35] M. Wuttig, J. T. Stanley, H. Birnbaum, "Interstitial Solute Trapping in Irradiated and Quenched Iron," submitted for publication.

[36] N. E. Hinkle and N. K. Smith, "Tensile Tests on Irradiated Iron," Quarterly Progress Report: Irradiation Effects on Reactor Structural Materials, Nov., Dec. 1966-Jan. 1967, BNWL-CC-1053. Pacific Northwest Laboratory, Richland, Washington, 11.4-11.8, Feb. 15, (1967).

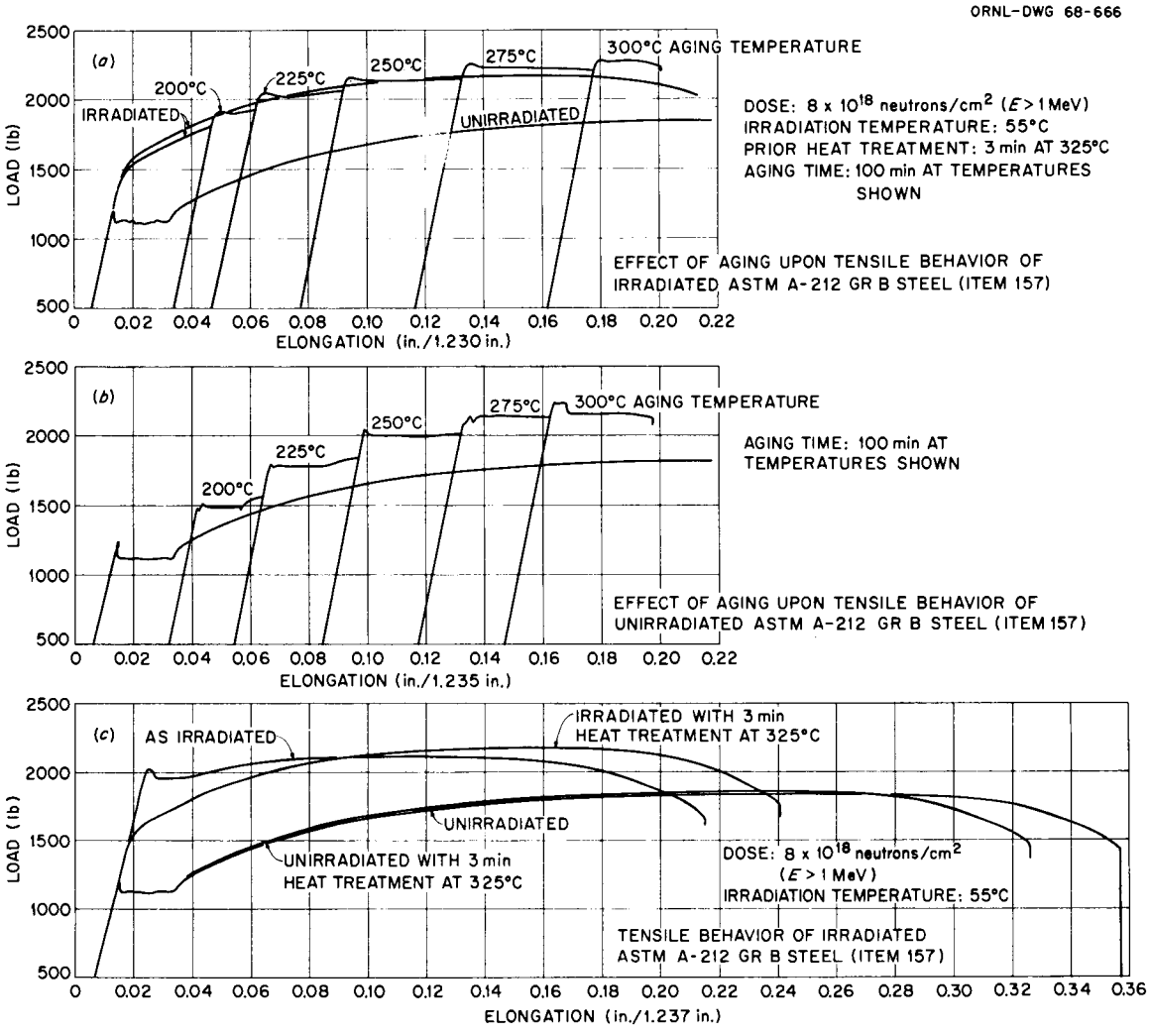

Fig. 13. Load-Elongation Curves for Unirradiated and Irradiated ASTM A-212-B Steel (Item 157).

aged specimen lies above that of the other specimen. It is convenient to define the strain aging effect by the quantity $\Delta\sigma = \sigma_{LY} - \sigma_f$, where σ_{LY} is the lower yield stress and σ_f is the flow stress observed in the preceding stress-strain cycle just before unloading. Wilson and Russell showed that restraining of a strain-aged specimen puts some of the nitrogen back into solution and allows the strain aging to reoccur.[32] This mechanism accounts for the results observed in our experiments which were carried out with repeated strain aging cycles as shown in Fig. 13.

Figure 13a shows load-elongation curves for irradiated specimens of ASTM A-212-B steel and also the load-elongation curve for the unirradiated specimen shown in Fig. 13b. The results shown in Fig. 13a indicate that the strain aging effects are much smaller in the irradiated specimen compared to the unirradiated specimen.

The load elongation curves for unirradiated and irradiated specimens are compared in Fig. 13c with load elongation curves for both types of specimens given a three minute anneal at 325°C before testing. The effect of the 3 min anneal is negligible for the unirradiated specimen, but the load-elongation curve for the irradiated specimen is changed considerably.

The strain aging effect $\Delta\sigma$ is plotted vs aging temperature in Fig. 14 for the specimens discussed above and for some additional specimens. In the following discussion of Fig. 14 it is important to remember that the total strain increases as the temperature increases, and thus the changes shown in Fig. 14 may be partly a result of the preceding strain history of the specimen. Figure 14 shows results for two unirradiated specimens: an unirradiated specimen given no heat treatment other than that received during plate manufacture (open squares) and an unirradiated

specimen given an additional treatment of 10^4 min at 325°C (open circles). The results for this latter specimen are the most interesting because the strain aging anneals were started at a lower temperature than those for the former specimen. According to Wilson and Russell[37,38] the maximum strain aging effect occurs in 10^4 min at 60°C. Assuming the strain aging effect is due to nitrogen, we calculate that 100 minutes at 150°C are equivalent to about 1100 minutes at 60°C, and 100 minutes at 200°C are equivalent to about 4×10^5 minutes at 60°C. Therefore, for the present experiment we would expect the maximum strain aging effect to occur between 150°C and 200°C, and this seems to agree with the results shown in Fig. 14 for the unirradiated specimen. The maximum strain aging effect observed by Wilson and Russell was 8000 psi[38] and this is in reasonable agreement with the present results. It seems likely that the decrease of strain aging effect with increasing temperature shown in Fig. 14 is more a function of strain history than increasing temperature.

The strain aging results for three irradiated specimens are also shown in Fig. 14. All of these irradiated specimens were given an anneal after irradiation and before testing. These results show that strain aging effects are greatly reduced by irradiation (filled triangles), presumably because the nitrogen is trapped and can no longer

---

[37]D. V. Wilson and B. Russell, "The Contribution of Atmosphere Locking to the Strain-Aging of Low Carbon Steels," Acta Met., 8, 36, (1960).

[38]D. V. Wilson and B. Russell, "The Contribution of Precipitation to Strain Aging in Low Carbon Steels," Acta Met., 8, 468, (1960).

migrate to the dislocations. However, upon annealing for 10^4 min at 325°C the traps for nitrogen are removed and the original strain aging effect is restored (filled squares). A short anneal (3 min at 325°C) restores only a fraction of the initial strain aging effect.

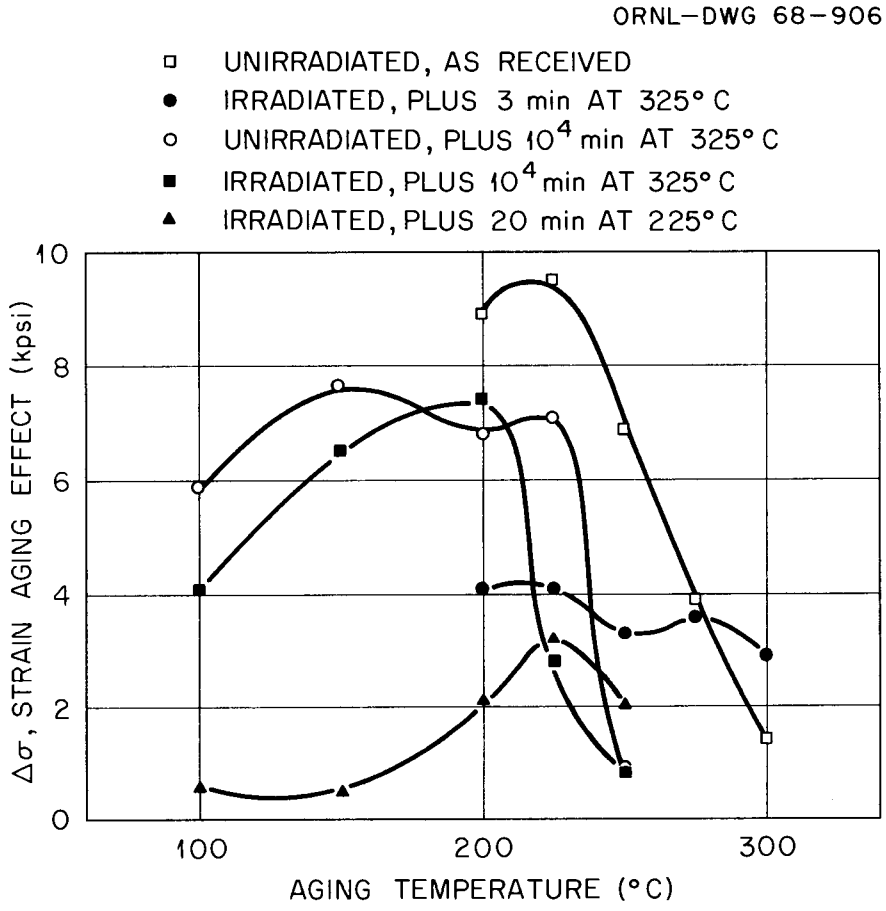

Fig. 14. Strain Aging of ASTM A-212 Gr. B. Steel (Item 157) as a Function of Aging Temperature. Aging Time 100 min. at Each Temperature Except 20 Minutes at Each Temperature for Triangle Points.

Effect of Thermal Neutrons on the Tensile Properties of ASTM A-212-B and A-302-B Steels

R. G. Berggren, W. J. Stelzman, and M. S. Wechsler

Thermal neutrons can produce radiation damage in steels since the iron nucleus gains a significant recoil energy from the emission of gamma rays after capture of a thermal neutron.[39] We have previously reported[40] no observable difference in Charpy V-notch impact properties of unshielded and cadmium shielded specimens of ASTM A-212-B and ASTM A-302-B steels irradiated in the Oak Ridge Research Reactor. We have conducted tensile tests on specimens of these two steels irradiated in the same capsules as the previously reported Charpy V-notch specimens. Half of the specimens of each steel were irradiated inside a 0.040-inch-thick cadmium shield and the other specimens were irradiated without cadmium shielding. The results of these tension tests are presented in Table 3. No significant effect of cadmium shielding was observed in either steel. The tension tests were conducted at room temperature and a strain rate of 2.7×10^{-4} sec^{-1}. Exposure temperature was 60°C. In this irradiation facility a thermal to epithermal neutron ratio of 3:1 (cadmium ratio of 4:1) and a thermal to fast (E > 1 Mev) neutron ratio of 7.5:1 has been previously measured. A much higher thermal to fast neutron flux ratio will be required for study of the effects of thermal neutron irradiation.

---

[39] M. S. Wechsler, "Fundamental Aspects of Radiation Effects on Diffusion-Controlled Reactions in Alloys," in Radiation Effects on Metals and Neutron Dosimetry, ASTM-STP-341, 86, American Society for Testing and Materials, Philadelphia, (1963).

[40] R. G. Berggren, W. J. Stelzman, and T. N. Jones, "Radiation Effects on Pressure Vessel Steels," Radiation Metallurgy Section Solid State Division Progress Report for Period Ending July, 1967, ORNL-4195, 4, (1967).

Table 3. Tensile Properties of Irradiated ASTM A-212-B (SSD Item 157) and ASTM A-302-B (SSD Item 127-D) Steels and Effect of Cadmium Shielding

SSD Item	Fast Neutron Dose (E > 1 Mev)	Irradiation Temperature	Upper Yield	Lower Yield	Ultimate Strength	Fracture[a] Strength	Elongation		
							Luders	Uniform[b]	Total[c]
	($\times 10^{18}$ n/cm^2)	(°C)	(ksi)	(ksi)	(ksi)	(ksi)	(%)	(%)	(%)
157(e)	0	--	--	44.7	74.1	58.7	1.5	18.3	27.7
	0	--	--	44.2	74.1	58.3	--	--	--
	0	--	--	45.2	74.4	59.3	1.7	19.1	29.9
	0	--	--	44.6	74.1	58.3	1.6	18.2	27.8
Without Shielding	4.5	70	76.6	75.2	82.9	65.4	1.9	10.7	18.8
	5.1	70	79.3	77.3	84.1	67.5	2.1	9.3	17.1
Cadmium Shielded (d)	4.5	70	77.0	74.6	83.1	65.7	1.7	11.5	21.7
	5.1	72	78.1	76.3	82.8	64.8	2.0	10.8	20.0
	5.5	73	78.6	77.2	84.3	67.5	1.5	8.2	17.8
127-D (e)	0	--	57.0	56.6	84.5	63.8	0.8	12.9	20.9
	0	--	--	54.5	82.7	58.9	0.9	12.7	21.1
	0	--	--	54.9	82.7	62.2	0.7	14.6	23.4
	0	--	57.3	55.3	83.6	62.7	0.8	11.5	18.7
Without Shielding	4.8	64	91.5	88.2	92.9	66.0	2.8	5.8	13.7
	5.5	67	92.9	89.9	93.3	68.5	0.5	5.7	13.5
	5.8	69	94.1	91.5	94.3	68.4	1.2	4.9	12.7
Cadmium Shielded (d)	5.1	67	92.7	89.3	93.7	71.1	3.1	7.1	15.5
	5.5	71	93.9	90.5	93.9	69.0	1.8	6.1	14.3
	5.5	73	92.7	90.5	93.7	68.8	2.3	5.4	12.3

[a] Fracture load/original area

[b] Average elongation at maximum load

[c] From load-elongation record

[d] Specimen shielded with 0.040 inches cadmium

[e] Item 157 from 1/4 thickness; Item 127-D from 1/3 thickness

Properties of 12-Inch-Thick ASTM A-533-B, Class I, Steel*

R. G. Berggren and T. N. Jones

Material characterization tests are in progress on the first 12-inch-thick plate of ASTM A-533-B, Class I, steel procured for the Heavy Section Steel Technology (HSST) program. This steel was formerly known as ASTM A-302-B, modified (per ASME Pressure Vessel Code, Interpretation Case 1339). Material from this plate will be incorporated in our irradiation effects studies when characterization tests indicate this plate is satisfactory for irradiation studies. Characterization tests will include tensile tests, Charpy V-notch impact tests, Drop weight tests (P-1, P-2, and P-3 specimens), hardness, chemical composition, and metallographic examination. Tests are being conducted on longitudinal, transverse, and through-thickness specimens cut from several depths in the plate.

This first 12-inch-thick ASTM A-533-B, Class I, plate (HSST plate 01) was produced by the Lukens Steel Company. The ingot (138,000 pounds) was produced in a basic electric furnace, aluminum deoxidized (0.7 lb/ton), and vacuum degassed in the ladle. The ingot was 108 inches wide, 40 inches thick, and 127 inches high. The ingot was then slabbed and rolled to plate form. The rolling reduction ratio was 3.33, cross rolling ratio 1.4, and the finishing temperature was 1650°F. The plate was sand cooled after rolling. The trimmed plate weighed 106,420 pounds and measured 260 inches long, 120 inches wide, and 12 inches thick. The mill test report is given in Table 4.

---

*Work conducted under the Heavy Section Steel Technology Program.

The plate was heat treated by Combustion Engineering, Inc. Heat treatment consisted of normalizing (1675-1700°F for 4 hours and air cooling) to simulate hot-forming operations, austenitizing at 1550-1650°F for 4 hours, quenching in agitated water, tempering at 1225°F for 4 hours, and air cooling. The plate was then flame cut and stress relieved at 1125-1175°F for 40 hours. All heat treatment operations were monitored with thermocouples buried in the plate.

Test results, already obtained for specimens from the central region of this plate, are presented in Fig. 15. As expected, the highest yield and ultimate strengths and the lowest Drop Weight NDT temperatures were obtained for specimens from near the plate surfaces. The properties are quite uniform through the central eight inches of the plate except for some decrease in ductility and hardness at the mid-thickness. The slightly poorer properties at mid-thickness are probably due to the higher inclusion content observed at mid-thickness.

Table 4. Mill Test Report for HSST Plate 01, ASTM A-533 Grade B, Class I Steel, Lukens Heat No. A1008.

Chemical Composition	Ladle	Check
Carbon	0.22%	0.22%
Manganese	1.45%	1.48%
Phosphorus	0.011%	0.012%
Sulfur	0.019%	0.018%
Silicon	0.22%	0.25%
Nickel	0.62%	0.68%
Molybdenum	0.53%	0.52%

Physical Properties:

Yield Strength	70,100 psi
Ultimate Tensile Strength	95,000 psi
	93,600 psi
Elongation (2")	27%

Test pieces heated to 1575-1625°F, held 4 hours, program cooled per cooling rate for 12 inch plate, tempered at 1200-1250°F held 4 hours and cooled, then stress relieved at 1125-1175°F held 20 hours and furnace cooled to 600°F.

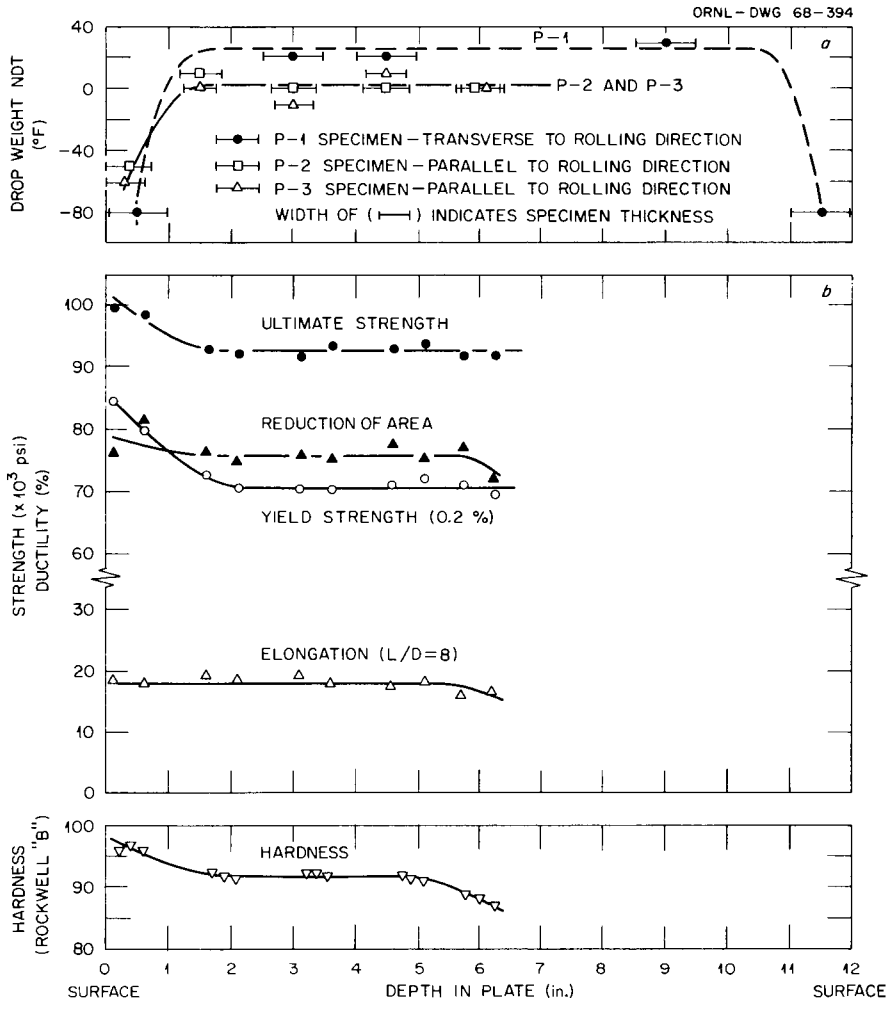

a. THESE DATA WERE OBTAINED BY R.G. BERGGREN, SOLID STATE DIVISION, ORNL

b. THESE DATA WERE OBTAINED BY D.A. CANONICO, METALS AND CERAMICS DIVISION, ORNL

Fig. 15. Mechanical Properties of HSST Plate 01; 12-Inch Thick ASTM A-533-B, Class I Steel (Central Region).

The Interaction Between Oxygen and Radiation-Produced Defects in Niobium

J. T. Stanley, J. M. Williams, and W. E. Brundage

Introduction

In previous reports[41-43,44] we have shown that oxygen migrates to radiation-produced defects in neutron-irradiated niobium upon annealing at temperatures near 150°C. A kinetic analysis has been presented[45] which supports the hypothesis that small dislocation loops act as traps for the oxygen atoms. In the present report, results are presented which show that oxygen trapped at the dislocation loops can be returned to solution by annealing above 250°C.

Experimental Procedures

The work described in this report was carried out on specimens described previously[43]. Briefly, several specimens were prepared containing 50 ppm oxygen and irradiated to a fluence of 2×10^{18} neutrons,

---

[41] J. T. Stanley and W. E. Brundage, "The Interaction of Radiation Produced Defects and Interstitial Impurity Atoms in Niobium," Quarterly Progress Report: Irradiation Effects on Reactor Structural Materials, May-June 1966, BNWL-CC-784. Pacific Northwest Laboratory, Richland, Washington, 10.30, August (1966).

[42] J. M. Williams, J. T. Stanley, and W. E. Brundage, "The Interaction of Radiation Produced Defects and Interstitial Impurity Atoms in Niobium," Quarterly Progress Report: Irradiation Effects on Reactor Structural Materials, Nov. 1966-Jan. 1967, BNWL-CC-1053. Pacific Northwest Laboratory, Richland, Washington, 11.18, February (1967).

[43] J. T. Stanley, J. M. Williams, W. E. Brundage, "The Effect of Oxygen on 'Stage III' Annealing in Neutron-Irradiated Niobium," Quarterly Progress Report: Irradiation Effects on Reactor Structural Materials, May-July 1967, BNWL-532. Pacific Northwest Laboratory, Richland, Washington, 11.17, August (1967).

[44] J. M. Williams, W. E. Brundage, and J. T. Stanley, "The Effect of Oxygen on 'Stage III' Annealing in Neutron-Irradiated Niobium," to be published in Metals Science Journal.

[45] R. Bullough, J. T. Stanley, and J. M. Williams, "The Kinetics of Migration of Impurities to Small Dislocation Loops," to be published in Metal Science Journal.

E > 1 MeV, at 50°C. The specimens were placed in the torsion pendulum apparatus and annealed at approximately 150°C for about 10^4 minutes. Internal friction measurements were made at frequent intervals during this anneal period. After this initial anneal period, internal friction measurements were made as a function of temperature and the results will be described below.

In some instances the specimen was removed from the torsion pendulum, annealed in a high vacuum furnace, and then replaced in the torsion pendulum for further measurements. The high-vacuum system used in these anneals employed a liquid-nitrogen cold trap and metal gasket seals. A pressure of about 1×10^{-7} torr was maintained during the anneal. The specimen was placed in a fused quartz tube attached to this system and heated by an external furnace. It was not possible to achieve rapid heating or cooling in this system. One specimen was annealed in situ in the torsion pendulum. In this case somewhat more rapid heating and cooling was obtained, but the vacuum was not as good (about 5×10^{-5} torr) and the specimen was stressed (about 4000 psi) during the anneal.

Results

The migration of oxygen to radiation-produced traps and thus its effective removal from solid solution can be detected independently by internal friction and electrical resistivity measurements. In the previous work,[43] a rather close agreement in the fractional decrease of the two properties upon post-irradiation annealing at 150°C was shown, although some discrepancy existed toward the mid-range of the annealing (see Fig. 10, Ref. 43). A second niobium sample cut from the same wire

and given an identical thermal and irradiation treatment as the previous sample has now been tested. Using improved temperature measurement and control for the internal friction measurements, we find that the resistivity and internal friction results agree over the entire annealing range (Fig. 16).

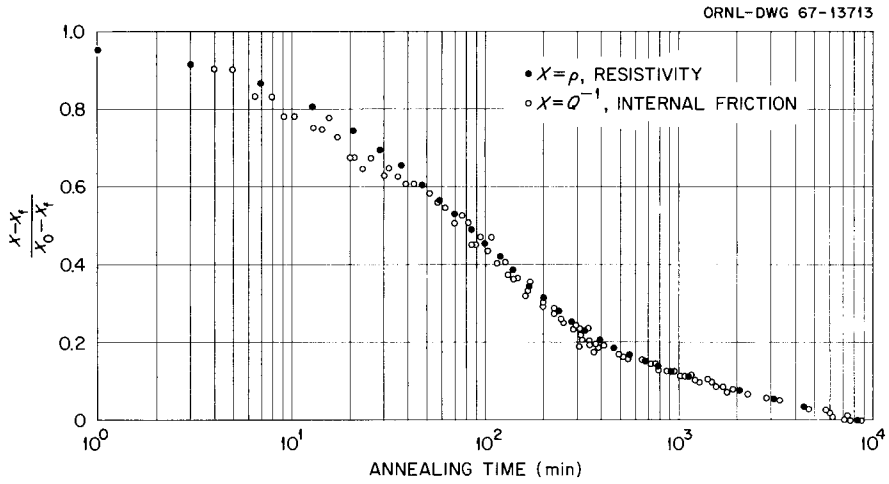

Fig. 16. Normalized Resistivity and Internal Friction Decrease Versus Log of Annealing Time at 150°C for Sample G-3 (Resistivity) and G-2 (Interal Friction) Irradiated to 2 x 10^{18} n/cm^2 (E > 1 Mev) at 40-50°C. X_o and X_f Refer to the Property Immediately After Irradiation and After Annealing for 8000 min., respectively.

The close comparison between the annealing kinetics of resistivity and internal friction is significant because it bears on the origin of the "Stage III" post-irradiation resistivity annealing observed at about 0.15 T_m (T_m = melting temperature) for the BCC metals generally. The internal friction peak at 150°C in niobium is known to be due to oxygen in solid solution, and thus the "Stage III" resistivity decrease in niobium must also be due to oxygen. By inference, we are led to suspect that the "Stage III" annealing in the other BCC metals is also due to interstitial impurities.

Since the oxygen is now known to be removed from solid solution at radiation-produced defect traps, the question arises as to how high a temperature is necessary to dissociate the oxygen from the defect traps. Figure 17 shows internal friction as a function of temperature of measurement up to 340°C for a sample previously irradiated and then annealed (aged) at 150°C for about 10^4 minutes. Two broad peaks, centered at 230 and 270°C are seen in addition to the residual oxygen peak at 160°C. These additional peaks are no longer present after the first run (circles), as can be seen from the second run (triangles). Figure 17 also shows that the 150°C oxygen peak is increased for the second run; this is discussed further below.

Figure 18 shows internal friction measurements made on another irradiated specimen after the 150°C aging. The measurements again indicate the presence of additional internal friction peaks at temperatures above the oxygen peak, but in this case the measurements were interrupted starting at 250°C to return to the oxygen peak temperature (153°C). Upon returning to the higher temperatures, a decrease in the internal friction was noted at 240°C, at 250°C, and at 260°C. Then the measuring temperature was reduced to 153°C for another measurement of the oxygen peak height. Upon returning again to 250°C, a further decrease in the internal friction was noted. Thus, the high temperature peaks were removed by temperature cycling. Figure 18 also shows the internal friction measurements after annealing at 300°C (triangles) and over a range from 325° to 400°C (filled circles). After annealing at these temperatures, the oxygen has returned to solution. The background internal friction at temperatures above the oxygen peak is

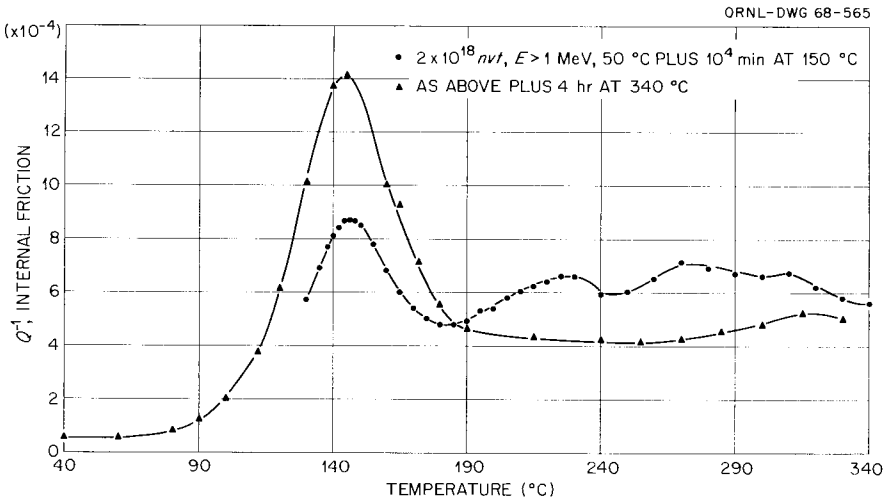

Fig. 17. Internal Friction of Neutron-Irradiated Niobium Containing 50 ppm Oxygen. Frequency = 0.9 cps. Sample G-1.

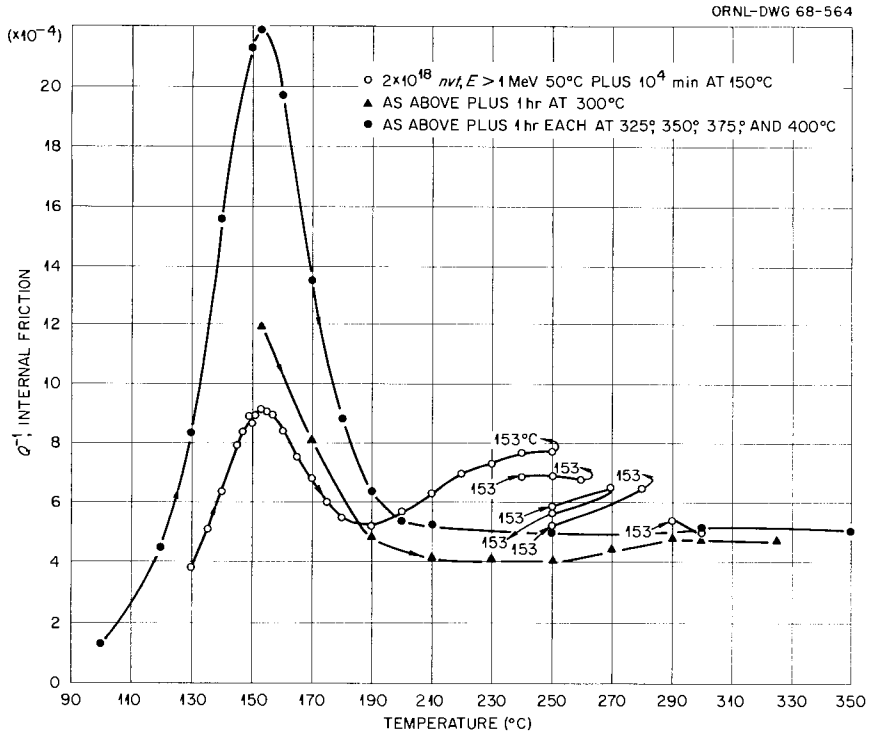

Fig. 18. Internal Friction of Neutron-Irradiated Niobium Containing 50 ppm Oxygen. Frequency = 1.37 cps. Sample G-2.

higher than at temperatures below the oxygen peak. The same feature occurs in the unirradiated specimen but is not so large.

In Fig. 19 the height of the oxygen peak is plotted as a function of annealing temperature for the two irradiated specimens discussed above. Note that the oxygen peak returns at lower annealing temperatures for the stressed specimen even though the annealing time is shorter. Also for anneals at 350°C or lower the oxygen peak shows a slight decrease upon additional aging at 150°C. The oxygen peak height is greater than before irradiation for specimen G-1 annealed at 500°C for 4 hours, and the shape of the curve for specimen G-2 suggests that it will also go above the original peak height after additional anneals at a higher temperature. The measurement of the oxygen peak height of specimen G-1 after the 500°C anneal was made twice. First the peak height was measured on the specimen as annealed, and then the specimen was removed from the torsion pendulum and etched to remove about 0.002 in. from its diameter. After this latter treatment the peak height was again measured and found to be the same as the peak height before etching. Thus the increase of the oxygen peak above the pre-irradiation value is not due to surface contamination by pick-up of oxygen from the vacuum system during annealing.

Discussion

The internal friction measurements described above have shown several new features which must be explained by any model of the trapping mechanism: (1) Two new internal friction peaks appear in irradiated niobium containing oxygen; (2) These new peaks are removed by cycling between high and low temperatures; (3) The background internal friction at temper-

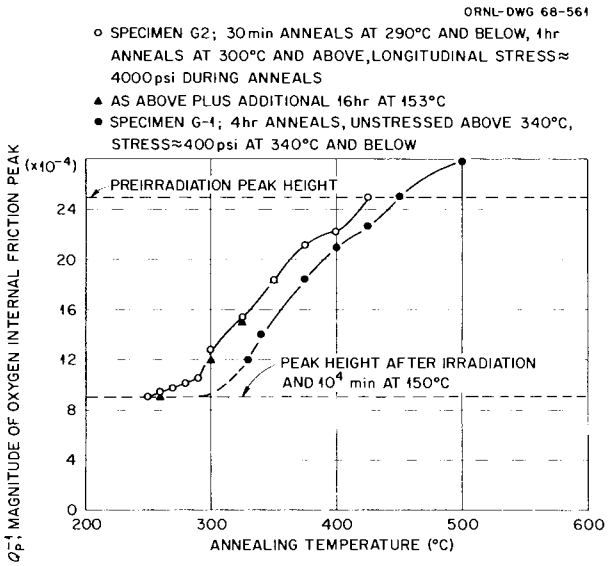

Fig. 19. The Return of Oxygen to Solution in Irradiated Niobium. Specimens G-1 and G-2 Irradiated to 2 x 10^{18} n/cm^2 (E > 1 Mev) at 40-50°C and Annealed $\approx 10^4$ minutes at $\approx$ 150°C, then Annealed at Temperatures and Times Shown.

atures above the oxygen peak is increased by irradiation; (4) The traps for the oxygen anneal out when the oxygen dissociates from them; (5) A uniaxial stress applied during the anneal aids in removal of the traps; (6) After irradiation and annealing to about 500°C, the oxygen peak is higher than before irradiation. Possibly all of these points are not directly connected with the trapping mechanism, and in particular, feature 6 might be observed in unirradiated specimens. We have postulated that the small dislocation loops produced by irradiation act as traps for the oxygen atoms, and we believe that all of the above features can be explained by this mechanism.

In particular, the extra peaks may be analogues of the cold work peak observed in deformed b.c.c. metals which contain interstitial impurities. These cold work peaks have been the subject of a number of

investigations,[46-50] and several different models have been proposed to account for the observations. In Schoeck's[51] model of the cold work peak the anelastic strain arises from motion of the dislocation, which is restricted by the drag of the impurity atmosphere. According to this model the peak temperature depends on the length of the dislocation segment between nodes or precipitate pinning points. This feature would explain the lower temperature of the peaks in the neutron-irradiated specimen (-230°C and 270°C) compared to the temperature of the oxygen cold work peak in niobium which is at about 420°C.[50] The same effect would also explain the presence of two peaks in neutron-irradiated niobium if we assume two distinct loop sizes, one size for vacancy loops and another for interstitial loops. However, more experiments must be performed before a detailed theory can be developed. The peculiar way in which these peaks disappear upon thermal cycling is somewhat difficult to explain. One possibility is that precipitation of an

---

[46] W. Köster, L. Bangert, and R. Hahn, "Das Dämpfungsverhalten von gerecktem technischem Eisen," Archive Eisenhüttenw., 25, 569, (1954).

[47] K. Kamber, D. Keefer, and C. Wert, "Interactions of Interstitials with Dislocations in Iron," Acta Met., 9, 403, (1961).

[48] D. P. Petarra, "Internal Friction in Iron at Temperatures in the Range 0°C to 500°C at Frequencies near 1 c/s," Thesis, Columbia University (New York, 1962).

[49] G. Schoeck and M. Mondino, "Internal Friction Due to Interstitial-Dislocation Interaction in Ta," J. Phys. Soc. of Japan, 18, Suppl. 1, 149, (1963).

[50] D. J. van Ooijen and A. S. van der Goot, "The Internal Friction of Cold-Worked Niobium and Tantalum Containing Oxygen and Nitrogen," Acta Met., 14, 1008, (1966).

[51] G. Schoeck, "Friccion Interna Debido a La Interaccion Entre Dislocaciones Y Atomos Solutos," Acta Met., 11, 617, (1963).

oxide takes place on the dislocation loop. The precipitates do not form at the higher temperature because of a low supersaturation factor, but upon cooling to low temperature nucleation takes place. The increase of background internal friction at temperatures above the Snoek peak is also observed in cold worked material, but no detailed explanation for this effect has been given.

The conclusion that dissociation of oxygen from the traps and annealing of the traps occur simultaneously (point 4 above) is drawn from the observation that the peak height observed immediately after a high temperature anneal is not changed substantially by an additional aging treatment of up to 16 hours at 153°C. Figure 16 shows that 16 hours (960 minutes) is long enough to complete most of the trapping reaction in the as-irradiated specimen. It is true that for anneals at or below 325°C there was some slight amount of retrapping of oxygen after the 16-hour aging at 153°C. This behavior would be expected from the nature of the dislocation traps. A calculation shows that about 7 oxygen atoms are trapped for each lattice point on the dislocation core. It is likely that all of the oxygen atoms which are trapped are not in the dislocation core. Thus, we would expect the oxygen atoms which are at the edge of the atmosphere to be rather loosely bound. These loosely bound atoms might evaporate at moderately elevated temperatures leaving the dislocation core still filled with tightly bound atoms. It is only after these tightly bound oxygen atoms have evaporated that the dislocation loop can anneal out. This mechanism suggests that annealing of loops in specimens containing other interstitial impurities such as carbon or nitrogen might occur at a different temperature than in a specimen containing only oxygen.

The effect of stress in aiding the annealing process is a rather unexpected result. We believe that the stress of 4000 psi is below the yield stress of this specimen at the temperature of the measurement. The specimen was examined in the microscope after the measurements were made, and no visible signs of flow were seen. An upper limit of 1.6% elongation can be set on the strain since the difference of specimen length before and after the measurements was known to be less than 1/16 inch.

The increase of peak height above the value observed before irradiation (point 6) indicates that some of the oxygen was trapped at a defect structure before the irradiation. It is possible that vacancy loops or clusters formed during the cooling of the specimen from the final annealing temperature (1100°C) prior to irradiation and that part of the oxygen became trapped at these defects.

Trapping of Oxygen and Nitrogen in Neutron-Irradiated Vanadium

J. T. Stanley, J. M. Williams, and W. E. Brundage

Several years ago we attempted to observe the trapping of oxygen and nitrogen in neutron-irradiated vanadium. Only a small decrease in the oxygen and nitrogen peaks was observed after a neutron fluence of 5×10^{17} neutrons/cm^2, E > 1 Mev.[52] We have now irradiated additional vanadium specimens to a higher fluence, 7.2×10^{17} E > 1 Mev, and measured the decrease of the oxygen and nitrogen peaks as a function of time at the peak temperatures.

---

[52] J. T. Stanley, "In-Reactor Internal Friction Measurements of Interstitial Rearrangements in BCC Metals," Quarterly Progress Report: Irradiation Effects on Reactor Structural Materials, Nov., Dec., 1963 and Jan., 1964, HW-80794, Hanford Laboratories, Richland, Washington, 10.1, February (1964).

Figure 20 shows the internal friction as a function of temperature for one of the unirradiated specimens. The oxygen peak at 182°C is considerably wider than would be expected for a single relaxation process, and we believe that this specimen may also contain carbon. According to Powers and Doyle[53] the carbon peak occurs at 170°C while the oxygen peak occurs at 182°C in vanadium for 1 cps vibration frequency.

Figure 21 shows the relative decrease of the oxygen and nitrogen peaks as a function of time at the respective peak temperatures, 185°C and 275°C respectively. For these measurements the specimen was held first at the oxygen peak temperature (185°C) and the oxygen peak decreased to about 50% of its initial value. The specimen was then held at the nitrogen peak temperature (275°C), and the nitrogen peak decreased to about 80% of its initial value. Upon returning to the oxygen peak temperature some recovery of the oxygen peak was noted.

The total amount of nitrogen in solution before irradiation was about 1200 ppm atomic while the amount of oxygen in solution was only 167 ppm, as determined by the internal friction peak heights and conversion factors given by Powers and Doyle.[53] Thus the fact that some of the oxygen is apparently forced out of the loops by the nitrogen does not necessarily mean that the binding energy of nitrogen atoms to dislocations is greater than that of oxygen, since nitrogen is present in much greater amounts than oxygen.

---

[53]R. W. Powers and M. V. Doyle, "Diffusion of Interstitial Solutes in Group V Transition Metals," J. Appl. Phys., 30, 514, (1959).

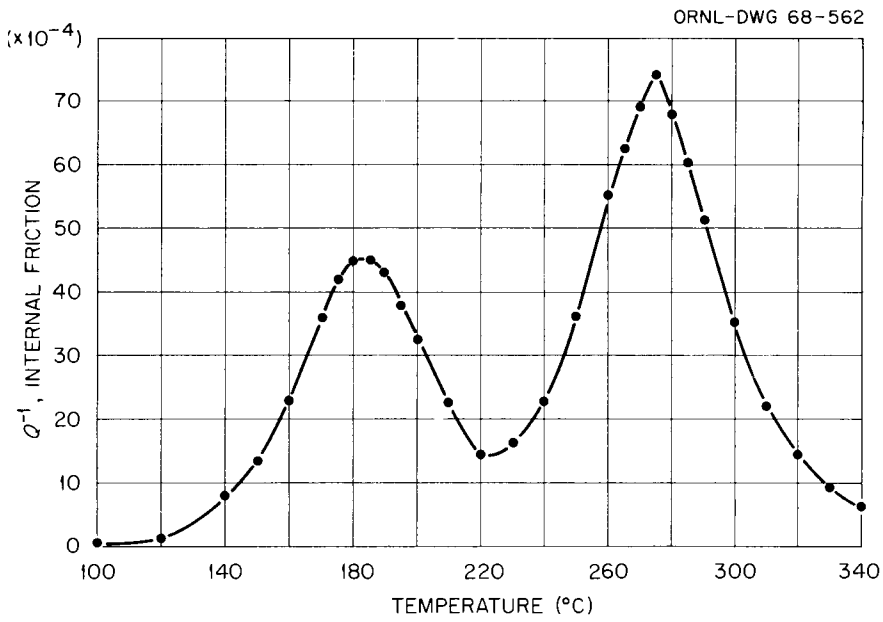

Fig. 20. Internal Friction of Vanadium as a Function of Temperature, Specimen V-D-3 Annealed 45 min. at ≈1230°C, 3 x 10^{-8} torr. Frequency 1.12 cps.

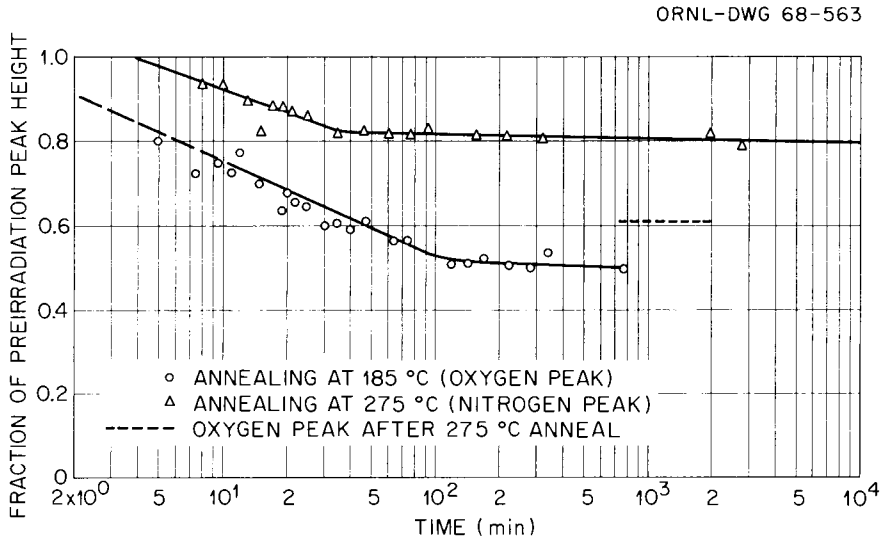

Fig. 21. Relative Decrease With Time of Oxygen and Nitrogen Peaks of Neutron-Irradiated Vanadium Specimen V-D-3. Fluence 7 x 10^{17} n/cm^2 (E > 1 Mev) at 60°C.

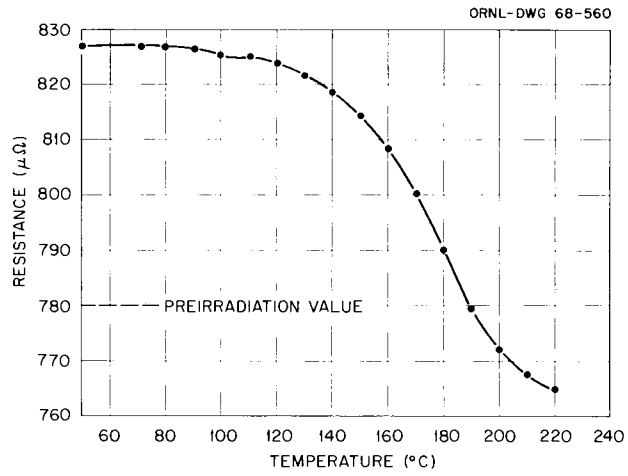

Fig. 22. Isochronal Annealing of Resistance of Vanadium Specimen V-D-5 Neutron-Irradiated to 7 x 10^{17} n/cm^2 (E > 1 Mev) at 60°C. Annealing Time 20 min. at Each Temperature Shown.

Figure 22 shows the resistivity decrease of a neutron-irradiated vanadium specimen as a function of annealing temperature. This specimen contained the same amount of interstitial impurity as the internal friction specimen discussed above, and was given an identical irradiation. As the figure shows, there is a large resistivity annealing stage centered at about 180°C, which corresponds with the temperature of the oxygen internal friction peak. Presumably another resistivity annealing stage corresponding to the nitrogen internal friction peak will be observed as the annealing temperature is increased further. It was mentioned above that the internal friction measurements indicated the presence of carbon in solution in this specimen in addition to oxygen and nitrogen. Since the carbon and oxygen atoms have very nearly equal jump rates at a given temperature, we would expect the resistivity annealing stages for carbon and oxygen to overlap. There is a small dip in the resistivity annealing curve shown in Fig. 22 at 100°C, which could be caused by the slightly greater mobility of carbon. This dip

does not show up very well in the figure because of the scale, but it is certainly a real effect and very apparent when the data are plotted on an expanded scale. The annealing stage shown in Fig. 22 occurs at a homologous temperature of about 0.21 T_m. The 0.15 T_m temperature for vanadium is 50°C.

The Annealing Characteristics of Neutron Irradiated Niobium

S. M. Ohr, R. P. Tucker,* and E. D. Bolling

Sometime ago, Makin and Minter[54] first reported the observation of a large increase in the yield stress in neutron irradiated niobium upon post-irradiation annealing. They concluded that in their niobium "radiation-anneal hardening" resulted from the condensation of radiation-produced vacancies along dislocation lines. In a recent study using internal friction and electrical resistivity techniques, Williams et al.[55] found that the temperature range and activation energy associated with the previously reported radiation-anneal hardening agree closely with those characteristic of oxygen migration in niobium. Support for attributing the hardening to oxygen lies in the high oxygen impurity level of 1600 wt ppm reported by Makin and Minter.

In the present study, the annealing characteristics of neutron irradiated niobium, relatively free of oxygen, have been investigated in

---

*Oak Ridge Graduate Fellow from the University of Tennessee under appointment from Oak Ridge Associated Universities.

[54]M. J. Makin and F. J. Minter, "The Mechanical Properties of Irradiated Niobium," Acta Met., 7, 361, (1959).

[55]J. M. Williams, J. T. Stanley, and W. E. Brundage, "The Interaction of Radiation Produced Defects and Interstitial Impurity Atoms in Niobium," Quarterly Progress Report: Irradiation Effects on Reactor Structural Materials, Nov. 1966-Jan. 1967, BNWL-CC-1053. Pacific Northwest Laboratory, Richland, Washington, 11.18, February (1967).

terms of tensile properties and transmission electron microscopy. Using the electron microscope, direct observations have been made of the annealing of irradiation induced defects. In particular, the defect size distribution following post-irradiation anneals was measured in order to seek microstructural evidence for the radiation-anneal hardening observed for annealing temperatures of 200°C and higher. Also, the nature of the defects has been investigated.

Experimental Procedures

The niobium used in this study was obtained from the CIBA Corporation in the form of dendritic powder. Thin sheet tensile samples of 0.005-inch thickness were prepared by cold rolling single crystal rods grown by an electron beam floating zone technique.[56] These sheet samples were given a recrystallization anneal at 1050°C for one hour in a dynamical vacuum of approximately 3×10^{-8} torr to give an average grain size of 44 μ. The impurity content was determined at this point and the results are shown in Table 5. Irradiation was carried out in the Hydraulic Facility of the Oak Ridge Research Reactor to a fluence of 2×10^{18} neutrons/cm^2 (E > 1 Mev) at a temperature below 50°C.

Both irradiated and unirradiated samples were annealed for two hours at temperatures from 200°C to 800°C in a vacuum better than 10^{-8} torr. Thin foils suitable for transmission electron microscopy were prepared by electropolishing in a solution, 85 parts nitric acid and

---

[56] R. E. Reed, "Electron Beam Floating Zone Refining of Niobium," in Proceedings of the Second International Conference on Electron and Ion Beam Science and Technology, April 17-20, 1966, Gordon and Breach Publishers, New York. To be published.

15 parts hydrofluoric acid by volume. The foils were examined in the Hitachi 11 A electron microscope operated at 100 kv and equipped with tilting and rotating stages.

Tensile Results

Figure 23 shows the lower yield stress, determined at 24°C, of irradiated and unirradiated samples as a function of annealing temperature for two hour anneals. In addition to an increase in the yield stress of 5.8 kg/mm^2 upon neutron irradiation, there is a further increase of up to 8.5 kg/mm^2 on annealing in the temperature range 200 to 400°C. As the annealing temperature is raised further the yield stress gradually recovers and finally reaches the pre-irradiation value at 800°C.

A characteristic feature of the present observations is radiation-anneal hardening in the temperature range 200 to 400°C; whereas, Makin and Minter observed hardening in the range 100 to 200°C. Furthermore, it should be emphasized that we observed no radiation-anneal hardening in the range 100 to 200°C even though the annealing time employed in the present study is two hours compared to one hour used by Makin and Minter. A second point of interest is the increase in the yield stress of unirradiated samples also in the range of 200 to 400°C.

In regard to the yielding characteristics we have noted that the yield drop, that is prominent after neutron irradiation, diminishes upon annealing up to the annealing temperature of 400°C. The yield drop then returns after anneals at temperatures greater than 500°C.

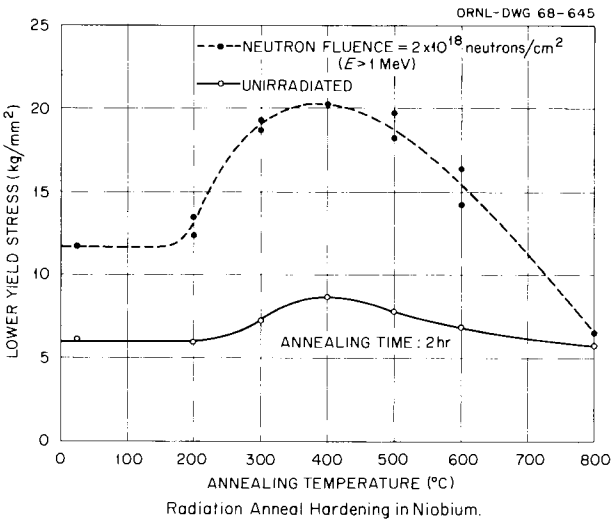

Radiation Anneal Hardening in Niobium.

Fig. 23. The Lower Yield Stress of Neutron-Irradiated and Unirradiated Niobium as a Function of Annealing Temperature for Two-Hour Anneals.

Table 5

IMPURITY CONTENT OF NIOBIUM IN WEIGHT PARTS PER MILLION

Impurity	Content	Impurity	Content
C	60	Ta	20
O	38	W	10
H	2	Zr	10
N	5	Hf	5
		Fe	1

Transmission Electron Microscopy

Figure 24 shows irradiation damage in the form of black spots under the kinematical diffraction condition for samples irradiated and subsequently annealed for two hours at 200, 300, and 400°C. Plots of the defect density as a function of spot size, measured on a Zeiss particle size analyzer, for as-irradiated and after the post-irradiation anneal at 400°C are shown in Fig. 25. Although more counts are needed to assess accurately changes upon annealing, there is a significant change in the peak size from 80 Å to 130 Å. There is a very slight decrease in the overall density of spots, which indicates that the defects simply grow in size in this range of temperatures.

The annealing of defects after two hours at 500, 600, and 800°C is shown in Fig. 26. The most noticeable feature is the appearance of numerous small spots throughout the sample after the anneal at 600°C. Figure 27 shows that the usual large defects have been denuded in the vicinity of a grain boundary, whereas the small defects show no denudation at the grain boundary. These observations are similar to those made by Makin et al.[57] in neutron irradiated copper following a mild anneal at 300°C. They inferred that the large defects are formed by the condensation of interstitial atoms and the small defects are vacancy clusters.

---

[57] M. J. Makin, A. D. Whapham, and F. J. Minter, "The Formation of Dislocation Loops in Copper During Neutron Irradiation," Phil. Mag., 7, 285, (1962).

PHOTO 90504

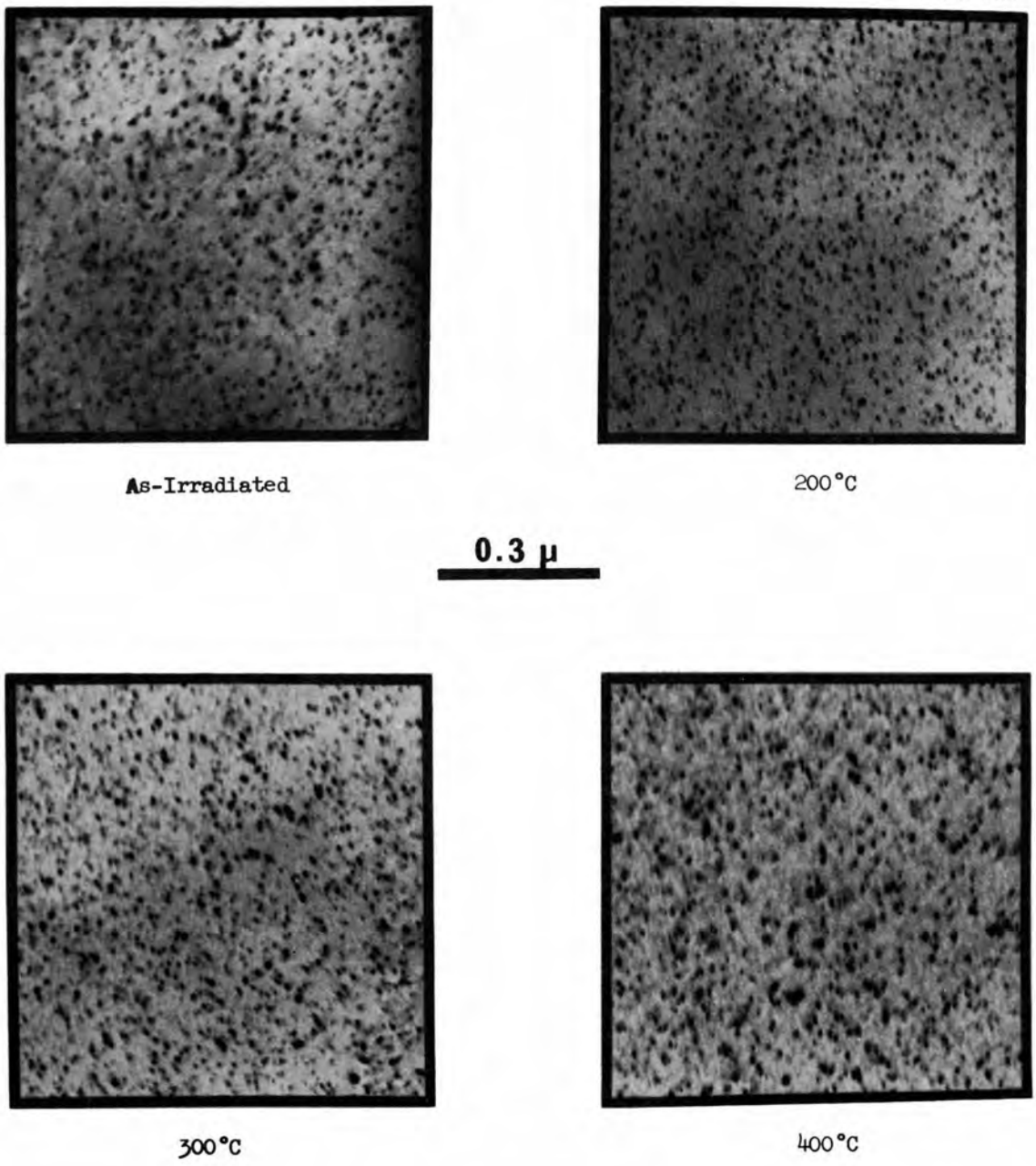

Fig. 24. Spot Damage in Neutron-Irradiated Niobium After Two-Hour Post-Irradiation Anneals at Temperatures Indicated. Fluence, 2×10^{18} neutrons/cm^2, E > 1 Mev.

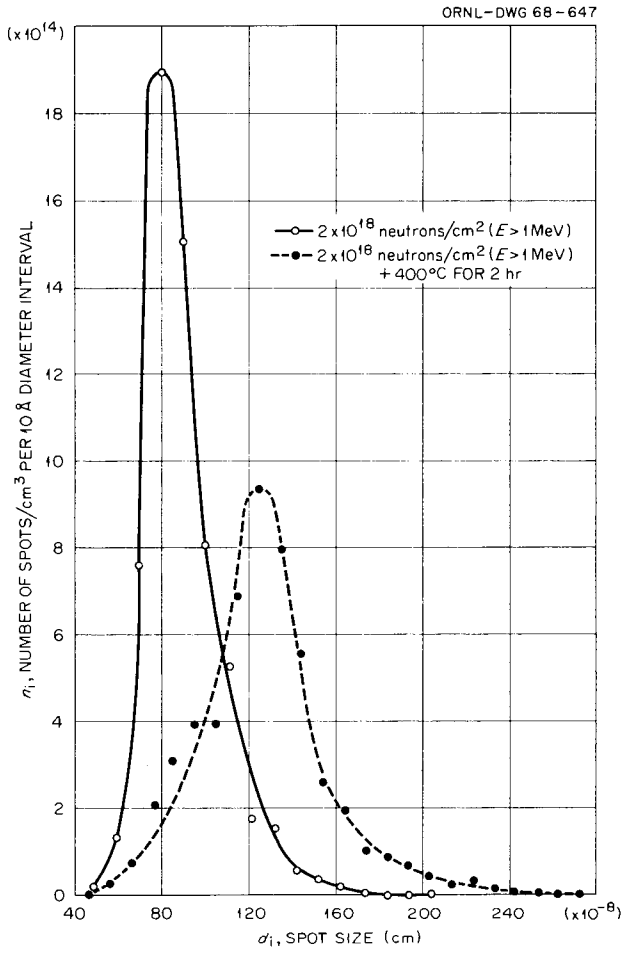

Fig. 25. Defect Size Distribution for Niobium As-Irradiated and After the Post-Irradiation Anneals at Temperatures Indicated.

PHOTO 90503

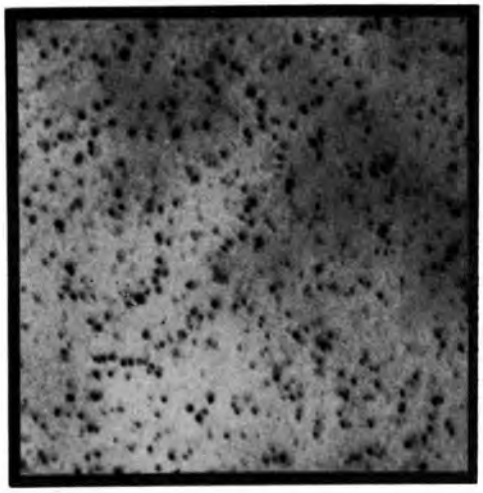

500°C

0.3 μ

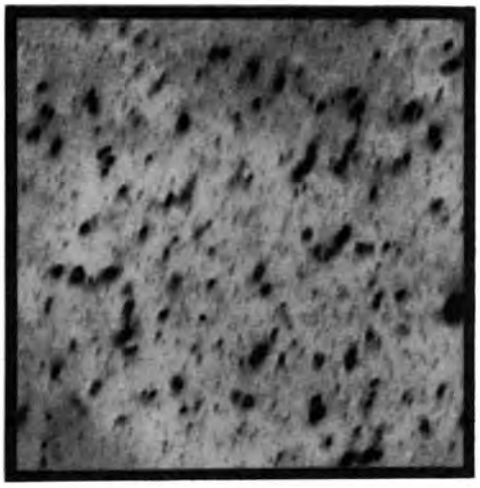

600°C

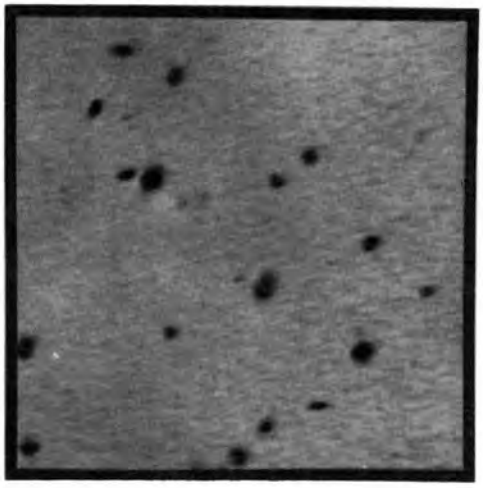

800°C

Fig. 26. Spot Damage in Neutron-Irradiated Niobium After Two-Hour Post-Irradiation Anneals at Temperature Indicated. Fluence, 2×10^{18} neutrons/cm^2, E > 1 Mev.

Fig. 27. Spot Damage in Neutron-Irradiated Niobium After Two-Hour Post-Irradiation Anneal at 600°C Showing Two Types of Defects. The Large Defects have been Denuded in the Vicinity of a Grain Boundary, whereas the Small Defects Show No Denudation.

Following the anneal at 800°C for two hours, most of the defects have annealed out leaving a small number of large defects resolvable in the electron microscope as dislocation loops. We have analyzed these large dislocation loops on the basis of the electron diffraction contrast theory[58] to determine the nature of the loops. In our analysis, use is

---

[58] A. Howie and M. J. Whelan, "Diffraction Contrast of Electron Microscope Images of Crystal Lattice Defects," Proc. Roy. Soc., A267, 206, (1962).

made of the stereo techniques in deciding the sense of inclination of loop planes. It is found that the loops of both interstitial and vacancy types are present, the former being somewhat more predominant. We have previously shown evidence that the defects visible in as-irradiated samples are mostly dislocation loops of the interstitial type.[59] Thus, it is quite reasonable to trace the origin of the large vacancy loops back to the small defects observed after the 600°C anneal.

Discussion

The present work has shown that in niobium containing 38 ppm oxygen and 60 ppm carbon radiation-anneal hardening does not occur in the temperature range at which oxygen atoms are believed to migrate. Instead the hardening is observed in the temperature interval 200-400°C in which carbon atoms are mobile.

Transmission electron microscopy of irradiated and annealed niobium has revealed changes in defect size distribution. We have previously obtained in as-irradiated niobium a reasonable correlation between the defect size distribution on the observed increase in the yield stress, on the basis of the elastic interaction between moving dislocations and the defects.[59] The predicted increase in the yield stress is

$$\Delta \tau = \frac{G\, b}{4} \left(\Sigma\, n_i d_i\right)^{1/2}$$

where G is the shear modulus, b is the Burgers vector, and n_i is the density of defects of size d_i. Based on the defect size distribution

---

[59] S. M. Ohr, R. P. Tucker, and M. S. Wechsler, "Radiation Hardening in B.C.C. Metals Niobium and Iron," in Proceedings of the International Conference on Strength of Metals and Alloys, Japan Inst. of Metals, (1968).

shown in Fig. 25 for the two hour anneal at 400°C, the increase in the yield stress on annealing is predicted as 0.34 kg/mm^2 compared to the observed anneal hardening of 8.5 kg/mm^2. Thus, the changes in the defect size distribution could not account for the anneal hardening.

Two other sources of hardening may be considered, one involves irradiation induced defects too small to be visible in the electron microscope and the other, interstitial impurities. If one accepts that all of the visible defects in the as-irradiated sample are interstitial in nature, vacancies could agglomerate into submicroscopic clusters during post-irradiation anneals. At 400°C these clusters could reach a critical size that is effective in impeding dislocation motion, thus causing the increase in the yield stress. At 600°C these vacancy clusters have grown sufficiently in size so as to become visible for the first time in the electron microscope. Evidence against such a mechanism is found in the work of Williams et al.[60] The resistivity of one of their samples, containing 30 ppm carbon and less than 3 ppm oxygen, has increased on irradiation, but it decreased well below the pre-irradiation value in the temperature interval 200 to 320°C. This implies that the species migrating in this temperature range is not directly identifiable with radiation induced defects.

The most reasonable interpretation of the present data can be made in terms of interstitial carbon. As was already pointed out, the anneal

---

[60]J. M. Williams, J. T. Stanley, and W. E. Brundage, "The Interaction of Radiation Produced Defects and Interstitial Impurity Atoms in Niobium," Quarterly Progress Report: Irradiation Effects on Reactor Structural Materials, Nov. 1966-Jan. 1967, BNWL-CC-1053. Pacific Northwest Laboratory, Richland, Washington, 11.18, February (1967).

hardening is observed precisely in the range of temperatures at which carbon atoms are found to migrate.[60] Another evidence in support of this mechanism is found in our present observations that the unirradiated samples also show a slight increase in the yield stress in this temperature range. After the recrystallization anneal the most of the carbon atoms are expected to have precipitated from the lattice due to extremely low solid solubility in niobium. Evidence exists that carbon is redissolved into the lattice during neutron irradiation.[61] Upon annealing in the range of 200 to 400°C, carbon atoms are expected to migrate to irradiation induced dislocation loops and are trapped there. Transmission electron microscopy has shown that the moving dislocations in neutron irradiated niobium during plastic deformation sweep up the defects thus creating defect free channels.[62] It appears that the presence of trapped interstitial atoms at the defects creates further difficulty in the sweep-up process and impedes the motion of dislocations.

Fluence Dependence of Radiation Hardening in Polycrystalline Niobium

M. S. Wechsler, R. P. Tucker, and S. M. Ohr

Introduction:

The form of the relationship between the increase in yield stress and neutron fluence has been the subject of some interest, since it provides a direct test of models of radiation hardening. Furthermore, in

---

[61] J. T. Stanley and W. E. Brundage, "The Interaction of Radiation Produced Defects and Interstitial Impurity Atoms in Niobium," Quarterly Progress Report: Irradiation Effects on Reactor Structural Materials, May-June 1966, BNWL-CC-784. Pacific Northwest Laboratory, Richland, Washington, 10.30, August, (1966).

[62] R. P. Tucker and S. M. Ohr, "Direct Observation of Neutron Irradiation Damage in Niobium," Phil. Mag., 16, 643, (1967).

connection with the use of structural metals in radiation environments, it is often useful to have a basis for extrapolating the results for low or moderate neutron exposures to the higher exposures anticipated in service. This is especially true today in view of the high exposures appropriate to fast breeder reactor systems. However, the earlier work on the fluence dependence of radiation hardening has been largely devoted to the face-centered cubic metals, especially copper, as was reviewed recently by Makin.[63] In this report, we describe some results for the body-centered cubic metal niobium.

The models for radiation hardening are based on the idea that the radiation introduces clusters of defects which act as barriers to dislocation motion. In the dispersed barrier model, the defect clusters are assumed to be scattered at random in the metal lattice with a density proportional to the neutron fluence, at least at low radiation levels. The range of cluster sizes that produces maximum hardening is not known exactly. However, it has been shown[59,64] that the temperature dependence of the yield stress in niobium is not greatly changed upon neutron irradiation. From this we infer that the clusters are fairly large and thermal vibrations are not effective in assisting dislocations in surmounting them. The clusters responsible for the hardening may therefore be visible by transmission electron microscopy. The

---

[63] M. J. Makin, "Radiation Damage in Face-Centered Cubic Metals and Alloys," in Radiation Effects, edited by W. Sheely, Gordon and Breach Science Publishers, Inc., New York, (1968).

[64] S. M. Ohr, R. P. Tucker, and M. S. Wechsler, "Radiation Hardening in B.C.C. Metals Niobium and Iron," Radiation Metallurgy Section Solid State Division Progress Report for Period Ending July 1967, ORNL-4195, 34, (1967).

size distribution of clusters has been determined[59,64] from electron microscope photographs for two particular fluence levels, 5×10^{17} and 2×10^{18} neutrons/cm^2 ($E > 1$ Mev). Based on these and a strong-barrier model of radiation, the predicted increases in yield stress upon irradiation were shown to be consistent with those actually observed. In the present study, we report on the measurement of radiation hardening in niobium over a range of fluences from 7×10^{16} to 4×10^{18} neutrons/cm^2 ($E > 1$ Mev). The shape of the hardening curve is analysed on the basis of several models.

If a cross section σ_B is assigned to the production of the clusters responsible for the radiation hardening, the number produced per unit volume by a fluence Φ may be written as

$$N_v = N \sigma_B \Phi$$

where N is the atomic density. The average spacing of clusters (barriers to dislocation motion) on the slip plane is then

$$\ell = \frac{1}{(N_v d)^{1/2}} = \frac{1}{(N \sigma_B d\Phi)^{1/2}} \qquad (2)$$

to within a geometrical factor[65] where d is the effective size of the cluster or barrier. In the constant line tension approximation, the breakaway stress σ is given by [66]

$$F = \frac{\sigma}{2} b \ell \qquad (3)$$

---

[65] U. F. Kocks, "On the Spacing of Dispersed Obstacles," Acta Met., 14, 1629, (1966).

[66] D. K. Holmes, "Radiation Damage in Non-Fissionable Metals," in The Interaction of Radiation With Solids, North Holland Publishing Co., Amsterdam, 1964, 147.

where F is the strength of the barrier. Associating this stress with the increase in stress upon irradiation, $\Delta\sigma$, we have from Eqs. (2) and (3):

$$\Delta\sigma = \frac{2F}{b}\left(N\,\sigma_B\,d\,\Phi\right)^{1/2} \qquad (4)$$

which predicts an increase in stress proportional to the square root of the fluence. Despite the simplifications inherent in the derivation of this relation, it is instructive to see how well it is obeyed for the neutron-irradiated niobium under investigation.

Experimental Details:

The starting niobium stock was obtained from CIBA Corporation in the form of niobium powder. The powder was drop cast, given several electron-beam zone passes, and rolled to 5-mil sheet from which tensile samples, 4.2 mm wide and 12.7 mm gage length, were stamped out. The samples were then given a recrystallization anneal at 1050°C, which produced a grain size of about 44 μ. The photomicrograph in Fig. 28 shows the grain structure. A chemical analysis of the recrystallized material is given in Table 5.

The samples were irradiated for various lengths of time in Tube 12 of the Hydraulic Facility of Position F-8 in the Oak Ridge Research Reactor. The neutron flux as determined by nickel monitors was 2.0 x 10^{13} neutrons per cm^2 sec (E > 1 Mev) and the irradiation temperature was below 50°C. Following a waiting period for radioactive decay, the samples were tested at room temperature at a crosshead speed of 0.01 cm/min which corresponds to a strain rate of 1.3 x 10^{-4} sec^{-1}.

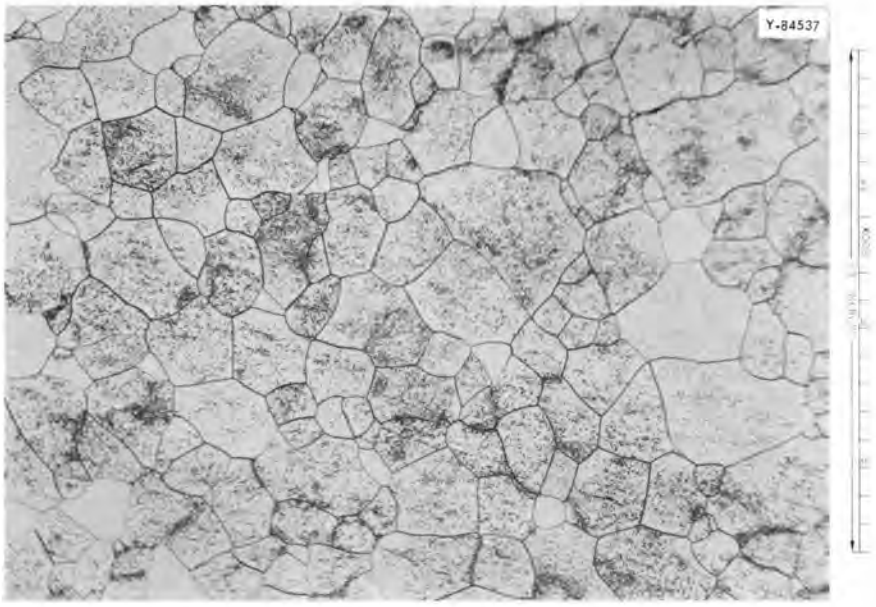

Fig. 28. Grain Structure in Niobium After Recrystallization at 1050°C for 1 Hour. Etch Pits are Observable in Most Grains. Etchant: 10 Parts HF, 10 Parts H_2SO_4, 10 Parts H_2O, 1 Part H_2O_2.

Results:

Figure 29 shows the stress-strain curves as a function of neutron fluence. The irradiation causes an increase in upper and lower yield stresses and a decrease in uniform and fracture strains. These effects are significant even at fluences below 10^{17} neutrons/cm^2 (E > 1 Mev).

The dependence of the increase in the upper and lower yield stresses on neutron fluence is illustrated in Fig. 30. Each point represents the average value of several determinations for each fluence level. It is seen that the increase in yield stress is proportional to the square root of the fluence, as predicted by Eq. (3), only for the measurements at the lower fluences (below about 10^{18} neutrons/cm^2 E > 1 Mev). At higher fluences, the yield stress increases less rapidly.

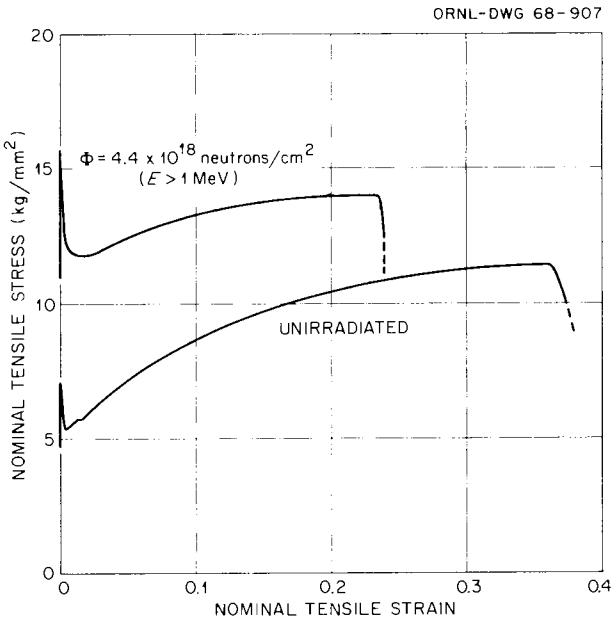

Fig. 29. Stress-Strain Curves for Polycrystalline Niobium Sheet Samples Tested in Tension at 25°C.

Table 6

RADIATION HARDENING IN NIOBIUM

b, Burgers vector, {110} <111> slip	2.85 Å
Nb^3, N = atomic density	1.30
G, shear modulus, {110} <111>(Ref. 58)	4280 kg/mm^2
B, Eq. (5) and Fig. 30	0.58 x 10^{-8} $(\frac{kg}{mm^2})$.cm
σ_B, barrier production cross section, using d = 80 Å (text)	
(1) infinitely strong barriers, F = 0.8 Gb^2 (Refs. 59,64)	0.02 barns
(2) loop hardening, F = 0.25 Gb^2 (Refs. 59,64)	0.2 barns
σ_c, cluster production cross section (Ref. 62)	0.04 barns
σ_s, neutron scattering cross section (Ref. 71)	8 barns

Discussion:

The curves drawn through the experimental points in Fig. 30 indicate two straight line portions. It is reasonable to assume that the initial portions of the curves correspond to hardening of the type described by Eq. (4). In this case, the slope, B, of the initial line is given by

$$B = \frac{2F}{b} (N \sigma_B d)^{1/2} \qquad (5)$$

From Fig. 30 we find $B = 0.58 \times 10^{-8}$ (kg/mm^2). cm for the lower yield stress. As we have said, the cluster size critical to radiation hardening is not well known. However, if we choose a size near the size observed by transmission electron microscopy, the cross section σ_B may be calculated from (5) and compared to other pertinent cross sections (Table 6). The observations of Tucker and Ohr[67] indicated that the cluster size distribution peaks at about 80 Å for $\Phi = (0.5 - 2.0) \times 10^{18}$ neutrons/cm^2 (E > 1 Mev); hence we take d = 80 Å. Now, for infinitely strong barriers, Kocks[68] and Foreman and Makin[69] have shown that $F = 0.8\ Gb^2$, where G is the shear modulus. On the other hand, Ohr et al.[59,64] have indicated that for loop hardening $F = 0.25\ Gb^2$. A calculation of G for {110}⟨111⟩ shear based on the room temperature

---

[67] R. P. Tucker and S. M. Ohr, "Direct Observation of Neutron Irradiation Damage in Niobium," Phil. Mag., 16, 643, (1967).

[68] U. F. Kocks, "A Statistical Theory of Flow Stress and Work Hardening," Phil. Mag., 13, 541, (1966).

[69] A. J. E. Foreman and M. J. Makin, "Dislocation Movement Through Random Arrays of Obstacles," Phil. Mag., 14, 911, (1966).

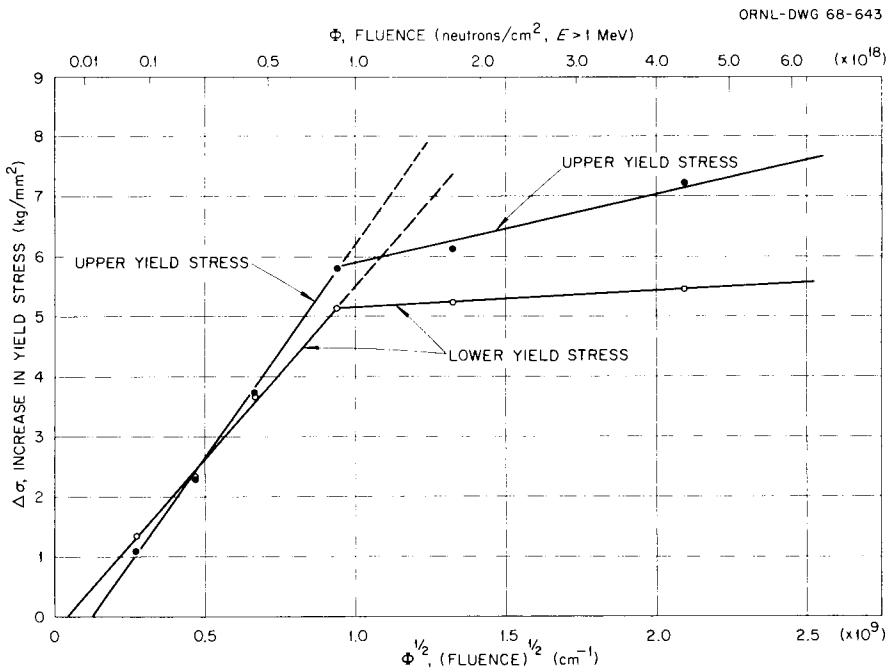

Fig. 30. Increase in Yield Stress Versus $\Phi^{1/2}$ for Polycrystalline Niobium, Showing Straight Line Fit to Low-Φ Portion. Irradiation Temperature, <50°C. Test Temperature, 25°C.

elastic constants given by Carroll[70] gives G = 4280 kg/mm^2. As indicated in Table 6, the σ_B deduced from these considerations are 0.02 and 0.2 barns for infinitely strong barriers and for loop hardening, respectively. It is difficult to tell at this time how reasonable these σ_B values are. However, it is interesting that these cross sections bracket the cross section for the production of clusters visible by transmission electron microscopy, i.e. the value σ_c = 0.04 barns deduced from Tucker and Ohr's observation[67] that 5 x 10^{15} clusters/cm^3 are present in a foil irradiated to 2 x 10^{18} neutrons/cm^2,

[70]K. J. Carroll, "Elastic Constants of Niobium from 4.2° to 300°K," J. Appl. Phys., 36, 3689, (1965).

E > 1 Mev. It is of interest, also, to compare these cross sections with the neutron scattering cross section[71] of about 8 barns. Since the σ_B's fall between 0.02 and 0.2 barns, we conclude that only one barrier is produced per 40 - 400 neutron collisions.

A further point illustrated in Fig. 30 is the reduced slope for $\phi \gtrsim 10^{18}$ neutrons/cm^2. A saturation in the rate of hardening has been observed previously for FCC metals[72,73] and is one of the puzzling features of radiation hardening since it occurs at ϕ levels too low to be explained easily in terms of overlap of clusters. Another possibility has been treated by Varley.[74] In a kinetic analysis of the nucleation and growth of clusters, he showed that a time is reached at which no new loops are formed while those already present grow in size.

Still another possibility is that the strength of the barriers depends upon the formation of complexes between defect clusters and interstitial impurities. Williams et al.[75] have shown that the annealing stage at about 150°C in irradiated niobium is associated with the motion

---

[71] D. J. Hughes and R. V. Schwartz, "Neutron Cross Sections," BNL-325, 201-202, (1958).

[72] M. J. Makin, "Radiation Damage in Face-Centered Cubic Metals and Alloys," in Radiation Effects, edited by W. Sheely, Gordon and Breach Science Publishers, Inc., New York, (1968).

[73] M. J. Makin and F. J. Minter, "Irradiation Hardening in Copper and Nickel," Acta Met., 8, 691, (1960).

[74] J. H. O. Varley, "The Agglomeration into Clusters of Interstitial Atoms and Vacancies Generated by Fast Neutron Irradiation," Phil. Mag., 7, 301, (1962).

[75] J. M. Williams, W. E. Brundage, and J. T. Stanley, "The Effect of Oxygen on 'Stage III' Annealing in Neutron-Irradiated Niobium," to be published in Metals Science Journal.

of interstitial oxygen to radiation-produced clusters. Also, the radiation anneal hardening discussed in another section of this report[76] indicates that the motion of interstitial impurities to defect clusters is responsible for an additional increment of hardening upon annealing. It might be suggested that defect-impurity aggregation takes place early in the irradiation in the present experiments. This process requires a species of interstitial impurity mobile at the irradiation temperature (below 50°C) and on the exhaustion of the supply of these at fluence levels of about 10^{18} neutrons/cm^2. Perhaps hydrogen is a possibility, since it is known to be introduced easily into refractory metals[77], and is likely to be mobile at the temperature of irradiation.

Deformation of Irradiated and Unirradiated Nb Single Crystals in Compression

H. D. Guberman and R. E. Reed

The present investigation was undertaken to evaluate the effect of neutron irradiation upon the deformation characteristics of niobium. In particular, we wished to determine how the increase in flow stress upon neutron irradiation was apportioned between the thermal and athermal components of stress. Such information is necessary for developing detailed models which will enable us to understand the nature of radiation-induced hardening. In this report we present the results of testing at 194°K, 298°K and 525°K for unirradiated Nb and samples irradiated to 1.1×10^{17} and 8.3×10^{17} n/cm^2, E > 1 Mev.

---

[76] S. M. Ohr, R. P. Tucker, and E D. Bolling, "The Annealing Characteristics of Neutron Irradiated Niobium," this report.

[77] G. D. Westlake and W. R. Gray, "A Pitfall in the Preparation of Metal-Hydrogen Alloys for Transmission Electron Microscopy," Appl. Phys. Lett., 9, 3-4, July (1966).

The material used in this investigation was notably purer than that used in prior studies of the properties of Nb.[78] Single crystals were grown by an electron-beam floating zone technique which involved three passes of the molten zone. The starting material was a CIBA stock which was particularly low in Ta and W.[78] The resistivity ratio of the material between room temperature and 4.2°K ranged between 471 and 494. The crystals were grown with a ⟨491⟩ rod axis such that the maximum resolved shear stress fell on the {110}⟨111⟩ slip system.

Compression samples were cut from the zoned rod by a spark erosion process utilizing a 0.25 mm Cu wire as the cutting tool and the No. 6 spark setting of the Servomet spark machine. The ends of the samples were lapped by hand until they were flat and parallel to within 0.06°. The samples were then lightly polished in a solution of $HF:HNO_3$ (1:4) chilled in an ice and water bath to reduce the possibility of charging with hydrogen. The sample dimensions after fabrication were typically 9.5 mm in length and 4.3 mm in diameter.

Irradiations were performed in the Hydraulic Facility of the Oak Ridge Research Reactor with the samples shielded by cadmium tubing about 1.2 mm in thickness. The irradiation temperature was 88° ± 5°C. The samples were stored at room temperature for about two weeks to allow the radioactivity to decay prior to testing.

---

[78] R. E. Reed, this report.

All the compression tests were carried out on a floor model Instron testing machine in a fixture designed to ensure axiality of loading. The crosshead speeds were varied between 0.02 in/min and 0.002 in/min for strain-rate change measurements. The stress measurements reported here are from the higher strain rate. The samples were tested in air at room temperature and in an oil bath (Dow-Corning Silicone Oil No. 200, vicosity 50 cs) which was also used as the high temperature bath. At elevated temperatures the oil was heated by thermistor controlled electric immersion heaters to the desired temperature. The lower temperature was achieved by a dry-ice and acetone bath. During testing the fluids were constantly stirred to ensure uniformity of temperature distribution. During the high temperature tests, the oil bath and the compression jig were first raised to the testing temperature and then the sample was inserted in order to minimize the time at an elevated temperature. The samples normally reached the yield point within four minutes after immersion and the entire test was completed after about seven minutes.

The results of the mechanical testing are summarized in Table 7 and the pertinent data are displayed in Fig. 31. The data show a significant temperature dependence of the yield stress which is somewhat affected by the neutron irradiation. The high temperature tests were carried out at a temperature which, according to Conrad,[79] is in the

---

[79]H. Conrad, "The Relation Between the Structure and Mechanical Properties of Metals," Proceedings of the Conference held at the National Physical Laboratory, Teddington, Middlesex, 503, January (1963).

Table 7

SUMMARY OF MECHANICAL MEASUREMENTS+

	Temp.	Flow Stress or L.Y.S. (kg/mm^2)	U.Y.S. (kg/mm^2)
Non-Irrad.	298°K	1.63 ± .06	-
1.1 x 10^{17}n/cm^2	298°K	2.25 ± .07	2.89 ± .03
8.3 x 10^{17}n/cm^2	298°K	2.98 ± .04	3.8 ± .4
Non-Irrad.	500° - 525°K	0.286 ± .005	-
1.1 x 10^{17}n/cm^2	525°K	1.00 ± .04	1.05 ± .02
8.3 x 10^{17}n/cm^2	525°K	1.26 ± .04	1.64 ± .02
Non-Irrad.	194°K	9.28 ± .04	-
1.1 x 10^{17}n/cm^2	194°K	12.2 ± .2	12.7 ± .4
8.3 x 10^{17}n/cm^2	194°K	12.5	16.1

+All stresses are resolved shear stresses

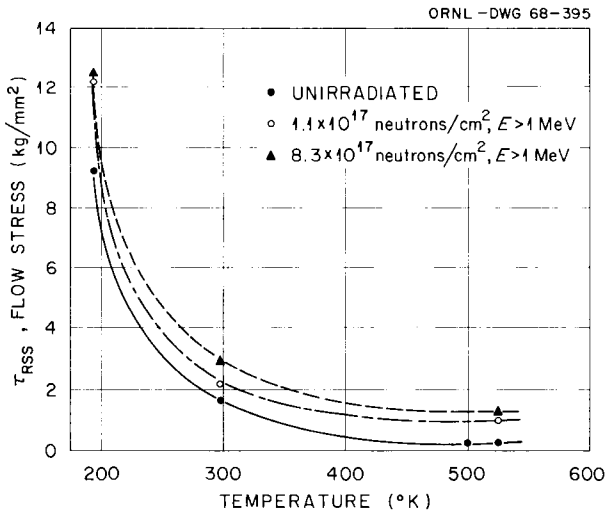

Fig. 31. Yield Stress vs Temperature as a Function of Neutron Irradiation for Compression Tests on High-Purity Nb Single Crystals.

region where the thermal component of stress (also known as the effective stress) has been reduced to zero leaving only the athermal component, i.e. that which is associated with long range dislocation interactions. The high temperature data indicates that neutron irradiation has a significant effect upon the athermal component of stress. However, the non-parallel relationship of the curves in Fig. 31 suggests that there is also an effect upon the thermal component of stress especially at lower temperature.

Measurements were also made of the activation volume V*, a parameter of interest from the thermal activation theory of deformation. The activation volume may be defined by the following expression.

$$\frac{V^*}{kT} = \left.\frac{\ln \dot{\epsilon}}{\tau^*}\right)_T$$

where $\dot{\epsilon}$ is the strain rate, τ^* is the effective stress and the other symbols have their usual meanings. This parameter may also be related to the microscopic size and spacing of the obstacles to dislocation motion. The activation volume was determined with respect to strain as a function of temperature and radiation fluence (Figs. 32 and 33).

At room temperature v* appears to be independent of strain and slightly higher than the value found earlier for niobium grown in different ways from other starting material.[80] At 194°K v* appears to to have a tendency to decrease with strain. It is interesting to note that at 525°K where presumably the effective stress has been reduced

---

[80] R. W. Armstrong, R. E Reed, and H. D. Guberman, "Characterization of the Strain Rate Dependence of the Shear Stress for Niobium Single Crystals," Scripta Met., 1, 1257, (1967).

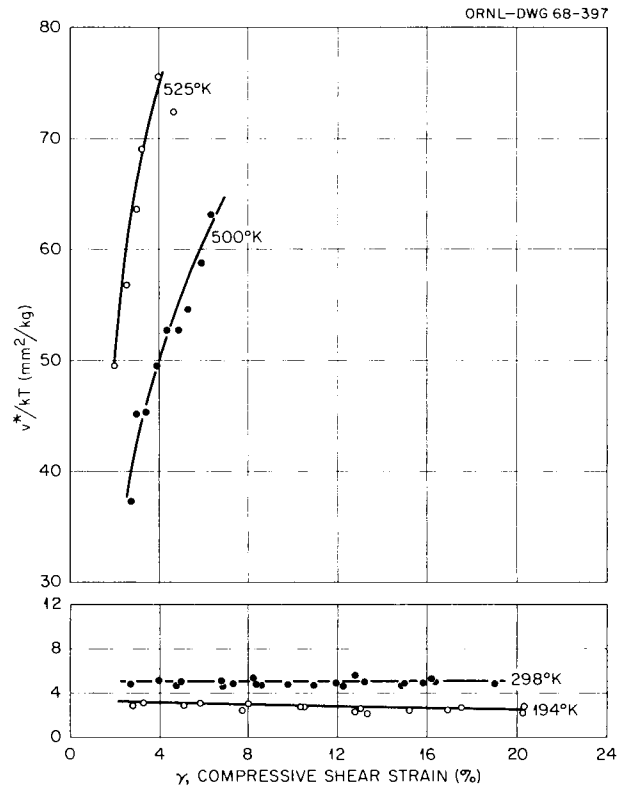

Fig. 32. Activation Volume vs Shear Strain as a Function of Temperature for Unirradiated High Purity Nb Single Crystals.

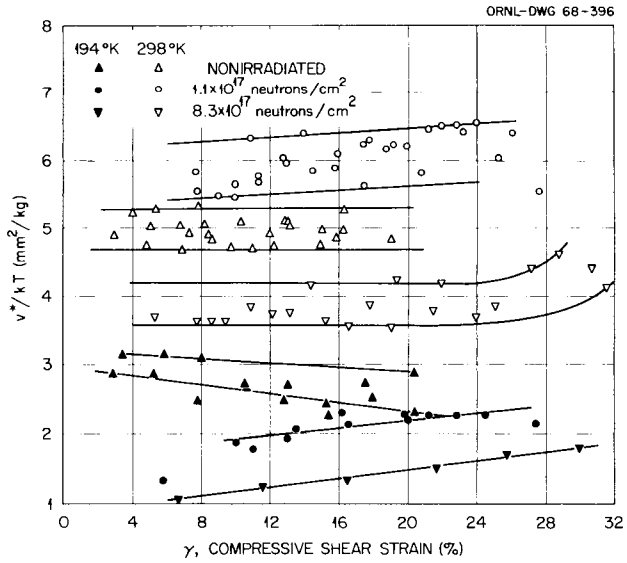

Fig. 33. Activation Volume vs Shear Strain as a Function of Temperature and Neutron Dose for High Purity Single Crystal Nb.

to zero and consequently there ought to be no effect of a change in strain rate, all the samples still showed a measurable strain-rate sensitivity. The effect has been reduced an order of magnitude as evidenced by the extremely high values of v*. Of further interest is the significant increase in v* with increasing strain.

The observation of strain-rate sensitivity at a temperature where one would expect it to be absent might be taken as evidence that the effective stress had not been reduced to zero and that consequently, we are not observing the athermal component of stress, τ_G. However, the measurements on the unirradiated Nb indicate that the yield stress is no longer changing with temperature in this temperature range. Therefore, it seems reasonable to accept this value of the stress as the athermal component of stress. The observed strain rate dependence might then be accounted for by the argument that the mobile dislocation density is not remaining constant during the strain rate change as is commonly assumed.[81] At lower temperatures this phenomenon would be unobserved because the relatively large effective stress is already acting to produce a strain rate sensitivity.

Neutron irradiation significantly affects the activation volume at 298°K and 194°K (Fig. 33). At room temperature the lower radiation dose increases v* while the higher dose decreases v*. At 194°K the value of v* is decreased progressively as the dose is increased. These references

---

[81] J. W. Christian, "A Comment on the Relation Between Dislocation Velocity and Effective Flow Stress," Acta Met., 15, 1257, (1967).

pertain particularly to the value of v^* at the lower yield point or initial flow stress. It is noteworthy that the slopes of the $v^* - \gamma$ curves are significantly changed especially at the low temperature, after irradiation.

These changes in the activation volume are entirely consistent with the values of the effective stress, τ^*, determined from the flow stress measurements (Table 8). It has been well established that the activation volume decreases as the effective stress increases.[82] Thus the increase and decrease in v^* at room temperature for the lower and higher doses is accompanied by a decrease and increase in τ^* . Similarly at 194°K, the decreasing v^* is accompanied by an increase in τ^* as the neutron dose is increased. This shows quite clearly that there is an effect of neutron irradiation upon the effective stress. At 298°K it is not as large as the effect on the athermal component of stress, but it is larger than the change in the athermal component at 194°K (Table 8).

At the present time no effort will be made to interpret these results except perhaps to point out that there may be some correlation with observations of defects in neutron irradiated Nb by transmission electron microscopy.[83] Small dislocation loops were found after doses greater than about 5×10^{17} n/cm^2 (E > 1 Mev) but not at doses lower

---

[82] H. Conrad, "The Relation Between the Structure and Mechanical Properties of Metals," Proceedings of the Conference held at the National Physical Laboratory, Teddington, Middlesex, 503, January (1963).

[83] R. P. Tucker and S. M. Ohr, "Direct Observation of Neutron Irradiation Damage in Niobium," Phil. Mag., 16, 643, (1967).

than that. Note that this falls between the two doses used in this experiment. An obvious extension of this work is to subject the samples tested to examination by transmission electron microscopy.

Table 8

Athermal and Thermal Components of Stress+

	τ_G (kg/mm^2)	$\tau^*_{298°K}$ (kg/mm^2)	$\tau^*_{194°K}$ (kg/mm^2)
Non-Irrad.	0.29	1.34	9.0
1.1 x 10^{17} n/cm^2, E > 1 Mev	1.00	1.25	11.2
8.3 x 10^{17} n/cm^2, E > 1 Mev	1.26	1.72	12.2

+All stresses are resolved shear stresses

Spark-Machining Damage in Niobium Single Crystals as Indicated by Etch Figures

H. D. Guberman

The preparation of metallic single crystals for research purposes by electric spark-machining has become increasingly popular. Numerous references, however, have already been made to various aspects of physical damage introduced by this technique, for example, the depth of damage in 70:30 brass[84] the formation of cleavage cracks in tungsten and molydenum[85,86], the temperature rise in the vicinity of a spark-cut,[87] and residual stresses in a spark-cut surface.[88] The latter reference also discusses phase changes and reviews the nature of spark-machined surfaces in general. In this note we report some observations concerning the distribution of dislocations in the vicinity of a spark-machined notch in single crystals of niobium.

---

[84] L. E. Samuels, "Surface Damage Produced by the Electric-Spark Cutting Process," J. Inst. Metals, 91, 191, (1962).

[85] P. Beardmore and D. Hull, "Nucleation of Cleavage Cracks in Tungsten and Molybdenum by Spark-Machining," J. Inst. Metals, 94, 14, (1966).

[86] L. Van Someren, "Cleavage Cracks Induced by Spark Machining," J. Inst. Metals, 94, 368, (1966).

[87] J. R. Hancock, J. G. Grosskreutz, and C. Q. Bowles, "Note on Specimen-Temperature Rise During Electric-Spark Cutting of Aluminum and Copper," J. Inst. Metals, 94, 74, (1966).

[88] H. K. Lloyd and R. H. Warren, "Metallurgy of Spark-Machined Surfaces," J. Iron Steel Inst., 203, 238, (1965).

Samples were sectioned by a spark-cutting device (see below) from a 1/2-inch-diameter single crystal with its longitudinal axis parallel to the ⟨111⟩ direction such that the surfaces to be studied were normal to the ⟨111⟩. The crystals were grown from a seed by an electron-beam floating zone process.[89] After sectioning, the samples were deeply polished in $HF:HNO_3$ (1:4) until a highly polished disc approximately 3-4 mm in thickness remained. A notch was then cut into the sample normal to the ⟨111⟩ axis using the Servomet spark-machine on No. 4 and No. 6 spark settings. Kerosene was used for the dielectric fluid. A locally designed device using 0.25 mm copper wire moving at a speed of about 5.3 cm/min was the cutting tool. The sample was then chemically etched after a carbon decoration treatment[90] to enable the grown-in dislocation substructure and spark-induced dislocation configurations to be observed by optical microscopy. For comparison, a notch was also introduced mechanically into a sample with a Gillings-HamCo thin sectioning machine and a 0.2 mm SiC wheel rotating at 6500 rpm.

In each case the distribution of dislocations in the vicinity of the cut was generally like that indicated in Fig. 34. The major features are zones of plastic deformation that extend beyond the notch in the direction of cutting. The directions about which these plastic zones appear to be symmetrically arranged lie approximately 40° to 50° from the direction of cutting. A region of extremely high dislocation density, such that etch figures cannot be resolved, is found adjacent to

---

[89] R. E. Reed, "Electron Beam Floating Zone Refining of Niobium," in Proceedings of the Second International Conference on Electron and Ion Beam Science and Technology, April 17-20, 1966, Gordon and Breach Publishers, New York. To be Published.

[90] H. D. Guberman, "Stress Dependence of Dislocation Velocity in Single Crystal Niobium," Acta Met., in press.

the cut surface at the root of the notch (Figs. 35 and 36). In the case of the No. 4 spark only, this region of extremely high dislocation density was found along the entire boundary of the cut. Numerous slip traces extending far beyond the area of view in Fig. 35 were observed in the case of the No. 4 spark. The depths of damage observed in the above examples are summarized in Table 9. The dimensions were determined either from the furthrest extent of recognizable slip traces or from the depth at which the dislocation density became equal to the average initial density in the matrix.

From these observations it is apparent that the damage decreases as one decreases the spark energy. Therefore, it is very likely that one may be able to reduce the damage even further, if it is necessary in a given situation, by operating at a still lower spark energy. It is also interesting to note that the damage produced by a careful mechanical cutting operation does not compare unfavorably with that produced by spark-machining in the intermediate spark range.

The high density of dislocations in the vicinity of the spark-cut surface gives evidence of the severity of the treatment the surface receives. Undoubtedly, some of the deformation is associated with the thermal stresses produced by the quenched material at the spark-produced crater.[88] However, the depth of penetration of the deformation and the particular distribution of the dislocations indicate that shock waves of considerable amplitude (especially at the higher spark energies) are generated and propagate through the bulk material.

Table 9

SUMMARY OF DEPTH OF DAMAGE ASSOCIATED WITH CUTTING[a]

	a (mm)	b (mm)
No. 4 Spark	0.75	1.5
No. 6 Spark	0.04	0.22
Cut-Off Wheel	0.15	0.40

[a]These dimensions were measured in the regions shown in Fig. 34.

ORNL-DWG 67-12797

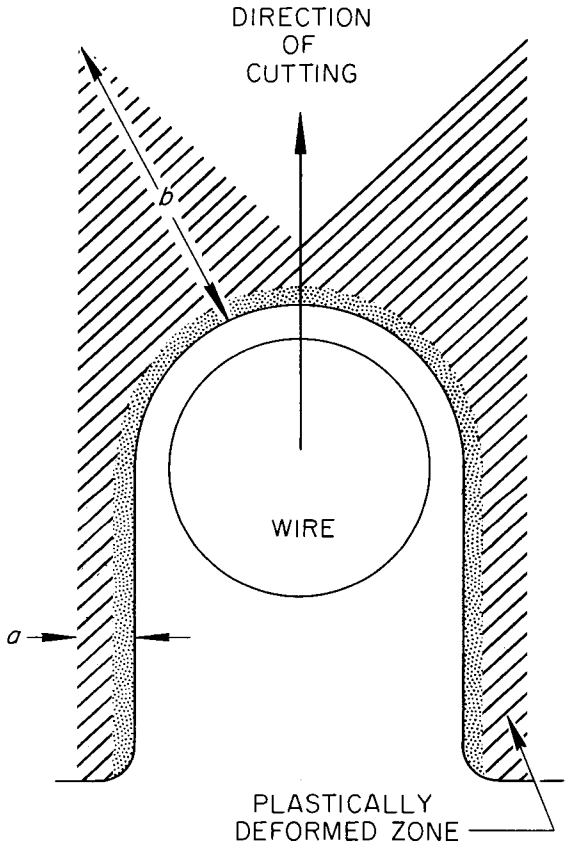

Fig. 34. Schematic of Spark-Cut Notch and the Region of Plastic Deformation.

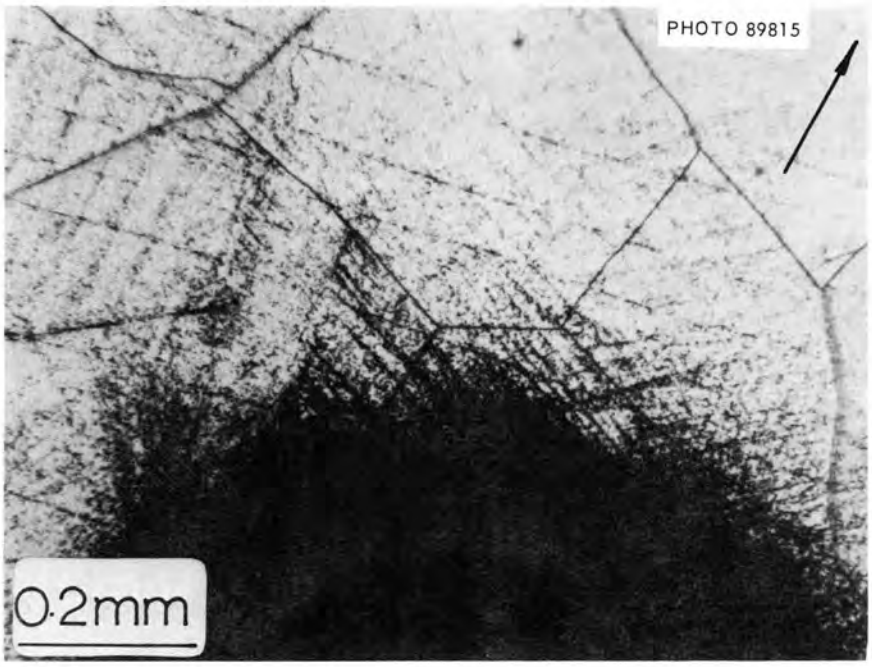

Fig. 35. Etch Pattern of the Root of the Notch Produced by No. 4 Spark on the Servomet Spark Machine. The Arrow Indicates the Direction of Motion of the Cutting Tool. Sub-Grain Boundaries and Spark-Induced Slip Traces are Observable.

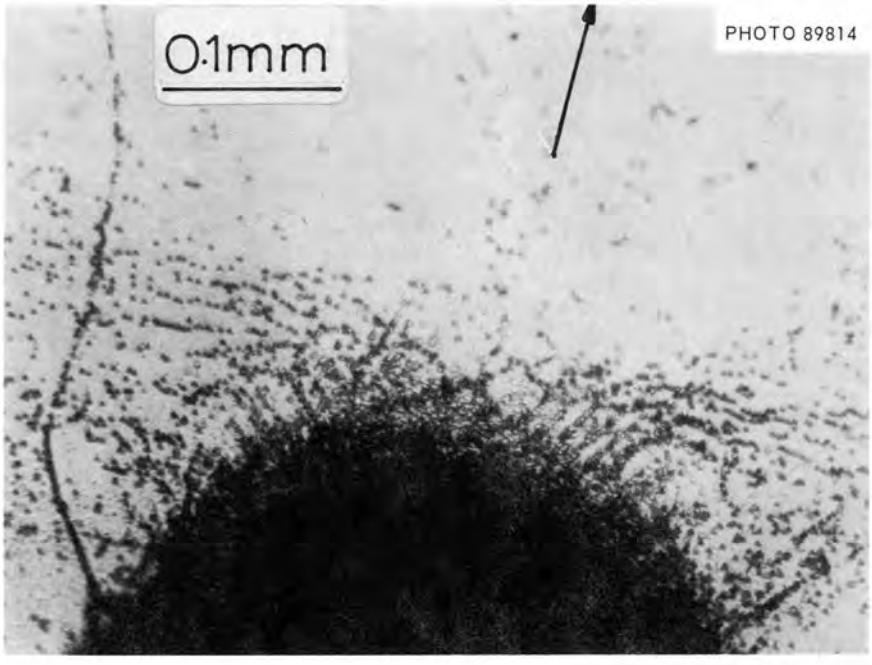

Fig. 36. Etch Pattern at the Root of the Notch Produced by a No. 6 Spark.

Evaluation of Niobium Source Materials Suitable for Electron Beam Float Zone Melting*

R. E. Reed, R. P. Tucker, and C. L. Brooks

Niobium metal from three sources was electron beam float-zone melted (EBFZM) in an evaluation test to find a suitable starting material for purification and growth of single crystals. Prior work[91] had shown that it was important to obtain a starting material low in Ta and W since these two metallic impurities could not be removed from niobium by the EBFZM technique. An initial evaluation[92] of niobium starting material prepared by electrodeposition from a molten salt[93] revealed that this type material was very promising as a source of low Ta and W niobium metal. However, it generally was received as a powder or porous chips and required an additional consolidation step to obtain a rod form suitable for EBFZM. This report describes the material characterization results obtained on Wah Chang Corp. electron beam drip melt ingot, DuPont Co. D3 granules, and CIBA Ltd dendritic powder after purification and crystal growth using a practical standard EBFZM schedule.

---

*Work performed under the Research Materials Program.

[91] R. E. Reed, "The Preparation and Purification of Single Crystals of Niobium," Radiation Metallurgy Section Solid State Division Progress Report for Period Ending February 1966, ORNL-3949, 35, (1966).

[92] R. E. Reed, "Niobium: Purification and Perfection," Radiation Metallurgy Section Solid State Division Progress Report for Period Ending January 1967, ORNL-4097, 20, (1967).

[93] G. W. Mellors and S. Senderoff, "Electrodeposition of Coherent Deposits of Refractory Metals: I. Niobium," J. Electrochem. Soc., 112, 266, (1965).

Experimental Procedure

A. Starting Materials:

The starting materials will be described separately as each had a different handling schedule for obtaining a rod form suitable for EBFZM.

1. Wah Chang Corp. Electron Beam Melted Ingot. --A 1-inch diameter bar, 3-ft long, which was formed from a 3-in. diameter electron beam drip melted ingot was purchased from Wah Chang Corp., Albany, Oregon. This rod was cold swaged down to 4.8-mm diameter. Rods were prepared for EBFZM by cutting to length, chemical polishing, washing in distilled water, and air drying. The chemical analyses for this material are listed in Table 10.

2. DuPont Co. D3 Granules. --Fifty pounds of niobium D3 granules were purchased from E. I. DuPont de Nemours and Co., Pigments Department, Wilmington, Delaware. The granules were consolidated by drop casting into 5/8-in. diameter rod, 5-in. long, using arc melting. This resulted in an increase in both the Ta and W impurity levels due to the Ta striking peg and W tipped electrode present in the arc casting furnace. The drop cast ingot was then cold swaged to 4.8-mm diameter rod. These rods were then prepared in the same way as the Wah Chang material for EBFZM. The chemical analyses for this material are also listed in Table 10.

3. CIBA Dendritic Powder. --Ten pounds of dendritic niobium powder was purchased from CIBA Ltd., Basle, Switzerland. This material had been prepared by electrodeposition from a molten salt. It was characterized by a low Ta and W content and a high Na content, as determined by neutron activation analysis. In order to avoid Ta and W contamination, the following schedule was used to consolidate this powder.

Table 10

Chemical Analyses of the Niobium
Starting Material Prior to EBFZM

Element	Material Source		
	Wah Chang wt. ppm	DuPont wt. ppm	CIBA wt. ppm
C	42	50	48
O	120	110	20
N	46	10	16
H	5	15	3
Ta	350	321	22
W	274	89	3
Fe	20	20	6
Zr	60	<1	<1
Cr	6	20	6
Ni	<1	80	8
Cu	<1	<1	3

Note: All other elements undetected or less than 1 wt. ppm.

a) The powder was packed into 5/8-in. diameter copper tubing which had been carefully cleaned and etched.

b) The tube was evacuated with a liquid nitrogen trapped mechanical pump and sealed under vacuum.

c) It was then cold swaged down to approximately 5/16-in. diameter.

d) After etching off the copper tubing, a niobium powder rod compact was obtained about 5-mm diameter and strong enough to EBFZM.

e) This powder compact was then zone melted for one pass in 5×10^{-6} torr at a zone speed of about 20 cm/hr. It was found that out-

gassing passes in the solid state were ineffective in preventing "spitting" when the molten zone was formed. Thus, the powder compact was melted completely through on the first pass.

f) A second pass was then made at 5×10^{-7} torr vacuum and 20 cm/hr zone speed.

g) The as-zoned rod was cold swaged to 4.8-mm diameter rod. This was done to obtain a constant diameter rod.

h) The as-swaged rod was prepared for EBFZM in the same manner as the other two starting materials.

The chemical analyses for this material are given in Table 10.

B. EBFZM Procedure:

All of these starting materials were further purified using a practical standard EBFZM procedure. High-purity as-zoned niobium single crystals with a resistance ratio $\left[R_{300°K}/R_{4.2°K(15\ kgauss)}\right]$ equal to 1400 have been previously grown.[92] However, this involved multipasses (10 passes) and high vacuums (8×10^{-10} torr). It was considered desirable to attain high purities using a more practical EBFZM schedule. The following procedure was used.

1. The specimen and a seed crystal were loaded into the electron beam zone refiner (Materials Research Corp. Model EBZ-94) which was equipped with a Viton O-ring on the stainless steel bell jar Wheeler seal. All other seals were copper gaskets.

2. The system was evacuated overnight without a bake, using a liquid nitrogen trapped 10-in. diffusion pump with a water baffled 4-in. diffusion pump as a booster pump. The base pressure attained was 5×10^{-8} torr.

3. Three zone passes were made on the 4.8-mm diameter rod over a 18-cm length, using a zone speed of 10 cm/hr. The vacuum was 3×10^{-7}, 1×10^{-7}, and 5×10^{-8} torr during the first, second, and third pass, respectively.

4. For some of the CIBA material, the first pass was made in a vacuum containing 1×10^{-5} torr oxygen. This was done by using a variable leak connected to a pure oxygen supply. The leak rate was adjusted to maintain 1×10^{-5} torr pressure on the ion gage. The second and third pass was made with the variable leak closed in a vacuum of 1×10^{-7} and 5×10^{-8} torr, respectively.

C. Annealing Procedure:

Some of the as-zoned rods were further treated in a high-vacuum annealing furnace. A bakeable stainless steel chamber was evacuated using a 6-in. diffusion pump trapped with first a water cooled baffle and then a liquid nitrogen cooled trap. The foreline of the pump contained a 2-in. diffusion booster pump which had a water baffle on it. A bakeable r.f. 20 KW power feedthrough was used to place an induction coil in the center of the chamber. The specimens were hung in the center of the coil with a split Ta radiation shield between them and the coil.

A typical annealing sequence would be :

1. Place the samples in the chamber and pump it to about 5×10^{-8} torr vacuum.

2. Bake the stainless steel chamber overnight at 250°C.

3. The pressure after cooling the chamber will be about 5×10^{-9} torr. The specimens are then annealed at 2350°C, as measured by an optical micropyrometer, for 5 hours. The pressure at the start of the

anneal was about 1 x 10^{-7} torr and near the end of the anneal about 2 x 10^{-9} torr.

4. The r.f. power was shut off quickly at the end of the anneal.

D. Material Characterization:

The rods were examined for purity using several methods. Direct methods were chemical analyses such as neutron activation analyses for Ta and W, vacuum fusion analyses for O, N, and H, Leco combustion analyses for C, and spark source mass spectrographic analyses for other metallic impurities. Indirect methods were: resistance ratios measured between room temperature and liquid helium temperature in a 15 kilogauss magnetic field; and a flow stress measured at the lower yield point of the resolved stress-strain tensile curve. The tensile specimens were prepared by centerless grinding and chemical polishing as described in a previous report.[94] The tensile testing was done at room temperature on a table model Instron machine at a strain rate of 1.7 x 10^{-4} sec^{-1}. The specimens were oriented with the tensile axis near <491> such that the Schmid factor for slip on the (101) $[\bar{1}11]$ system was 0.5.

Experimental Results

Table 11 summarizes the chemical analyses obtained on the three starting materials after the various purification steps. Comparing these data with those in Table 10, it is evident that the three-pass EBFZM schedule had little effect upon the carbon content of the starting materials. However, the oxygen and nitrogen content of the Wah Chang

[94] R. E. Reed, "Effect of the Number of Zone Passes on the Flow Stress of Niobium Single Crystals," Radiation Metallurgy Section Solid State Division Progress Report for Period Ending July 1966, ORNL-4020, 23, (1966).

Table 11. Chemical Analyses of Niobium after Various Purification Steps

Material Source	Spec. No.	Treatment	Chemical Analysis (wt. ppm)										
			C	O	N	H	Ta	W	Fe	Cr	Ni	Zr	Cu
Wah Chang	58d	Zoned	42	22	4	2	356	268	6	6	<1	20	1
	59d	Zoned & Annealed	32	25	3	1	309	233	<1	<1	<1	6	<1
DuPont	D12d	Zoned	42	14	3	1	313	88	<1	6	3	<1	3
	D13d	Zoned & Annealed	30	35	3	4	272	74	<1	<1	<1	<1	<1
CIBA	C14d	Zoned	51	27	8	2	21	2	<1	<1	<1	<1	<1
	C20d	Zoned (oxygen)	27	27	8	2	17	2	<1	<1	<1	<1	<1
	C21d	Zoned (oxygen) & Annealed	44	32	1	2	20	2	<1	<1	<1	<1	<1

and DuPont material was appreciably reduced. In the case of the CIBA material, when oxygen gas was bled into the vacuum system during the first pass, the carbon content was lower.

The metallic impurities excepting Ta and W in the starting materials were reduced by the EBFZM. In addition, they were further reduced during the high-temperature anneal. However, the interstitial impurity level was not apparently affected much by the anneal. In the case of the annealed oxygen-treated CIBA material, there was even an increase in the apparent interstitial impurity level, particularly carbon.

Table 12 lists the measured resistance ratios obtained on the three starting materials after various treatments. The average as-zoned resistance ratios were 302, 530, 150, and 416 for the Wah Chang, DuPont, CIBA, and CIBA with oxygen treatment, respectively. The CIBA starting material for specimens 15a and 15d had an abnormally high carbon content (114 ppm), and thus the as-zoned average ratio of about 88 was not normal for the CIBA material with the standard EBFZM schedule.

The annealing treatment increased the resistance ratio in all cases. The CIBA material that had the oxygen treatment during EBFZM had the highest resistance ratio (i.e., about 1500) after annealing at 2350°C for 5 hours in 2×10^{-9} torr vacuum. However, it should be pointed out that the high resistance ratio does not necessarily mean a low-impurity content. Table 11 shows that the high-temperature anneal had little effect upon the measured total impurity.

The resolved shear stresses at the lower yield points for <491> niobium single crystals deformed in tension at room temperature at a strain rate of 1.7×10^{-4} sec^{-1} are listed in Table 13 for the three

materials. It is evident that the annealing treatment had a profound effect upon this flow stress. With the exception of Spec. C15a, which had an anomalously high carbon starting material, the anneal decreased this flow stress for all three materials by approximately 30 to 40%. Again, it should be pointed out that the chemical analyses show that the anneal did not appreciably affect the measured impurity levels.

Table 12. Resistance Ratios of Niobium after Various Treatments

Source	Spec. No.	Treatment	$\frac{R_{300°K}}{R_{4.2°K(15\ kgauss)}}$
Wah Chang	58a	Zoned	299
	58d	Zoned	304
	59a	Zoned	299
	59b	Zoned	300
	59d	Zoned	310
	59d	Zoned and Annealed	734
	58a	Zoned-Centerless Grind-Chemical Polish	230
	59a	Zoned-Centerless Grind-Chemical Polish-Anneal	722
	59b	Zoned-Centerless Grind-Chemical Polish-Anneal	727
DuPont	D12a	Zoned	533
	D12d	Zoned	534
	D13a	Zoned	519
	D13d	Zoned	534
	D13d	Zoned and Annealed	951
	D12a	Zoned-Centerless Grind-Chemical Polish	404
	D13a	Zoned-Centerless Grind-Chemical Polish-Anneal	1003
CIBA	C14a	Zoned	138
	C14d	Zoned	162
	C15a	Zoned	86
	C15d	Zoned	91
	C15d	Zoned and Annealed	111
	C14a	Zoned-Centerless Grind-Chemical Polish	113
	C15a	Zoned-Centerless Grind-Chemical Polish-Anneal	99

Table 12. (Continued)

CIBA	C20a	Zoned (oxygen)	398
	C20d	Zoned (oxygen)	445
	C21a	Zoned (oxygen)	391
	C21d	Zoned (oxygen)	429
	C21d	Zoned (oxygen) and Anneal	1512
	C20a	Zoned (oxygen)-Centerless Grind-Chemical Polish	326
	C21a	Zoned (oxygen)-Centerless Grind-Chemical Polish-Anneal	1332

Table 13. Resolved Shear Stress at the Lower Yield Point for <491> Niobium Single Crystals Deformed in Tension at Room Temperature at a Strain Rate of 1.7×10^{-4} sec^{-1}

Source	Spec.	Treatment	τ_{ly} (kg/mm^2)
Wah Chang	58a	Zoned	1.51
	59a	Zoned and Annealed	1.00
	59b	Zoned and Annealed	0.96
DuPont	D12a	Zoned	1.32
	D13a	Zoned and Annealed	0.83
CIBA	C14a	Zoned	1.88
	C15a	Zoned and Annealed	1.96
	C20a	Zoned (oxygen)	1.39
	C21a	Zoned (oxygen) and Annealed	0.94

Discussion

The results indicate that the CIBA material with oxygen treatment during EBFZM is an excellent source of high-purity niobium single crystals with a low Ta and W content. The high-temperature anneal was very effective in attaining high resistance ratios and low flow stresses. The annealed CIBA material had a flow stress (τ_{1y}) of 940 g/mm^2 with a resistance ratio of 1330. The results for the DuPont starting material were equally good but the higher Ta and W content (i.e., about 270-ppm Ta and 70-ppm W vs about 20-ppm Ta and 2-ppm W for the Dupont and CIBA, respectively) made it less suitable for neutron irradiation experiments. The Wah Chang niobium was least desirable as a starting material as it had about 350-ppm Ta and 270-ppm W.

The fact that a high-temperature anneal in high vacuum increases the resistance ratio and decreases the flow stress of niobium has been well documented.[95,96] However, this effect has been attributed to a purification of the metal during the anneal, particularly a reduction in oxygen and nitrogen content, and a reduction of the dislocation density. The high-temperature anneal does reduce the dislocation density.[97] However, the chemical analyses, as shown in Table 11, indicate that the anneal does not necessarily reduce the interstitial impurity content. Figure 37 is an attempted correlation between the

---

[95]G. Taylor and J. W. Christian, "The Effect of High Vacuum Purification on the Mechanical Properties of Niobium Single Crystals," Acta Met., 13, 1216-1218, (1965).

[96]M. S. Duesbery, R. A. Foxall, and P. B. Hirsch, "The Plasticity of Pure Niobium Single Crystals," Journal de Physique, Colloque C3, Supplement au n° 7-8, Tome 27, juillet-aout 1966, C3-193.

[97]R. E. Reed, H. D. Guberman, and T. O. Baldwin, "The Growth of Niobium Single Crystals with Good Crystalline Perfection," Crystal Growth, Pergamon Press, New York, 1967, 829-832.

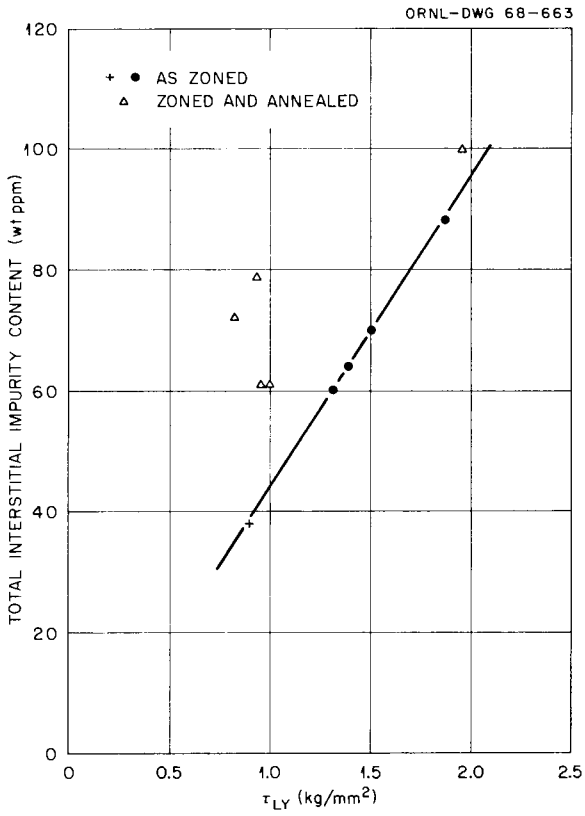

Fig. 37. Correlation of the Total Interstitial Impurity Content With Resolved Shear Stress at the Lower Yield Point for Niobium Single Crystals.

total interstitial impurity content in weight ppm and the resolved lower yield shear stress. The data point denoted by the cross is from a compression test on an as-zoned <491> niobium single crystal of Parma material which had a resistance ratio of 1420.[98] Apparently, there is a good correlation between the as-zoned impurity content and the flow stress regardless of the starting material. The data points from the annealed crystals do not correlate at all.

---

[98]R. E. Reed, "Niobium: Purification and Perfection," Radiation Metallurgy Section Solid State Division Progress Report for Period Ending January 1967, ORNL-4097, 20, (1967).

Figure 38 is an attempted correlation between the resistance ratio and the flow stress. The curve is again drawn through the data for the as-zoned material. However, in this case the data from the annealed specimens show a better correlation and fall near or on the curve. Again, the various Ta and W contents of the starting materials do not seem to appreciably affect the results.

From the correlation in Fig. 38, it can be tentatively concluded that when the interstitial impurity atom is distributed such that it is an effective electron scattering center, it is also best distributed to hinder the initiation of plastic flow, as measured by the lower yield stress. However, from Fig. 37 it can be concluded that the total interstitial impurity content does not correlate well with the flow stress. Evidently, the type of distribution of the impurity atoms is an important factor. Thus, the annealed crystals had a lower percentage of the total impurity content acting as effective electron scattering centers.

It is not clear just what type of distribution of the impurity atom would be an effective electron scattering center and also hinder the initiation of plastic flow. Complete interstitial solid solution of the impurity may have this effect as this type of distribution would have the largest electron scattering cross section. Also, this distribution could offer the largest resistance to the operation of dislocation sources. Complete interstitial solid solubility of the impurities could also reduce the number of sources available. Both of these cases would raise the stress needed to initiate plastic flow. The annealing treatment could then be assumed to reduce the amount of impurity content which is in interstitial solid solution.

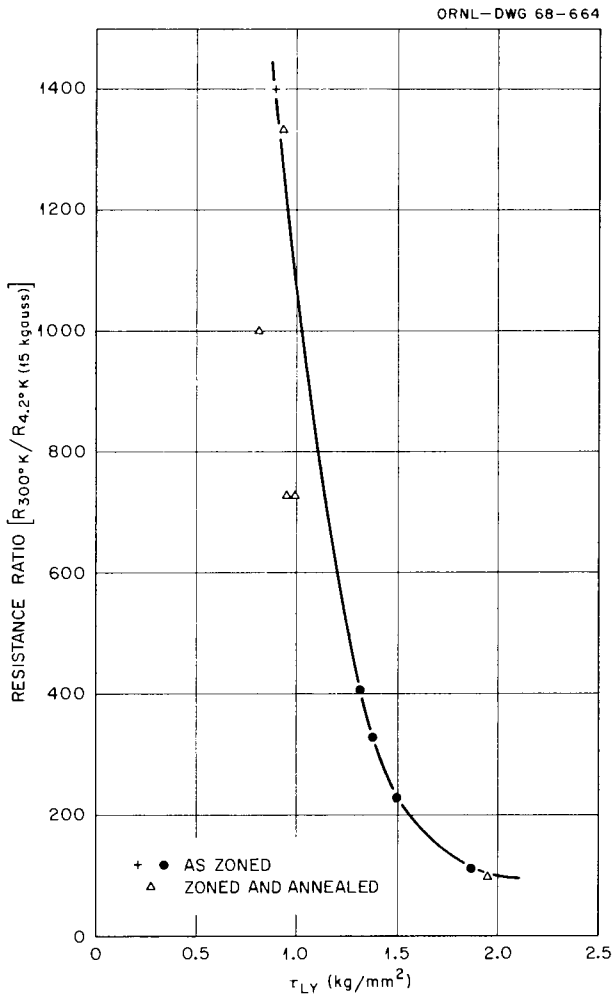

Fig. 38. Correlation of the Resistance Ratio with the Resolved Shear Stress at the Lower Yield Point for Niobium Single Crystals.

The characteristic thermal history of a point on the specimen after the EBFZM treatment would be a total amount of time near the melting point of about 3 minutes followed by a slow cool. The thermal history of the annealed specimens would be a total time of 5 hours at a temperature of 100°C below the melting point followed by a fast cool. The difference in the cooling rates is estimated to be a factor of 15. Unfortunately, such thermal histories would be expected to give just the opposite relative amounts of interstitial impurities in solid solution,

as needed to explain the data. A long time high-temperature anneal followed by a fast cool would be expected to result in more interstitial impurities in solid solution than a short time anneal followed by a slower cooling rate. Thus, perhaps some other type of impurity distribution is effective, such as clustering, formation of coherent precipitates, etc. Interaction of impurities with the dislocation substructure could also be a possibility.

Another interesting detail is apparent in Table 12. Here, the centerless ground tensile specimen after chemical polishing so that all evidence of cold work was removed (as measured by the back reflection Laue x-ray technique) exhibited resistance ratios lower than the as-zoned rods. Even annealing such a tensile specimen did not raise the resistance ratio to the level of an as-zoned and annealed specimen. The lower ratio of the chemically polished specimens could be due to the presence of hydrogen charged into the specimen during polishing. Also, residual cold work could be responsible. The fact that the high-temperature anneal does not return the resistance ratio fully to the as-zoned and annealed value may indicate that the grinding operation damages the entire cross section of the sample and the anneal does not entirely remove this effect. However, such an anneal would be expected to remove any hydrogen.

Conclusions

1. The CIBA dendritic powder was the most suitable starting material for producing high-purity niobium single crystals by EBFZM.

2. A high-temperature anneal in high vacuum will greatly increase the resistance ratio and lower the flow stress of the niobium.

3. The effect of the anneal may be a redistribution of the interstitial impurities rather than a purification.

Previous reports in this series are:

ORNL-TM-920	Period Ending June 30, 1964
ORNL-TM-960	Period Ending September 30, 1964
ORNL-TM-1000	Period Ending December 31, 1964
ORNL-TM-1100	Period Ending March 31, 1965
ORNL-TM-1200	Period Ending June 30, 1965
ORNL-TM-1270	Period Ending September 30, 1965
ORNL-TM-1400	Period Ending December 31, 1965
ORNL-TM-1500	Period Ending March 31, 1966
ORNL-TM-1570	Period Ending June 30, 1966
ORNL-TM-1700	Period Ending September 30, 1966
ORNL-TM-1720	Period Ending December 31, 1966
ORNL-TM-1825	Period Ending March 31, 1967
ORNL-TM-1941	Period Ending June 30, 1967
ORNL-TM-2020	Period Ending September 30, 1967
ORNL-TM-2090	Period Ending December 31, 1967

INTERNAL DISTRIBUTION

1–3. Central Research Library
4–5. ORNL – Y-12 Technical Library Document Reference Section
6–15. Laboratory Records Department
16. Laboratory Records, ORNL R.C.
17. ORNL Patent Office
18. G. M. Adamson, Jr.
19. T. E. Banks
20. J. H. Barrett
21. S. E. Beall
22. R. J. Beaver
23. M. Bender
24. R. G. Berggren
25. D. S. Billington
26. E. E. Bloom
27. A. L. Boch
28. E. S. Bomar
29. B. S. Borie
30. G. E. Boyd
31. R. A. Bradley
32. R. B. Briggs
33. R. E. Brooksbank
34. W. E. Brundage
35. D. A. Canonico
36. R. M. Carroll
37. J. V. Cathcart
38. A. K. Chakraborty
39. Ji Young Chang
40. G. W. Clark
41. K. V. Cook
42. G. L. Copeland
43. W. B. Cottrell
44. C. M. Cox
45. F. L. Culler
46. J. E. Cunningham
47. H. L. Davis
48. V. A. DeCarlo
49. J. H. DeVan
50. C. V. Dodd
51. R. G. Donnelly
52. J. H. Erwin
53. K. Farrell
54. J. S. Faulkner
55. J. I. Federer
56. D. E. Ferguson
57. R. B. Fitts
58. B. E. Foster
59. A. P. Fraas
60. J. H Frye, Jr.
61. W. Fulkerson
62. T. G. Godfrey, Jr.
63. R. J. Gray
64. W. R. Grimes
65. H. D. Guberman
66. D. G. Harman
67. W. O. Harms
68–70. M. R. Hill
71. N. E. Hinkle
72. D. O. Hobson
73. H. W. Hoffman
74. R. W. Horton
75. W. R. Huntley
76. H. Inouye
77. G. W. Keilholtz
78. B. C. Kelley
79. R. T. King
80. J. Komatsu
81. J. A. Lane
82. J. M. Leitnaker
83. T. B. Lindemer
84. A. P. Litman
85. H. R. Livesey
86. A. L. Lotts
87. R. N. Lyon
88. H. G. MacPherson
89. R. E. MacPherson
90. M. M. Martin
91. W. R. Martin
92. R. W. McClung
93. H. E. McCoy, Jr.
94. H. C. McCurdy
95. R. E. McDonald
96. W. T. McDuffie
97. D. L. McElroy
98. C. J. McHargue
99. F. R. McQuilkin
100. A. J. Miller
101. E. C. Miller
102. J. P. Moore
103. W. L. Moore
104. J. G. Morgan
105. F. H. Neill

106. G. T. Newman
107. T. M. Nilsson
108. T. A. Nolan (K-25)
109. S. M. Ohr
110. A. R. Olsen
111. P. Patriarca
112. W. H. Pechin
113. A. M. Perry
114. S. Peterson
115. R. A. Potter
116. R. B. Pratt
117. M. K. Preston
118. R. E. Reed
119. D. K. Reimann
120. A. E. Richt
121. P. L. Rittenhouse
122. W. C. Robinson
123. M. W. Rosenthal
124. C. F. Sanders
125. G. Samuels
126. A. W. Savolainen
127. J. L. Scott
128. J. D. Sease
129. O. Sisman
130. G. M. Slaughter
131. S. D. Snyder
132. K. E. Spear
133. I. Spiewak
134. J. T. Stanley
135. W. J. Stelzman
136. J. O. Stiegler
137. D. B. Trauger
138. R. P. Tucker
139. G. M. Watson
140. M. S. Wechsler
141. A. M. Weinberg
142. J. R. Weir, Jr.
143. W. J. Werner
144. H. L. Whaley
145. G. D. Whitman
146. J. M. Williams
147. R. K. Williams
148. R. O. Williams
149. J. C. Wilson
150. R. G. Wymer
151. F. W. Young, Jr.
152. C. S. Yust
153. A. F. Zulliger

EXTERNAL DISTRIBUTION

154–157. F. W. Albaugh, Battelle, PNL
158–160. R. J. Allio, Westinghouse Atomic Power Division
161. A. Amorosi, Argonne National Laboratory
162. R. D. Baker, Los Alamos Scientific Laboratory
163. C. Baroch, Babcock and Wilcox
164. V. P. Calkins, General Electric NMPO
165. S. Christopher, Combustion Engineering, Inc.
166. D. B. Coburn, Gulf General Atomic, Inc.
167. D. F. Cope, RDT, SSR, AEC, Oak Ridge National Laboratory
168. G. W. Cunningham, AEC, Washington
169. G. K. Dicker, Division of Reactor Development and Technology, AEC, Washington
170. D. E. Erb, Division of Reactor Development and Technology, AEC, Washington
171. E. A. Evans, General Electric, Vallecitos
172. W. C. Francis, Idaho Nuclear Corporation
173. A. J. Goodjohn, Gulf General Atomic, Inc.
174. S. P. Grant, Babcock and Wilcox
175. J. F. Griffo, Division of Space Nuclear Systems, AEC, Washington
176. R. G. Grove, Mound Laboratory
177. D. H. Gurinsky, Brookhaven National Laboratory
178. A. N. Holden, General Electric, APED
179–181. J. S. Kane, Lawrence Radiation Laboratory, Livermore

182. Haruo Kato, Albany Metallurgy Research Center, P.O. Box 70, Albany, Oregon 97321
183. L. Kelman, LMFBR Program Office, Argonne National Laboratory
184. E. E. Kintner, AEC, Washington
185. J. H. Kittel, Argonne National Laboratory
186. E. J. Kreih, Westinghouse, Bettis Atomic Power Laboratory
187. W. J. Larkin, AEC, Oak Ridge Operations
188. W. L. Larsen, Iowa State University, Ames Laboratory
189. C. F. Leitten, Jr., Linde Division, Union Carbide Corp.
190. P. J. Levine, Westinghouse Advanced Reactor Division, Waltz Mill Site, Box 158, Madison, Pa. 15663
191. J. J. Lombardo, NASA, Lewis Research Center
192. J. H. MacMillan, Babcock and Wilcox
193. C. L. Matthews, RDT, OSR, AEC, Oak Ridge National Laboratory
194. M. McGurty, General Electric, NMPO
195. A. Mullunzi, Division of Reactor Development and Technology, AEC, Washington
196. M. Nevitt, Argonne National Laboratory
197. R. E. Pahler, Division of Reactor Development and Technology, AEC, Washington
198. S. Paprocki, Battelle Memorial Institute
199. W. E. Ray, Westinghouse Advanced Reactor Division, Waltz Mill Site, Box 158, Madison, Pa. 15663
200. W.L.R. Rice, AGMR, AEC, Washington
201. B. Rubin, Lawrence Radiation Laboratory, Livermore
202. F. C. Schwenk, Division of Reactor Development and Technology, AEC, Washington
203. W. F. Sheely, Division of Research, AEC, Washington
204. P. G. Shewmon, Argonne National Laboratory
205–207. J. M. Simmons, Division of Reactor Development and Technology, AEC, Washington
208. L. E. Steele, Naval Research Laboratory
209. R. H. Steele, Division of Reactor Development and Technology, AEC, Washington
210–212. D. K. Stevens, Division of Research, AEC, Washington
213. A. Strasser, United Nuclear Corporation
214. A. Taboada, Division of Reactor Development and Technology, AEC, Washington
215. A. Van Echo, Division of Reactor Development and Technology, AEC, Washington
216. James Watson, Gulf General Atomic, Inc.
217. C. E. Weber, AEC, Washington
218. J. F. Weissenberg, RDT, OSR, General Electric, NMPO
219. G. W. Wensch, Division of Reactor Development and Technology, AEC, Washington
220. G. A. Whitlow, Westinghouse Advanced Reactor Division, Waltz Mill Site, Box 158, Madison, Pa. 15663
221. E. A. Wright, AEC, Washington
222. Laboratory and University Division, AEC, Oak Ridge Operations
223–237. Division of Technical Information Extension